The origin of double-peak emission-line Galaxies

Daniel Maschmann

PSL
UNIVERSITÉ PARIS

THÈSE DE DOCTORAT
DE L'UNIVERSITÉ PSL

Préparée à l'Observatoire de Paris
Carried out at Paris Observatory

L'origine des galaxies à raies d'émission en doubles-pics
The origin of double-peak emission-line galaxies

Soutenue par
Defended by

Daniel Maschmann

Le 20 septembre 2022
20th September 2022

École doctorale n°127
Doctoral School n°127

Astronomie et Astrophysique d'Ile-de-France

Spécialité
Speciality

Astronomie et Astrophysique
Astronomy and Astrophysics

LERMA l'Observatoire de Paris

Composition du jury :
Composition of the Jury:

Hélène Sol Directrice de recherche, LUTH - Observatoire de Paris	*Présidente du jury*
Anne-Laure Melchior Maîtresse de conférence, LERMA - Observatoire de Paris	*Directrice de thèse*
Françoise Combes Professeure, LERMA - Observatoire de Paris	*Directrice de thèse*
Sara Ellison Professeure, University of Victoria	*Rapporteure*
Karen Masters Professeure, Haverford College	*Rapporteure*
Igor Chilingarian Astronome, CfA Harvard and Smithonian	*Examinateur*
Philippe Amram Professeur, Laboratoire d'Astrophysique de Marseille	*Examinateur*

Andromeda nebula (Chambers 1904, p.6)

> "There is one elliptic nebula which stands out beyond all the rest, yet its great size, brilliancy, and peculiar features forbid its being regarded as a typical elliptic nebulae. I am here alluding to the "Great Nebulae in Andromeda," Messier's 31st. Its ellipticity is considerable; it is likewise very long, and has a bright central condensation which renders it readily discoverable by the naked eye on a clear night not far from the star η Andromeda of magnitude $4\frac{1}{2}$. [...] No telescope has yet resolved this object distinctly into stars, though several hundred stars have been counted within its limits. This object is, however, probably stellar, and may one day be proved to be such." (Chambers 1904, p. 116-117)

I cannot remember the exact moment when I was shown a picture of a galaxy and told that it was a galaxy consisting of billions of stars situated outside our Galaxy, the Milky Way. My parents gave me books about space and the Universe from an early age on, and for me this knowledge seemed natural. What Chambers wrote in 1904 in his book 'The story of the stars', however, is simply a description of an object that is a mystery. While reading such texts, I try to put myself in such a perspective and situations. What was it like to look at the Andromeda nebula and wonder about its nature? And what must that feeling of amazement have been like when he found out later? With thoughts like these, I ask myself what am I looking at all the time without any clue of the underlying truth which might be general education one day in the future?

Abstract

A central aspect in understanding how galaxies evolved over cosmic time is to characterise their mass growth. Galaxy mergers, in particular, play an important role, since they can transform the galaxy's morphology and fuel star formation. Since galaxy mergers can rapidly relax after colliding or cannot be identified as such due to a lack of resolution, detection methods are crucial to study them. Double-peak emission-line galaxies have been used extensively in order to identify dual active galactic nuclei which are late stages of galaxy mergers. In this thesis, a more general discussion on the phenomenon of double-peak emission-line galaxies is presented. To this end, a double-peak galaxy sample consisting of 5 663 galaxies is selected from the Sloan Digital Sky Survey and the properties are studied in detail. To get a deeper understanding in the underlying mechanisms, double-peak signatures arising in disc models and simulations of isolated galaxies and galaxy mergers are analysed. To further understand the connection between star formation and double-peak emission-line galaxies molecular gas observations, conducted with the IRAM 30m telescope, are presented and analysed. In conclusion, there is a clear favouring of bar structures and minor mergers, which can explain the observed double-peak signatures and are also consistent with the characteristics found. This thesis shows that double-peak emission-line galaxies are an important aspect for high redshift observations and present a potential method of identifying galaxy mergers in larger upcoming surveys.

Résumé

La caractérisation de la croissance de la masse des galaxies est centrale pour la compréhension de leur évolution au cours du temps cosmique. Les fusions de galaxies jouent un rôle particulièrement important car elles peuvent transformer la morphologie des galaxies et alimenter leur formation d'étoiles. Comme les galaxies issues d'une fusion peuvent atteindre un état dynamique stabilisé rapidement après une fusion ou qu'il se peut qu'elles ne soient pas identifiées comme issues d'une fusion en raison d'un manque de résolution, les méthodes de détection sont cruciales pour les étudier. Les galaxies à raies d'émission doubles ont été beaucoup utilisées afin d'identifier les noyaux actifs de galaxies doubles qui correspondent à des étapes tardives des fusions de galaxies. Dans cette thèse, une discussion plus générale sur le phénomène des galaxies à raies d'émission à doubles-pics est présentée. À cette fin, un échantillon de galaxies à doubles-pics composé de 5663 galaxies est sélectionné dans le Sloan Digital Sky Survey et ses propriétés sont étudiées en détail. Afin de mieux comprendre les mécanismes sous-jacents, les signatures de doubles-pics apparaissant dans les modèles de disques et les simulations de galaxies isolées et de fusions de galaxies sont analysées. Pour mieux comprendre le lien entre la formation d'étoiles et les galaxies à raies d'émission à doubles-pics, des observations de gaz moléculaire, réalisées avec le télescope de 30m de l'IRAM, sont présentées et analysées. En conclusion, les barres et les fusions mineures sont nettement privilégiées comme explications des signatures à doubles-pics car cohérentes avec les caractéristiques trouvées. Cette thèse montre que les galaxies à raies d'émission à doubles-pics sont un aspect important pour les observations à haut redshift et représentent une méthode potentielle d'identification des fusions de galaxies dans les grands relevés à venir.

Danksagung, Remerciement, Acknowledgement

Ich erinnere mich noch ganz genau, wie wir als Kinder Sternschnuppen am frühen Nachthimmel beobachtet haben. Mein Vater wusste immer ganz genau was gerade am Himmel zu sehen war und zeigte meinem Bruder und mir mit seinem Teleskop die Planeten wie Jupiter, Mars oder Saturn. Für mich war das unglaublich aufregend, da mir die Größenordnungen, welche wir dort betrachteten, unvorstellbar vorkamen. Ich habe in diesen Nächten nicht beschlossen, in meinem späteren Leben eine Doktorarbeit über Galaxien zu schreiben. Der Weg dahin war ganz und gar nicht linear und bleibt mir als ein spannendes Abenteuer im Gedächtnis. Aber eine Leidenschaft hat mein Vater schon früh in mir geweckt: die Wissenschaft. Mit vielen Experimenten hat mein Vater uns schon als Kinder die Welt erklärt und unsere Neugier genährt. In der Mittel- und Oberstufe war es auch mein Vater, welcher mir maßgeblich die Mathematik beigebracht hat und mich somit gut auf die Universität vorbereitet hat. Vielen Dank Papa, dass Du den Wissenschaftsgeist in mir geweckt hast und ihn stets mit neuem Wissen gefüttert hast.

Den Weg, welchen ich im Laufe meines Studiums eingeschlagen habe, führte mich an viele verschiedene Orte und zeigte mir die unterschiedlichsten Kulturen. Dabei waren fremde Sprachen das Werkzeug, das mir Tür und Tor geöffnet hat. Besonders hat meine Mutter mich begeistert, in andere Sprachen und Kulturen einzutauchen. Sie hat mir immer geholfen, English und Französisch zu lernen und hat mich stets ermutigt auch die gelernten Sprachen anzuwenden. Ohne diese Inspiration wäre ich sicher nicht für ein Jahr nach Kamerun gegangen oder wäre nicht so einfach auf die Idee gekommen, meine Doktorarbeit in einem anderen Land zu schreiben. Vielen Dank Mama, dass Du mir das nötige Werkzeug gegeben hast, um in die Welt hinauszugehen. Für mich ist es immer ein schönes Gefühl heimzukommen, mit meiner Familie Zeit zu verbringen und mich mit euch über die neusten Ereignisse auszutauschen. Danke Mama, Papa und Tim, dass ihr mich unterstützt und mir einen so guten Rückhalt bietet.

Après mon Erasmus à l'Observatoire de Paris, il était clair pour moi que je voulais faire une thèse en astrophysique. Mais le chemin entre les ambitions initiales et l'obtention d'un poste de doctorat n'est pas de tout repos. Je suis donc heureux qu'Anne-Laure, qui avait encadré mon stage pendant mon année Erasmus, m'ait aidé à retrouver le chemin de l'Observatoire. Je te remercie particulièrement d'avoir pris le temps de continuer à correspondre avec moi alors que j'étais en Allemagne pour poursuivre nos recherches, ainsi que de m'avoir appris à rédiger et à publier des articles scientifiques. Mais je te remercie surtout de m'avoir supporté et de t'être battue pour que je trouve un poste comme doctorant à l'Observatoire afin que nous puissions continuer à faire des recherches ensemble. Merci d'avoir été une directrice de thèse aussi formidable et attentionnée. Je considère ma thèse de doctorat comme la période où j'ai le plus appris dans ma vie. C'était une véritable aventure de se plonger dans ces sujets si divers, d'observer des galaxies inexplorées avec des télescopes et d'ajouter, chemin faisant, une petite pierre à la science. Ce voyage scientifique a été particulièrement guidé par Françoise. Je te suis très reconnaissant d'avoir toujours pris le temps de répondre à mes questions et de pouvoir remettre en perspective tous les sujets grâce à ton impressionnante vue d'ensemble.

Pour moi, l'Observatoire de Paris est un lieu particulier pour les rencontres qu'on y fait et desquelles découlent des collaborations. J'ai été particulièrement heureux de travailler avec Anaelle. Je suis très reconnaissant que tu m'aies appris tant de choses sur les simulations et la dynamique des galaxies et c'était formidable de publier les résultats de notre travail commun. Merci pour tous les moments agréables et le meilleur gâteau au chocolat à la framboise. Merci aussi de m'avoir aidé à améliorer mon français. Grâce à toi je ne fais plus de fautes lorsque je conjuguer des verbes en français.

Auch Dir, Barbara, möchte ich ganz herzlich danken für die tolle gemeinsame Forschung und die schönen Kaffeepausen. Mit Dir gemeinsam zu programmieren und wie Detektive Galaxiefusionen zu rekonstruieren, bleibt mir als tolle Erinnerung im Gedächtnis. Merci aussi au partenair de bureau le plus cool de l'Observatoire, Romain, et aux belles discussions sur Dieu et le monde que nous avons eues pour nous aider à procrastiner un peu.

Eine Doktorarbeit muss nicht nur wissenschaftlich betreut werden, denn man durläuft häufig Höhen und Tiefen. Danke Martina, dass Du immer ein offenes Ohr für alle meine Probleme hattest und mir immer geholfen hast, nicht den Kopf hängen zu lassen. Vielen Dank auch, dass du mich immer wieder dazu gebracht hast, meine Arbeit zu planen und nicht monatelang in Details zu versinken. Ich werde unsere langen Gespräche sehr vermissen. Ich möchte auch Vim danken, dass er sich für mein Thema begeistert hat und mir mit viel Rat beigestanden hat. Een grote dank je wel.

When it comes to international collaborations Igor is definitely someone who taught me so much and helped me being ambitious with my research. I am happy that we both share a passion about mountains and climbing and that we find ways to collaborate on some common topics from time to time. I would also like to thank Ivan who found on multiple occasions time to answer questions on spectroscopy. Of course, I can't talk about my Russian friends without mentioning Kirill and Anton. Thank you so much for the nice evenings with nice discussions we had.

I still remember very long discussions on double-peak emission-line galaxies at the IAP with Gary and Anne-Laure. Thank you Gary for taking your time at the beginning of my thesis to understand our research and helping us to figure out what double peak galaxies might be.

I would like to thank Sara and Karin who not only participated in my thesis jury but also took a huge effort to review this manuscript. With your questions and comments you helped me a lot to improve my manuscript and gave me guidance to defend this thesis. I, furthermore, would like to thank Hélène and Philippe for being part of my thesis jury and for supporting me during this stressful time. I really enjoyed answering your questions and the later discussion

Il y a de ces moments dont on se souvient avec joie et qui nous rendent heureux quand on y repense. Avec toi, Quentin, j'en ai vécu d'innombrables. Tu as été le colocataire le plus cool que j'ai jamais eu et tu m'as appris à apprécier le chaos à sa juste valeur. Partir en randonnée, explorer les catacombes de Paris ou simplement passer une soirée à cuisiner de bonnes choses avec un verre de vin ne sont que quelques-uns de ces moments si spéciaux que j'ai passés avec toi.

J'ai passé une partie non-négligeable de mon temps à Paris à en parcourir les souterrains. J'y ai découvert un monde qui n'était pas affecté par l'agitation ou le stress. Je n'aurais jamais découvert les plus beaux endroits des catacombes parisiennes en les explorant seul. Je suis profondément reconnaissant envers tous ces inconnus qui se sont rapidement transformés en amis dans ces tunnels sans fin. Ils m'ont permis de prendre part à cette culture passionnante. Je tiens à remercier tout particulièrement les créateurs de Katastrophy, car votre atelier m'a offert la plus belle des récompenses le soir après la remise de ce manuscrit.

Liebe Marie, ich bin so froh, dass wir uns gefunden haben. Auch wenn Du in einem anderen Fach promovierst, hat es sich so angefühlt, als würden wir gemeinsam promovieren. Du bist die Beste und ich finde wir können uns gegenseitig so gut unterstützten, begeistern und zuhören.

Je tiens aussi à remercier tout particulièrement l'excellente équipe de LERMA. Vous êtes vraiment les meilleurs et c'était toujours un plaisir de faire les fous avec vous pendant les pauses et pendant le travail. Je voudrais remercier tout particulièrement Elise, Woihiba, Tarikakan, Phillippe, Juliette, Samuel, clements Muriel et Pélagie. Mais je suis aussi très reconnaissante aux innombrables autres personnes que je n'ai pas citées pour leur gentille compagnie.

Für mich war es schon immer einer der schönsten Abenteuer, raus in die Natur und auf Wanderschaft zu gehen. Für mich ist dies einer der stärksten Gegenpole zum Arbeitsleben und ich bin dankbar, dass ich die besten Weggefährten dafür gefunden habe. Danke Ragna, Andreas, Laura, der eine David und der andere David, dass man mit euch die Welt erkunden kann.

Contents

1 Scientific context **1**

1 Introduction . . . 1
2 The galaxies outside the Milky Way . . . 3
2.1 Galaxy taxonomy . . . 3
2.2 Galaxy formation and evolution . . . 8
2.3 Galaxy mergers . . . 9
3 The view of galaxies at different wavelengths . . . 11
3.1 The spectral energy distribution of a star forming spiral galaxy . . . 11
3.2 Gas in galaxies . . . 15
3.3 Colour, SED and morphology . . . 18
3.4 Properties of active galactic nuclei . . . 21
3.5 Ionised gas diagnostics . . . 24
4 Star formation in galaxies . . . 25
4.1 Star formation rate estimators . . . 26
4.2 The stellar mass of a galaxy . . . 28
4.3 The main sequence of star-forming galaxies . . . 28
4.4 Evolution of star formation over cosmic time . . . 30
5 Kinematic signatures in ionised gas emission-lines . . . 32

2 Double-peak emission-line galaxies **37**

1 Double-peak emission-line galaxies in the SDSS catalogue . . . 39

3 Double-peak emission lines in modelled and simulated galaxies **69**

1 The mechanisms behind double-peak emission-line galaxies . . . 71

4 Molecular gas in double-peak emission-line galaxies **93**

1 Central star formation in double-peak gas rich radio galaxies . . . 95

5 Conclusion **129**

1 The current state of double-peak emission line galaxies . . . 129
2 High resolution observations . . . 130
3 Resolving kinematics with integrated field spectroscopy . . . 131

4 Double-peak emission line galaxies in cosmological simulations 131
5 Exploring the high-redshift Universe 132
6 Final remark 132

Bibliography **133**

List of Figures

1.1 The Hubble sequence. . . . 4
1.2 Sérsic Profile of a galaxy . . . 5
1.3 SDSS band-pass filters . . . 6
1.4 SDSS optical spectroscopy . . . 6
1.5 Galaxy distribution in the SDSS . . . 7
1.6 Star formation history from Madau & Dickinson (2014) . . . 9
1.7 Illustration of different galaxy mergers . . . 10
1.8 Spectral energy distribution of a spiral galaxy . . . 12
1.9 HI and CO spectroscopic observation of galaxies . . . 15
1.10 Ionised-gas emission-line spectra . . . 17
1.11 Colour-magnitude diagram of galaxies . . . 19
1.12 Galaxy SED and morphology as seen with PEGASE 3 . . . 21
1.13 SED of the galaxy CGCG 218-007 hosting an AGN . . . 22
1.14 BPT diagram . . . 24
1.15 SED of stellar populations and their star-formation history . . . 26
1.16 Illustration of the main sequence of star-forming galaxies . . . 29
1.17 Galaxy evolution on the main sequence over cosmic time . . . 31
1.18 Long-slit spectroscopy of a double-peak galaxy observed by Gerke et al. (2007) . . . 33
1.19 Chandra X-ray observations from Comerford et al. (2011) . . . 34
1.20 Radio observation of a dual AGN from Müller-Sánchez et al. (2015) . . . 34

CHAPTER 1

Scientific context

1 Introduction

During a moonless night in an area with no significant light pollution, it is possible to see up to 2000 stars on the night sky with bare eyes. While star gazing, one will notice, that some regions are more crowded than others as if they are a part of a large pile of stars. The largest structure, we can see, stretches across the entire sky like a stripe, which is called in Western cultures the Milky Way. If you are, for example, in a central European country and look at the night sky during the early night in Autumn, you can find in the east an object which seems like a nebula. You have to know exactly in which direction you must look (00h 42m 44.3s +41° 16′ 9″) and with naked eyes you can vaguely make out a faint nebula, the Andromeda Nebula. If you use a telescope, you can clearly see an elliptical structure that is quite bright in its centre. You can find many more of these nebulae whereas the Andromeda nebula, also known as Messier's 31 (M31), is the brightest one (Messier 1781). Today, we know that these nebulae are galaxies outside our own Galaxy, the Milky Way. But how do we know this?

At the beginning of the last century, Henrietta Leavitt found a way to measure the distance to Cepheid variable stars. She discovered a close relation between the absolute magnitudes and the pulse frequency of these stars, allowing the estimation of their distance from the difference between apparent and absolute magnitude (Leavitt 1908; Leavitt & Pickering 1912). This allowed a first estimation of the size of the Milky Way. Using this method, Harlow Shapley measured the distance to 69 globular clusters and estimated and found the longest distance to be 67 000 pc (Shapley 1918).

On 26 April 1920 at the Smithsonian Museum of Natural History, a fundamental debate on the nature of nebulae took place. The main actors of this debate were Harlow Shapley and Heber Curtis. Today, this debate is known as 'The Great Debate'. Shapley was convinced that these nebulae are situated inside our own Milky Way which makes up the entire Universe. One major argument was based on estimated size of the Milky Way. If one considers the Andromeda nebula to be an individual system like the Milky Way it would be at a distance of 10^8 light years due to its apparent size. In Shapley's opinion, this distance was not imaginable and a diffuse nebular inside the Milky Way would be more plausible (Shapley & Curtis 1921). Curtis

argued that the number of novae, which are a short bright flash of young stars, was much higher in nebulae (external galaxies) than in other parts of the Milky Way. In addition to that, he observed these events to be significantly less bright than such events known from other parts of the Milky Way. He concluded that this can only be explained if the Andromeda Nebula is a galaxy outside the Milky Way, which contains about as many stars as our Galaxy (Shapley & Curtis 1921).

In the same decade, Hubble measured the distance of about 285 000 pc to the nebulae M31 and M33, proving Curtis' idea to be correct (Hubble 1925). His distance measurements were based on the observations of Cepheid variable stars, he was able to identify in the outskirts of these nebulae. Hubble also estimated the distance to further nebulae, leading to the discovery that the more distant a galaxy is, the faster it moves away from us (Hubble 1929). Hence, the distance D to a galaxy can be calculated from a spectroscopic measurement of its recession velocity v_{rec}:

$$D = v_{rec}/H_0, \tag{1.1}$$

where H_0 is the Hubble constant, which is an empirical constant in units of $km\,s^{-1}\,/\,Mpc$. With the connection between the spectroscopic shift to redder colours and v_{rec}, one can quantify this shift with the redshift z:

$$1 + z = \frac{\lambda_{obs}}{\lambda_{emit}}, \tag{1.2}$$

where λ_{obs} and λ_{emit} are the observed and the emitted (also called rest-frame) wavelengths, respectively.

From the observational data, presented by Hubble, Georges Lemaître came up first with a theory of an expanding Universe (Lemaître 1927). He then inferred from an extrapolation to the past the idea of a Big Bang as the beginning of the Universe (Lemaître 1931). In combination with the mathematical description of a curved space time which Alexander Friedmann derived earlier from the Einstein field equation (Friedmann 1922), the foundation for modern cosmology was set. To this day, these concepts are fundamental and form the pillars of cosmology describing a flat universe, dominated by dark energy, cold dark matter and baryonic matter, called the ΛCDM-Universe. This model is assumed throughout this thesis with a parametrisation of the fraction of matter density $\Omega_m = 0.3$, the fraction of the dark energy density $\Omega_\Lambda = 0.7$ and a Hubble constant of $H_0 = 70\,km\,s^{-1}\,/\,Mpc$. In this model, the distance estimation as provided in equation 1.1 is a rough estimation and is only valid for small distances (Weinberg 1972). In fact, in an expanding universe one cannot simply measure distances as in an Riemannian space. Therefore, alternative concepts were introduced in order to discuss distances and time measurement in the Universe. When describing the Universe, the comoving distance gives estimates which do not change over time as it cancels out the expansion of the Universe. The luminosity distance gives the relation between the apparent and absolute magnitude of an object by including the expansion of the Universe. The lookback time estimates how far we are looking back to the past when observing distant objects (Peebles 1993).

Today, we know from observations that there are at least 2 trillion galaxies in the visible Universe (Conselice et al. 2016). The best estimation of the age of the Universe is 13.787 ± 0.020 billion years, estimated from observation with the Plank satellite of the cosmic microwave background which is a relic radiation from an early stage of the Universe (Planck Collaboration et al. 2020).

According to the Big Bang theory, the first atoms (mostly hydrogen and helium) formed

during the nucleosynthesis at around 10 seconds to 20 minutes after the Big Bang. This gas then collapsed into the first stars at about 100 to 400 million years after the Big Bang. Areas with higher mass concentration accumulated a larger gravitational potential and ultimately became the first galaxies. The earliest and most distant galaxy observed so far is HD1 which formed just 330 million years after the Big Bang (Harikane et al. 2022). This means that the galaxies we see today in the local Universe have had over 13 billion years to evolve. This implies that the further we look into the Universe, the further we are looking back into the past. We can thus consider observations of distant galaxies as snapshots of the Universe at an earlier age. The timescales with which galaxies rotate and internal processes happen are of the order of several hundred million years prohibiting us to observe how individual galaxies evolve. Thus, the snapshots we observe of the Universe at different ages are static.

Personally, I have to admit that the question, why galaxies look the way they do, fascinates me tremendously. And I am not alone: Galaxy formation and evolution is one of the big topics studied by the astrophysical community. Even though it seems almost impossible to converge towards well-founded theories about such objects located at unimaginable distances, I decided to contribute to this topic with my thesis. Therefore, I will give an overview of observational astrophysics in the present chapter and will explain how galaxy mergers are a fundamental part of galaxy evolution. In the second chapter, I will discuss how galaxy mergers can be detected via their spectroscopic signatures in the form of double-peaked emission lines. I will describe how I identified 5663 of these galaxies and analyse their characteristics (Maschmann et al. 2020). In order to get a deeper understanding of these galaxies, I will discuss in the third chapter analytical galaxy models and galaxy simulations in order to reproduce double-peak emission-line signatures (Maschmann et al. in revision). In the fourth chapter, I will present molecular gas observations I conducted with the IRAM 30m telescope for a sub-sample of star-forming double-peak galaxies and discuss the origin of their enhanced star formation (Maschmann et al. 2022b). I will finally conclude on the origin of double-peak emission-line galaxies in chapter five and give an outlook for future research on this field. Some figures in this thesis are adopted from the literature: namely Fig. 1.2, 1.6, 1.17, 1.18, 1.19 and 1.20. This is stated with the according reference in the title of each figure. All other figures are produced by myself, including all figures in the peer review journal articles which are parts of this thesis, with the exception of Fig. 2 and 10 in Chapter 3.

2 The galaxies outside the Milky Way

2.1 Galaxy taxonomy

As it became clear after the Great Debate that the observed nebulae are outside our own Galaxy, the Milky Way, a new field of research emerged: extra-galactic astronomy. The first steps in order to systematically study these objects was to find recurring features and characterise them. Just as a taxonomist systematically describes the biological world of our planet in order to later develop theories from the patterns found, astronomers started categorising galaxies at the beginning of the last century. Edwin Hubble conducted a systematic description of galaxies observed in the Northern Hemisphere and gathered all possible characteristics such as brightness and their approximate distance (Hubble 1926). He gathered 400 galaxies and studied their morphology. By looking at such a large sample of galaxies, it is immediately apparent that

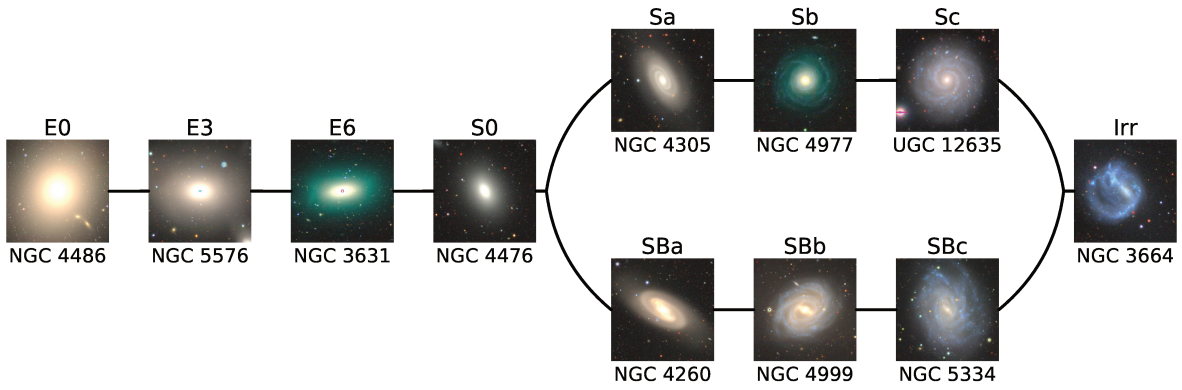

Figure (1.1) The Hubble sequence. This diagram is based on the classification scheme established in Hubble (1926, 1927, 1936) and divides galaxies into different morphological categories. The main features are spheroidal bulges, disc- and bar structures. To represent each galaxy types, *rgb*-images from the Legacy Survey (Dey et al. 2019) are shown to illustrate their morphology. The four galaxies on the left side are mainly characterised by their large central bulge. The galaxy on the left (E0) has a perfectly spherical shape whereas the galaxies E3 and E6 exhibit an increasingly flatter profile. The galaxy noted as S0 is still dominated by a bulge but shows a clear disc structure. These galaxy types are known as early-type galaxies. On the right hand side, six spiral galaxies are presented in two categories: on top (resp. bottom), disc galaxies with a central bulge (resp. bar) are shown. Barred galaxies are indicated with a 'B' in their type name. From left to right, the domination of their bulge/bar intensity decreases. On the right, an irregular galaxy is shown exhibiting none of the main features discussed above. To identify the shown galaxies, their names are denoted underneath each snapshot.

two main patterns occur most frequently: elliptical, bulge-like shaped galaxies and galaxies exhibiting a disc as expected due to rotation. Hubble developed a scheme known as the Hubble sequence which is shown in Fig. 1.1. Disc galaxies can be further distinguished as some have a central bulge and some an additional bar structure. Also elliptical galaxies can be divided according to their ellipticity (Hubble 1927, 1936). Later, Gérard de Vaucouleurs found further features how to distinguish the morphology of galaxies (de Vaucouleurs 1959). He found a more precise subdivision for various bar structures that he observed and that Hubble's sequence was insufficient.

Elliptical galaxies are often called 'early-type' galaxies and disc galaxies 'late-type'. However, spiral galaxies with massive bulges i.e. of type Sa or SBa are often called early-type spiral galaxies. This nomenclature was first introduced in Hubble (1926) and is based on the assumption that the Hubble sequence describes the evolution of galaxies, similar to an early-to-late evolution of stars. From left to right, elliptical galaxies would evolve into lenticular galaxies and finally transform into spiral galaxies either with or without a bar. As discussed in Baldry (2008), this interpretation is wrong and was never intended by Hubble. As will be discussed in Sect. 2.3, one can consider a galaxy evolution in the opposite direction.

2.1.1 Bulge and Disc decomposition

In the early phase of extra-galactic astronomy, galaxies were categorised by certain features such as bulges, bars or a discs. The next step is to describe such features with the help of models, in order to describe them in a mathematical way. An empirical model, known as the de Vaucouleurs's law, describes the surface brightness profile of elliptical galaxies (de Vaucouleurs

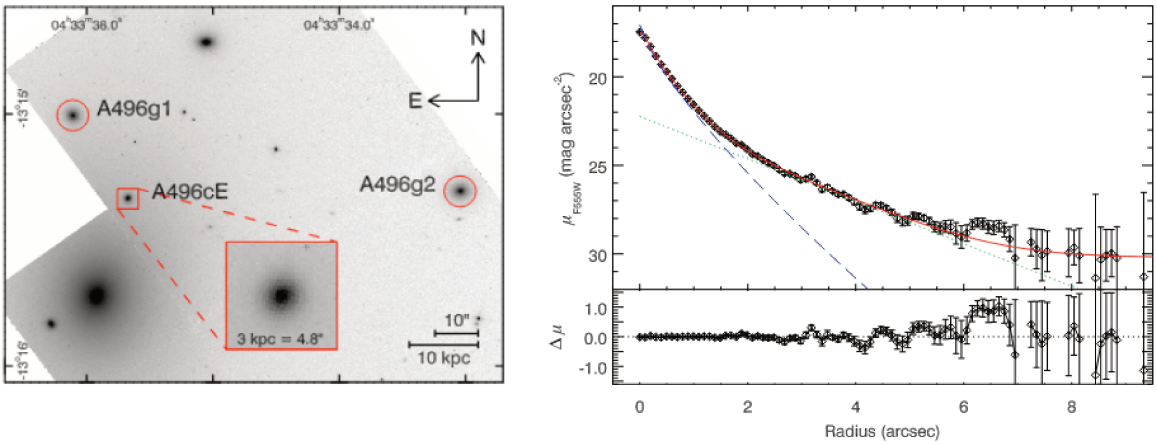

Figure (1.2) Compilation of figure 1 and 2 from Chilingarian et al. (2007). On the left panel, HST WFPC2 observations of the galaxy cluster Abell 496 are shown. On the right panel, the best fit for A496cE with a two-component Sérsic profile to the HST filter F555 observation is shown with the residuals on the bottom. The dashed blue line show the Sérsic function and the dotted green line the exponential disc component the combination of the two components is shown with red lines.

1948):

$$I(R) = I_e \exp\left\{ -7.669 \left[\left(\frac{R}{R_e} \right)^{1/4} - 1 \right] \right\}, \tag{1.3}$$

where R_e is the radius of the isophote containing half of the total flux and I_e is the surface brightness at the radius R_e. This model has been further developed into a more general model, the Sérsic profile, which can describe not only elliptical galaxies, but also spiral galaxies (Sérsic 1963). This model has an additional parameter the Sérsic index n:

$$I(R) = I_e \exp\left\{ -b_n \left[\left(\frac{R}{R_e} \right)^{1/n} - 1 \right] \right\} \tag{1.4}$$

where b_n is a dimensionless scale factor depending on the Sérsic index. This quantity can be computed using the gamma function Γ and the incomplete gamma function γ by satisfying the relation $\gamma(2n; b_n) = \frac{1}{2}\Gamma(2n)$ (Ciotti & Bertin 1999). The Sérsic profile with an Sérsic index $n = 4$ reduces to a de Vaucouleurs profile as presented in equation 1.3. Normal galaxies have a Sérsic index between 1/2 and 10, where an $n = 1$ Sérsic profile corresponds to an exponential function and is used to model a disc. The Sérsic index correlates with the quantities such as the galaxy brightness, size and concentration and can therefore be used as a proxy to the morphological type (Trujillo et al. 2001).

As can be seen in the Hubble sequence (see Fig. 1.1), many galaxies composed of two main components: a bulge and a disc. In fact, only rare cases of pure disc galaxies or elliptical galaxies can be best described with a single Sérsic profile. Often two components are needed: one for a bulge and a second component with a Sérsic index $n = 1$, which describes an exponential disc component. In Fig. 1.2, an example of a galaxy fitted with a two-component Sérsic fit by Chilingarian et al. (2007) is shown. Meert et al. (2015) fitted systematically a single Sérsic profile or a Sérsic profile plus an exponential component to a sample of 7×10^5 galaxies of the SDSS (see Sect. 2.1.2). They found that for about 90 % of this sample the galaxies are best described by a two-component Sérsic fit.

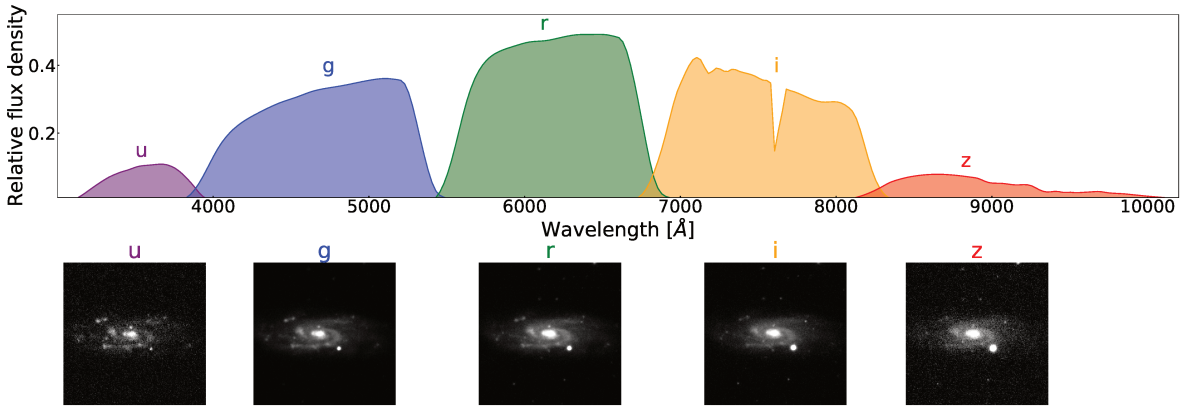

Figure (1.3) Band-pass filter system of the SDSS. On the top panel, the response function of each photometric filter used by the SDSS (for detailed description of the photometric system see Fukugita et al. 1996) is shown. On the bottom panel, a galaxy observed by the SDSS with each individual band is presented. It can be seen that e.g. the u and the z-bands show more noise which is due to their lower efficiencies. However, as further discussed in Sect. 3.1, the u-band filter is more affected by dust inside the observed galaxy in comparison to the band-pass filter at larger wavelengths.

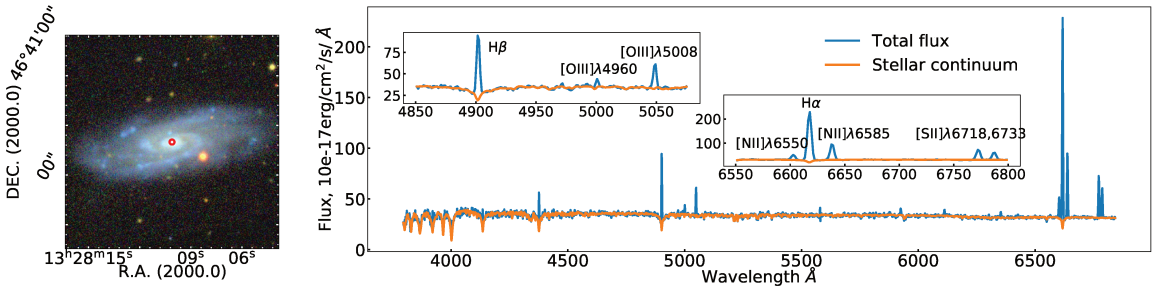

Figure (1.4) A spectroscopic observation of the central 3″ with the SDSS spectrograph. On the left, an rgb-image composed from the photometric u, r and i-bands of the SDSS (see Fig. 1.3) is displayed and the central spectroscopic observation is marked by a red circle. The corresponding spectrum is shown on the right. In blue, the total flux is shown and in orange, the best fit of the stellar continuum is shown. To highlight spectral features like ionised gas emission lines two zooms into the regions around the Hβ and Hα emission lines are shown. (For a detailed discussion on the significance of the spectra features, see Sect. 3.5)

2.1.2 The Sloan Digital Sky Survey: mapping the Universe

Galaxy Evolution is a subject that has seen many successes over the last century due in particular to ever-improving telescopes. One invention stands out among others: photo detection based on Charge-Coupled Device (CCD) (Boyle & Smith 1970). This technology made it possible to acquire digital photometric and spectroscopic observations, allowing a larger community to benefit from observations. Most importantly, it enabled the creation of survey programmes that systematically mapped parts of the sky and measured the redshifts of galaxies using spectroscopic imaging. Such surveys allow astronomers to test their theories on sufficiently large samples and to make statistically significant statements. The first survey which gathered the redshift of 2401 galaxies was the Center for Astrophysics (CfA) redshift survey (Huchra et al. 1983) and allowed to estimate the spatial distribution of galaxies. The data suggested a clustering structure of galaxies but it was the second redshift survey CfA2, consisting of 18 000 galaxies, which revealed the structure of the Universe (Geller & Huchra 1989). In fact, galaxies are distributed in a 3D structure which resembles a honeycomb or bubbles enclosing large voids.

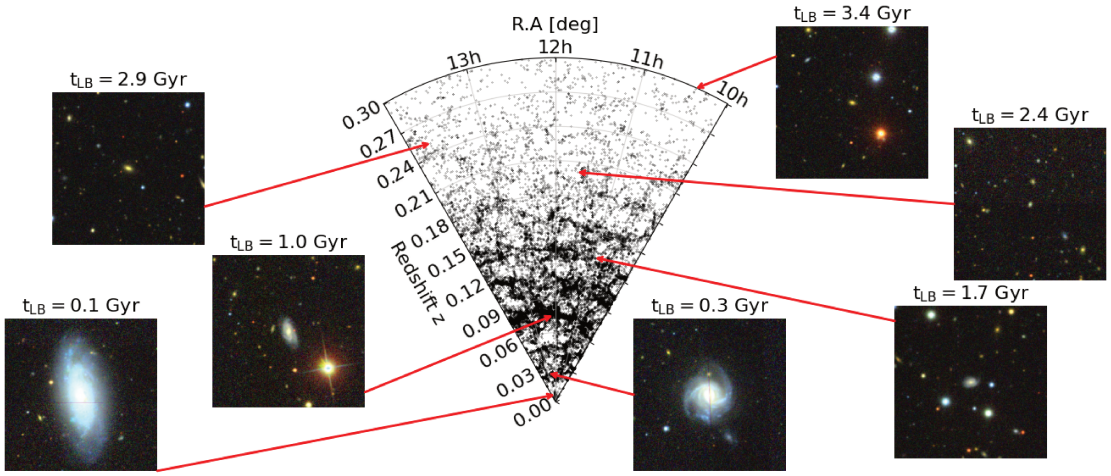

Figure (1.5) Galaxy distribution in the SDSS. Galaxies from the sky region of 10h < R.A. < 14h and 0° < Dec. < 6° with SDSS spectroscopic measurements. The distribution of the R.A. and the redshift is shown on a polar diagram in the centre. Since the redshift is a surrogate for the distance of a galaxy, this representation visualises the structure of the Universe. To illustrate the distances of galaxies at different redshifts, six galaxies are shown with SDSS *rgb*-images. For each galaxy, the lookback time t_{LB} is indicated on top of the snap shots.

The largest redshift survey today is the Sloan Digital Sky Survey (SDSS) which observed about one third of the sky with multi-colour imaging and provides spectra of more than 3 million objects using different instruments (for Data Release (DR) 17 see Abdurro'uf et al. (2022) and references therein). The first complete sample, including galaxy spectra, was finalised in 2009 and encompassed more than 920 000 galaxies (Abazajian et al. 2009). The photometric observations are performed using a CCD camera with 5 colour bands: u, g, r, i and z (Fukugita et al. 1996). The response function of the SDSS photometric systems to the observation of a galaxy is shown in Fig. 1.3 for each band. The spectral observations cover the central 3″ of each galaxy which are above the Petrosian (1976) r-band magnitude limit of $r = 17.77$. This results in a volume-limited galaxy sample (Malmquist 1925) till a redshift of $z = 0.35$ and a flux-limited sample till a redshift of $z = 0.55$. The spectra are observed in the wavelength range 3800 - 9200 Åwith an average resolution of $\lambda/\Delta\lambda = 2000$ (Abazajian et al. 2009). Such a spectral observation is shown in Fig. 1.4.

In Fig. 1.5, the spatial distribution of galaxies observed by the SDSS is presented up to a redshift of $z = 0.3$. In addition to this, the *rgb*-images of galaxies randomly selected at different redshifts are shown. For the galaxies of the local Universe at a redshift $z < 0.05$, the morphological structure is well visible, whereas for the galaxies at $z \geq 0.1$, it is challenging to guess their morphological type. Galaxies, in the far outskirts of this distribution, appear only as dots. Galaxies, at a redshift of $z = 0.2$, are situated at a comoving distance of about 800 Mpc. As the speed of light is constant, the time light needs to reach us from this distance is 2.4 Gyr which is also known as the lookback time, t_{LB}. This means that we can see the SDSS as a collection of snapshots of the Universe at different stages of evolution. Thus, the SDSS is an excellent basis to studying the properties of the Universe today and how galaxies evolved in the last few billion years.

2.2 Galaxy formation and evolution

Galaxies, as we observe them with telescopes, formed after the Big Bang. A decisive factor in their formation was dark matter, which collapsed and formed local gravitational potentials. Baryonic matter, on the other hand, was still in equilibrium with photons in the first hundred Myr. Only after these were decoupled in the so-called last scattering, the gas could fall into the dark matter halos and form the first galaxies. This was about 400 Myr after the Big Bang. Looking at the various galaxy categories seen in the local Universe (see Sect. 2.1), one quickly comes to the question of how such galaxies were formed and how they could become so large. Two types of models have been used to explain this: top-down and bottom-up. The former assumes that a large gas cloud collapses and forms a large galaxy without receiving material from outside. The bottom-up model, on the other hand, assumes that small components form and grow in a hierarchical principle into a large galaxy through many mergers. Eggen et al. (1962) described that rotating discs were formed from gas clumps that have grown in the early Universe and which introduced an angular momentum by falling into the galaxy. In the following, the disc cooled down, enabling stars to form in these clouds (for a review, see Gott 1977). However, this model was actually disfavoured because it would not allow the presence of stars in a halo, which is exactly what is observed in the outskirts of spiral galaxies. In order to explain the chemical abundances, morphologies and the colours of globular clusters in the halo of our Milky Way, Searle & Zinn (1978) suggested that protogalactic fragments must have fallen into the Galaxy significantly later than the epoch of the formation of its central region. They were not able to explain their observations using a top-down model and suggested a "*more chaotic origin for the Galaxy*" (Searle & Zinn 1978).

Such a model was suggested by White & Rees (1978) where many gas clouds formed small progenitors of the size of globular clusters and then subsequently merged together, building up more and more massive galaxies. A more complete picture is given with simulations in Steinmetz & Navarro (2002): they reproduced different morphological types with N-body/gas-dynamical simulations. They found that disc structures formed by smooth accretion of cooled gas and spheroid galaxies are the result of the destruction of pre-existing discs during mergers. Furthermore, they described how bar structures are triggered by satellites causing tides in the disc. In particular, they demonstrated that smooth accretion of gas onto a major merger remnant can rebuild a disc structure. These findings suggest, that one cannot simply see the Hubble sequence as one forward evolution. It is rather that there are many different transformation channels to change the morphology of a Galaxy: major mergers can turn spiral galaxies into elliptical galaxies, gas accretion can rebuild a disc or can cause the emergence and destruction of a bar and repetitive minor mergers can build up larger bulges and transform spiral galaxies into S0 or even elliptical galaxies (Bournaud & Combes 2004).

Our current understanding of hierarchical structure formation was reviewed by Somerville & Davé (2015) in which the authors underline a great agreement between observations and cosmological simulations. However, they criticise that many of the core processes used in cosmological simulations are phenomenological implementations and still poorly understood. With a focus on the Inter-Stellar Medium (ISM), Naab & Ostriker (2017) pointed out how galaxies are shaped by internal regulation processes during their mass growth. Through radiation and energetic winds, star-formation feedback and an active SMBH can interfere and regulate star formation in a galaxy. These processes are discussed in more details in Sect. 3.4 and 4 as they play a major

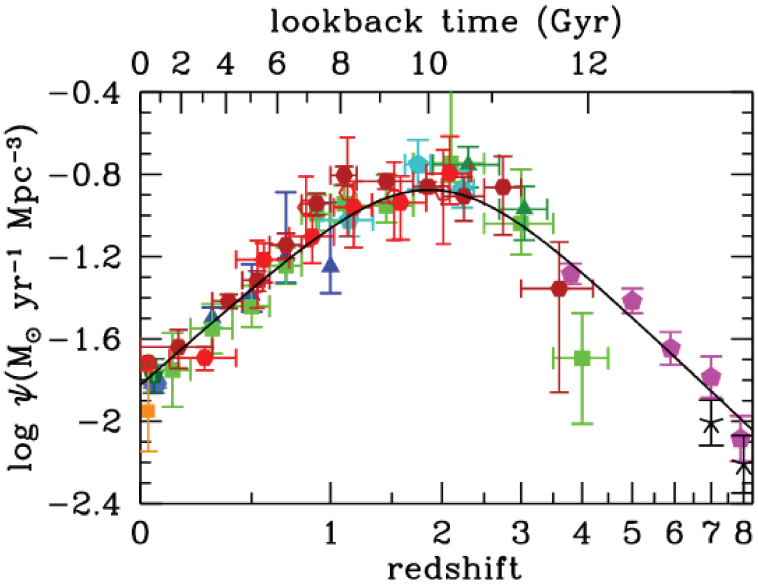

Figure (1.6) Star formation history from Madau & Dickinson (2014). On the y-axis, the estimated star-formation rate per comoving volume is shown and on the x-axis, the redshift, which is transformed into lookback time on the top. The data points are the measurements gathered from the literature and the black line is the best fit describing this evolution.

role in the understanding of how galaxies evolve.

By estimating the star-formation rate (detailed description, in Sect. 4.1), one can estimate how many star formation happened at which epoch, per unit of comoving volume. A global summary of this star formation density was compiled by Madau & Dickinson (2014) and summarised in a single plot. In Fig. 1.6, one can clearly see that the star-formation rate is not constant over cosmic time: the earliest galaxies, although their hydrogen content was abundant, did not form stars very effectively. This is mainly due to the fact that young stars are mostly composed only of hydrogen and are therefore very unstable. They ionise their environment through strong radiation, preventing molecular clouds from forming into new stars (Abel et al. 2002). However, this dominance has diminished by $z = 2$ and star formation has experienced a maximum, before decreasing steeply till the present day. What exactly the driving mechanism on large scales is, is still up for debate, but in individual observations it is possible to pinpoint what deprives galaxies from their star-forming fuel. For instance, the environment can interrupt the gas accretion (e.g. Kauffmann et al. 2004) or massive halos can shock-heat the in-falling gas (Dekel & Birnboim 2006) which prevents effective star formation.

2.3 Galaxy mergers

Our own Galaxy, the Milky Way, is gravitationally bound with its closest neighbour, the Andromeda Galaxy. These two galaxies are approaching each other with less then $200\,\mathrm{km\,s^{-1}}$ (Peebles et al. 2001) which will ultimately lead to a collision (van der Marel et al. 2012). It is estimated that this merger will eventually be completed in less then 5 billion years, resulting in an elliptical galaxy (Cox & Loeb 2008). The merging of two galaxies plays a major role in our current understanding of galaxy evolution. Numerous observations of galaxy mergers outside of our Galaxy exist and numerical simulations can further help us to understand this phenomenon. So fortunately, we do not have to wait till we crash into the Andromeda galaxy to study such

Figure (1.7) A compilation of interacting galaxies and ongoing galaxy mergers. To illustrate different types of mergers a compilation of 6 peculiar galaxy mergers seen by the Legacy Survey (Dey et al. 2019) is shown. On the left, the interaction of an elliptical with a spiral galaxies at a projected separation of 40 kpc is shown. A hint of a tidal feature in the outskirt of a spiral arm can be seen in the top of the spiral galaxy. In the second snapshot from the left, a minor merger between a large elliptical galaxy and a smaller galaxy can be seen. This merger is already advanced as the larger participant has already stripped away the majority of the disc structure of the minor galaxy leaving only the central bulge surrounded by tidal tails. In the two middle images, two major merger systems in an early stage are shown as they show far out-reaching tidal tails. The two right images show post-coalescence mergers as they exhibit strong perturbations. They are also isolated excluding the possibility that a fly-bye event created these perturbations.

an event.

Toomre & Toomre (1972) first proposed that mergers can enrich the ISM of galaxies and increase their star formation (for a detailed description of star formation see Sect. 4.1). Studies of star-forming galaxies in cluster environments showed that past merger events can fuel star formation, leading to younger stellar populations (Bothun & Dressler 1986; Pimbblet et al. 2002). Observations (e.g. Combes et al. 1994; Bergvall et al. 2003) of close galaxy pairs and galaxy-galaxy interactions revealed the presence of larger molecular gas reservoirs in comparison to isolated galaxies. In addition to the observations, simulations demonstrated merger induced central star-bursts (Mihos & Hernquist 1994a, 1996) and illustrated the underlying mechanism: the gas inside the disc loses its angular momentum due to the torques caused by the interacting galaxy, allowing the gas to fall onto the galaxy centre, eventually fuelling a central star-burst. The merging of two or more galaxies can proceed in many different ways and the morphology of the resulting galaxy strongly depends on the initial parameters such as the mass ratio or kinematic impact parameters (Di Matteo et al. 2007). Two main merger categories are the most prominent ones in the literature: major and minor mergers. A merger between two galaxies is considered as a major merger if the galaxies have an approximately equal mass ratio. There is no strict limit at what mass ratio galaxy mergers are considered minor mergers but common ratios are between 1:4 (Lotz et al. 2004) and 1:10 (Mihos & Hernquist 1994b).

Close interacting galaxies can be identified by their distance and the measurement of their projected velocities (e.g. De Propris et al. 2005). With this approach, 1716 galaxies were selected from the SDSS DR4 with a mass ratio of up to 1:10 (Ellison et al. 2008). This sample revealed that the interaction of a galaxy pair in a low density environment shows the largest triggered star formation rates (Ellison et al. 2010). By selecting additional galaxy pairs in the SDSS DR7 (in total 21 347), Patton et al. (2011) demonstrated a direct link between galaxy interactions and a central starburst. By extending their search to galaxies with an active nuclei (see Sect. 3.4), Ellison et al. (2011) showed that nuclear activity can also be triggered by galaxy-galaxy interaction.

Galaxies that are in close interaction with each other can be identified using spectroscopic redshifts. One can even determine the mass ratio and study the characteristics of both galaxies involved. However, this becomes a real challenge once the merger is advanced and only one

object is observed. Only early stages of major mergers can be identified by extensive tidal tails (e.g. Toomre & Toomre 1972) but once the resulting galaxy has settled, a merger can only be detected through asymmetries or visible perturbations (Ellison et al. 2013). In such systems, it is no longer straightforward to reconstruct the characteristics of the progenitors, their mass ratio or estimate for how long the merger is going on.

Non-parametric photometry diagnostics such as the Gini-coefficient or the shape asymmetry can be used to detect perturbations and deviations from a smooth shape. The most common used parameters, including a Sérsic profile are discussed in Rodriguez-Gomez et al. (2019). Based on such parameters, Lotz et al. (2004) distinguished galaxy mergers at different stages of merging from galaxies on the Hubble sequence. They applied these diagnostics to a large galaxy sample of 3009 galaxies at $0.2 < z < 1.2$ and found a nearly constant merger rate, while measuring an evolution for non-merger Hubble types (Lotz et al. 2008). A more elaborate analysis which included the calibration of merger rate estimators with cosmological simulations, could distinguish between major and minor mergers (Lotz et al. 2011). They estimated that minor mergers occur three times more frequently than major mergers at $z \sim 0.7$ and indicated a little evolution with redshift. Relying on merger estimators trained with a supervised linear decomposition analysis, Nevin et al. (2019) were able to compute the predictor coefficients to estimate the major and minor merger probabilities for a given system up to $z < 0.075$. However, these estimators are based on simulations, it is hence difficult to check their reliability for late merger stages and the proper identification of post-coalescence minor mergers. Minor mergers are usually less violent than major mergers and thus harder to identify. In addition, all the associated effects such as star formation enhancement or AGN fuelling are difficult to disentangle. In particular at a late stage, a minor merger can hardly be distinguished from an isolated galaxy with no interaction at all. However, using machine-learning algorithms, trained on cosmological simulations, Bottrell et al. (2022) showed that post-coalescence mergers can be properly identified though imaging. They also included maps of stellar kinematics, which did not significantly contributed to the detection in comparison to the photometry. Nevin et al. (2021), in contrast, trained kinematic predictors to identify galaxy mergers from velocity maps and found an accuracy of up to 80 %. However, applying these algorithms is still challenging.

In fact, the detection of a past merger in a specific galaxy is of great importance in order to understand how galaxies have evolved over the last 10 billion years. Conselice et al. (2005), concluded that major mergers are the main source of star formation in galaxies at $z > 1.5$, whereas minor mergers and gas accretion from the surroundings is the dominant mechanism for $z < 1.5$. It has been shown that for elliptical galaxies a recent minor merger can be identified though dust lanes (Shabala et al. 2012; Davis et al. 2015). However, this galaxy type does not host the majority of star formation in the Universe at $z < 1.5$. Hence, in order to understand the mass assembly of galaxies in the late Universe, a proper identification of post-coalescence minor and major mergers is crucial but challenging to obtain since merger systems relax rapidly.

3 The view of galaxies at different wavelengths

3.1 The spectral energy distribution of a star forming spiral galaxy

When making photometric observations of the night sky, one aspect is most important: In what wavelength range was the image taken? For example, the photometric band-pass filters of the

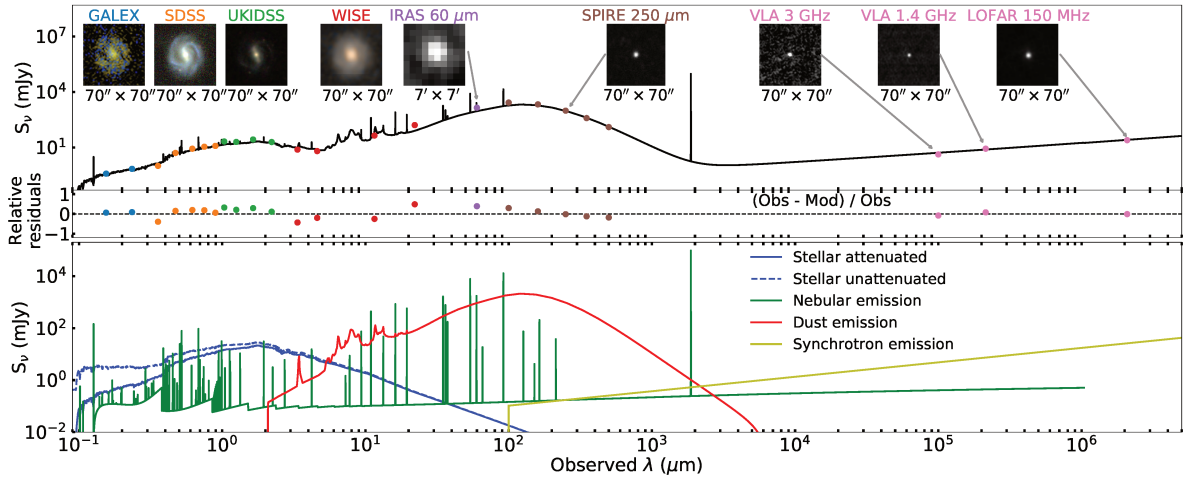

Figure (1.8) Spectral energy distribution of the galaxy J132443.67+323225.0. On the *top* panel, photometric flux measurements at different wavelengths are shown with coloured dots and the best fitting SED model obtained with CIGALE (Boquien et al. 2019) is shown with a black line. To illustrate different flux measurements, the observations are shown in snapshots above the measurements. Each snapshot is titled with the observation facility used to obtain it and the resolution is indicated below the snapshot. Below the *top* panel, the relative residuals are shown and on the *bottom* panel, a SED-model decomposition provided by CIGALE is shown.

SDSS, presented in Sect. 2.1.2, cover the range between 3543 and 9134 Å, roughly corresponding to the wavelengths visible to the human eyes. However, galaxies also emit light in wavelengths that are invisible to humans. Figure 1.8 shows, for an exemplary spiral galaxy, the intensity with which it emits light in the various wavelength bands from ultraviolet to radio waves. The distribution of this light is called spectral energy distribution (SED) and provides information about different components and ongoing processes inside the galaxy. The SED observations shown in Fig. 1.8 are modelled with the SED-fitting tool CIGALE (Boquien et al. 2019). This allows to present the isolated spectral components in the bottom panel and to discuss them individually. The main components are the light emitted from stars making up the stellar continuum, dust emission, gas emission and radio continuum emission. In some galaxies, an AGN significantly contributes to the SED or in some cases is the dominant light source. This is subsequently discussed in Sect. 3.4. The galaxy presented here, however, shows no sign of a significant AGN contribution. Since gas emission is of particular importance for this thesis, it is described in greater detail in Sect. 3.2.

3.1.1 The stellar continuum

A single star, in thermal equilibrium, radiates light in a continuous spectrum which approximates a blackbody spectrum. The peak flux of the spectrum is determined by the surface temperature of the star. Furthermore, the atmosphere of stars absorbs light at specific wavelengths, depending on the elements and the temperature. The observation of a galaxy can also be seen as the observation of about trillions of stars at the same time (considering a galaxy with the size of the Milky Way). Since there are many different types of stars in a galaxy, one no longer observes a single blackbody spectrum but a superposition of all contributing stars, building up a continuum spectrum. In addition, due to thermal effects in the atmosphere of stars one see broader absorption lines with a range of 200-300 $\mathrm{km\,s^{-1}}$. These can be seen as characteristic dips in the spectrum. In the bottom panel of Fig. 1.8, the stellar continuum of the galaxy is

shown with a solid blue line. The stellar continuum is the main light source observed in the UV, optical and near Infra-Red (IR) wavelengths. For the galaxy in Fig. 1.8, observations from the Galaxy Evolution Explorer (GALEX) satellite in the Far UV (FUV) and Near UV (NUV) band at 1350 - 2750 Å(Martin et al. 2005) were used. The optical light was observed with the ground based 2.5-m wide-angle optical telescope at Apache Point Observatory which was used to conduct the SDSS (see Sect. 2.1.2). The near-IR light was observed by the United Kingdom Infrared Telescope (UKIRT) in the wavelength range from 0.836 to 2.380μm (Lawrence et al. 2007). In the bottom panel of Fig. 1.8, the stellar spectrum is shown with dashed blue lines as if one would observe the total light emitted by stars towards our direction. However, we observe an attenuated spectrum because dust inside the galaxy blocks a part of the light, effecting mostly the UV and optical bands.

3.1.2 Cosmic dust

If one would try to observe the barycentre of our Milky Way with an optical telescope, it would not matter whether the telescope dome is open or not: the barycentre of the Milky Way simply cannot be observed in the optical wavelengths, since clouds of cosmic dust happen to cover this region. This dust is made up of different particles which range from the molecular size up to about 100 μm. Cosmic dust has long been a nightmare for astronomers, preventing them to observe many parts of the Milky Way or making it impossible to know how much light is obscured in distant galaxies. This changed drastically with the introduction of IR astronomy as it allows to directly observe the dust. Dust clouds absorb light in the UV and optical wavelengths which causes the dust to heat up. The dust then radiates in the form of a blackbody spectrum (Boulanger 1999). Such a spectrum is presented in the bottom of Fig. 1.8. What is striking is a complex emission structure around the mid-IR region at approx $5 - 15\,\mu$m. This structure comes from a superposition of many different carbon-hydrogen compounds called Polycyclic Aromatic Hydrocarbons (PAHs). These compounds emit light at discrete wavelengths resulting in a specific signature which provides insights about the ISM within a galaxy (Ossenkopf & Henning 1994; Allamandola et al. 1999).

Modelling the emission from UV to optical light allows one to draw a solid conclusions about how much light has been absorbed in the UV and optical bands and was re-emitted in the IR (Draine & Lee 1984; Draine 2003; Draine & Li 2007). A consistency between the UV and IR emission can be reproduced by radiative transfer models Fioc & Rocca-Volmerange (e.g. 2019).

In order to observe dust in the far-IR our own Milky Way and in other galaxies, space-based telescopes are needed. This is due to the fact that molecules, such as water vapor, CO_2 or oxygen, in our atmosphere absorbs IR light. The first All sky Survey at these wavelengths was the Infrared Astronomical Satellite (IRAS), which launched on 25 January 1983 and observed the sky at 12, 25, 60, and 100 μm (Neugebauer et al. 1984). For the SED fit as shown in Fig. 1.8, IRAS observation at 60 μm are used. Mid-IR observations with higher resolutions but at smaller wavelengths were provided by the Wide-field Infrared Survey Explorer (WISE) which was launched on 14 December 2009 and imaged the sky in the wavelength bands 3.4, 4.6, 12, and 22 μm (Wright et al. 2010). Mid-IR observations can be carried out with ground based telescopes at the wavelength at 2-7 μm however, the atmosphere highly perturbs the observations. To estimate the far-IR wavelengths of the dust continuum, the Herschel Space Observatory was launched on the 14 May 2009 and was able to observe the night sky in a

wavelength range from 55 to 672 μm (Pilbratt et al. 2010). As shown in Fig. 1.8, these far-IR observations allow a correct modelling of the dust continuum providing an estimation of the peak blackbody radiation and thus the dust temperature.

As it will be explained in Sect. 3.2 and 4.1, star-formation sites are particularly dusty and stop the majority of optical light. Only in the IR wavelengths it is possible to see through the dense dust clouds and study the fundamental processes of early star formation. The Spitzer satellite, for example, has made a major contribution to the understanding of such processes (Evans et al. 2009). Nevertheless, there are still many questions that require higher sensitivity and resolution in the mid-infrared range. This is where the recently launched James Webb Space Telescope will contribute, as it will shed light on the dustiest star nurseries in nearby galaxies (Lee et al. 2022).

3.1.3 Radio continuum emission

When stars form in dense giant gas clouds, many super giant stars are formed due to the abundance of hydrogen in these sites. These type of stars are very instable and go supernova only a few thousand years after their formation. In the resulting supernova remnant, charged particles, mostly electrons and positrons, are accelerated and then emit synchrotron radiation when interacting with the galaxies magnetic field (Condon 1992). The resulting synchrotron spectrum is described by a power law of $S(\nu) \propto \nu^{\alpha}$, where $S(\nu)$ is the radio flux and α is the spectral index defined as:

$$\alpha = \frac{\log(F_{\nu_2}/F_{\nu_1})}{\log(\nu_2/\nu_1)}, \tag{1.5}$$

where ν_1 and ν_2 are two different radio frequencies. Synchrotron radiation emitted by star-formation sites have a typical spectral index of about $\alpha = -0.7$ (Condon 1984). However, AGN can, as well, contribute significantly to the radio continuum, as further explained in Sect. 3.4.2

In order to perform radio observations with high enough sensitivity and resolution, extremely large telescopes are needed. This is mostly limited by to the highest possible resolution from the diffraction limit $\theta_d = 1.22\lambda/D$, where D is the telescope diameter (Wilson et al. 2008). Thus, in order to distinguish radio sources with an arc-minute resolution at the radio continuum of e.g. 20 cm, a telescope size of about 850 m; which is nearly impossible to build. However, there is a solution to that: radio-interferometry. This technique combines the signal of multiple smaller telescopes. Therefore, the signal of a set of multiple separated radio antennae is combined mathematically with a correlator and an image can be calculated using the mathematical technique called aperture synthesis (see chapter 9 in Wilson et al. 2008). One major drawback is that due to the low telescope surface, covered by the individual antennae, compared to a single dish telescope with a diameter of the largest base-line, long integration times are needed to obtain faint signals. Furthermore, this technique only detect structures of the size the antenna configuration is optimised for. Thus, the maximal detectable object size is limited by the smallest spacing of the antennae, arranged in the radio array (Michelson & Pease 1921).

The radio continuum of the galaxy presented in Fig. 1.8 was measured with the Very Large Array (VLA) as part of two survey programs of the Northern hemisphere: the Faint Images of the Radio Sky at Twenty-Centimeters (FIRST) at 1.4 GHz (White et al. 1997) and the Very Large Array Sky Survey (VLASS) at 3 GHz (Lacy et al. 2020). The galaxy was also observed with the Low Frequency Array (LOFAR) as a part of the LOFAR Two-metre Sky Survey (LoTSS) at 150 MHz (see Shimwell et al. (2019) for DR1). Combining these radio emissions, a spectral

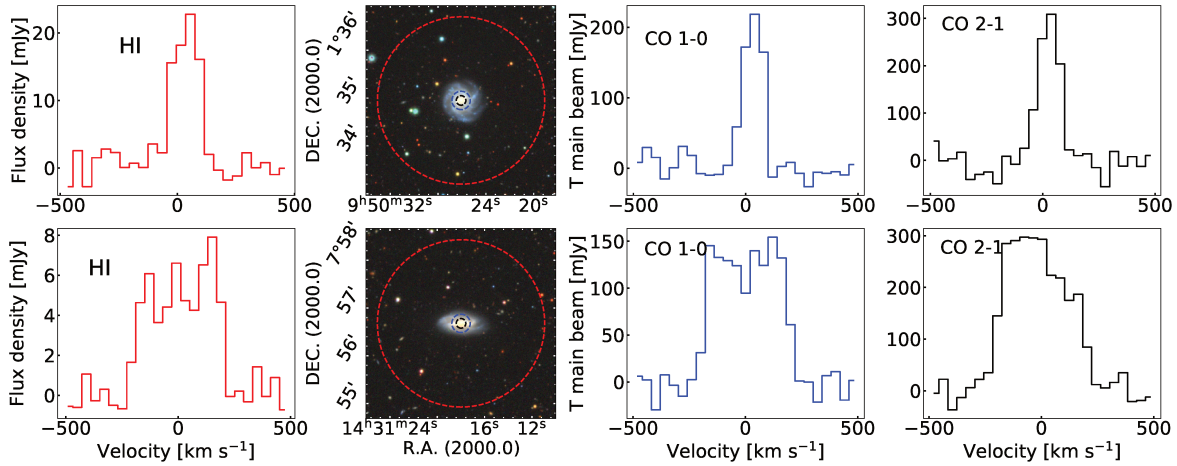

Figure (1.9) HI and CO spectroscopic observation of two galaxies. On the left, two HI spectra observed with the Arecibo 305 m telescope (Giovanelli et al. 2005). The telescope beam of the size of 3.5′ is shown with a red dashed line on the galaxy snapshots from the Legacy survey (Dey et al. 2019), shown next to the HI spectra. On the right, CO observations with the IRAM 30m telescope of the two transitions CO(1-0) and CO(2-1) are shown[1]. In order to visualise the dependency on Doppler shift, the galaxy shown on the top panels is nearly face-on. The galaxy on the bottom panels is inclined by 70°. Due to the Doppler shift caused by rotation, the observed lines of the inclined galaxy is broader than those of the face-on.

index of $\alpha = -0.6$ is measured for the galaxy in Fig. 1.8 as presented with a yellow line.

3.2 Gas in galaxies

Whereas the stellar-, radio- and dust- continuum spectra are characterised by extended emission over a range of wavelengths, the light coming from gas is different: it is observed as emission lines at discrete wavelengths. These discrete emission lines originate from electrons transitioning from excited energy levels back to their ground state. Hence, the spectroscopic signature of gas depends on multiple factors: temperature, density, elements and ionisation state.

3.2.1 Atomic hydrogen gas

Hydrogen plays a special role, since in its atomic form it either absorbs light when cold and dense (50-100 K and 20-50 cm^{-3}) at 21 cm or emits light at this discrete wavelength when it is warm and less dense (6000-10000 K and 0.2-0.5 cm^{-3}) (Ferrière 2001). The 21-cm line originates from the transition of the electron between the two hyperfine levels of the ground state $1s$ and is also called the spin-flip transition. In Fig. 1.9, observations of the warm atomic Hydrogen gas (HI) and the molecular gas (CO) is shown for 2 galaxies: one face-on and one strongly inclined (70°) galaxies. From the rest HI line intensity, S_{HI}, one can directly calculate the atomic hydrogen mass (Meyer et al. 2017):

$$\left(\frac{M_{HI}}{M_\odot}\right) = \left(\frac{2.356\,10^5}{(1+z)}\right)\left(\frac{D_L}{Mpc}\right)^2\left(\frac{S_{HI}\,\Delta v}{Jy\,km\,s^{-1}}\right), \tag{1.6}$$

where D_L is the luminosity distance and Δv the line width in $km\,s^{-1}$. The gas mass provides information about how much atomic hydrogen is present inside and the direct environment of a galaxy. This gas can further cool down and fuel star formation in form of molecular gas clouds (Leroy et al. 2008; Bigiel et al. 2008).

3.2.2 Molecular gas

When atomic hydrogen cools down and becomes denser due to gravity, two hydrogen atoms always bond together to form a molecule. Such gas clouds have temperatures of about 10 K and reached concentrations of 10^2 - $10^5\,\mathrm{cm}^{-3}$ (Williams et al. 2000). Due to its simple symmetry, the cold molecular hydrogen has no emission lines and is therefore invisible. However, far less abundant molecules are found in these clouds, which show transitions even at such low temperatures. The most common ones are CO, H_2O and HCN. All these molecules have emission lines in the IR and radio wavelengths which make them excellent tracers of molecular gas (Johnstone et al. 2003; Kauffmann et al. 2017). The most used tracers are the CO low-J transition $\mathrm{CO(J \rightarrow J-1)}$ because their wavelengths are in the mm-range and hence can be observed with ground-based radio antennas (Dame et al. 1987). In Fig. 1.9, CO(1-0) and CO(2-1) emission lines are shown for two galaxies. The observations were obtained with the IRAM 30m telescope[1].

The intrinsic CO luminosity $\mathrm{L'_{CO}}$ can be calculated from the velocity integrated transition line flux $\mathrm{F_{CO(J\rightarrow J-1)}} = \mathrm{S_{CO(J\rightarrow J-1)}}\,\Delta\mathrm{v}$ following Solomon et al. (1997):

$$\left(\frac{\mathrm{L'_{CO(J\rightarrow J-1)}}}{\mathrm{K\,km\,s^{-1}\,pc^2}}\right) = \frac{3.25\times10^7}{(1+\mathrm{z})}\left(\frac{\mathrm{S_{CO(J\rightarrow J-1)}}\,\Delta\mathrm{v}}{\mathrm{Jy\,km\,s^{-1}}}\right)\left(\frac{\nu_{\mathrm{rest}}}{\mathrm{GHz}}\right)^{-2}\left(\frac{\mathrm{D_L}}{\mathrm{Mpc}}\right)^2, \tag{1.7}$$

where $\mathrm{D_L}$ is the luminosity distance and ν_{rest} the rest CO line frequency. From the intrinsic CO luminosity, one can estimate the molecular gas mass:

$$\mathrm{M_{H_2}} = \alpha_{\mathrm{CO}}\,\mathrm{L'_{CO(J\rightarrow J-1)}}/\mathrm{r_{J1}},, \tag{1.8}$$

where α_{CO} is the luminosity-to-molecular-gas-mass conversion factor of the CO(1-0) line.

$$\mathrm{r_{J1}} = \mathrm{L_{CO\,(J\rightarrow J-1)}}/\mathrm{L_{CO\,(1\rightarrow0)}} \tag{1.9}$$

is the luminosity ratio between higher transitions $\mathrm{CO(J \rightarrow J-1)}$ and CO(1-0) which depends on the gas temperature. For example, a mean value of $\mathrm{r_{21}} = 0.77$ was found for usual star-forming galaxies, whereas for galaxies with a strong excess in their IR emission a mean value $\mathrm{r_{21}} = 0.83$ was found Genzel et al. (2015). The conversion factor α_{CO} of the Milky Way is $\alpha_{\mathrm{G}} = 4.36 \pm 0.9\,\mathrm{M_\odot/(K\,km\,s^{-1}\,pc^2)}$, which includes a correction for 36 % of interstellar helium (Strong & Mattox 1996; Abdo et al. 2010). However, this conversion factor is not constant for all galaxies but can be estimated using the gas-phase metallicity Z (Wolfire et al. 2010; Bolatto et al. 2013), which quantifies the abundance ratio between hydrogen and heavier elements. This can be estimated from emission line ratios of the ionised gas in the optical wavelength range (see Sect. 3.2.3). An estimation of a metallicity-based conversion factor which was e.g. adopted by Genzel et al. (2015), Tacconi et al. (2018), and Freundlich et al. (2021), can be calculated as:

$$\alpha_{\mathrm{CO}} = \alpha_{\mathrm{G}}\sqrt{0.67\times\exp(0.36\times10^{8.67-\log\mathrm{Z}})\times10^{-1.27\times(8.67-\log\mathrm{Z})}}. \tag{1.10}$$

The molecular gas mass in a galaxy can be understood as a reservoir for ongoing star formation. These two variables are tightly correlated, as discussed in detail in Sect. 4.1.

[1] As the principal investigator of the observing run number 166-20, I observed the CO(1-0) and CO(2-1) lines with the IRAM 30m telescope located at Pico Veleta in Spain between 23rd to the 29th December 2020.

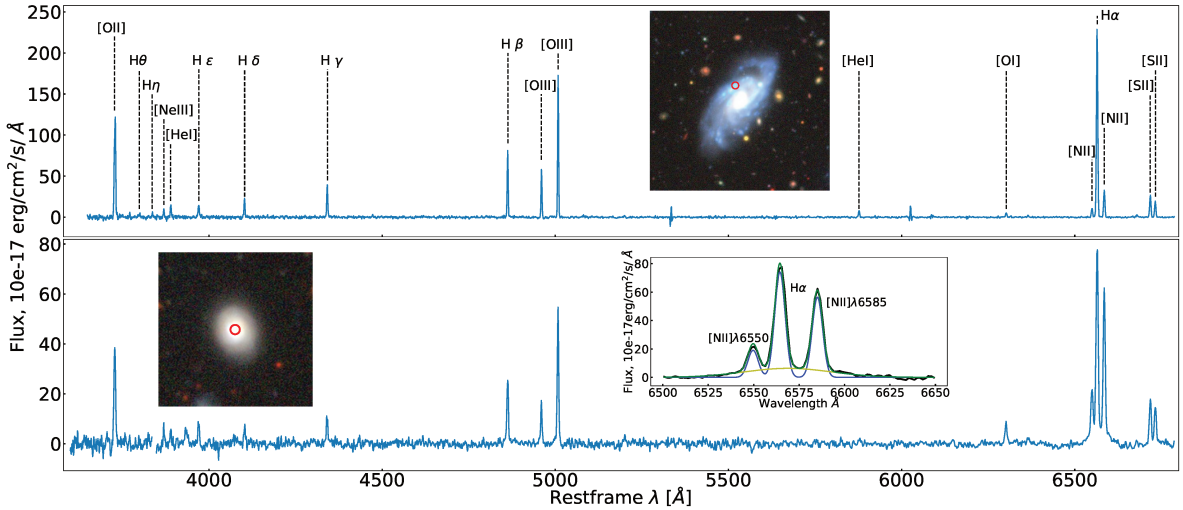

Figure (1.10) Ionised-gas emission-line spectra of an HII region (top panel) and an AGN (bottom panel). To compare to other spectra e.g. as shown in Fig. 1.4, these spectra are shown in rest frame wavelength. For the top panel, all detected emission lines are indicated by black dashed lines (see Table 1.1). For both spectra, the Legacy Survey snapshots are shown and the position of the 3″ SDSS spectra are shown with red circles. For the AGN spectra, a zoom-in of the Hα emission line is shown in order to visualise the broad-line region. The Hα broad-line component is shown with a yellow Gaussian function and the narrow-line component of the Hα and [NII]λ6550, 6585 doublet are shown with blue lines. The total fit is shown by a green line.

3.2.3 Ionised gas

When molecular gas clouds compress further under the pressure of gravity, stars will eventually form and illuminate the gas cloud from inside with a UV radiation of up to 100 eV (Dopita & Sutherland 2003). This UV radiation will ionise the atoms as for example the ionisation energy needed for a hydrogen atom is 13.6 eV. The ionised atoms then capture free electrons and emit light at discrete wavelengths while electrons decay further down to lower energy levels. These regions can be detected due to their distinct emission-line signature with UV, optical and IR spectroscopy. Such regions with a particle density 10^2 - 20^4 cm^{-3} are called HII regions. In the Milky Way, HII regions are made up of about 90 % of hydrogen, about 7 % helium and heavier elements (Shaver et al. 1983).

On the top panel of Fig. 1.10, the optical ionised-gas emission-line spectrum of a HII region, measured by the SDSS, is shown. The most prominent emission line in this spectrum is the Hα line emitted at a rest wavelength of 6564.64 Å. This is the first line transition of the Balmer series as it is emitted when an electron in an hydrogen atom falls from the energy level n=3 to n=2. Since many of such ionised gas emission lines play an important role in this thesis, the most important emission lines are listed in Table 1.1 and indicated in Fig. 1.10.

HII regions are not the only sources of ionised-gas emission lines. Binary star systems or supernova remnants can ionise the interstellar gas with a X-ray spectrum which is dominated by high energetic X-ray photons (also referred as hard X-ray spectrum) (Townsley et al. 2011). Also the gas accretion disc of a SMBH can be a strong X-ray source which ionises the interstellar gas. From an observational perspective, such emissions can be dominated by less probable transitions e.g. the oxygen [OIII]λ4960.3, 5008.2 doublet. These lines are also called "forbidden" lines because we would never observed them in a lab on Earth, due to their vanishing probability. In inter-stellar gas however, they can be observed due to the fact that less dense gas is ionised

Line name	Wavelength in air Å	Wavelength in vacuum Å
[O II]	3726.032	3727.092
Hθ	3797.904	3798.982
Hη	3835.391	3836.479
[Ne III]	3868.760	3869.857
[He I]	3888.647	3889.749
H ϵ	3970.079	3971.202
H δ	4101.742	4102.900
H γ	4340.471	4341.692
H β	4861.333	4862.692
[O III]	4958.911	4960.296
[O III]	5006.843	5008.241
[He I]	5875.624	5877.255
[O I]	6300.304	6302.049
[N II]	6548.050	6549.862
H α	6562.819	6564.635
[N II]	6583.460	6585.282
[S II]	6716.440	6718.298
[S II]	6730.810	6732.671

Table (1.1) Ionised gas emission lines values measured in air and vacuum[2]. All optical emission lines emitted by ionised gas and most frequently measured in a SDSS spectra. All emission lines are indicated in real SDSS spectra in Fig. 1.10.

and electrons can spend enough time in excited states and thus less probable transitions can happen. In dense regions, on the other hand, this would not happen because electrons change their energy state more frequently due to collisions (Mo et al. 2010). In Fig. 1.10, a SDSS spectra of the central region of galaxy hosting an AGN is shown. In comparison with the spectra of a HII region, one can see different emission line proportions. Based on these differences, one can use emission-line ratios to characterise the underlying process, discussed in detail in Sect. 3.5.

Emission lines of galaxies observed in the SDSS show a mean full-width-half-maximum (FWHM) value of $246 \pm 128\,\mathrm{km\,s^{-1}}$. This is due the turbulence in gas clouds, Doppler-shift from rotation and broadening when multiple HII regions are included inside the spectroscopic measurement. For some AGNs, however, only the Balmer lines are known to exhibit an additional broad line component with a Doppler-shift of up to several $1000\,\mathrm{km\,s^{-1}}$ (Goad et al. 2012). Since this component is not observed in less probable emission lines such as [OIII]λ5008.2, it must originate from dense gas. In fact, the origin is the accretion disc around the SMBH, which also explains the high velocities (Mo et al. 2010). In Fig. 1.10, the presented AGN exhibits a broad line component in its Balmer lines.

3.3 Colour, SED and morphology

The galaxy, shown in Fig. 1.8, has been observed by many telescopes at different wavelengths, allowing a good modelling of the individual SED components. However, such a favourable data situation is not always the case and often only a few measurements of the SED are available. It is therefore, challenging to find the best fitting model of the SED with only a few data points. Depending on the dominant processes, the shape of the SED changes: for example, a recently

[2]Exact values taken from https://physics.nist.gov/PhysRefData/ASD/lines_form.html

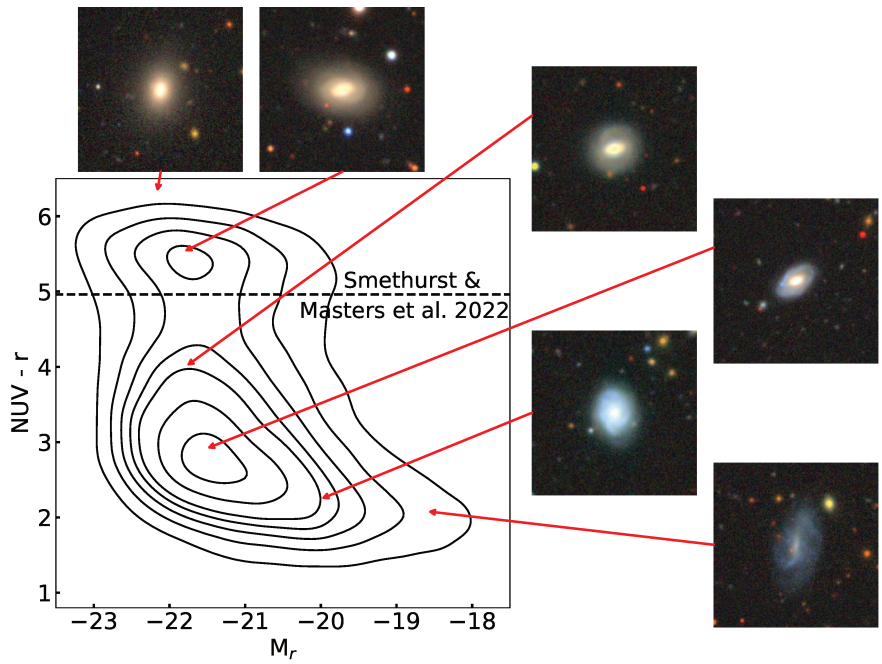

Figure (1.11) Colour-magnitude diagram of galaxies. On the x-axis (resp. y-axis) the absolute r-band magnitude M_r (resp. the colour $NUV - r$) is shown. Contours show the distribution of SDSS galaxies with Galactic dust and k-corrected magnitudes (Chilingarian et al. 2017). The dashed line shows the best separation between the red sequence on top and the star-forming main sequence on the bottom (Smethurst & Masters, et al., (2022)). To illustrate the different galaxy morphology found at different locations on this diagram, six randomly picked galaxies are shown with snapshots of the Legacy Survey (Dey et al. 2019) and red arrows show their location on the colour-magnitude diagram.

formed stellar population has a different SED shape in comparison to an old one. One of the simplest methods to investigate galaxies is to look at the difference in magnitude between two or more band-pass filters (de Vaucouleurs 1961), which provides an estimation of the colour, i.e. the wavelength dominating the filter measurements.

In Fig. 1.11, the absolute magnitude M_r estimated from the r-band observations of the SDSS is shown on the x-axis. This is calculated from using the luminosity distance D_L:

$$M_r = r - 25 - 5\log_{10}(D_L) \tag{1.11}$$

On the y-axis, the difference between the GALEX NUV-band and the SDSS r-band magnitude is shown. To illustrate how different galaxies behave on this diagram, contours show the distribution of the entire SDSS DR7 (see Sect. 2.1.2).

As we know from Equation 1.2, the entire SED is shifted towards redder colours for galaxies at higher redshift. This implies that the colour of a galaxy probes not always the same part of the SED. This shift can be corrected by a factor, the so-called k-correction, calculated for a given redshift with an interpolation of multiple optical and near IR colour measurements (Chilingarian et al. 2010). Hence, in Fig. 1.11, only k-corrected colours are shown provided by Chilingarian et al. (2017). The colours are furthermore corrected for dust attenuation originating from dust clouds inside the Milky Way. Intrinsic dust extinction is not accounted for here. In fact, star-forming galaxies with a substantial dust content are observed at redder colours as discussed e.g. by Gonçalves et al. (2012); Sodré et al. (2013); de Sá-Freitas et al. (2022).

M_r measures the brightness in the r-band of the galaxies and a distribution of about 6 orders

of magnitudes is observed in Fig. 1.11. The $NUV - r$ colour, on the other hand, separates galaxies between red and blue galaxies with a clear dichotomy. To illustrate the distribution of the galaxy types in this diagram, galaxies at different points were randomly selected and the corresponding rgb-images from the Legacy Survey are shown. The lower population is dominated by blue galaxies showing discs and spiral features. The upper sequence is populated by red bulge dominated and elliptical galaxies. This correlation between morphology and galaxy colour has been known for a long time (de Vaucouleurs 1961; Chester & Roberts 1964). From the study of stars in the Milky Way, it is known, that young, recently formed stars are brighter in the blue part of the optical spectrum, whereas old stars tend to redder colours (e.g. VandenBerg et al. 2013). Based on this distinction, the upper concentration in Fig. 1.11, centred at $NUV - r \sim 5.5$, is also called the passive sequence and the lower one the star-forming sequence (Strateva et al. 2001). However, red spiral galaxies or blue elliptical galaxies can also be found in the blue and the red sequence, respectively. This was investigated in Smethurst & Masters, et al., (2022) with a precise morphological categorisation and threshold values which best divide these two populations on a colour-magnitude diagram. For a $NUV - r = 4.961$ threshold, they calculated a completeness of 65.8 % for bulge dominated galaxies in the red sequence and 92.8 % for disc dominated galaxies in the blue sequence.

Considering this dichotomy in the context of galaxy evolution over cosmic time, the question naturally arises how disc galaxies can destroy their morphology and become red elliptical galaxies without any star formation? In fact, since $z = 1$, the number of elliptical galaxies has approximately doubled (Bell et al. 2004; Faber et al. 2007), suggesting that at the present epoch the build-up of the passive sequence is still ongoing. What exactly stops star formation in galaxies and transforms them into elliptical galaxies is still up for debate. As discussed in Sect. 2.3, major mergers can produce such a transformation but are rare since $z = 1$. Thus other mechanisms are required. Schawinski et al. (2014) found past major mergers to be one of the transformation channels a triggered AGN heats up molecular gas clouds and therefore prevent star formation. Another transformation channel they described is by preventing gas entering the galaxy halo. Both mechanisms would result in a rapid transition between the blue and the red sequence. The region between these two populations is less dense and called the "green valley", first defined by Salim et al. (2007). Galaxies with colours $4 > NUV - r > 5$ are mostly massive galaxies that recently dropped out the main star-forming sequence (see Sect. 4.3) due to star-formation quenching or are quiescent galaxies, experiencing a resurgence of their star-formation activity caused by gas accretion (Salim 2014). Hence, the green valley is a useful tool in order to study the quenching mechanism of galaxies.

In order to qualitatively distinguish the difference between red passive elliptical and blue star-forming spiral galaxies, the modelling framework for spectral evolution PEGASE 3 (Fioc & Rocca-Volmerange 2019) was used in order to compare these two galaxy types. Fig. 1.12 presents the distribution of the k-corrected and Galactic extinction corrected colours $g - r$ and $r - i$ for elliptical and spiral galaxies selected from the SDSS. The selection is performed with a machine-learning algorithm trained by Domínguez Sánchez et al. (2018) as described in detail in Maschmann et al. (2020). A clear separation is visible with the elliptical galaxies concentrated at $g - r \sim 0.8$ and $r - i \sim 0.35$, whereas the spiral galaxies are spread over a large range of colours. To understand the evolution of such galaxies, an elliptical galaxy was modelled with PEGASE 3 assuming a strong star-formation cycle, followed by a radical gas exhaustion from 3 Gyr on. Subsequently, the gas from its surrounding is prevented from entering the galaxy and

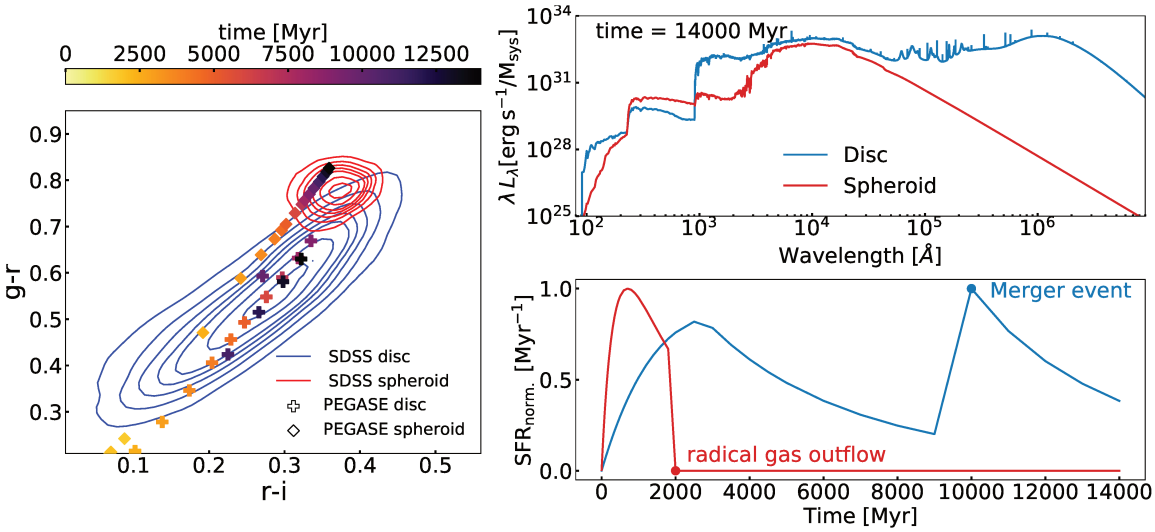

Figure (1.12) Galaxy SED and morphology as seen with PEGASE 3. On the left, a colour-colour diagram shows the distribution of different galaxy types. On the x-axis (resp. y-axis), the colours $r - i$ (resp. $g - r$) are shown. Elliptical and disc galaxies selected from the SDSS using Domínguez Sánchez et al. (2018) are shown with red and blue contours respectively. The displayed colours are calculated using Galactic dust and k-corrected magnitudes (Chilingarian et al. 2017). On the right, simulated spectra for two galaxies, one disc and one elliptical, produced with PEGASE 3 (Fioc & Rocca-Volmerange 2019), are shown. On the top, the spectra at redshift $z = 0$ are shown and on the bottom, their star-formation history. To illustrate the evolution of the two galaxies over time, the colours of these two galaxies are shown with markers on the left panel.

no star formation can happen. On the right part of Fig. 1.12, the star-formation history over cosmic time and the spectra at present day are shown. The evolution of the colours of this galaxy is as well shown, indicating a migration to the red sequence. In contrast to this, a spiral galaxy is modelled with an exponential declining gas supply over cosmic time. Furthermore, a major merger event replenished the gas reservoir instantaneous 4 Gyr ago resulting in a star-forming galaxy at the present day. In the colour evolution, we see a slow migration towards redder colours which is then stopped by the merger event and keeps the galaxy inside the star-forming sequence. The difference between the star-forming spiral and the quiescent elliptical galaxies is striking when looking at these spectra at present time: this clearly shows the connection between morphological type and the SED of galaxies. Based on this connection, the blue sequence on the bottom in Fig. 1.11 is associated with the main sequence of star-forming galaxies, whereas the red sequence, on the top, is known as the quiescent sequence, consisting of galaxies with quenches star formation (see Sect. 4.3).

3.4 Properties of active galactic nuclei

3.4.1 Discovery of AGN

Heber Curtis is not only known for his participation on the Great Debate with Harlow Shapley on the size of the Universe (see Sect. 1). He is also known for detailed catalogues in which he described his observations of celestial bodies. In Curtis (1918), he noted the following commentary for the elliptical galaxy M87:

> "*Exceedingly bright; the sharp nucleus shows well in* 5^{m} *exposure. The brighter central portion is about* $0'.5$ *in diameter, and the total diameter is about* $2'$*; nearly round. No*

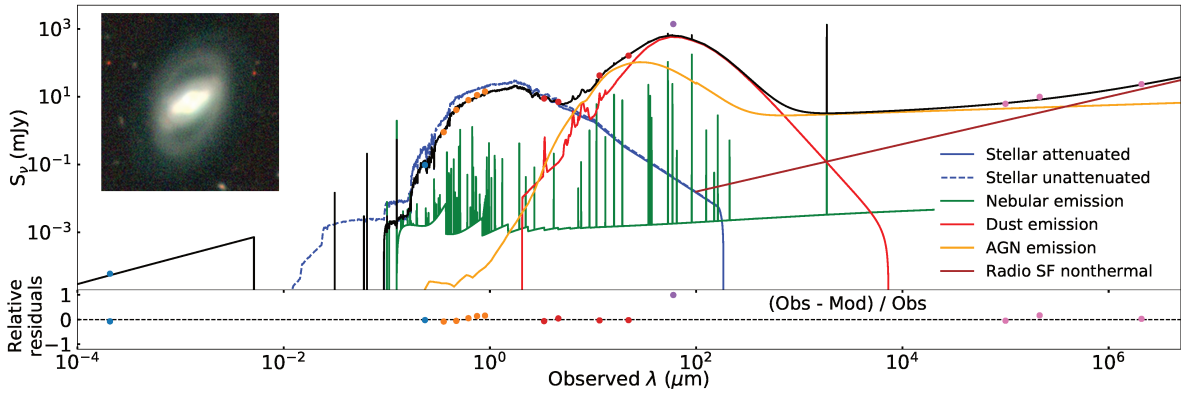

Figure (1.13) SED of the galaxy CGCG 218-007 hosting an AGN. The SED with the best fitting model provided by CIGALE (Boquien et al. 2019). In comparison to the SED shown in Fig. 1.8, this galaxy has additional X-ray observations. Furthermore, an AGN component is included in the SED model. Note that one data point observed by IRAS at 60 μm shows significant deviation from the model in comparison to other estimations. This is due to a contamination of a neighbouring galaxy which cannot be resolved by the IRAS detector.

> *spiral structure is discernible. A curious straight ray lies in the gap in the nebulosity in p.a. 20°, apparently connected with the nucleus by a thin line of matter. The ray is brightest at its inner end, which is 11″ from the nucleus.*"

What he described as a 'curious straight ray' is the first description of a jet which corresponds to the ejection of ionised matter accelerated to relativistic velocities by the central SMBH of a galaxy. However, the underlying mechanism was not clear at the epoch and detailed studies at different wavelengths of such objects were needed.

Seyfert (1943) found that the emission lines in the central nuclei of NGC 3516 and NGC 7469 are broadened up to a velocities of 8500 km s^{-1}. About a decade later, the nomenclature 'active galactic nuclei' was first introduced by Viktor Ambartsumian (Israelian 1997). With the rise of radio astronomy, many bright radio sources were identified, such as M87 (Stanley & Slee 1950; Baade & Minkowski 1954). Using radio interferometry, the radio jet was then identified as an extended radio source by Turland (1975). A few years earlier, the nucleus of M87 has been confirmed as one of the first X-ray sources (Bradt et al. 1968). One discovery in the early 1960s had a major impact in order to understand all these observations: the spectroscopic measurement of the star-like object 3C 273 revealed a redshift of 0.158 (Schmidt 1963). This distance implied that the optical luminosity of this quasi-stellar object (quasar) is 100 times brighter then all other identified galaxies with identified radio sources. With the detection of such objects at even higher redshift (Greenstein 1963), it was clear that the observed brightness cannot be of stellar origin as discussed in Hoyle & Fowler (1963a,b). It was Edwin Salpeter and Yakov Zeldovich who independently came up with an explanation (Zeldovich 1964; Salpeter 1964): an accretion disc of hot dense gas swirling into the SMBH at the centre of the galaxy is the engine powering the observed intense radiation.

3.4.2 AGN contribution to the SED

AGN are a major part of extra-galactic astronomy, where quasars are only the most extreme cases. In fact, many galaxies show signs of AGN activity as for example Maiolino & Rieke (1995) estimated 5 - 16 % of all nearby galaxies, indicate an AGN in their spectra. Also, not all AGN are visible since many are hidden behind dust obscuration as for example discussed in Assef et al.

(2013). In Fig. 1.13, the SED of a galaxy hosting an AGN is shown from the X-ray to radio wavelengths. The best fitting model obtained with the SED fitting tool CIGALE (Boquien et al. 2019; Yang et al. 2020, 2022) finds a significant AGN contribution. One characteristic of AGN is a strong X-ray source. Even though close binary stellar objects can emit X-rays originating from matter exchange (see Chapter 16 in Tauris & van den Heuvel 2006), AGN can reach a significant higher X-Ray luminosity from jets or hot coronal gas around the SMBH (e.g. Aird et al. 2010). The X-ray emission of the AGN, shown in Fig. 1.13, was obtained in the band of 2-10 keV with the space based X-ray observatory XMM-Newton (Turner et al. 2001).

The central region around the SMBH in an AGN is radiating in wavelengths ranging from UV to far-IR and only in very strong quasars this radiation is over-shining the entire SED of its host galaxy (Yang et al. 2020, 2022). The SMBH is surrounded by a dense accretion disc which can be identified with broad Balmer emission lines (see Sect. 3.2.3). An inner torus surrounds this region within the scale of a few pc (Combes et al. 2019). This region is enclosed by an outer torus on the scale of a few 100 pc (Maiolino & Rieke 1995). Strong UV radiation heats up this region which then re-emits light with a blackbody spectrum. Hence, in many AGN most of the UV-to-optical light is attenuated by a dusty torus and dust clouds in the galaxy (e.g. Assef et al. 2013). As shown in Fig. 1.13, the AGN contribution is dominant in the mid-IR regime but insignificant in the UV and optical wavelengths.

In Fig. 1.13, one can also find a significant contribution of the AGN to the radio continuum emission. Relativistic jets produced by the AGN and shock regions accelerate electrons and positrons (Meisenheimer et al. 1989). These charged particles emit synchrotron radiation while interacting with the strong magnetic field inside the jet (see e.g. Meisenheimer et al. 1989; Krause et al. 2012). Similarly to the sychrotron radiation from star-forming regions (see Sect. 3.1.3), the emission caused by AGN is as well described by a power law of $S(\nu) \propto \nu^{\alpha}$. In contrast to the spectral index associated with star formation of $\alpha \sim -0.7$ (Condon 1984), the synchrotron spectra of an AGN is observed to be flat $\alpha \sim 0$ or even positive (Linfield 1982; Perley 1982; Bridle & Perley 1984), reaching values up to $\alpha \sim 2.5$ (Mhaskey et al. 2021). The AGN-spectral index of the measured for the galaxy in Fig. 1.13 is $\alpha = -0.1$, whereas the synchrotron radiation emitted by star formation is described by $\alpha = -0.7$. This means, for the galaxy presented in Fig. 1.13, that the AGN is dominating the synchrotron emission at higher energies whereas lower energies are dominated by the star-forming component. In the case of a strong AGN, also the low frequency synchrotron spectrum can be dominated by the AGN. The galaxy, shown in Fig. 1.13, however, is considered as a radio silent AGN with no extended radio lobe detected. Only 1 in 10 AGNs are radio loud exhibiting extreme radio emission (Wilson & Colbert 1995), with luminosities of up to $10^{26}\,\mathrm{WHz}^{-1}$ at 2.7 GHz (Urry & Padovani 1995).

3.4.3 Influence of AGN on the host galaxy

AGNs are not only important as individual objects since they affect their host galaxy and influence their evolution. For example, strong ionising radiation emitted by the AGN can heat up gas and prevent star formation (Di Matteo et al. 2005; Croton et al. 2006; Cattaneo et al. 2009). AGN driven gas outflows can expel also the entire gas reservoir of a galaxy (Silk & Rees 1998; King 2003; Murray et al. 2005; Fabian et al. 2006; Fabian 2012). The intensity of an AGN depends on the accretion rate and does not always have such a drastic effect on the host galaxy. In fact, AGN outflows can compress molecular clouds enhancing the star-formation efficiency

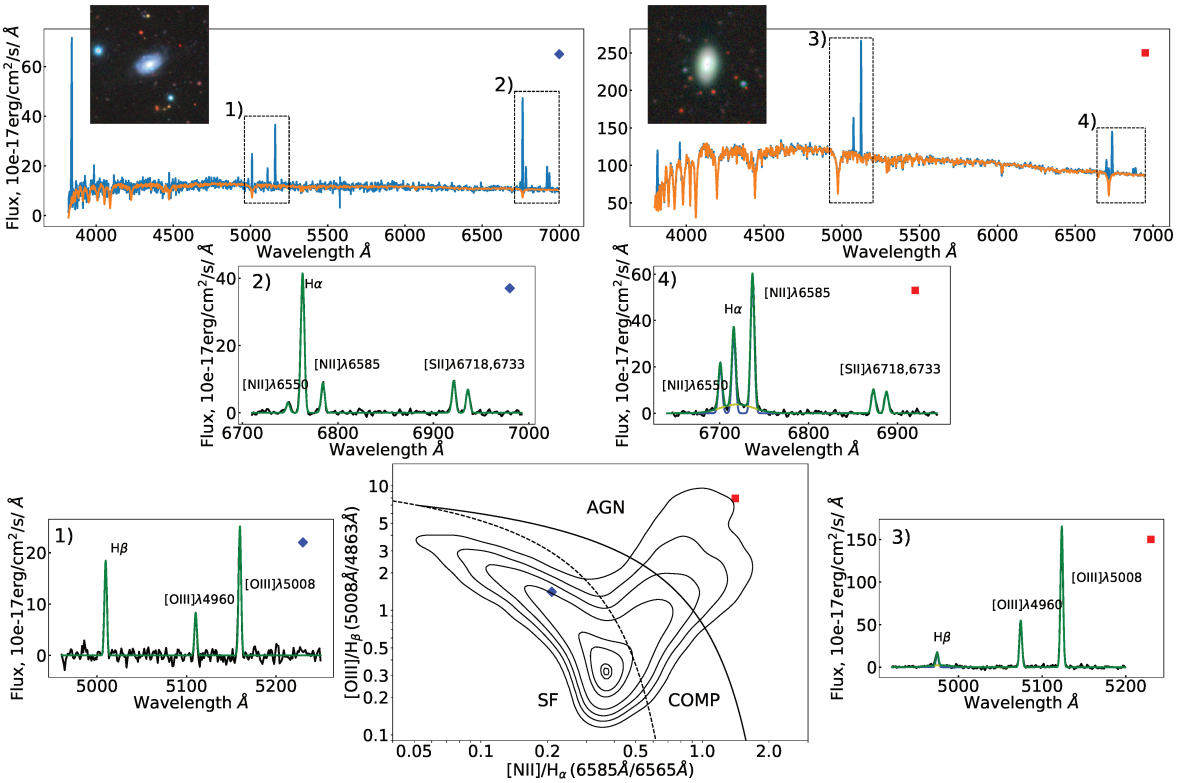

Figure (1.14) BPT diagram of two galaxies. On top panels, the optical spectra of two galaxies are shown. On the left (resp. right) side, a star-forming galaxy (resp. a galaxy hosting an AGN) is shown. The stellar continuum provided by Chilingarian et al. (2017) is shown with orange lines. To illustrate the emission lines needed for the BPT diagram, the continuum subtracted emission line spectra near the Hα and Hβ emission lines is shown with zoom-ins. In the middle of the bottom panels, the BPT diagram with [NII]λ6585/Hα on the x-axis and [OIII]λ5008/Hβ on the y-axis is shown (Baldwin et al. 1981). The contours show the distribution of the SDSS with galaxies exhibiting all four needed emission lines with at least a S/N $>$ 3. The black dashed and solid lines separate observations classified as HII, composite (comp) or as AGN (Kewley et al. 2001, 2006). The situation of the above star-forming and AGN-hosting galaxies are shown with blue and red markers respectively.

(Silk 2005, 2013; Gaibler et al. 2012).

For individual galaxies, it is difficult to estimate how strong AGN activity can affect the host galaxy. It is also challenging to determine the AGN contribution to the SED with only a few data points. Diagnostic diagrams based on optical emission lines of the ionised gas are a popular method since redshift surveys such as the SDSS provide optical spectra for a large sample of galaxies (see Sect. 2.1.2). These diagrams can provide information about the ionisation state of the gas and distinguish between the radiation from HII regions of an ionising AGN emission as discussed in the next section.

3.5 Ionised gas diagnostics

As discussed in Sect. 3.2.3, ionised-gas emission lines can have different origins and thus the intensity proportions of different lines strongly vary between different galaxy types as illustrated in Fig. 1.10. An empirical classification based on the emission line ratios was first introduced by Baldwin, Phillips, & Terlevich (1981). Hence, the diagram is often referred as the BPT diagram. Such a diagram is shown in Fig. 1.14 with the emission-line-flux ratios [NII]λ6585/Hα on the

x-axis and [OIII]λ5008/Hβ on the y-axis. The contours are all SDSS galaxies with a signal to noise S/N < 3 in all four needed emission lines. One notices a distribution shaped like a seagull with two extended wings.

In order to categorise different galaxy types, Kewley et al. (2006) introduced empirical limits shown as solid and dashed black lines in Fig. 1.14. Line ratios, situated below the dashed line, are classified as HII regions, since the underlying process is star formation. Galaxies which are situated above the solid line are considered to be AGN. In order to illustrate the different emission-line ratios, the SDSS spectra of two galaxies are shown with a zoom-in to the region of emission lines used for the BPT diagram. Their positions on the BPT diagram are shown with red and blue markers. It is now evident that the left galaxy is dominated by star formation which is in agreement with its blue colour and the relative strong Hα emission line. The right galaxy hosts an AGN. A clear kinematic confirmation for this is the detected broad line component in the Hα-emission line and the fact that forbidden lines such as [NII]λ6585 and [OIII]λ5008 are significantly stronger than Balmer emission lines. The two lines used to distinguish between these two kinds of galaxies encloses a region where galaxies are classified as '*composite objects whose spectra contain significant contributions from both AGN and star formation*' (Kewley et al. 2006).

In order to further characterise galaxies, additional BPT diagrams are used. These diagrams use ([SII]λ6718 + [SII]λ6733)/Hα (resp. [OI]λ6302/Hα) on their x-axis in comparison the the BPT diagram shown in Fig. 1.14, while the y-axis is the same. These diagrams allow a better distinction between Seyfert, AGN and low-ionisation narrow emission line regions (LINER) (Kewley et al. 2006; Schawinski et al. 2007). The latter galaxy type is characterised by the absence of emission lines that require high ionisation energies such as Helium (Heckman 1980) and are mostly elliptical galaxies (Shields 1992).

BPT diagrams allow one to check whether an individual galaxy can be characterised more by star formation or whether an AGN dominates the emission-line spectrum. It must be said that gas is also affected by dust and therefore BPT diagrams cannot detect an AGN, for example, if it is completely shielded by dust (e.g. Assef et al. 2013). Since different processes can occur in different places in a galaxy, spatially resolved spectroscopy such as integrated field spectroscopy can localise AGNs or HII regions and help to better study the structure of galaxies (e.g. Belfiore et al. 2016).

4 Star formation in galaxies

One fundamental aspect of SED modelling, such as shown in Figs. 1.8, 1.13 or 1.12, is to mimic the build-up of the stellar population over cosmic time. A simple approach is to consider all stars of the same age, which can be a rough approximation often used to estimate the stellar continuum in optical spectra (e.g. Chilingarian et al. 2017). Considering the strong variance of cosmic star-formation history discussed in Sect. 2.2, it is clear that the star-formation history of an individual galaxy is highly complex. In addition, feedback mechanisms from an AGN and star formation can have a significant impact on the star-formation history and is challenging to reproduce by e.g. simulations (Naab & Ostriker 2017). To establish a more realistic model of past star formation, one can assume a continuous star-formation rate (SFR) that declines exponentially. One can further improve this model by assuming two different stellar populations (e.g. Boquien et al. 2019): (1) an old stellar population which started forming at the beginning

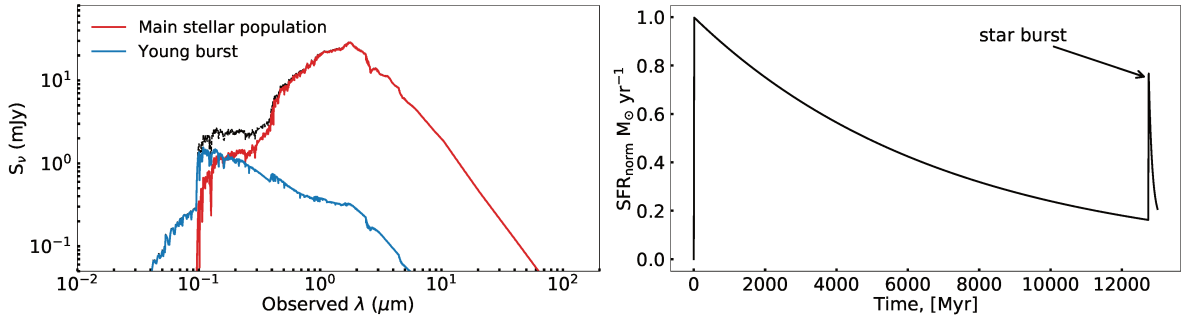

Figure (1.15) SED of stellar populations and their star-formation history. On the left, the SED of two stellar populations is shown similar to the stellar component presented in Fig. 1.8. In red, the SED of an old stellar population is shown, which started forming 13 000 Myr ago. In blue, a young stellar population is shown which originates from a 1 000 Myr old starburst. With a black dashed line, the total stellar spectrum is shown. On the right, the star formation rate is shown, modelled by an exponentially declining star formation history. The main (resp. young) stellar population declines with an e-fold of 7 000 Myr (resp. 100 Myr).

of the Universe and building up the main population of the galaxy. (2) A second population of young stars and a more rapidly declining star-formation history, accounting for a recent starburst caused by gas accretion or a merger. Such a model, computed with CIGALE, is illustrated in Fig. 1.15. The main stellar component started forming 13 000 Myr ago and declines with an e-fold of 7 000 Myr. As shown on the left of Fig. 1.15, this stellar population makes up the main emission of the SED with a dominance at red colours. Younger stars, produced by a recent short burst 1 000 Myr ago with an e-fold of 100 Myr build up only 1 % to the total stellar mass of the modelled SED. As can be seen on the SED, this contribution of the young stellar component is less intense in comparison to the main stellar population. However, the young stars are brighter in the UV and blue optical light. This is why we see galaxies with ongoing star formation exhibiting blue colours as illustrated in Fig. 1.11.

One quantity, of particular interest in order to study the evolutionary state of galaxies, is their SFR at the time of the observation. From the modelled star-formation history, such as the one shown in Fig. 1.15, one can directly obtain the SFR. However, such an estimation is strongly depending on the chosen model which is an approximation (e.g. Boquien et al. 2019). In fact, it is possible to directly measure the current SFR from the calibration of the luminosity at different wavelengths. This is due to the fact that HII regions contribute to the SED over a large range of wavelengths (see Sect 3.1). Such calibrations have been performed in the radio continuum (e.g. Condon et al. 2002), the IR continuum (e.g. Hunter et al. 1986; Lehnert & Heckman 1996; Kennicutt 1998a), optical emission lines (Rosa-González et al. 2002) and UV continuum (Meurer et al. 1995; Kennicutt 1998a). In order to get an overview of the tools used to estimate star formation, the most commonly ones are discussed in the following.

4.1 Star formation rate estimators

The light of young stars, dominated by UV emission, is absorbed by dust and re-emitted in the thermal IR spectrum (Kennicutt 1998a). This makes the far-IR (FIR) luminosity, in the range 10-300 μm, a sensitive star-formation tracer. A commonly-used calibration to convert the far-IR luminosity into a SFR was provided by Kennicutt (1998b):

$$\mathrm{SFR(FIR)[M_\odot yr^{-1}]} = 5.8 \times 10^9\, \mathrm{L_{FIR}[L_\odot]} \tag{1.12}$$

where L_{FIR} is the bolometric luminosity of the FIR emission. While inspecting the AGN contribution to the SED in Fig. 1.13, one notices that the AGN significantly contributes to the total FIR luminosity and biases the SFR estimation (Sanders & Mirabel 1996). In order to distinguish between IR emission from an AGN and star formation sites, an accurate SED modelling is needed.

As discussed in Sect 3.2.3, the Hα emission line has a close connection to HII regions, as long as the ionisation is not dominated by an AGN, and can hence be used as a star formation tracer calibrated in Kennicutt et al. (1994) and Madau et al. (1998):

$$\mathrm{SFR(H}\alpha)[\mathrm{M}_\odot \mathrm{yr}^{-1}] = 7.9 \times 10^{-42}\, \mathrm{L(H}\alpha)[\mathrm{ergs\,s}^{-1}], \tag{1.13}$$

where L(Hα) is the Hα emission-line luminosity. In contrast to the far-IR spectrum, the optical spectra is affected by dust and therefore the measured luminosity is only probing a fraction of the star formation. However, an extinction correction of the Hα luminosity can compensate this. The intrinsic Hα luminosity $L_{int}(H_\alpha)$ can be calculated from the observed Hα luminosity $L_{obs}(H_\alpha)$ following Calzetti (2001):

$$\mathrm{L_{int}(H}\alpha) = \mathrm{L_{obs}(H}\alpha)\, 10^{0.4\mathrm{k(H}\alpha)\mathrm{E(B-V)}}, \tag{1.14}$$

where $k(H_\alpha)$ is the reddening curve computed for the Hα rest-frame wavelength (Calzetti et al. 2000). The colour excess E(B-V), between the observed colour B-V and the intrinsic colour (Cardelli et al. 1989), is often referred as dust extinction. This can be estimated using the observed emission line ratio Hα/Hβ:

$$\mathrm{E(B-V)} = 1.97 \log_{10}\left[\frac{(\mathrm{H}\alpha/\mathrm{H}\beta)_{\mathrm{obs}}}{2.86}\right], \tag{1.15}$$

following Momcheva et al. (2013) and Domínguez et al. (2013). This formula is based on the assumption that the gas is at a temperature of $T = 10^4\,K$ with an electron density of $n_e = 10^2\,cm^{-3}$. A case B recombination (the gas is optically thick to radiation just above 13.6 eV) would then result in an intrinsic Hα/Hβ ratio of 2.86 (Osterbrock & Ferland 2006). Using the dust corrected Hα luminosity, one can calculate the star-formation ratio using equation 1.13 (Kewley et al. 2002). As reviewed in Kennicutt (1998a), the SFR can be also estimated from the forbidden emission-line doublet [OII]λ3727, 3730 or the UV continuum. These estimators, however, are reliable only if dust attenuation can be estimated.

A more complex approach to estimate the SFR was performed for a large sub-sample (10^5 galaxies) of the SDSS by Brinchmann et al. (2004). Their SFR estimation relied on ionised-gas emission-line modelling described in Charlot & Longhetti (2001). They, furthermore, take the gas excitation into account using BPT diagrams (see Sect. 3.5) and estimate the AGN contribution to the Hα emission line. Since the SDSS optical spectrum is only probing the central 3″ region, this estimation is not a representative estimation of the SFR for the entire galaxy. In order to model the total SFR, they computed photometric apertures of the galaxies with the $g-r$ and $r-i$ SDSS photometric-band measurements and extrapolated the spectral-based SFR for the entire galaxy. They used the SFR estimated in the fibre as a prior and assumed a similar star-formation distribution between the central region and the entire galaxy. This technique provides star-formation rates for the entire SDSS DR7 catalogue, enabling the estimation of the

local star formation density (Brinchmann et al. 2004).

Modern photometric surveys provide a good coverage over a large part of the sky and of the wavelength range. Especially, the GALEX and WISE satellites (see Sect. 3.1) added data points at the UV and near-IR wavelengths for galaxies observed in the optical by the SDSS. Based on this data set, Salim et al. (2016) performed an SED fitting for about 700 000 (SDSS) galaxies providing estimates such as the SFR and stellar masses. In order to separate systematical effects, they provide separated SFR estimations from the UV-optical SED and the mid-IR. By comparing their results to the SFR values found by Brinchmann et al. (2004), they find a very good agreement for galaxies of the main star-forming sequence. However, they find that mid-IR SFR values for galaxies with quenched star formation are strongly biased and for those hosting an AGN, the SFR can be over estimated up to 0.6 dex. In quenched galaxies, the bias originates from dust heating by an old stellar population and can reach up to 2 dex. Since the conversion from IR luminosity to SFR is fixed, the resulting SFR values is dominated by old stellar populations and is systematically overestimated. An AGN can also heat dust (see Sect. 3.4), which then radiates in IR, biasing the SFR.

Studies of star formation in the Universe span from the small scales such as molecular clouds in our own Galaxy up to the global SFR estimation of entire galaxies (as reviewed in Kennicutt & Evans 2012). These tools enable to explore the SFR over large parts of cosmic time as e.g. discussed in Sect. 2.2.

4.2 The stellar mass of a galaxy

To place the values of an estimated SFR, described in Sect. 4.1, into context, one needs to know the stellar mass M_* of a galaxy. As e.g. stated in Salim et al. (2016), only the specific star formation rate ($sSFR = SFR/M_*$) has a physical motivation as it probes how many stars are formed per stellar mass. For instance, large SFR values would have a fundamentally different meaning if they were measured in a large galaxy or in a dwarf galaxy.

As discussed in Sect. 3.1, one can rely on SED fitting to estimate the un-attenuated spectrum of the stellar population in a galaxy. Based on this luminosity, the stellar mass can be estimated if one assumes a mass-to-light-ratio of a galaxy. The main requirements are an accurate estimation of the luminosity function of a galaxy as e.g. provided by Blanton et al. (2003) and a modelling of the stellar composition. The latter predicts the luminosity fraction at a specific wavelength, each stellar population contributes. By adopting Monte-Carlo simulations of different star-formation histories, Kauffmann et al. (2003) modelled the mass-to-light-ratio for galaxies in the SDSS. This photometry-based stellar-mass estimation allowed the authors to estimate the mass distribution of the present Universe and to study the mass-size relation of different galaxy types.

4.3 The main sequence of star-forming galaxies

By combining the SFR, measured by Brinchmann et al. (2004) with the stellar mass, estimated by Kauffmann et al. (2003), one can further discuss the evolutionary state of galaxies in a M_*-SFR diagram. This is shown on the left panel of Fig. 1.16 for galaxies of the SDSS. It is striking, that, similarly to Fig. 1.11 a clear dichotomy between a star-forming galaxy population and a quenched one is visible. As already mentioned in Sect. 3.3, the blue sequence of galaxies corresponds to this main sequence of star-forming galaxies and the red sequence to the quiescent sequence. What was not so clear in Fig. 1.11 is the difference in mass. The fact that quiescent galaxies show

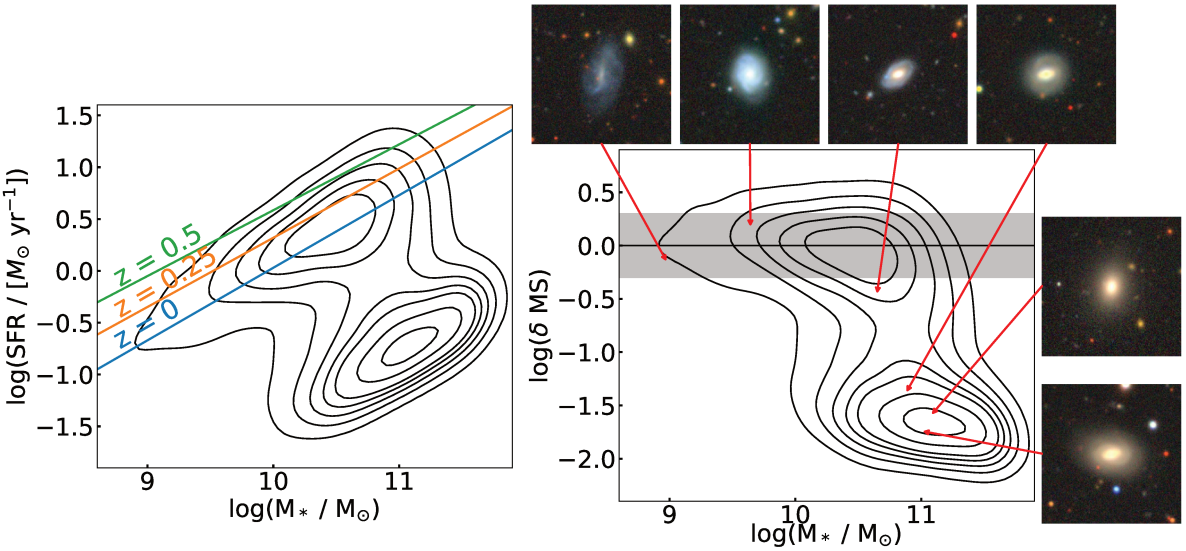

Figure (1.16) Illustration of the main sequence of star-forming galaxies. On the left panel, the distribution of the SFR and the stellar mass estimated by Brinchmann et al. (2004) and Kauffmann et al. (2003), respectively, is shown. The dichotomy, already observed in Fig. 1.11, is clearly visible with the main sequence of star forming galaxies on top and a sequence of quiescent galaxies on the bottom. The main sequence was parametrised by Whitaker et al. (2012) and shown for redshifts $z = 0, 0.25$ and 0.5 with coloured lines. On the right panel, the distance between the predicted main sequence and the measured SFR $\delta\mathrm{MS} = \mathrm{SFR}/\mathrm{SFR}_{\mathrm{MS}}$ is shown as a function of stellar mass. To illustrate the distribution of different galaxy types, the same galaxies shown with snapshots in Fig. 1.11 are shown here with their location on the diagram.

higher masses but similar absolute r-band magnitudes is due to the fact that high-mass galaxies have a higher mass-to-light-ratio (Kauffmann et al. 2003). Taking the model of hierarchical mass growth of galaxies over cosmic time (see Sect. 2.2), this distribution further supports the idea that star-forming galaxies are the progenitors of massive galaxies with quenched star formation.

As illustrated in Fig 1.6, the star-formation density is not constant over cosmic time. The SFR varies with redshift and so does the main sequence of star-forming galaxies. This shift was parametrised by Whitaker et al. (2012): a relation between the stellar mass and the SFR provides the expected SFR values for the main sequence for a given redshift. This relation is shown for $z = 0, 0.25$ and 0.5 with coloured lines on the left panel in Fig. 1.16. This relation further allows to compute the offset of an individual galaxy from the main sequence as $\delta\mathrm{MS} = \mathrm{SFR}/\mathrm{SFR}_{\mathrm{MS}}$. This offset is shown on the right panel of Fig. 1.16. The main sequence is situated at $\delta\mathrm{MS} = 0$ with a scatter, estimated from observation of 0.3 dex (e.g. Noeske et al. 2007b; Rodighiero et al. 2011; Whitaker et al. 2012; Schreiber et al. 2015). In order to illustrate the different galaxy types found along this distribution, the snapshots of the exact same galaxies shown in Fig. 1.11 are displayed in the right panel of Fig. 1.16. Their position on the diagram describing the distance to the main sequence shows good agreement with their position on the colour-magnitude diagram: on the one hand, elliptical galaxies of the red sequence are found to be quenched and shifted up to 2 dex below the main sequence. On the other hand, blue galaxies, mostly discs, are scattered around the main sequence.

The distribution of galaxies along the main sequence is a useful tool to characterise their evolutionary state of galaxies and has been extensively used to study the behaviour of galaxy samples over cosmic time (e.g. Noeske et al. 2007b; Whitaker et al. 2012; Speagle et al. 2014; Schreiber et al. 2015; Tacconi et al. 2018). One key question in galaxy evolution till the present

day is how galaxies evolve along the main sequence and what makes them drop beneath the main sequence (Conselice 2014).

4.4 Evolution of star formation over cosmic time

The review on the cosmic star-formation history of Madau & Dickinson (2014) gives a complete picture on the current understanding of star formation at different epochs. While dust-obscured star formation might have a significant contribution to the cosmic star-formation history, the authors find an overall trend of declining star formation since $z \sim 2$. However, they point out that we know little about the internal mechanisms ruling galaxies: how gas reaches the inner central part of galaxies and cools down to form stars or how star formation is regulated by outflows and inflows or possible mergers. The tight connection of star formation and stellar mass evolution over cosmic time can be reproduced by hydrodynamic simulations (e.g. Davé et al. 2011; Dekel et al. 2013; Torrey et al. 2014; Sparre et al. 2015). The declining star-formation activity can also be modelled, assuming a tight connection between the mass assembly of the dark matter halo and the gas supply of the galaxy (Tacchella et al. 2013). This raises one particular question: '*What is the mechanism that keeps the evolving galaxy so tightly confined to the vicinity of the main sequence ridge until it quenches and falls below the main sequence?*' (Tacchella et al. 2016). As found in Noeske et al. (2007b,a), most galaxies do not experience a disruptive merger fuelling star formation since $z < 1$ and the majority of star formation happens in main-sequence galaxies which do not show signs of any recent merger. This motivates a model where gas is accreted through streams from the surroundings (Dekel et al. 2009). Also, minor merger events can play an important role as they transport gas into the central parts of galaxies, fuelling star formation (Dekel & Burkert 2014). Smooth gas accretion can also transport material from filaments into galaxies (e.g. Dekel et al. 2013) and explain the observed high frequency of disc morphology in main sequence galaxies (Genzel et al. 2006, 2008; Stark et al. 2008; Daddi et al. 2010). All these models can explain how galaxies shift up and down around the main sequence over their lifetime, before dropping significantly below it though star-formation quenching. Figure 1.17, taken from Tacchella et al. (2016), illustrates such an evolutionary path of a galaxy. A central aspect of these cycles is that minor mergers or counter rotating gas streams are causing disc instabilities. These events lead to a compaction phase with central star-formation enhancement, lifting the galaxy above the main sequence. The compaction can even lead to a so-called 'blue nugget phase', obscured at high redshift where a high central gas concentration and strong star formation leads to shorter depletion times and to inside-out quenching due to gas outflows. These phases can happen multiple times within the lifetime of a galaxy, shifting it up and down with respect to the main sequence. When the gas is depleted and the cooling of accreted gas is no longer possible due to a hot halo, the galaxy will ultimately fall under the main sequence and finally quench (Tacchella et al. 2016). One major aspect of such a model is that it can explain the transition towards bulge-dominated galaxies such as S0 and elliptical galaxies. Such a transformation can be produced by repetitive minor merger events with simulations turning disc-dominated galaxies into bulge-dominated galaxies as shown by Bournaud et al. (2007).

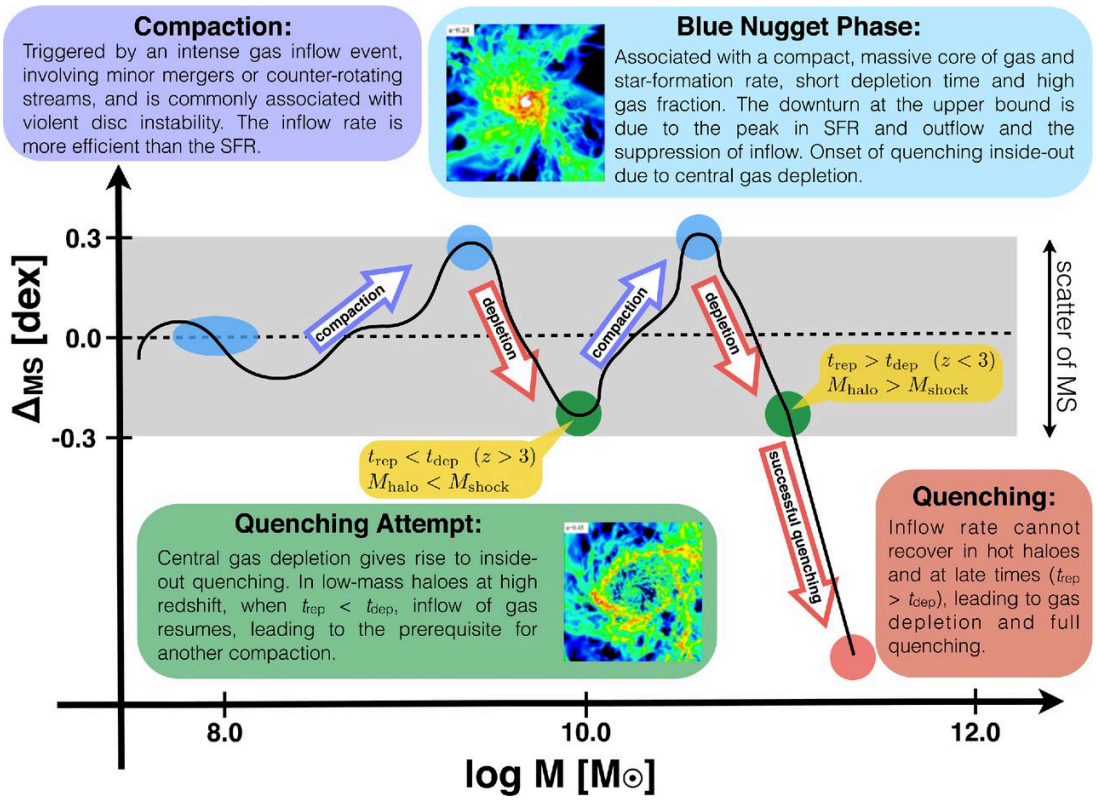

Figure (1.17) Galaxy evolution on the main sequence over cosmic time, taken from Tacchella et al. (2016, figure 11). This is an educational representation of how a galaxy goes through compaction phases caused by gas accretion and minor mergers in the course of its evolution. Such compaction phases are followed by gas depletion, when the accumulated gas reservoir transformed into stars is exhausted. This happens repetitively until the cooling mechanism of accreted gas is no longer effective, the galaxy then quenches its star formation and falls below the main sequence.

5 Kinematic signatures in ionised gas emission-lines

In our current understanding of galaxies, there is (most likely) a super-massive black hole (SMBH) at the centre of each galactic bulge (Heckman & Best 2014). The original idea of such a compact object is closely related to the observation of so-called quasi-stellar objects (also known as quasars) whose brightness exceeds anything known so far (see Sect. 3.4). In nearby galaxies with mostly inactive nuclei, Kormendy & Richstone (1995) discussed the reliability of evidences suggesting the presence of a massive dark objects in their centre. They select galaxies with a high central mass-to-light ratio and study the rotation curves estimated from stars and gas. They find stellar kinematics more robust than those from gas. In our own Galaxy, Eckart & Genzel (1996) and Ghez et al. (1998) observed the orbits of stars at the very centre and found that they all orbit a dark massive object. The mass density of this region was estimated with $10^9\,M_\odot\,pc^{-3}$ (Genzel et al. 1996). The most plausible explanation was that this must be a compact cluster of black holes with a masses of $10-20\,M_\odot$ or one SMBH. Relying on an analysis of long-term observations of the stars orbiting this object, Ghez et al. (2008) provided a precise mass measurement of $4.1\pm0.6\times10^6 M_\odot$. In M87, a direct observation of the accretion disc and the shadow of a SMBH has greatly strengthened the understanding that SMBHs are located at the very centre of a galaxy (Event Horizon Telescope Collaboration et al. 2019). In a very recent work, such a direct image was presented in Akiyama et al. (2022) for the SMBH of our own Milky Way Sgr A*.

Considering that galaxy mergers happen quite frequently, a logical conclusion is that such mergers will lead at one point to binary SMBH before finally coalescing. From major merger simulations, Begelman et al. (1980) estimated that the two cores will stay at a separation >1 kpc for $\sim$ 100 Myr, before forming a stable binary at separations of $0.01-1$ pc (Milosavljević & Merritt 2001). When both nuclei have an accretion disc and are active, it is possible to observe this phenomenon.

In Komossa et al. (2003), two nuclei were discovered in the merger system NGC 6240 with a separation less then 1 kpc, using X-ray observations. The first candidate of a close dual AGN was found using the Very Long Baseline Array (VLBA) which revealed the presence of two central, compact, flat-spectrum components (Maness et al. 2004), as expected from two AGN. With higher resolution, Rodriguez et al. (2006) confirmed two AGN with a projected separation of 7.3 pc. Interestingly, they performed optical spectral observations with the Hobby-Eberly Telescope and found indications of two velocity systems. Using a long-slit spectrometer, Gerke et al. (2007) observed a double-peak (DP) signature in the [OIII]λ4960, λ5008 emission line doublet in a galaxy at z=0.7. Their observations are summarised in Fig. 1.18. They measure a peak separation of $630\,km\,s^{-1}$ and a spatial separation of 1.2 kpc. From an HST image, they find a morphology that is consistent with a merger remnant. Including observations at different wavelengths, they describe the system as a dust-obscured AGN in an early-type galaxy. They conclude that the observations can best be explained by a dual AGN.

Based on the detection of such kinematic signatures, Comerford et al. (2009a) performed a systematic search for galaxy merger remnants and found a second dual AGN identified as a DP emission line. They, furthermore, found 32 AGN exhibiting a velocity offset between 60 to $300\,km\,s^{-1}$ with respect to the stellar continuum velocity, measured for the host galaxies. They conclude that these mis-alignments of the AGN are the result of a late stage of galaxy mergers.

Starting from the visual discovery of a close pair of two nuclei, Comerford et al. (2009b)

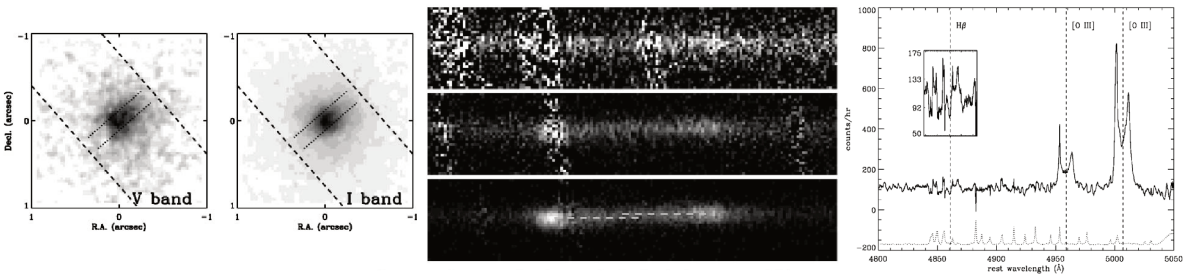

Figure (1.18) Long-slit spectroscopy of a double-peak galaxy observed by Gerke et al. (2007). A compilation of the figures 1, 2 and 3 from Gerke et al. (2007). On the left panel, the HST ACS observations with the broad band filters F606W and F814W (V and I) are shown. With dashed lines, the edges of the DEEP2 DEIMOS slit observations are shown. Dotted lines indicate the central part of which the spectra, shown in the middle and right panel, is extracted. On the middle panel, the 2D spectral observations of the Hβ, [OIII]λ 4960 and [OIII]λ5008 emission lines on the DEIMOS detector are shown from top to bottom respectively. The vertical shift between the two horizontal dashed lines in the bottom panel indicates the spatial position of the two [OIII]λ5008 emission line components. This separation corresponds to 1.2 kpc. On the right panel, the 1D spectrum is shown, which clearly reveals the DP signature.

measured a projected separation of 1.75 kpc in the system COSMOS J100043.15+020637.2. Using a long-slit spectrometer, they found a projected velocity difference of 150 km s^{-1}. This is indeed a less prominent DP signature, present in the 3″ SDSS spectra.

These results have revealed that there can be a link between a dual AGN and a DP emission line shape. If one takes this a step further and looks at large surveys such as the SDSS, which provides spectroscopic measurements of many galaxies, this offers a great opportunity to find large samples of dual AGN. Nevertheless, it is difficult to infer the underlying mechanism in the central kpc of a galaxy from just a single spectroscopic measurement and an image. Such a systematic search for a DP [OIII]λ5008 emission line was first performed by Wang et al. (2009) who found 87 DP AGN in the SDSS DR-7. By searching for DP [OIII]λ 4960 and λ5008 emission lines, Liu et al. (2010) who found 167 DP AGN and Smith et al. (2010) 148 DP AGN. However, they were not able to distinguish between a rotating disc scenario, ionised gas outflow or a dual AGN. They clearly state that "*spatially resolved optical imaging, spectroscopy, radio or X-ray follow-up are needed to draw firm conclusions*" (Liu et al. 2010). In a more general study, which also included non-AGN galaxies, Ge et al. (2012) found 3 030 DP galaxies. These works build a solid basis for in-depth studies using follow-up observations of peculiar systems.

Subsequently, many follow-up observations were carried out for interesting DP objects. Another technique is to resolve dual AGN with X-ray observations. In Comerford et al. (2011), this technique was carried out by using the Chandra X-ray Observatory. As can be seen in Fig. 1.19, two sources have been detected revealing a projected separation of 1.9 kpc. In addition, long-slit observations with the Kast Spectrograph on the Lick 3m telescope confirmed the same separation and found a projected velocity separation of 350 km s^{-1} (Comerford et al. 2011). However, even with high-resolution observations, it remains challenging to determine the exact configuration of the AGN. For example, a galaxy merger can also lead to an AGN with off-centred kinematics with respect to the stellar kinematics of the host galaxy. These offset-AGN create an emission line anomaly as well (Comerford & Greene 2014). In a larger study of 12 optical selected dual AGN with both high resolution HST and Chandra X-ray observations, Comerford et al. (2015) found 6 dual or offset AGN with a separation of less then 10 kpc and 6 single AGN.

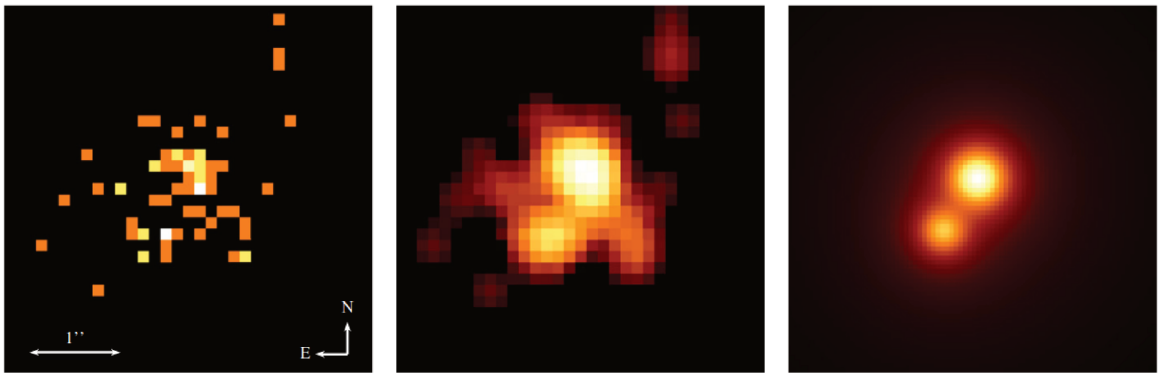

Figure (1.19) Chandra X-ray observations of a dual AGN candidate. Figure taken from Comerford et al. (2011, figure 2). The Chandra X-ray in the 0.5-8 keV range is shown on the left. In the middle panel, the X-ray data were smoothed with a 3 pixel radius Gaussian and on the right, a two-component model is shown, consisting of a two-dimensional Lorentzian with a varying power law. The size of the images is $4'' \times 4''$.

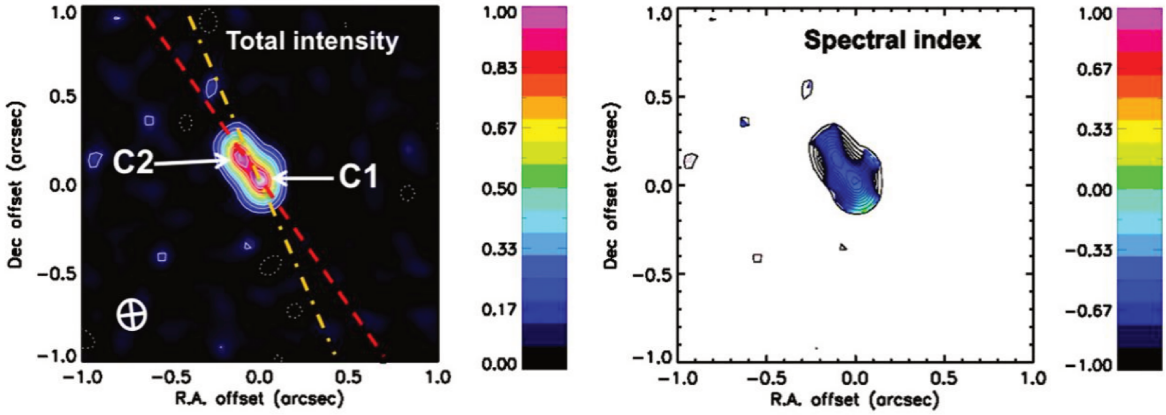

Figure (1.20) VLA image of dual AGN J1158+3231 observed at 8.5 GHz. Figure taken from Müller-Sánchez et al. (2015, figure 14). The contours on both images indicate the levels of the peak flux intensity between 10 % and +90 % with 10 % steps. On the left panel, the colour bar represents the total radio intensity. The positions of the two nuclei, C1 and C2, are marked with arrows. The photometric major axis is indicated with a red dashed line and a yellow dashed line marks the orientation of the two [OIII]λ5008 peaks, detected with long slit observations. On the right panel, the spectral index, calculated with additional VLA observations at 11.5 GHz, is displayed.

They, furthermore, find the dual or offset AGN to be 10 times more luminous than the single AGN ones. This enhancement can be explained by an effective inwards funneling of gas during a past merger event.

Using high-resolution multi-band Very Large Array observations in combination with optical long-slit spectroscopy, Müller-Sánchez et al. (2015) conducted a detailed study of 18 DP AGN. In three galaxies, they found two separated optical components with emission line ratios typical of AGN. Figure 1.20 displays the two nuclei of one of those three galaxies, which have a projected separation between 0.6 and 1.6 kpc and which have been individually detected with radio emission at 8.5 and 11.5 GHz. The fact that both nuclei have a flat spectral index, confirms the hypothesis of a dual nuclei. They found that perturbed gas kinematics are responsible for the DP emission line signature in 75 % of the cases while 10 % remain ambiguous.

Based on a large sample of 71 AGN at $z < 0.1$ which exhibit a DP [OIII]λ5008 line in their SDSS spectra, Nevin et al. (2016) performed a systematic classification using additional

long-slit spectroscopic observations. They conclude, that for about 86 % of their sample, the DP profiles are produced by moderate-luminosity AGN outflows. In 6 % of the cases, they found a rotating disc and the remaining 8 % are ambiguous. They also state that they are not able to confirm a dual AGN with long-slit observations only. More generally, Comerford et al. (2018) have described a link between DP emission lines and galaxy mergers. They performed a kinematic analysis with long-slit spectra of 95 DP galaxies. They found that the majority of the observed DP emission lines are due to AGN driven outflows. They also found 8 galaxies with close companions and twice as many AGN in such systems. They concluded that 3 % of all AGN with DP emission lines found in the SDSS are mergers with visible dual nuclei in the SDSS image.

The search for dual AGN is an essential piece of the puzzle in understanding the hierarchical mass growth of galaxies. AGN are particularly suitable for such a search, as they are luminous compact sources and are traced by strong [OIII]λ5008 line emission. However, all merger epochs do not exhibit a visible AGN phase. Ge et al. (2012) performed a DP emission line search including not only the [OIII]$\lambda 5008, 4960$ doublet but also the Hβ, Hα, the [NII]$\lambda 6550, 6585$ doublet and the [SII]$\lambda 6718, 6733$ doublet. They found that the majority of DP galaxies do not show any signs of AGN activity and can be normal star-forming galaxies. Although it is difficult to draw a clear conclusion with only one central spectroscopic observation, a systematic view of the general phenomenon of DP emission line galaxies can contribute to the understanding of galaxy mergers. It was this what motivated me to started my PhD thesis and worked on the articles Maschmann & Melchior (2019); Maschmann et al. (2020); Mazzilli Ciraulo et al. (2021); Maschmann et al. (2022b) and Maschmann et al. (2022a), which are the central results of this thesis.

CHAPTER 2

Double-peak emission-line galaxies

Considering the many different types of galaxies that have been described by rigorous surveys of the night sky, one question is particularly important: How did galaxies grow to the size we see in the Universe today? In recent decades, a number of proposed modelling predict a hierarchical growth of galaxies (e.g. Somerville & Davé 2015). Smaller galaxies merge and form larger galaxies. This idea has had a lot of success and is able to explain many observations. In large surveys, galaxies approaching each other or galaxies in the middle of a chaotic merger are observed. One finds also large galaxies absorbing smaller ones in a minor merger. With the help of simulations relying on the the ΛCDM model, it is possible to determine the exact duration of such processes and we know that after a short time, mergers are difficult to distinguish from isolated galaxies or to accurately infer the state of a merger even though tidal features can be still detected. It is therefore of great importance to find diagnostics enabling to identify late stages of galaxy mergers.

Ionised-gas emission lines are measured at a specific wavelength, defined by the underlying quantum mechanical process. The detection of a red (resp. blue) shifted component of a discrete wavelength is caused by the recession (resp. approach) velocity of the source, known as the Doppler-shift. If in a galaxy two peaks are detected instead of one in an emission-line spectrum, it is clear that a part of the detected gas is moving towards us and the other is receding away from us. This diagnostic has often been used to find dual AGN, which are the end-product of a merger. However, it is also clear that AGN are not very common and double-peaked (DP) AGN are even rarer. So it is clear that such galaxies do not help us to probe the hierarchical build-up of massive galaxies.

This is where I contributed with the peer reviewed journal article (Maschmann et al. 2020). If one searches for DP emission-line galaxies in general, one will find not only AGN. With an automatic selection procedure, I managed to find 5663 such galaxies consisting of only 7 % AGN. With a detailed study of different galaxy characteristics, I succeeded in identifying special features in comparison to galaxies exhibiting single-peaked (SP) emission lines. The latter sample is selected with the same redshift and stellar-mass distribution as the DP sample. Normally, one would assume that DP galaxies are more likely galaxy mergers which is not the case: only about 10 % are mergers, as many as in the SP sample. However, it is striking, that DP galaxies

exhibiting larger bulges and S0 galaxies are more frequent among them than in SP galaxies. About 36 % of the DP galaxies are S0 galaxies compared to only 20 % of the SP sample. Furthermore, a detailed study of the measured gas kinematics has shown that there are no direct correlations between the DP structure and the galaxy inclination. In addition, DP galaxies show significantly larger velocity dispersions in the stellar continuum. For example, if one looks at the galaxies that actively form stars, another difference becomes apparent: DP galaxies form more stars in their centre than SP galaxies.

All these arguments indicate that a central DP signature is compatible with the scenario of a past minor merger. Gas can be effectively channeled into the centre of a galaxy, triggering enhanced star formation. A detailed discussion of other alternatives, such as outflows, concludes that DP galaxies are a possible indicator for detecting late stages of minor mergers that are responsible for central bulge growth as seen in Bournaud et al. (2007).

Astronomy & Astrophysics manuscript no. output
December 11, 2022

Double-peak emission line galaxies in the SDSS catalogue. A minor merger sequence.

Daniel Maschmann[1,2], Anne-Laure Melchior[1], Gary A. Mamon[3], Igor V. Chilingarian[4,5], Ivan Yu. Katkov[5,6]

[1] Sorbonne Université, LERMA, Observatoire de Paris, PSL research university, CNRS, F-75014, Paris, France
e-mail: Daniel.Maschmann@rwth-aachen.de, A.L.Melchior@obspm.fr
[2] RWTH Aachen University, Institute for Theory of Science and Technology, Aachen, Germany
[3] Institut d'Astrophysique de Paris (UMR 7095: CNRS & Sorbonne Université), 98 bis bd Arago, F-75014 Paris, France
[4] Center for Astrophysics – Harvard and Smithsonian, 60 Garden St. MS09, Cambridge, MA, 02138, USA
[5] Sternberg Astronomical Institute, M.V. Lomonosov Moscow State University, 13 Universitetsky prospect, Moscow, 119991, Russia
[6] New York University Abu Dhabi, Saadiyat Island, PO Box 129188, Abu Dhabi, UAE

Received 02 March 2020/ accepted 23 July 2020

ABSTRACT

Double-peak narrow emission line galaxies have been studied extensively in the past years, in the hope of discovering late stages of mergers. It is difficult to disentangle this phenomenon from disc rotations and gas outflows with the sole spectroscopic measurement of the central 3″. We aim to properly detect such galaxies and distinguish the underlying mechanisms with a detailed analysis of the host-galaxy properties and their kinematics. Relying on the Reference Catalogue of Spectral Energy Distribution (RCSED), we developed an automated selection procedure and found 5 663 double-peak emission line galaxies at $z < 0.34$ corresponding to 0.8% of the parent database. To characterise these galaxies, we built a single-peak no-bias control sample (NBCS) with the same redshift and stellar mass distributions as the double-peak sample (DPS). These two samples are indeed very similar in terms of absolute magnitude, [OIII] luminosity, colour-colour diagrams, age and specific star formation rate, metallicity, and environment. We find an important excess of S0 galaxies in the DPS, not observed in the NBCS, which cannot be accounted for by the environment, as most of these galaxies are isolated or in poor groups. Similarly, we find a relative deficit of pure discs in the DPS late-type galaxies, which are preferentially of Sa type. In parallel, we observe a systematic central excess of star formation and extinction for double peak (DP) galaxies. Finally, there are noticeable differences in the kinematics: The gas velocity dispersion is correlated with the galaxy inclination in the NBCS, whereas this relation does not hold for the DPS. Furthermore, the DP galaxies show larger stellar velocity dispersions and they deviate from the Tully-Fisher relation for both late-type and S0 galaxies. These discrepancies can be reconciled if one considers the two peaks as two different components. Considering the morphological biases in favour of bulge-dominated galaxies and the star formation central enhancement, we suggest a scenario of multiple, sequential minor mergers driving the increase of the bulge size, leading to larger fractions of S0 galaxies and a deficit of pure disc galaxies.

Key words. galaxies: kinematics and dynamics, galaxies: interactions, galaxies: evolution, galaxies:irregular, techniques: spectroscopic, methods: data analysis

1. Introduction

The evolution of galaxies over cosmic time is largely determined by their mass growth and is thus connected to their environment and their merger rate. It is well observed that the mix of morphological types of galaxies depends on the environment (Dressler 1980; Whitmore et al. 1993). The star formation rate (SFR) of galaxies is a well-suited diagnostic to characterise their evolutionary state. Galaxies can, on the one hand, enhance their star formation rate through interaction with their environment (Bothun & Dressler 1986; Pimbblet et al. 2002), but, on the other hand, they can also be quenched by the environment (Balogh et al. 1998). Isolated galaxies are thought to refuel their discs with gas from extended halos and from cosmic filaments, while galaxies located in massive clusters will evolve passively (Balogh et al. 1998). The assembly and growth of galactic discs and galaxies in general are some of the key issues of galaxy simulations (e.g. Mo et al. 1998). Accretion from filaments is motivated by numerical simulations (e.g. Bond et al. 1996), while observational detection is based on filaments of galaxies in cluster environments (e.g. Laigle et al. 2018; Sarron et al. 2019) and the Lyα forest tomography (e.g. Lee et al. 2018). The latter approach is the only one that directly detects so-called gas accretion.

The identification of merging galaxies is usually based on morphology (e.g. Lotz et al. 2004) or detection of dynamically close pairs (e.g. De Propris et al. 2005). Relying on the latter technique, Ellison et al. (2008) identified 1716 galaxies with companions in the Sloan Digital Sky Survey (SDSS) Data Release (DR) 4 with stellar mass ratios between $0.1 < M_1/M_2 < 10$. Further studies of this sample found that star formation due to galaxy interactions can be triggered in low-to-intermediate density environments (Ellison et al. 2010). By extending their search to SDSS DR7, they increased their sample to 21 347 galaxy pairs and found evidence for a central starburst induced by galaxy interactions (Patton et al. 2011). By including quasi stellar objects (QSO) in their search, Ellison et al. (2011b) found that active galactic nuclei (AGN) activity can occur well before the final merging of a galaxy pair and is accompanied by ongoing star formation.

The original prediction that merging should go up to the black hole coalescence (e.g. Begelman et al. 1980) has not been observed yet. But earlier steps have been explored, and several

dual AGNs, which is a late stage of a galaxy merger (Genzel et al. 2001; Koss et al. 2016, 2018; Goulding et al. 2019), or even a triple nucleus (Deane et al. 2014; Pfeifle et al. 2019), have been detected. While about 40% of ultra-luminous infrared galaxies exhibit a double nucleus (Cui et al. 2001), Koss et al. (2018) discuss that gas-rich luminous AGNs are often hidden mergers. Green et al. (2010) were first to identify a galaxy merger resulting in a binary quasar with a projected separation of 21 kpc and a radial velocity difference of 215 km s^{-1}. Mergers with a binary quasar have also been associated with an offset and/or DP [OIII]λ5008 emission line (e.g. Comerford et al. 2009, 2013). Many systematic searches for dual AGNs have been conducted at different wavelengths (Liu et al. 2011, 2013; Koss et al. 2012; Fu et al. 2015) to discuss the nature of dual AGNs.

Using the direct detection of DP narrow emission lines, Wang et al. (2009), Liu et al. (2010), Smith et al. (2010), and Ge et al. (2012) selected large galaxy samples from several galaxy surveys. In most of these works, the search for double-peak emission lines are motivated by the search for dual AGNs or dual galactic cores. Starting from such samples, Comerford et al. (2012) conducted long-slit observations on double-peak emission line galaxies to find kiloparsec-scale spatial offsets and to constrain the selection of dual AGNs. Using the Hubble Space Telescope and the space based X-ray telescope Chandra, Comerford et al. (2015) confirmed a dual AGN, with a separation of 2.2 kpc, resulting from an extreme minor merger (460:1) creating a DP [OIII]λ5008 emission line. Follow-up observations with the Very Large Array enabled the detection of three dual AGNs, AGN wind-driven outflows, radio-jet driven outflows, and one rotating narrow-line region producing DP narrow emission lines (Müller-Sánchez et al. 2015). Long-slit observations of DP galaxies enable them to distinguish between AGN-driven outflows and a rotating disc (Nevin et al. 2016), as further supported by Monte Carlo simulations in Nevin et al. (2018). Furthermore, Comerford et al. (2018) associated double-peak emission line galaxies with galaxy mergers, concluding that at least 3% of galaxies with DP narrow AGN emission lines found in the SDSS spectra are galaxy mergers identified in SDSS snapshots.

In this article, we build an objective selection procedure for DP narrow emission line galaxies to test whether we can identify different merger stages. We did not constrain our search to dual AGNs candidates and we dis not include a visual selection in contrast to previous galaxy samples. We based our work on the value-added Reference catalogue of Spectral Energy Distributions (RCSED) (Chilingarian et al. 2017).

This work is organised as follows. In Sect. 2, we describe the pipeline developed to automatically select galaxies with spectra exhibiting double-peak emission lines and describe the selection of a no-bias control sample (NBCS). Sect. 3 classifies this double-peak sample (DPS) relying on ionisation diagrams and on morphology and compare it with previous works. In Sect. 4, we analyse the properties of the DPS and compare them with the NBCS. In Sect. 5, we discuss our results followed by a conclusion in Sect. 6.

A cosmology of $\Omega_m = 0.3$, $\Omega_\Lambda = 0.7$ and $h = 0.7$ is assumed in this work.

2. Detection of double-peak emission line galaxies in RCSED catalogue

2.1. Spectroscopic data

The RCSED contains 800 299 galaxies selected from the SDSS DR7 spectroscopic sample (with a spectral resolving power $R = 1500 \ldots 2500$) in the redshift-range $0.007 < z < 0.6$ (Chilingarian et al. 2017). This catalogue provides k-corrected photometric data in the ultraviolet, optical, and near-infrared bands observed by the Galaxy Evolution Explorer (GALEX), SDSS, and the UK Infrared Telescope Deep Sky Survey (UKIDSS).

The RCSED catalogue also provides optical SDSS spectra in 3-arcsec circular apertures up to a magnitude limit of r = 17.77 mag (Abazajian et al. 2009) and a best-fitting template. The template assumes either a simple stellar population (SSP) model or an exponentially declining star formation history (EXP-SFH) (Chilingarian et al. 2017). The best-fitting template subtracted from an original spectrum provides an emission line spectrum in the observed wavelength range [3600 Å, 6790 Å]. In Fig. 1, we show major emission lines extracted from stellar continuum subtracted spectra of three different galaxies, studied in this article as they exhibit double-peak emission lines as described in Sect. 2.2.

In the RCSED catalogue, each emission line spectrum was fitted with two different functions: (1) a Gaussian function and (2) a non-parametric distribution. In case (1), two Gaussian functions were adjusted to all allowed and all forbidden transitions. The case (2) is based on an algorithm, which adapted an arbitrary shape to all emission lines simultaneously, again grouped by the transition type. The non-parametric fit is able to fit complex line shapes such as a DP and AGN-driven outflows, and can also reveal low-luminosity AGN broad line components (Chilingarian et al. 2018). The catalogue provides the fluxes resulting from these two procedures for several emission lines, χ^2 per number degree of freedom (Ndof), hereafter χ^2_ν, the equivalent width (EW) and other parameters, as specified in Chilingarian et al. (2017).

2.2. Automated selection procedure

We developed an automated three-stage selection procedure to find DP galaxies. The first stage pre-selects galaxies with a threshold on the S/N, and performs successively the emission line stacking, line adjustments and empirical selection criteria. Some emission lines are individually fitted at the second stage to select first DP candidates. We also selected candidates showing no DP properties to be the control sample (CS). Stages 1 and 2 are summarised in Fig. 2. At the third stage, we obtained the final DPS using the fit parameter of each line, as shown in Fig. 3. Hereafter, we explain in detail each step of the selection procedure.

2.2.1. Preliminary candidates

We first restricted the analysis to galaxies with detectable emission lines, in order to define a preliminary sample on which a subsequent emission line fitting can be applied. Hence, we selected objects with a S/N > 10 in the [OIII]λ5008 or H$\alpha\lambda$6565 lines. To secure the detection of the S[II]λ6718 and S[II]λ6733 lines within the spectra bandwidth, we added the condition $z < 0.34$. We thus kept a sample containing 276 239 objects from the RCSED catalogue.

We then selected 189 152 galaxies, which have a S/N > 5 in at least three emission lines among H$\alpha\lambda$6565, H$\beta\lambda$4863, H$\gamma\lambda$4342, [OIII]λ5008, [OI]λ6302, [NII]λ6550, and [NII]λ6585. As described above, the non-parametric fit adapts to the line shape and is thus able to fit a DP structure. It is hence possible to disentangle single Gaussian profiles from non-Gaussian profiles. With the reduced χ^2_ν value of the single

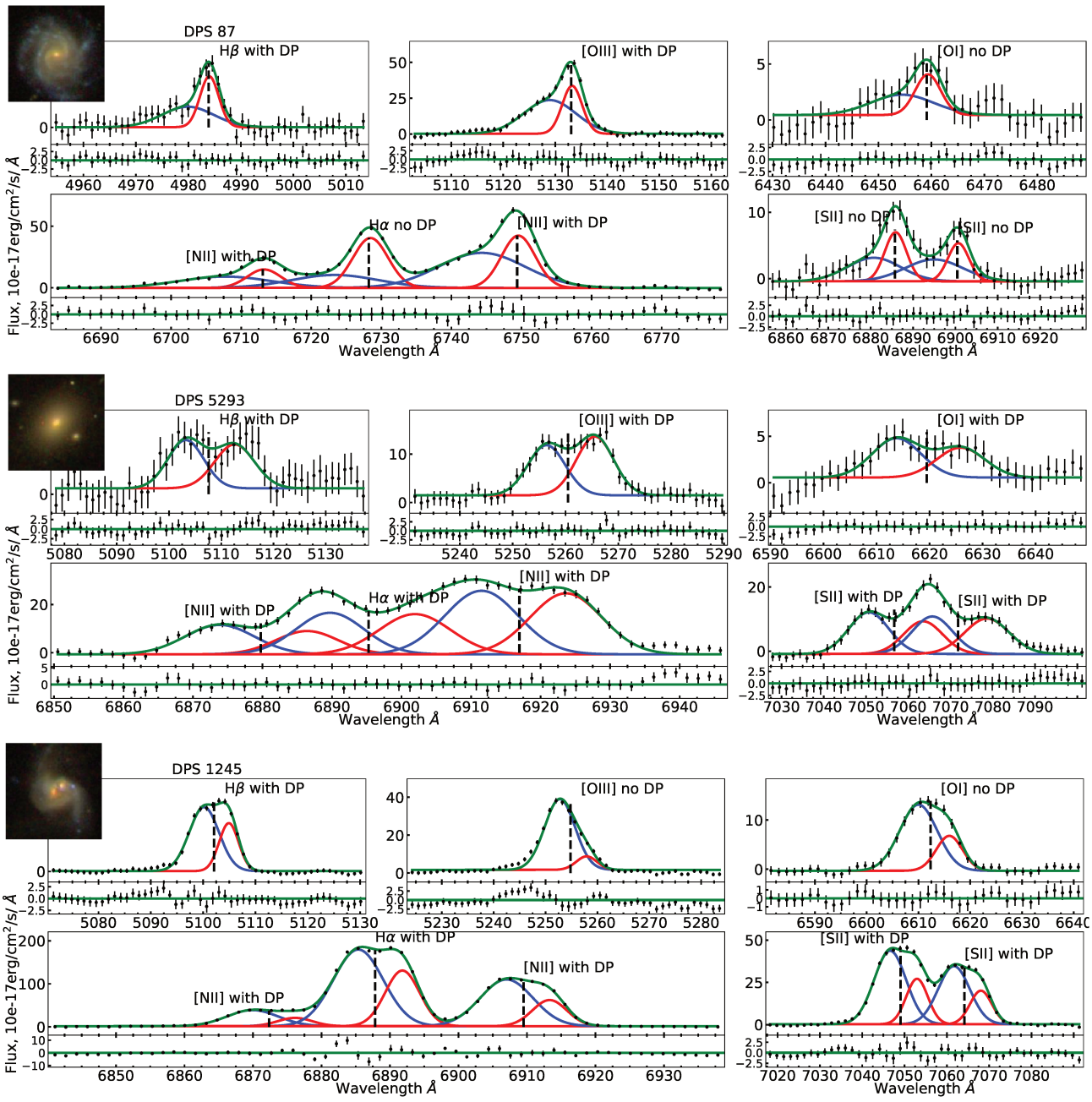

Fig. 1. Emission lines of three DP galaxies, namely H$\beta\lambda$4863, [OIII]λ5008, [OI]λ6302, [NII]λ 6550, H$\alpha\lambda$6565, [NII]λ 6585, [SII]λ6718 and [SII]λ 6733. For each panel, we display on the top left, the 62″ × 62″ SDSS snapshot. Each displayed line is fitted with a double Gaussian function as explained in Sect. 2.2. We show the blueshifted Gaussian component as blue lines and the redshifted component as red lines. The green line is a superposition of the two Gaussian components. Below each emission line we show residuals. We flag lines with a confirmed DP selected with criteria described in Sect. 2.2 as 'with DP' and flag the others as 'no DP' for failing the criteria. The black dashed vertical line indicates the position of the stellar velocity of the host galaxy, computed by Chilingarian et al. (2017). The top spectra are for a face-on spiral galaxy at a redshift of z = 0.02 with a Δv_{DP} = 232 km s^{-1}, which resembles an outflow (discussed in Sect. 5.6). The middle spectra are for an elliptical galaxy at z = 0.05 showing a Δv_{DP} = 495 km s^{-1}. The bottom spectra are for a galaxy merger at z = 0.05 and Δv_{DP} = 269 km s^{-1}. This is one of 58 galaxies discussed in Maschmann & Melchior (2019) showing a DP structure probably associated with recent galaxy merger.

Gaussian and non-parametric RCSED fit, we can compared the spectra whose emission lines resemble a Gaussian shape with those spectra showing an unlikely Gaussian shape, such as a DP. We selected 99 740 galaxies with a larger χ^2_ν value for the Gaussian fit than for the non-parametric fit. They were classified as preliminary candidates. Spectra with a larger χ^2_ν value for the non-parametric fit were selected as the control sample (CS), since they have more likely a Gaussian shape (see detailed description in Sect. 2.2.3).

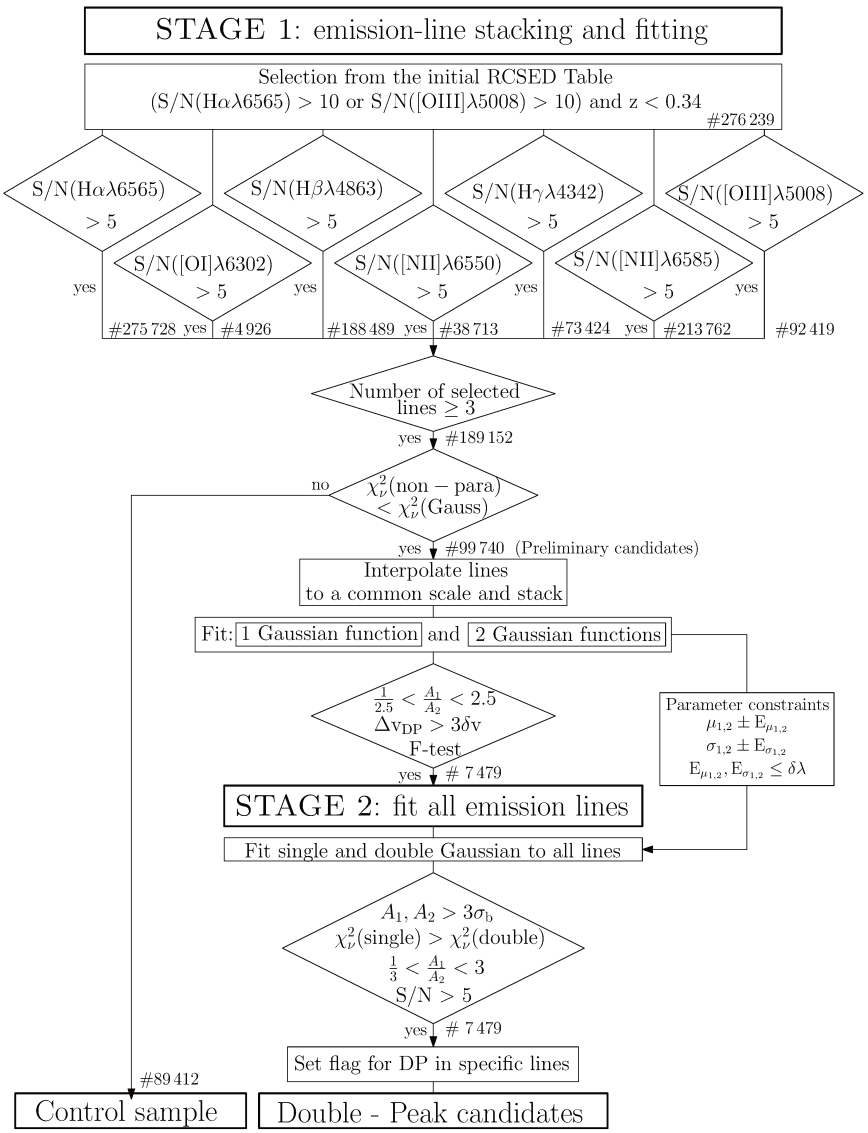

Fig. 2. Flowchart describing the first two stages of the automated selection procedure, detailed in Section 2.2. We list up all selection criteria and note the number of galaxies at each selection step. In stage 1 we select preliminary candidates and a control sample (CS) using emission line properties and χ^2 ratios from emission line fitting computed by Chilingarian et al. (2017). We visualise the stacking and fitting procedure and all selection criteria described in 2.2.2. In stage 2 we describe the individual fitting of each emission line and list up all criteria for the DP flag detailed in 2.2.4. We finally select 7 479 DP candidates and 89 412 galaxies for the CS.

2.2.2. Emission line stacking and fitting procedure

The emission line fittings performed in the RCSED catalogue is separated for Balmer and forbidden emission lines since they can originate from different parts of the galaxy (Chilingarian et al. 2017). For the preliminary selected galaxies, we only find ∼ 1% showing a deviation greater than the SDSS spectral resolution between the two fits regarding the emission line position or dispersion. The RCSED catalogue has also excluded SDSS objects classified as quasars or Seyfert 1 (Schneider et al. 2010) since the stellar population analysis or the k-correction (e.g. Chilingarian et al. 2010b) is not supporting these kind of objects (Chilingarian et al. 2017). Hence, most broad-line galaxies were not included and we were not investigating such line shapes in this study.

We can thus assume *a priori* the same or a similar shape in all emission lines. This motivates a stacking procedure of the different emission lines of each spectra. While the shape of a single emission line can be distorted by noise, genuine signals will be enhanced in the stacked spectra characterised by a reduced noise. To guarantee the significance of this procedure, we required S/N > 5 for all stacked emission lines. To stack the emission lines, we selected each emission line in the range of ±30Å with respect to the emission line position and transformed it into velocities. We calculated the velocity of each wavelength bin i as $v_i = \mathrm{c}\,(\Delta\lambda_i)/\lambda_{\mathrm{rest}}$, where $\Delta\lambda_i$ is the difference between the wavelength of the bin i and the observed emission line position and λ_{rest} its rest-frame wavelength. We calculated the stacked spectra by summing the flux of each selected emission line in each velocity bin v_i and add the uncertainties quadratically.

We isolated the H$\alpha\lambda$6565, [NII]λ6550 and [NII]λ6585 emission lines for the stacking procedure. They can overlap and cause artefacts in the stacked spectra. The [NII]λ6550, λ6585 doublet is characterised by a fixed flux ratio of

[NII]λ6585/[NII]λ6550 = 2.92 ± 0.32 (Acker et al. 1989). Using the non-parametric emission line fit from RCSED we could extrapolate and subtract the [NII] doublet, as done in Schirmer et al. (2013).

We fitted a single Gaussian function (g_{single}) and a double Gaussian function (g_{double}) against each stacked spectrum. We used the following functions for the adjustments:

$$g_{single}(v) = A\ \exp\left(\frac{(v-\mu)^2}{2\sigma^2}\right) + B\,, \quad (1)$$

where A is the amplitude, μ the mean and σ the standard deviation of the Gaussian function, v the velocity and B a constant accounting for the background noise level.

$$g_{double}(v) = A_1\ \exp\left(\frac{(v-\mu_1)^2}{2\sigma_1^2}\right) + A_2\ \exp\left(\frac{(v-\mu_2)^2}{2\sigma_2^2}\right) + B. \quad (2)$$

In Eq. (2), we used the same notation as Eq. (1) with subscripts (1,2) defining the first and second Gaussian components. All fitting procedures were performed using the data analysis framework ROOT[1]

We then applied criteria to select DP candidates with the fit procedure, as follows:

1. $1/2.5 < A_1/A_2 < 2.5$
2. $\Delta v_{DP} = |\mu_2 - \mu_2| > 3\,\delta v$
3. F-test

Criteria (1) ensures that one of the two possible peaks is not suppressed or does not represent only noise. Criteria (2) demands the separation of the two peaks to be three times greater than δv, the bin-width of the spectroscopic observation, transformed into a velocity, which is $3\delta v = 207\,\mathrm{km\,s^{-1}}$. The F-test of criteria (3) directly compares the two fitted models and demands a significant decrease in χ^2 relative to the increase in the Ndof for the double Gaussian fit (subset 'd') in comparison to the single Gaussian fit (subset 's'). Following Mendenhall & Sincich (2011), we calculated the F-statistic, as follows:

$$f_{stat} = \frac{(\chi^2_s - \chi^2_d)/(\mathrm{Ndof_s} - \mathrm{Ndof_d})}{\chi^2_d/\mathrm{Ndof_d}}, \quad (3)$$

and demanded the Fisher-distribution F to reject the single Gaussian hypothesis with a probability of less than 5% by using the cumulative distribution function:

$$F_{cdf}(f_{stat}|\mathrm{Ndof_s} - \mathrm{Ndof_d}, \mathrm{Ndof_d}) > 0.95. \quad (4)$$

With these criteria, we selected 7 479 galaxies.

The Gaussian velocity dispersions σ_i that we measured directly from the spectra need to be corrected for the instrumental broadening σ_{inst} (as e.g. discussed in Woo et al. 2004). We calculated the corrected dispersion as $\sigma_{i,corr} = \sqrt{\sigma_i^2 - \sigma_{inst}^2}$, where σ_i corresponds to σ, σ_1 and σ_2. The resolution of the SDSS spectra is not constant for the covered wavelength range and decreases towards higher wavelengths. To correct the stacked-spectra velocity dispersions, we used the mean σ_{inst} computed over the selected emission lines. We find a mean $\sigma_{inst} = 61 \pm 4\mathrm{km\,s^{-1}}$. In the subsequent analysis, we only discussed corrected velocity dispersions.

[1] © Copyright CERN 2014-18 (http://root.cern.ch/).

2.2.3. Control sample selection

For later analysis, we selected a Control Sample (CS) to compare with our DPS. This sample was selected during the first stage and corresponds to galaxies showing no evidence of any DP feature. The preliminary sample, selected in Sect. 2.2.1, contains 189 152 galaxies, and was then divided into two subsamples using the Gaussian and the non-parametric fits provided in the RCSED. We kept spectra exhibiting a larger χ^2_ν value for the non-parametric than for the Gaussian fit to select galaxies showing Gaussian shaped emission lines. With this criterion, we selected 89 412 galaxies, building up the CS. Since we considered the same S/N thresholds for emission lines and the same maximal redshift as for the DP candidates, this is a representative control sample. Nevertheless, as further discussed in Sect. 2.3, this CS still shows a selection bias in the redshift and stellar mass distributions, and a no-bias control sample (NBCS) is selected.

2.2.4. Individual emission line fitting

In the second stage of the selection procedure, we examined the following emission lines separately: H$\gamma\lambda$4342, H$\beta\lambda$4863, [OIII]λ5008, [OI]λ6302, [NII]λ 6550, H$\alpha\lambda$6565, [NII]λ6585, [SII]λ6718, and [SII]λ6733. We fitted a single and a double Gaussian function to each line. For the double Gaussian function, we set the parameters $\mu_{1,2}$ and $\sigma_{1,2}$ provided by the best fit of the stacked emission lines (see Sect. 2.2.2) and let them vary only inside their uncertainty range $\pm E_{\mu_{1,2}}$ and $\pm E_{\sigma_{1,2}}$. The uncertainties are usually smaller than the spectral bin size $\delta\lambda$ of the SDSS which means that these values are quasi fixed. In the case of uncertainties larger than $0.4 \times \delta\lambda$, we fixed them to $0.4 \times \delta\lambda$.

Using the best fit results of the single and double Gaussian fit functions, we applied the following criteria to flag each line if we detect a DP:

1. $A_1, A_2 > 3\,\sigma_b$
2. $\chi^2_\nu(\mathrm{single}) > \chi^2_\nu(\mathrm{double})$
3. $1/3 < A_1/A_2 < 3$
4. S/N > 5

where σ_b is the root mean square (RMS) of the background noise level measured on both sides of the emission line. The first criterion ensures that the amplitude of each DP component is significantly larger than the background noise. The second criterion constrains that the double Gaussian function is better fitting the data than the single Gaussian one. With the third criterion, we excluded emission lines where one DP component is suppressed. In this case, it is likely that the weak component represents noise or an artefact of a clumpy line shape. Maschmann & Melchior (2019) discussed genuine cases where one of the components is weak or suppressed despite a high S/N. Criteria four ensures that the fitted lines are detectable and are not just noise.

For those lines showing a DP according to the selection criteria above, we set a flag to highlight the specific line as a DP line.

2.2.5. Final selection of double-peak galaxies

In the third stage of the selection procedure, we excluded galaxies which do not show any DP in the strongest emission lines which are mostly misclassified due to an artificial DP structure created by the stacking procedure. This third-stage selection is illustrated in Fig. 3.

We kept spectra with the strongest line flagged as DP. In cases of two (resp. more than two) emission lines flagged as DP,

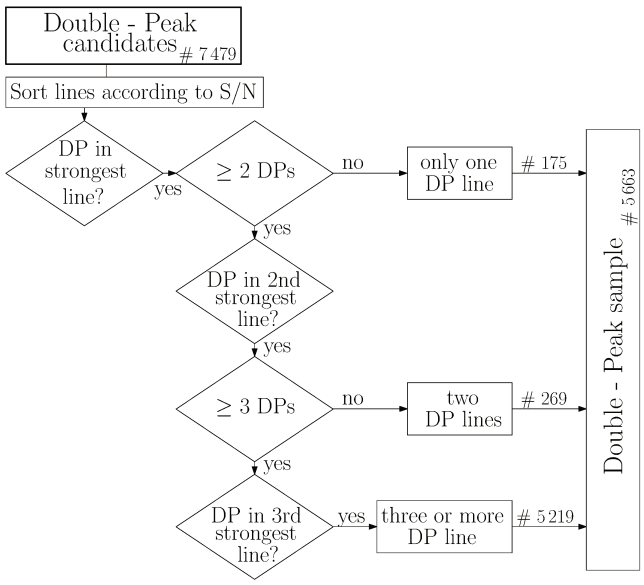

Fig. 3. Stage 3 of the selection procedure to find the final DPS. This algorithm sorts the fitted emission lines according to their S/N and uses the DP flags indicating confirmed DP in the specific line. All selected galaxies must have a confirmed DP in the strongest line. If the object has more than 1 (resp. 2) confirmed line(s), we must also find a DP in the second (resp. second and third) strongest line. This procedure excludes objects which have a falsely confirmed DP in some weaker lines. We finally get the DPS counting 5 663 galaxies. In Table 1, we present the distribution of DP galaxies for different number of confirmed DP.

we also demanded the second (resp. second and third) strongest line to be flagged as DP. With these criteria, we excluded 1 816 galaxies, which do not show a DP in their strong lines. This can occur for different reasons: (1) the fitting procedure can fail at specific lines because of a noisy line shape, (2) the spectra show only a DP structure in the stacked spectra but not in any individual line, or (3) DP occur only in weak lines, which are dominated by noise.

Our final DPS contains 5 663 galaxies with $\Delta v = |\mu_2 - \mu_1|$ between 211 and 582 km/s. In Fig. 4, we show distributions of the flux ratios between the two fit components of the H$\alpha\lambda$6565, [OIII]λ5008, H$\beta\lambda$4863 and [NII]λ6585 emission lines. There is a noticeable difference between the flux ratio $\phi_{\max}/\phi_{\min}$ of Hα and [OIII]. We also present the distribution of Δv_{DP} and the measured ratio of the amplitudes and velocity dispersions $\sigma_{\max}/\sigma_{\min}$ of the two components in the stacked spectra.

The number of confirmed DP lines varies between one and nine and is presented in Table 1. 92% (resp. 72%) of the selected galaxies exhibit three (resp. four) or more double-peak emission lines.

The automated selection procedure selected DP galaxies with an objective algorithm. This means that we did not need any visual inspection, which would have been a subjective factor in the sample selection. We show in Table 2 some fitting parameters of the first five galaxies of our DPS.

2.3. No-bias control sample

Figure 5 displays stellar mass (Kauffmann et al. 2003) as a function of redshift for the CS and for the DPS. We can observe that very few low-redshift objects are present in the DPS. This is obviously a selection bias: our method ends up excluding small systems with $M_* < 10^{10}\,M_\odot$. This is due to the fact that we cut $\Delta v_{DP} < 211 \mathrm{km\,s^{-1}}$: those two quantities are related through the Tully Fisher relation (Tully & Fisher 1977), as further discussed in Sect. 4.3.4. We thus indirectly cut on the redshift and the fibre size. Hence, most DP detections correspond to a fibre size larger than 3 kpc and massive galaxies which have $M_* > 10^{10.4}\,M_\odot$. The maximal redshift observed in the DPS is z = 0.32 (but this particular galaxy has no stellar mass approximation and is thus not represented in Fig. 5). Only < 1% of the DP galaxies have a redshift $z > 0.25$. This can be explained by the S/N cut of emission lines in the selection procedure (see Sect. 2.2.1). For comparison purposes, we defined a sample of ordinary galaxies showing no double-peak emission lines but following the same redshift and stellar mass distribution as the DPS. We randomly selected galaxies from the CS (defined in Sect. 2.2.3) following the same redshift-stellar mass distribution as the DPS. Therefore, we divided the redshift-stellar mass space into a grid of 20×20 boxes and randomly draw galaxies from the CS in each box, following the probability of finding a DP galaxy in the specific box. We were thus able to select 5 128 galaxies from the CS as shown in Fig. 6. In order to keep the same redshift-stellar mass distribution for the NBCS as the DPS, it is not possible to exceed 5 128 galaxies in the NBCS. This new sample has approximately the same redshift and stellar mass properties as the DPS but shows single Gaussian shaped emission lines and is hereafter called the no-bias control sample (NBCS). We present the redshift and stellar mass distributions for both samples in Fig. 6.

2.4. Comparison with other works on DP

In this Section, we compare our DPS with previous samples. In Table 3, we cross-identify our samples at different selection steps with four other works, which released galaxy samples defined with DP galaxies or asymmetric features. Namely, we present a comparison with the samples found by Wang et al. (2009) and Liu et al. (2010), which comprise 87 and 167 Type two DP AGNs detected with the [OIII]λ5008 line. The sample of Smith et al. (2010) comprises 148 quasars classified as type one and type two AGNs. Ge et al. (2012) conducted a much broader selection procedure and provide two samples: one composed of 3030 galaxies with double-peak emission lines (hereafter G12-DP) and a second one gathering 12 582 galaxies with top flat or asymmetric line shapes (hereafter G12-TFAS).

Our DP detection algorithm is based on a stacking procedure, which enables to study galaxies with at least three significant emission lines including a strong [OIII]λ5008 or H$\alpha\lambda$6565 line. These requirements are encoded among others in the preliminary selection (see Sect. 2.2.1). By comparing the sample of our preliminary candidates of 99 740 galaxies (see Sect. 2.2.1), we detect 71% (resp. 57%) of the sample found by Wang et al. (2009) (resp. Liu et al. 2010). Those galaxies, which fail our DP detection algorithm, show mostly different emission line shapes between the [OIII]λ5008 and H$\alpha\lambda$6565 lines. Those galaxies were then systematically sorted out in stage three of our selection procedure (see Sect. 2.2.5). We find only one DP galaxy in the RCSED catalogue selected by Smith et al. (2010), which also fails our final selection procedure due to an irregular H$\alpha\lambda$6565 shape where the algorithm is not able to adjust a double Gaussian function with fixed $\mu_{1,2}$ and $\sigma_{1,2}$ (see Sect. 2.2.5). These are studies based on AGN quasars (Schneider et al. 2010) which were excluded from both the RCSED (Chilingarian et al. 2017) and our present study.

By comparing our work to the catalogues provided by Ge et al. (2012), we find a detection rate of 75% (resp. 47%) for

Table 1. The DPS sorted into groups of number of confirmed DP lines

Number of lines with confirmed DP	1	2	3	4	5	6	7	8	9
Number of Objects	175	269	1149	1634	897	800	543	169	27

Table 2. The double-peak galaxy sample

Identifier	μ_1 km s^{-1}	μ_2 km s^{-1}	σ_1 km s^{-1}	σ_2 km s^{-1}	DP_{H_β}	Hβ flux$_1$ 10^{-17}erg cm^2 s^{-1}	Hβ flux$_2$ 10^{-17} erg cm^2 s^{-1}
(1)	(2)	(3)	(4)	(5)	(6)	(7)	(8)
DPS 1	-81 ± 9	219 ± 10	150 ± 6	119 ± 6	1	57 ± 5	33 ± 4
DPS 2	-194 ± 7	43 ± 11	91 ± 5	108 ± 8	0	25 ± 4	34 ± 5
DPS 3	-187 ± 11	163 ± 8	158 ± 10	109 ± 7	1	39 ± 4	27 ± 3
DPS 4	-89 ± 28	125 ± 27	110 ± 15	99 ± 13	1	47 ± 7	42 ± 8
DPS 5	-99 ± 6	148 ± 5	110 ± 4	106 ± 3	1	71 ± 5	58 ± 5

Notes: We provide the parameters obtained by the two fitting procedures described in sec. 2.2.2 and 2.2.4. The first column (1) provides the object identifier. We provide the fit-parameters and their uncertainties for the stacked spectra in columns (2-5). In column (6) we provide the DP flag exemplary for the H$\beta\lambda$4863 line and the flux of the two DP components in column (7) and (8). This table is available in its entirety in digital form and provides parameters for: H$\gamma\lambda$4342, H$\beta\lambda$4863, [OIII]λ5008, [OI]λ6302, [NII]λ 6550, H$\alpha\lambda$6565, [NII]λ 6585, [SII]λ6718 and [SII]λ 6733.

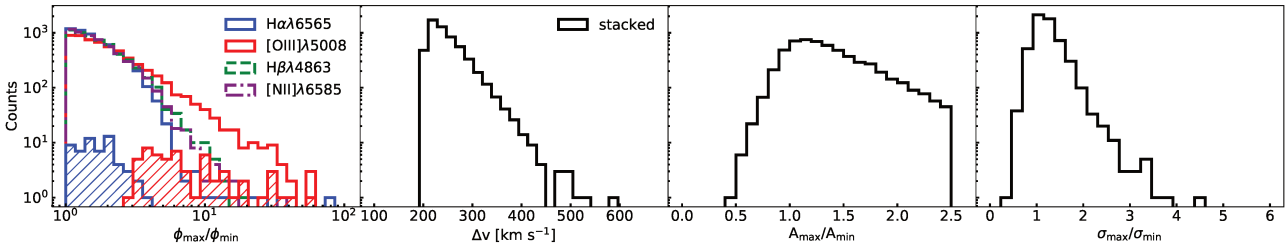

Fig. 4. Characteristics of the galaxies selected with a DP feature in their emission lines. From left to right: The first panel shows the flux ratio ϕ_{max}/ϕ_{min} of the stronger line divided by the weaker line for the individual emission lines H$\alpha\lambda$6565, [OIII]λ5008, H$\beta\lambda$4863 and [NII]λ6585. We display the H$\alpha\lambda$6565 and [OIII]λ5008 emission line ratios of the objects found in Maschmann & Melchior (2019) with blue and re hatched surfaces. The other panels display parameters computed on the stacked spectra (see Sect. 2.2.2). The second panel shows the velocity difference Δv between the two peak components taken from the stacking procedure. The third (resp. fourth) panel displays the amplitude (resp. velocity dispersion) ratio of the stronger and weaker line components of the stacked spectra.

the G12-DP (resp. G12-TFAS) sample of those detected in our preliminary sample. We find some similarities between the two catalogues but we find only 947 galaxies on the G12-DP sample and 2967 from the G12-TFAS sample. In addition, most of the galaxies found by Ge et al. (2012) have been discarded in our algorithm since they do not show a S/N > 5 in at least 3 emission lines, or are better fitted by a single Gaussian function than a non-parametric function (see Sect. 2.2.1).

In this work, we present a new DP sample with a very different selection procedure in comparison to previous works which all relied on visual inspection at some stage. Our sample was selected by an algorithm without any subjective post processing.

2.5. Summary

We developed an automated selection procedure to find double-peak emission line galaxies. We present 5663 such galaxies showing a wide range of possible emission line shapes (different Flux, Amplitude or σ ratios, see Fig. 4). Due to a wide range of explanation for DP phenomena, we classify our sample in the following and present an analysis.

3. Sample classification

3.1. Classification based on ionisation diagrams

To identify different galaxy types, BPT diagnostic diagrams provide an empirical classification based on optical emission line flux ratios first introduced by Baldwin, Phillips, & Terlevich (1981), which have been further tuned by Kewley et al. (2006b) and Schawinski et al. (2007). We used three different types of BPT diagrams: the first type uses the emission line flux ratio [OIII]5008/Hβ4863 on the y-axis and [NII]6585/Hα6565 on the x-axis as shown in Fig. 7. The second and third types of BPT diagrams use ([SII]6718 + [SII]6733)/Hα6565 (resp. [OI]6302/Hα6565) on the x-axis, while the y-axis is the same as the first type. We classified galaxies with the first BPT diagram into 4 groups: star-forming (SF) galaxies, active galactic nuclei (AGN), composite (COMP) galaxies and low-ionisation narrow emission line regions (LINER) (Schawinski et al. 2007). In the case of the DPS, we display each of the two emission line components in the BPT-diagrams, as the two peaks are most probably emitted from two different regions.

We classified the two emission line components according to their position on the BPT diagram if all four needed emission lines have a S/N > 3. In the case where we only have three emission lines with a S/N > 3, we computed the upper or lower limits derived from the uncertainties of the undetected emission line. If the constraints of these emission line ratios are unambiguous, we

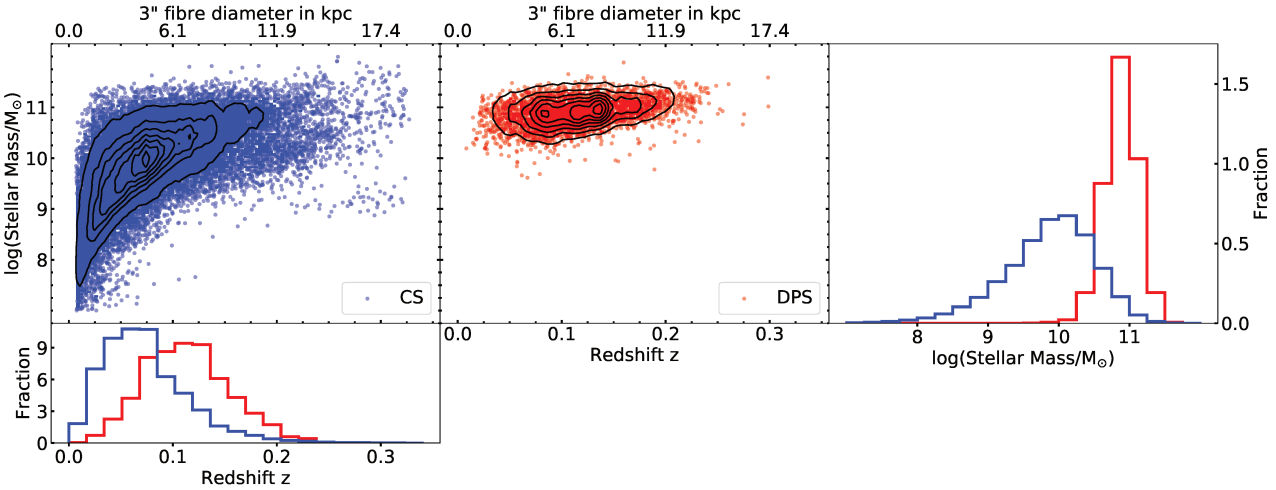

Fig. 5. Stellar mass-redshift distribution for the CS (blue, top left panel) and the DPS (red, top middle panel). The contours indicate the density level. In the top right panel, we show the histogram of stellar masses and, on the bottom left panel, the histogram of redshifts. We also display the fibre diameter corresponding to 3″ on top of the upper left and middle panels.

Table 3. Comparison of our DPS to other similar works with respect to the selection procedure of this work.

Previous work		Cross matched samples			
Sample	Size	RCSED	Preliminary Candidates	DP Candidates	DPS
Wang et al. (2009)	(87)	83	82	75	58
Liu et al. (2010)	(167)	135	129	114	73
Smith et al. (2010)	(148)	1	1	1	0
Ge et al. (2012) G12-DP	(3 030)	2 794	1 255	1 179	947
Ge et al. (2012) G12-TFAS	(12 582)	11 475	6 277	3 585	2 967

Notes: We present the comparison of our DPS to other similar works with respect to the selection procedure of this work. We show in the first column the reference of the sample and the size in the second. In the third column, we show a cross-match with the RCSED catalogue (Chilingarian et al. 2017). We display the number of galaxies found in the preliminary candidate sample, the DP candidates and the final DP galaxies in the last three columns, respectively (see Sect. 2.2.1, 2.2.2 and 2.2.5).

could classify them. Since the COMP region in the first BPT diagram borders the AGN and the SF regions, it was not possible to classify galaxies as COMP unambiguously using the flux limits. In Fig. 7, we show the classification of the single lines of the CS, the NBCS and each emission line component of the DPS. We also show with arrows upper or lower limits of these DP galaxies, which only have three significant emission line components. In all BPT diagrams, we colour-code the specific star formation ratio computed by Brinchmann et al. (2004).

The classification of the first BPT diagram type using all four emission lines with a S/N > 3 was used first. This classified about 67% of the bluer and the redder peaks. Galaxies with only three significant emission lines in the first diagram type were classified using the upper or lower limits, which comprises about 16% of the blue and the redshifted peaks. With the second and the third types of BPT diagrams, we only classified 0.4% of the two peak components with all four emission lines having a S/N > 3. Numerous peak components could not be classified using the upper or lower limits in the second or the third diagram types. This is because if the [NII]6585 line is weak, the [SII]6718, [SII]6733 or the [OI]6302 lines are usually not detected. To directly compare the DPS with the CS and the NBCS, we also performed the same BPT classification as for the CS and NBCS but with the non-parametric emission line fit performed by Chilingarian et al. (2017). This classification shows 80 to 90% agreement with those DP, classified the same way in each component (e.g. double SF). We present the final BPT classification in Table 4 for all the three samples, namely DPS, CS and NBCS.

We classified 88 945 (99.5%) galaxies of the CS, 5032 (98.1%) of the NBCS and 5423 (95.4%) galaxies from the DPS with an individual classification and 4818 (85.1%) using the non-parametric fit. The majority of the CS galaxies are SF 92%, while only a small amount is classified as COMP (5%) and only a few galaxies, about 2% (resp 1%), are classified as AGN (resp. LINER). This is not surprising since we know from Fig. 5 that the CS comprises many small galaxies. This classification is different for the NBCS: the majority (55%) is still classified as SF but we find around 24% to be classified as COMP, and 13% (resp. 6%) as AGN (resp. LINER). In comparison, we classified 45% of the DPS as SF using the non-parametric emission line fit. About 38% of the DPS are classified as COMP showing that we find less SF and more COMP galaxies in comparison to the NBCS. We find a similar AGN fraction of about 11% (13%). We find twice the fraction of galaxies classified as LINER in the NBCS (6%) in comparison to the DPS (3%).

By classifying each emission line component of the DPS, we find 29% (resp. 17%) to be classified as SF (resp. COMP) in both emission line components. We also find 14% of the DPS galaxies with one component to be classified as SF and the other one as COMP. According to Kewley et al. (2006b), COMP galaxies are

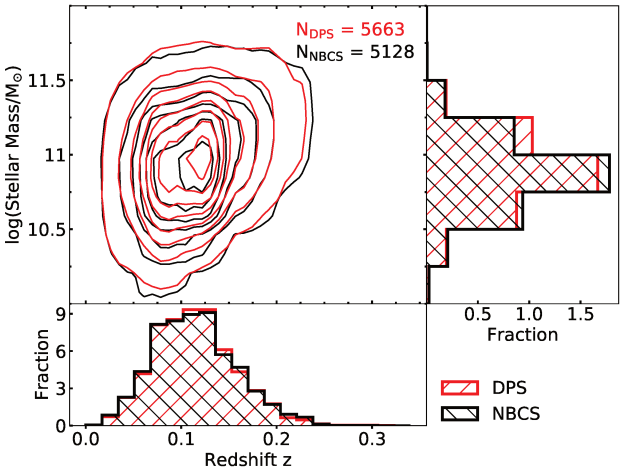

Fig. 6. Stellar mass-redshift distribution (see Fig. 5) for the DPS (red) and the NBCS (black). The selection of the NBCS is explained in Sect. 2.3. We also compute histograms for the redshift and the stellar mass for both samples for a better comparison. The NBCS follows the same distribution as the DPS and contains 5 128 galaxies.

a combination of a SF and a AGN nucleus or a SF and LINER emission. Counting all galaxies which have at least one emission line component classified as COMP, we find 45%. This is an excess of about a factor 2 in the DPS in comparison with the NBCS (24%). Counting only all galaxies classified as 'double SF' or 'SF and uncertain' in the second peak, we find 39% of the DPS, which is significant less in comparison with the NBCS (55%).

Many works published in the recent years were focused on double-peak emission line AGNs with the motivation to find dual AGNs (see Sect. 1). Here, we do not observe the DPS to be dominated by this type of galaxies. We observe about 7% double AGN or LINER classification and 3% with one AGN or LINER and one uncertain. We furthermore find 6% to show a mixed classification with one AGN or LINER component. In comparison with the NBCS, which comprises about 19% to be classified as AGN or LINER, we find less AGN and LINER in the DPS. We recall that QSO and Seyfert1 galaxies have been excluded from the RCSED (Schneider et al. 2010; Chilingarian et al. 2017), which can explain the lack of galaxies classified as AGN in this catalogue (see also Sect. 2.4). Smith et al. (2010) concentrated on DP QSO and find 148 DP galaxies, which are not treated in this work (see Sect. 2.4).

3.2. Morphological classification

We identified the morphological types of our galaxy samples using Domínguez Sánchez et al. (2018), which is a machine-learning-based algorithm to identify different types of galaxy morphologies. Different neuronal networks have been trained with SDSS *gri* colour composite images on various criteria to determine their morphology. To classify our samples, we used the following variables to define the probability of an observed feature: P_{disc} for disc features, P_{S0} for S0 galaxies, $P_{edge-on}$ for edge-on orientation, P_{merger} for visual merger and P_{bar} for a bar structure. The T-type relates each galaxy to a type classification on the Hubble sequence. To classify spiral galaxies according to their inclination, we calculated the inclination angle i as:

$$\cos i = \sqrt{\frac{(b/a)^2 - q_0^2}{1 - q_0^2}} \quad (5)$$

where b/a is the r-band minor-to-major axial ratio estimated by Meert et al. (2015), while q_0 is the intrinsic axial ratio of galaxies observed edge-on and is set to $q_0 = 0.2$. The inclination for galaxies with $b/a < 0.2$ is set to 90° (Catinella et al. 2012; Aquino-Ortíz et al. 2018). Relying on Domínguez Sánchez et al. (2018) and through inspection of the selected SDSS images, we find the following arguments:

– **Late-type galaxies (LTG)**, which are disc dominated[2], are selected by T-type > 0 and $P_{disc} > 0.5$.

Table 4. Classification based on BPT diagrams (see Fig. 7)

Criteria	Counts	fraction
DPS		
double SF	1617	(28.6 %)
double COMP	939	(16.6 %)
double AGN	385	(6.8 %)
double LINER	29	(0.5 %)
SF + COMP	784	(13.8 %)
SF + AGN	17	(0.3 %)
SF + LINER	9	(0.2 %)
COMP + AGN	167	(2.9 %)
COMP + LINER	64	(1.1 %)
AGN + LINER	59	(1.0 %)
SF + uncertain	570	(10.1 %)
COMP + uncertain	592	(10.5 %)
AGN + uncertain	110	(1.9 %)
LINER + uncertain	63	(1.1 %)
Not classifiable	258	(4.6 %)
DPS with non-parametric fit		
SF	2534	(44.7 %)
COMP	2153	(38.0 %)
AGN	630	(11.1 %)
LINER	174	(3.1 %)
Not classifiable	172	(3.0 %)
No-Bias Control sample		
SF	2811	(54.8 %)
COMP	1226	(23.9 %)
AGN	687	(13.4 %)
LINER	308	(6.0 %)
Not classifiable	96	(1.9 %)
Control sample		
SF	82065	(91.8 %)
COMP	4721	(5.3 %)
AGN	1623	(1.8 %)
LINER	536	(0.6 %)
Not classifiable	467	(0.5 %)

Notes: Following Kewley et al. (2006b) and Schawinski et al. (2007), we classify each two emission line component of the DPS individually, as explained in Sect. 3.1. We show all combinations of classification such as double (e.g. SF + SF) and mixed (e.g. SF + COMP) classifications. We also display those galaxies which are not classifiable in only one component (e.g. SF + uncertain) or in both. The classifications for the CS and the NBCS are also displayed for comparison.

[2] We refer throughout this article to LTG for all disc galaxies from Sa to Sd.

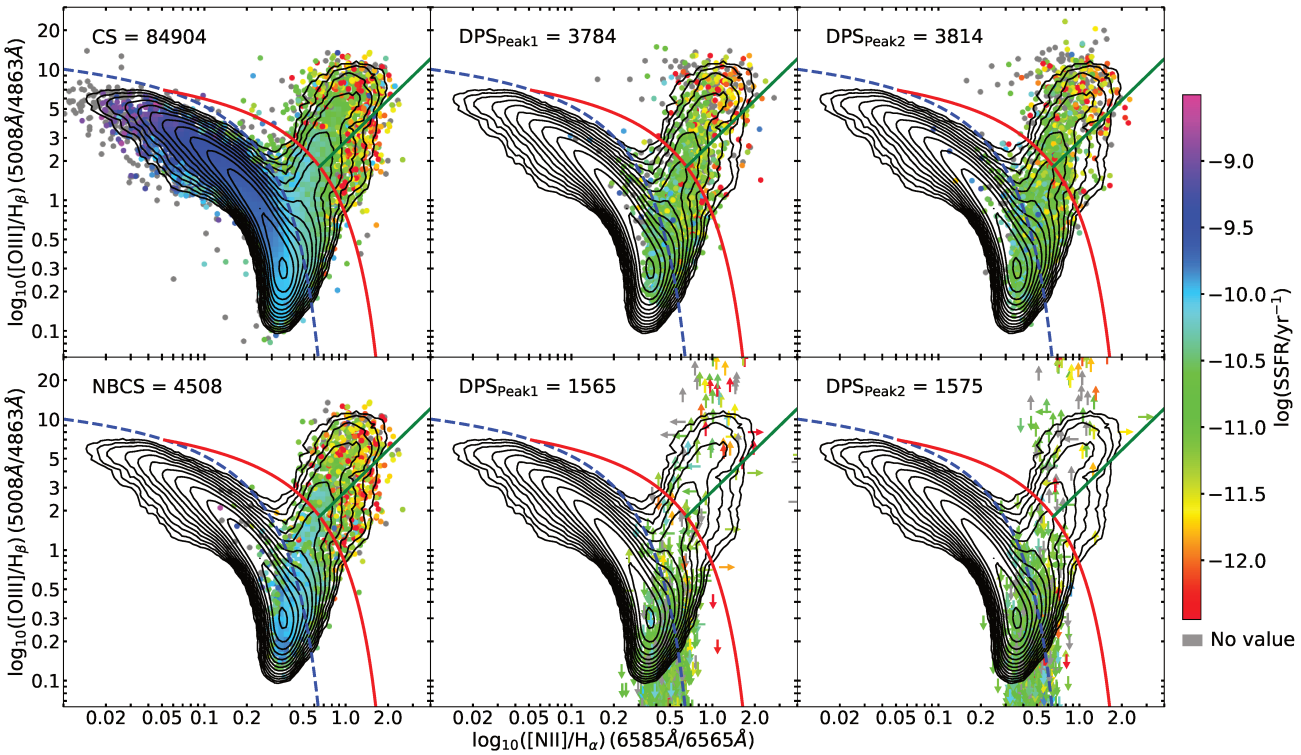

Fig. 7. BPT diagrams used to classify our samples into different galaxy types (Kewley et al. 2006b). The red line separates active galactic nuclei (AGN) and composite galaxies (COMP) (Kewley et al. 2001). AGNs and low ionisation narrow emission line regions (LINER) are separated by the green line (Schawinski et al. 2007) and the blue dashed lines separate star forming (SF) and COMP (Kewley et al. 2006b). We present the CS in the upper left panel and the NBCS in the lower left panel. In the upper middle (resp. right) panel, we show the blueshifted (resp. redshifted) peaks of DP galaxies with a S/N> 3 in the four emission line fluxes needed for the BPT diagram. In the lower middle and right panels, we display those emission line components of the DPS with three of the requested emission lines with S/N> 3 and the fourth S/N< 3. To classify them, we display arrows to indicate the limits derived by the uncertainties of weak emission lines. In all six panels, we apply the same colour-coding indicating the specific star formation rate (SSFR) computed by Salim et al. (2016). We display in all panels the same contour lines corresponding to the density of the CS. The corresponding classifications are presented in Table 4.

  - **Face-on** are identified as LTG with an inclination angle smaller than 30°. To further decrease the false-positive detection rate, we demand $P_{edge-on} < 0.1$.
  - **Edge-on** and strongly inclined galaxies are selected as LTGs with an inclination angle larger than 70° and $P_{edge-on} > 0.4$.
  - **Barred** galaxies are LTGs with $P_{bar} > 0.9$ and $P_{edge-on} < 0.5$
- **S0** galaxies are selected by a T-type ≤ 0, $P_{S0} > 0.6$, $P_{disc} < 0.3$ and $P_{edge-on} < 0.4$
- **Elliptical** are characterised by a T-type ≤ 0 and $P_{S0} < 0.3$
- **Merger** galaxies are selected by using $P_{merger} > 0.9$. This high threshold provides a sub-sample of merger with high purity enabling to test if visible merging processes are at the origin of DP galaxies.

To compare our galaxy samples with respect to their morphological classification, we did not apply any subjective correction to the selection. We computed the fraction of all classified types for the DPS, the CS and the NBCS in Table 5. Fig. 8 displays the redshift distribution for the different morphological types of the DPS and the NBCS. We observe merger and S0 galaxies to be more distant in comparison to LTG and elliptical galaxies. This can be the result of a classification bias as discussed in the training sample (Willett et al. 2013) used for the classification in Domínguez Sánchez et al. (2018). We thus might misclassified LTG as S0 galaxies because of their distance. In Fig. D.2,

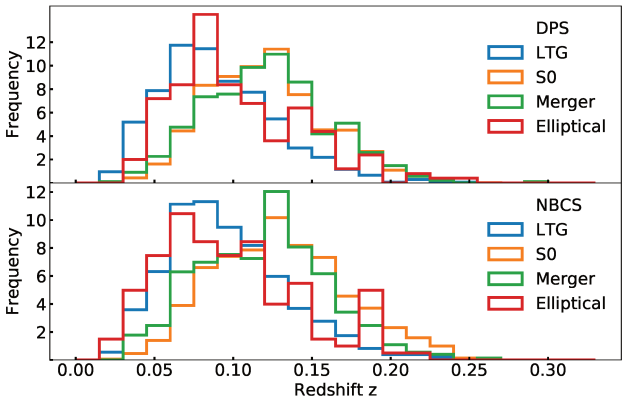

Fig. 8. Redshift distribution of the DPS for LTG, S0, merger, and elliptical galaxies. We unified the histogram surface of all four samples to 1.

we illustrate the morphological types, by showing 20 randomly selected galaxies for each type (except for the face-on LTGs, for which we show all ten cases).

In Table 5, we find that the majority of the CS galaxies are not classified (62%). This is due to a classification bias against small and weak galaxies (Domínguez Sánchez et al. 2018). The

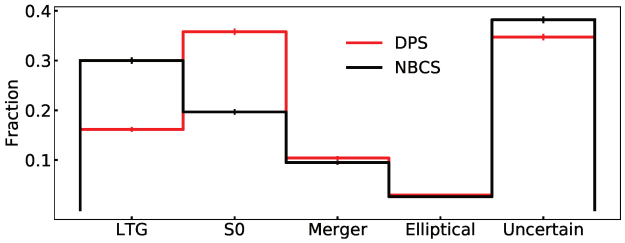

Fig. 9. Fraction of different morphological types for the DPs and the NBCS. The error-bars represent the binomial errors.

Table 5. The morphological classification of the DPS, the CS and the NBCS.

Type	DPS	NBCS	CS
LTG	914(16.1%)	1539(30.0%)	20157(22.5%)
Face-on	10(0.2%)	149(2.9%)	1609(1.8%)
Edge-on	54(1.0%)	114(2.2%)	3844(4.3%)
Bar	105(1.9%)	147(2.9%)	956(1.1%)
Elliptical	167(2.9%)	134(2.6%)	302(0.3%)
S0	2027(35.8%)	1009(19.7%)	7145(8.0%)
Merger	589(10.4%)	487(9.5%)	6524(7.3%)
Uncertain	1966(34.7%)	1959(38.2%)	55284(61.8%)

Notes: We used parameters provided by Domínguez Sánchez et al. (2018) and Meert et al. (2015), described in detail in sec. 3.2. The first column names the morphological type. The second (resp. third and fourth) column provides the number of galaxies and the percentage in parenthesis for the DPS (resp. CS and NBCS)

numbers of not classified galaxies in the DPS and the NBCS are comparable (35% and 38%). By comparing the morphological classification of the DPS and the NBCS, we find two noticeable effects. On the one hand, LTG are less numerous in the DPS (16%) than in the NBCS (30%). On the other hand, more S0 galaxies are present in the DP (36%) than in the NBCS (20%). These results are visualised in Fig. 9.

We find in both samples a similar merger rate of $\sim 10\%$. This observation is *a priori* contradictory to the idea of a DP structure due to a major galaxy merger but does not exclude the possibility that DP galaxies might be minor mergers, post-mergers or hidden merger. Furthermore, the same merger rate (10%) was found in a recent double-peak sample in the Large Sky Area Multi-object fibre Spectroscopic Telescope survey (Wang et al. 2019b). As a cross-check, we performed a visual inspection of the first 1000 galaxies in the DPS and the NBCS. We find a merger rate of 11.4 % (resp. 11.7 %) for the DPS (resp. NBCS), which is close to the merger rate we extracted from Domínguez Sánchez et al. (2018). By lowering the selection threshold for mergers (e.g. $P_{merger} > 0.8$ or $P_{merger} > 0.7$), we do not detect different merger rates in the DPS and the NBCS, but higher rates of misclassification.

We also classified LTGs in face-on (0.2%), edge-on (1.0%), and bar (1.9%) galaxies. We chose strict selection criteria to avoid false-positive classification for face-on and edge-on galaxies. These galaxy types are interesting since edge-on galaxies may exhibit a double horn due to a rotating disc, while face-on galaxies should not exhibit rotation in form of a DP. We do not observe any excess of edge-on galaxies in comparison to the NBCS (2.2%). In Sect. 4.3.3 and 4.3.4, we discuss arguments using the inclination.

We also provide cross-matches between the morphological types and the BPT classifications in Table D.1 and D.2 and provide a statistical significance test in A.

4. Analysis

4.1. General characteristics

To describe the characteristics of the DPS and compare them with the NBCS and the CS, we show in Fig. 10 the distribution of six parameters: the Galactic extinction and k-corrected absolute magnitude of the r-band M_r, SSFR = SFR/$M_\odot$, the luminosities of the [OIII]λ5008 and H$\alpha\lambda$6565 emission lines, stellar population ages, and stellar metallicities.

In every distribution, the CS differs from the DPS whereas the NBCS shows good agreement with the DPS, except for the H$\alpha\lambda$6565 luminosity. We discuss in Sect. 4.2 that this is related to a significant difference in the star formation activity. As discussed in Sect. 2.2.3 and 2.3, the CS follows a different stellar mass-redshift distribution in comparison to the DPS and the NBCS. On average, the CS shows smaller M_r, higher SSFR and smaller absolute luminosities in the [OIII]λ5008 and H$\alpha\lambda$6565 line than the DPS and the NBCS. This different behaviour observed for galaxies of the CS is mainly due to a sensitivity bias: low-mass galaxies pass the signal-to-noise ratio cut on the emission lines while the DPS and NBCS are large-mass galaxies (see Sect. 2.3).

The differences in the DPS and NBCS H$\alpha\lambda$6565 luminosities are small: $L_{H\alpha}$(DPS) = 41.16 ± 0.36 and $L_{H\alpha}$(NBCS) = 40.96 ± 0.42 (mean and standard deviation). However, using a the non-parametric Kolmogorov–Smirnov test to distinguish weather the two distributions are the same or not, we find a k-statistic of 0.235 marking the maximal distance of the cumulative distribution function and a p-value of 5×10^{-130}, strongly indicating that these two distributions are different.

We checked the extinction based on the Balmer decrement and found that DPS galaxies have slightly more extinction (0.25 mag higher in V) than the NBCS galaxies, while this effect is stronger for LTG and S0 galaxies (see Fig. C.1).

To approximate stellar ages, we used the spectral continuum fit performed with a SSP (Chilingarian et al. 2017). Due to the cut on the stellar masses (see Fig. 5 and 6), the CS is dominated by young stellar populations with an SSP-based age between 1 and 2 Gyr in 52% of the galaxies. Nearly all (97%) of these young galaxies are classified as SF (see Sect. 3.1). The NBCS and DPS show comparable distributions but with on average an older stellar population than for the CS. The majority (74% and 71% respectively) of the two samples is younger than 5 Gyr, while 47% (DPS) and 66% (NBCS) of these young galaxies are SF galaxies. We also find that 29% (resp. 23%) of the young DP galaxies (resp. NBCS) are classified as COMP. Last, we find 15% of the DPS to be classified with one peak as COMP and the second one as SF. As discussed in Sect. 3.1, we find an excess of the percentage of SF galaxies in the NBCS and CS whereas we do not find such a high excess in the DPS. We also show the stellar metallicity, computed by Chilingarian et al. (2017), and find that the DPS and the NBCS follow the same distribution, whereas the CS shows a different distribution with lower metallicity values. This is expected due to the difference in stellar mass of the different samples (Tremonti et al. 2004).

While we find many differences between the DPS and the CS, the NBCS and DPS distributions are similar. The NBCS is therefore well suited to identify the peculiarities of the DPS.

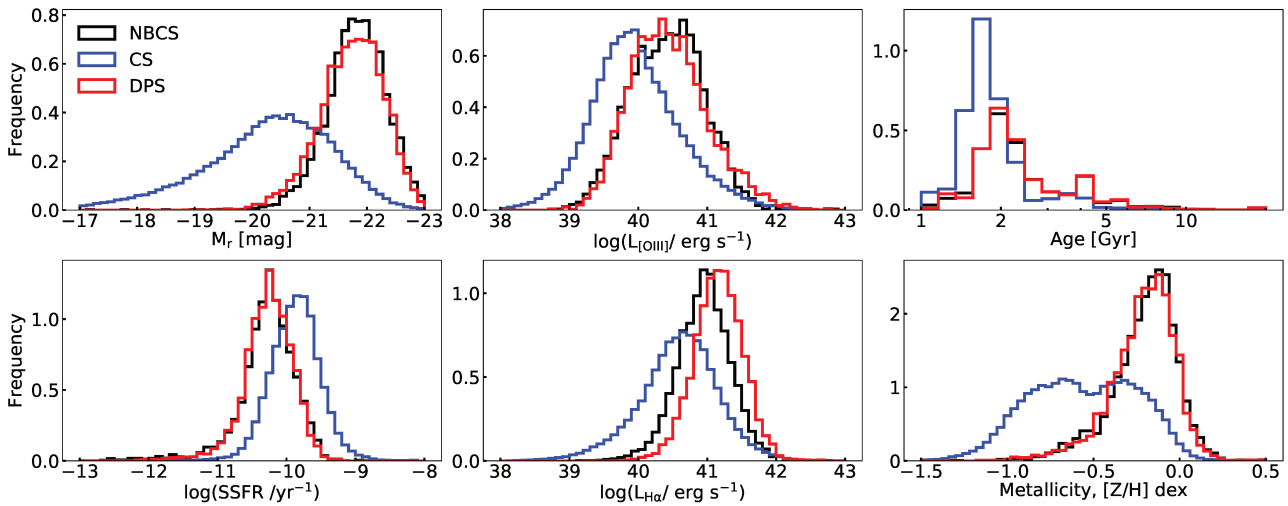

Fig. 10. Different parameters distributions of the DPS (red), the CS (blue) and the NBCS (black). The surfaces of all histograms are normalised to unity. In the upper left panel, we compute the absolute AB magnitude in the r-band with Galactic dust and K-corrections estimated by Chilingarian et al. (2017). The lower left panel shows the specific star formation ratio (SSFR) computed by Brinchmann et al. (2004). The middle upper (resp. lower) panel presents the absolute luminosity of the [OIII]λ5008 (resp. H$\alpha\lambda$6565) emission line. The absolute luminosity is calculated using the flux of the non-parametric emission line fit provided by Chilingarian et al. (2017). The right upper panel computes the age assumed by a single stellar population fit by Chilingarian et al. (2017). The right lower panel shows the stellar metallicity computed by Chilingarian et al. (2017).

4.2. Star formation vs. AGN excitation

SF is important to characterise the state of evolution of a galaxy and to estimate its growth rate. In Sect. 3.1 and 4.1, we find that the majority of the DPS, CS and NBCS show SF activity. At the same time, we find AGN activities (or galaxies classified as COMP) in the NBCS and the DPS. To further analyse and compare our samples, we used diagnostic colour-colour diagrams, specific star formation rate (SSFR) and stellar mass diagrams and compare the SFR of the 3″ SDSS fibre and of the total galaxy. According to Salim et al. (2007), the SFR of AGN computed by Brinchmann et al. (2004) can be overestimated. We therefore used the NUV-band to compute the SFR and found a good agreement to the SFR measured by Brinchmann et al. (2004) for our galaxies classified as AGN. We discuss AGN excitation of galaxies classified as composite galaxies and cross-match our catalogues with radio observations.

In Fig. 11, the $g - r$ vs. NUV $- r$ colour–colour diagram shows a single sequence with the star-forming blue cloud and the red sequence, characterised by quenched star formation (Strateva et al. 2001; Hogg et al. 2002; Ellis et al. 2005), separated by a critical value of NUV $- r = 4.75$. The blue cloud (resp. red sequence) is approximately represented by blue (resp. red) contours for LTGs (resp. elliptical galaxies) from the RCSED (compare with Chilingarian & Zolotukhin 2012). We find the DPS to be situated in the upper region of the blue cloud and only some outliers in the red sequence. We do not find significant effects for the different subsets classified in Sect. 3. We can thus conclude that the DPS and the NBCS are not quenched and are mainly associated with the main star forming sequence. The distribution of the DPS is more concentrated in the range centred at NUV $- r \sim 3.5$ than the NBCS (NUV $- r \sim 3.0$), which is centred in the blue cloud. This shift towards redder colours can be explained by considering shorter time scales τ of an exponential declining star formation history, as shown in Chilingarian & Zolotukhin (2012).

However, this is not the case for the DPS as their mean τ is slightly larger than for the NBCS. We argue that these redder

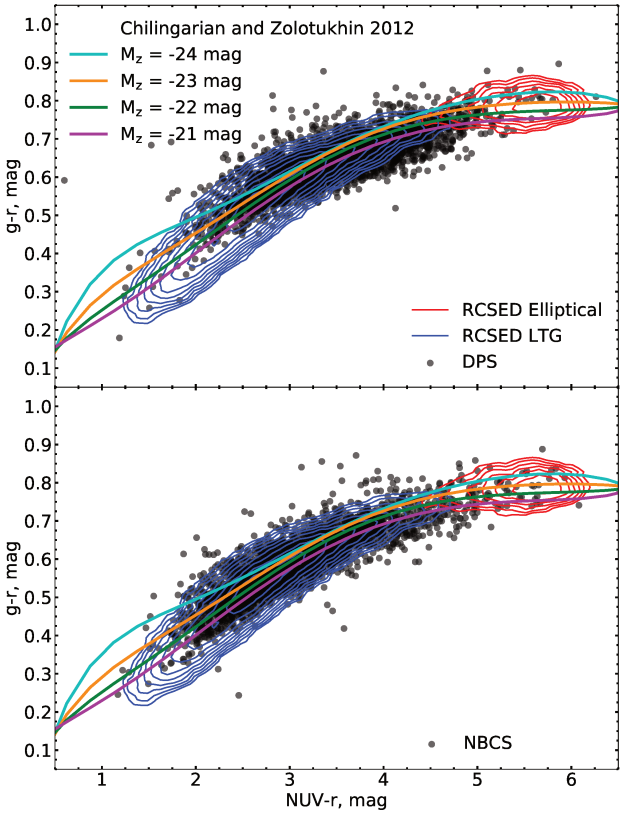

Fig. 11. Colour–colour relation between $g - r$ and NUV $- r$. We present LTG and elliptical galaxies selected from the RCSED catalogue using Domínguez Sánchez et al. (2018) as blue and red contours and show the DPS (resp. NBCS) as black dots in the top panel (resp. lower panel). We display the best-fitting polynomial surface equation of constant absolute z-band magnitudes with coloured lines (Chilingarian & Zolotukhin 2012).

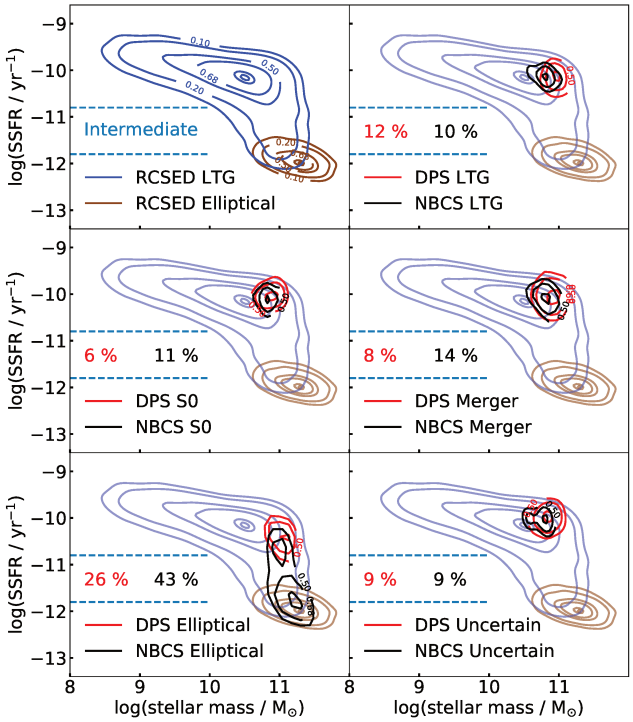

Fig. 12. SSFR as a function of stellar mass. The top left panel presents LTG and elliptical galaxies selected from the RCSED catalogue using Domínguez Sánchez et al. (2018) as blue and brown contours. These contours are also shown as a reminder in the other panels. We show contour lines indicating the 50%, 68% and 95% level for different morphological subsamples of the DPS (red) and the NBCS (black). We indicate with blue dashed lines the region of intermediate star formation ($-11.8 < \log(\mathrm{SSFR}/\mathrm{M}_\odot) < -10.8$) (Salim 2014) and display the percentage of the morphological types situated in this zone.

colours are most probably to the mean extinction estimated to $A_V = 0.25$, as displayed in the last column of Figure C.1.

We can notice some galaxies in the DPS situated below the two sequences in Fig. 11. This area is associated with post starburst galaxies which underwent a recent massive starburst that is now quenched (Chilingarian & Zolotukhin 2012). Such galaxies can be also situated in the surface, as they can be biased when a strong H$\alpha\lambda$6565 line contributes to the r-band magnitude, shifting the position of the galaxies into the plane. We find that this is not the case for DP galaxies, nor the NBCS. To confirm this, we studied the colour-colour diagram with colours $g-z$ and NUV$-z$, where this off-plane shift disappears.

In Fig. 12, we show the SSFR, taken from Brinchmann et al. (2004), as a function of the stellar mass, computed by Kauffmann et al. (2003). With this diagnostic diagram, Schiminovich et al. (2007) distinguished between the blue and the red sequence in terms of SSFR and stellar mass. Salim (2014) associated intermediate NUV$-r$ colours known as the 'green valley' with intermediate star formation of $-11.8 < \log(\mathrm{SSFR}/\mathrm{M}_\odot) < -10.8$ suggesting that these galaxies might be in transition. In Fig. 12, we show the distribution of LTGs and elliptical galaxies selected from the RCSED as reference. We display the 50%, 68% and 95% contour levels of different morphological types of the DPS and the NBCS. We find, depending on the morphological type, between 6% and 26% (resp. 8% and 43%) of the DPS (resp. NBCS) showing intermediate star formation. We only find a significant difference between the DPS and the NBCS for elliptical galaxies: only 26% of the elliptical DP galaxies show intermediate star formation whereas 43% of the elliptical galaxies of the NBCS are situated in this region. We find indeed very similar distributions for all different morphological types of the DPS and thus conclude that SF and the stellar mass are not depending on the morphological type.

Table 6. Median ratios of fibre and total SFR

	$\mathcal{R}$		
Type	z < 0.075	0.075 < z < 0.125	z > 0.125
	DPS		
double SF	$0.73^{+0.22}_{-0.25}$	$0.76^{+0.20}_{-0.20}$	$0.73^{+0.18}_{-0.21}$
double COMP	$0.56^{+0.35}_{-0.26}$	$0.67^{+0.24}_{-0.28}$	$0.64^{+0.25}_{-0.22}$
double AGN	$0.24^{+0.23}_{-0.11}$	$0.31^{+0.36}_{-0.17}$	$0.38^{+0.38}_{-0.20}$
LTG	$0.56^{+0.32}_{-0.30}$	$0.58^{+0.26}_{-0.29}$	$0.54^{+0.25}_{-0.24}$
S0	$0.62^{+0.31}_{-0.30}$	$0.73^{+0.21}_{-0.25}$	$0.74^{+0.19}_{-0.24}$
Elliptical	$0.40^{+0.39}_{-0.24}$	$0.49^{+0.33}_{-0.29}$	$0.61^{+0.20}_{-0.33}$
Merger	$0.56^{+0.33}_{-0.31}$	$0.70^{+0.28}_{-0.28}$	$0.71^{+0.26}_{-0.29}$
Uncertain	$0.60^{+0.34}_{-0.34}$	$0.73^{+0.22}_{-0.27}$	$0.67^{+0.20}_{-0.24}$
	NBCS		
SF	$0.36^{+0.24}_{-0.16}$	$0.43^{+0.23}_{-0.16}$	$0.53^{+0.19}_{-0.18}$
COMP	$0.29^{+0.34}_{-0.17}$	$0.42^{+0.34}_{-0.21}$	$0.48^{+0.26}_{-0.22}$
AGN	$0.14^{+0.16}_{-0.09}$	$0.28^{+0.27}_{-0.16}$	$0.28^{+0.30}_{-0.16}$
LTG	$0.28^{+0.25}_{-0.16}$	$0.34^{+0.21}_{-0.17}$	$0.38^{+0.21}_{-0.21}$
S0	$0.42^{+0.24}_{-0.25}$	$0.50^{+0.25}_{-0.24}$	$0.56^{+0.22}_{-0.25}$
Elliptical	$0.18^{+0.14}_{-0.09}$	$0.26^{+0.20}_{-0.10}$	$0.21^{+0.27}_{-0.10}$
Merger	$0.31^{+0.26}_{-0.15}$	$0.45^{+0.32}_{-0.25}$	$0.49^{+0.22}_{-0.24}$
Uncertain	$0.30^{+0.34}_{-0.16}$	$0.45^{+0.26}_{-0.18}$	$0.48^{+0.23}_{-0.19}$

Notes: We show the median and the 68 percentile of $\mathcal{R} = \mathrm{SFR}_{\mathrm{fibre}}/\mathrm{SFR}_{\mathrm{total}}$ for different ranges of redshift and galaxy types for the DPS and NBCS.

To discuss the SF in a quantitative way, we used SFRs estimated by Brinchmann et al. (2004) for the entire galaxies ($\mathrm{SFR}_{\mathrm{total}}$) and for the 3″ SDSS fibre ($\mathrm{SFR}_{\mathrm{fibre}}$). Since the proportion of a galaxy covered by the 3″ fibre depends on its redshift, we divided the DPS and the NBCS into three groups of redshift ranges: z < 0.075, 0.075 < z < 0.125, and 0.125 < z. In order to discuss the SF activities in detail, we especially examined the sub-samples classified as double SF and AGN, using the BPT classification performed in Sect. 3.1.

Hence, we present the comparison between the DPS and the NBCS with the difference between total and 3″ absolute r-band magnitude, the ratio of the Petrosian radii of 90% and 50%, the $\mathrm{SFR}_{\mathrm{fibre}}$ and the ratio $\mathcal{R} = \mathrm{SFR}_{\mathrm{fibre}}/\mathrm{SFR}_{\mathrm{total}}$. We show these observables for the three redshift groups for galaxies of the DPS classified as double-SF (resp. double-AGN) and SF (resp. AGN) galaxies of the NBCS in Fig. 13 (resp. Fig, 14). For double-SF galaxies of the DPS, we find an excess of luminosity in the centre and a higher $\mathrm{SFR}_{\mathrm{fibre}}$ in comparison to SF galaxies **of** the NBCS. This excess is most prominent for galaxies with a redshift z < 0.125, corresponding to maximal fibre diameter of 7.6 kpc. With respect to $\mathrm{SFR}_{\mathrm{total}}$, we find a clear enhanced-central-SF activity for double-SF galaxies of the DPS in comparison to SF galaxies of the NBCS. We find a median SFR ratio for double-SF galaxies of the DPS with a redshift z < 0.075 of $\overline{\mathcal{R}}_{\mathrm{DPS}} = 0.73^{+0.22}_{-0.25}$. For SF galaxies of the NBCS in the same redshift range we find $\overline{\mathcal{R}}_{\mathrm{NBCS}} = 0.36^{+0.24}_{-0.16}$. We find similar values for galaxies with a redshift 0.075 < z < 0.125, whereas this effect is **s**lightly weaker for galaxies with z > 0.125. This is due

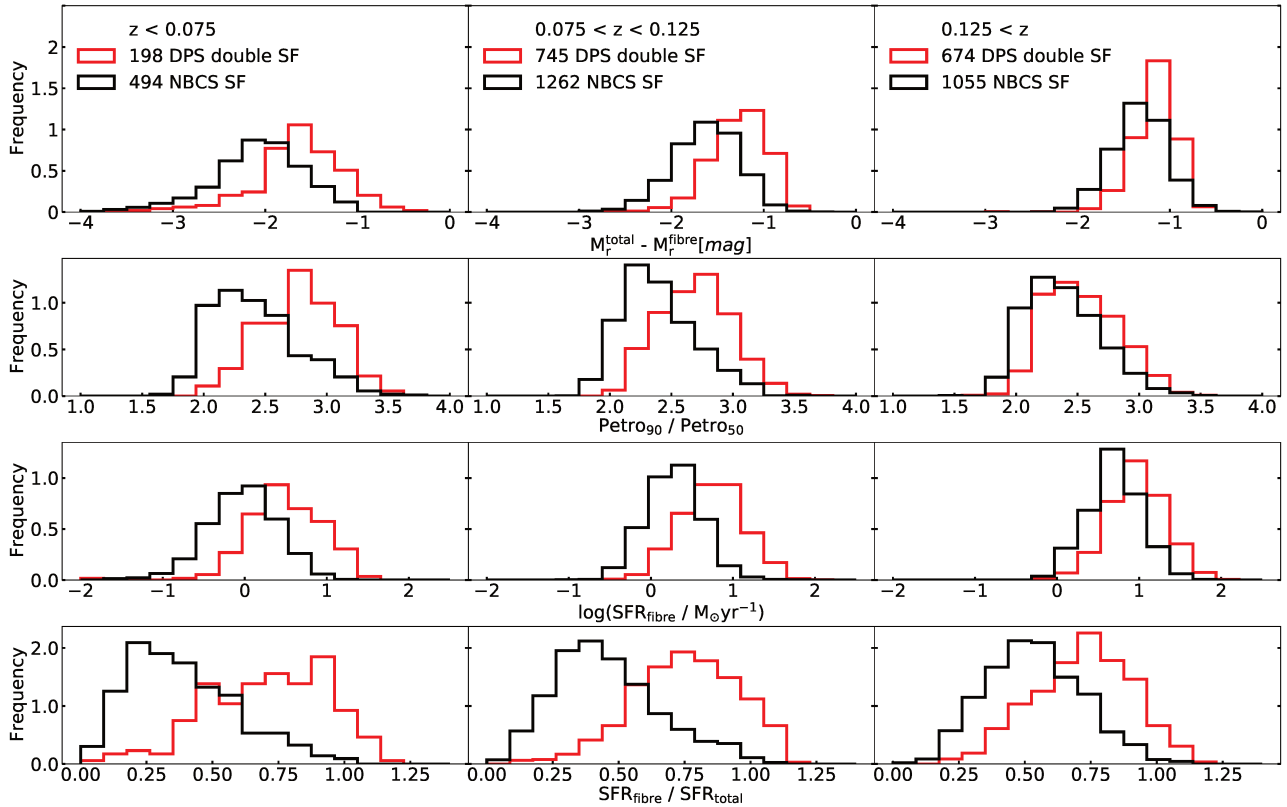

Fig. 13. Distribution of different observables within the 3″ SDSS fibre. We show in three columns three different ranges of redshift. We present galaxies of the DPS which are classified as double SF in red and galaxies classified as SF of the NBCS in black (see Sect. 3.1) In the top row we show the difference in absolute *r*-band magnitude of the total galaxy and the 3″ SDSS fibre. The colours are Galactic dust- and k-corrected (Chilingarian et al. 2017). In the second row we present the ratio of the radii comprising 90% and 50% of the Petrosian luminosity (Petrosian 1976) approximating the central brightness in comparison to the total galaxy. We show the star formation ratio of the 3″ SDSS fibre SFR_{fibre} in the third row and the ratio between fibre and total star formation (SFR_{fibre}/SFR_{total}) in the bottom row (Brinchmann et al. 2004).

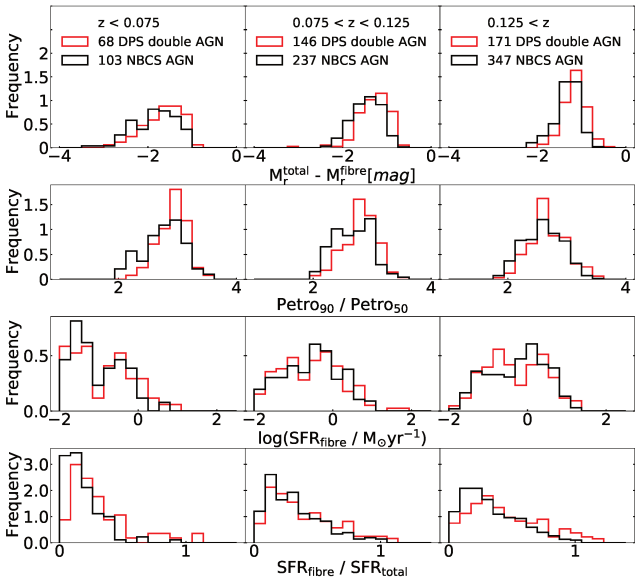

Fig. 14. Comparison of absolute *r*-band magnitude, Petrosian radii and SFR_{fibre} and SFR_{total} as in Fig. 13 but with DP galaxies classified as AGN in both peak components (red) and galaxies of the NBCS classified as AGN (black).

to the fact that for more distant galaxies the 3″fibre covers the majority of the surface of the galaxies, therefore SFR_{fibre} tends to SFR_{total}. We summarise the median SFR ratios and the 68-percentile for different galaxy types in Table 6. We also find an enhanced-central-SF for LTGs, S0 galaxies and galaxies classified as double COMP at lower redshift.

Double-AGN of the DPS follow the same SFR_{fibre} and SFR_{total} distributions as the AGNs of the NBCS and no enhancement of central SF activity or central luminosity is observed as shown in Fig. 14.

With the BPT classification in Sect. 3.1, we find less SF but more COMP galaxies in the DPS in comparison to the NBCS. Since COMP galaxies are understood to be a mixture of SF and AGN (Kewley et al. 2006b), we quantified the AGN excitation using the [OII]λ3728 and the [NeV]λ3426 emission lines.

(1) The ratio [OII]λ3728/[OIII]λ5008 can be used to distinguish between a pure AGN and SF. From photo-ionisation models, a value between 0.1 and 0.3 is used for a pure AGN (Tammour et al. 2015), while above a value of 0.3, the [OII]λ3728 flux is thought to be produced in SF sites (Osterbrock & Ferland 2006). Using the non-parametric emission line fit from Chilingarian et al. (2017), we find a mean ratio of [OII]/[OIII] = 0.23 ± 0.14 for galaxies classified as double AGN. For double SF (resp. COMP) galaxies, we find [OII]/[OIII] = 1.57 ± 0.56 (resp. 1.14 ± 0.54). This indicates that galaxies which are classified as COMP are dominated by SF. This effect can also be

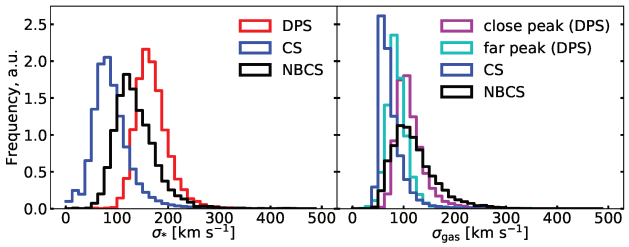

Fig. 15. Velocity dispersion distributions for the CS (blue), the NBCS (black) and the DPS (red, purple and orange). The left panel displays the stellar velocity dispersion σ_* computed from Chilingarian et al. (2017). The second panel shows the gas velocity dispersion $\sigma_{\rm gas}$. We compute the Gaussian emission line dispersion for the CS and the NBCS from (Chilingarian et al. 2017). For the DPS, we display the $\sigma_{1,2}$ of the emission line components, which is closer to the galaxy stellar velocity in units of $\sigma_{1,2}$ in magenta and the component which is more offset in cyan. For better comparisons, we unify the surface of the histograms of the left (resp. right) panel to 150 (resp. 100).

biased by extinction in dusty galaxy centres and must therefore be considered with caution.

(2) We then discuss galaxies with AGN activity based on the detection of the high-ionisation [NeV]λ3426 emission line (Gilli et al. 2010; Vergani et al. 2018). Due to redshift, the [NeV]λ3426 line is only detected in SDSS spectra from z > 0.2. We inspected spectra of the DPS galaxies classified as double-SF, -COMP and -AGN for [NeV]λ3426 detection. We find no galaxies classified as double-SF contrary to 62% of the galaxies classified as double-AGN having a detectable [NeV]λ3426 line. Only 4% of the $z > 0.2$ galaxies classified as double COMP show this line which supports the evidence that these are SF galaxies.

To discuss further aspects on the connection between AGN excitation and SF in our galaxy samples, we cross-matched the DPS and the NBCS with surveys of radio observations. It has been known for a long time that non-thermal radio emission is linearly correlated to the far-infrared flux (Helou et al. 1985; Condon 1992; Sanders & Mirabel 1996), while IR luminosity is a good SF tracer (e.g. Kewley et al. 2002). More recently, the radio luminosity at 150 MHz has been considered as a potential tracer of SF (Calistro Rivera et al. 2017; Wang et al. 2019a). We useed FIRST at 1.4 GHz (White et al. 1997) and the first data release of the LOFAR Two-metre Sky Survey (LoTSS) (Shimwell et al. 2019) at about 150 MHz. Roughly 20% (1154) of the DPS are detected with FIRST, but only 8% (395) of the NBCS. In the observed field of the LoTSS DR1 we find a detection rate of 73% (237) for the DPS and 56% (191) for the NBCS. We find a significant excess of radio sources at 1.4 GHz and a higher detection rate at 150 MHz for the DPS in comparison to the NBCS. We will further explore the radio properties of these galaxies in Maschmann et al. (in prep.).

4.3. Kinematic properties of the double-peak galaxies

4.3.1. Velocity distributions

To explore the gas and star kinematic properties of our samples, we present basic velocity estimates to assess possible differences between the DPS, the CS and the NBCS. In Fig. 15, we show the stellar velocity dispersion σ_* and the gas velocity dispersion $\sigma_{\rm gas}$.

The stellar velocity dispersion was computed in Chilingarian et al. (2017), fitted with a SSP and an EXP-SFH (see Sect. 2). We computed the χ^2_ν for both fit functions and selected the resulting stellar velocity dispersion from the best fitting function.

To compute the gas velocity dispersion for the CS and the NBCS, we used the velocity dispersion measured for all Balmer and forbidden lines in Chilingarian et al. (2017) and show the one of the strongest line. For double-peak emission lines, we used the stacked emission line spectra (see Sect. 2.2.2) and compute the $\sigma_{\rm close}$ which corresponds to the DP component closer to the galaxy velocity in units of σ and $\sigma_{\rm far}$ to the component which is more offset.

As shown in Fig. 15, we observe a higher σ_* for the DPS in comparison with the CS and the NBCS. The gas velocity dispersion $\sigma_{\rm gas}$ indicates higher velocities for the NBCS and the DPS in comparison to the CS. This is expected from the Tully-Fisher relation, since these two samples comprise more massive galaxies (Tully & Fisher 1977). For the DPS, we find the velocity dispersions, measured for the close peak, to be compatible with the gas velocity dispersions of the NBCS. For the far peak of the DPS, the velocity dispersions are systematically smaller.

4.3.2. Single Gaussian approximation for DP

To discuss possible mechanisms behind double-peak emission lines, we need to compare the gas kinematics of the DPS and the NBCS. In order to do so we used the single Gaussian approximation of the double-peak emission lines, as computed in Sect. 2.2.2.

A single Gaussian fit to the complex line shape of DP galaxies provides a measure of the velocity dispersion assuming the DP originates from one system. In Fig. 16 we show one stacked emission line, the double Gaussian fit and the single Gaussian fit performed in Sect. 2.2.2.

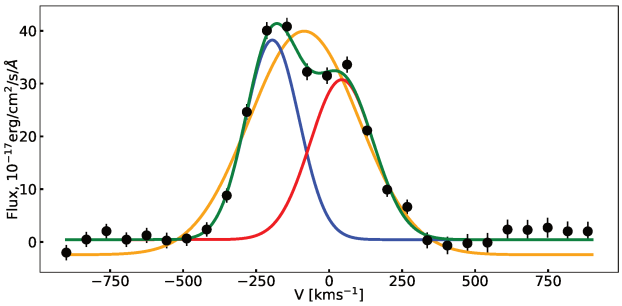

Fig. 16. Single Gaussian approximation. We compute the two Gaussian functions resulting from the double Gaussian fit procedure to the stacked emission line in 2.2. The blueshifted component is represented by a blue and the redshifted by a red line. In orange, we show the best fit of a single Gaussian function.

In Fig. 17, we show σ_* on the x-axis and on the y-axis $\sigma_{\rm gas}$ for the NBCS and $\sigma_{\rm single}$ for the DPS. We display the median and the 68% percentile of $\sigma_{\rm gas}$ and $\sigma_{\rm single}$ with a binning according to σ_*. The emission line parameters $\sigma_{1,2}$ and $\Delta v_{\rm DP}$ of the DPS are restricted by a lower limit, defined with the spectral resolution (see Sect. 2.2.2). We thus find a lower threshold of 114 km s^{-1}. Similarly, for the NBCS, we find a minimal $\sigma_{\rm gas}$ of 43 km s^{-1}.

By comparing $\sigma_{\rm gas}$ with σ_* of the NBCS, we find a linear relation described by $\sigma_{\rm gas} = 0.71\,\sigma_* + 23.8$ km s^{-1} (black dashed line in Fig. 17). This relation might be valid for $\sigma_{\rm single}$ and σ_* of the DPS for higher velocities ($\sigma_* > 150$ km s^{-1}). In this regime, we can assume a linear relation for the DPS but we still find a shift towards higher velocities in comparison to $\sigma_{\rm gas}$ of the

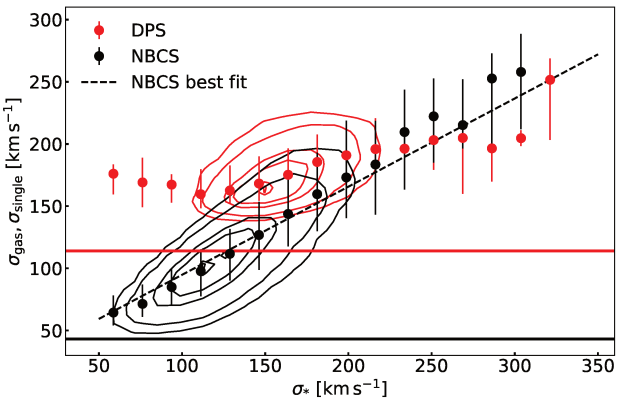

Fig. 17. Comparison of the stellar velocity distribution σ_* computed by Chilingarian et al. (2017) with the gas velocity distribution σ_{gas} for the NBCS and the velocity distribution of the single Gaussian approximation σ_{single} for the DPS. We show in red (resp. black) points the median and the 68% quantile for a binning according to σ_* of the DPS (resp. NBCS). For the DPS, the limitations in $\sigma_{1,2}$ and Δv_{DP} of the double Gaussian fit are restricted by the spectral resolution (see Sect. 2.2.2), leading to a restriction of a minimal σ_{single}, indicated with a red line. We also show the minimal σ_{gas} for the NBCS as a black line and the best fit of a linear function as a black dashed line.

NBCS. This suggests that the gas components of DP galaxies show higher velocities in comparison to σ_*, or that one part of the ionised gas is strongly perturbed or has an external origin.

4.3.3. Inclination

A double-peak emission line shape can of course also originate from a rotating disc. This has been discussed in detail in Elitzur et al. (2012) and shown in simulation in Kohandel et al. (2019). In order to test this specific scenario, we used a single Gaussian approximation of the double-peak emission lines (see Sect. 4.3.2) which, in the case of a rotating disc, would be an approximation for the gas velocity dispersion. We assumed here that the rotation disc is the main disc of the galaxy, and study the correlation of the velocity dispersion with the inclination angle i defined with the photometric analysis. Hence, we calculated the inclination angle following Eq. 5 using the minor-to-major axis measured by Meert et al. (2015) which provides reasonable results for spiral and S0 galaxies if the disc component exhibits good fit results (see Meert et al. 2015, for more details on fit results). As a cross-check for the measured inclination, we followed Yip et al. (2010) and find a dependency between the inclination angle and the Balmer decrement Hα6565/Hβ4863 used to calculate the inner galactic extinction. This trend is comparable to the one observed for the NBCS, but, as mentioned above, the extinction is slightly larger (0.25 mag) for DPS than for NBCS.

The area covered by the 3″ SDSS fibre depends on the redshift. The measured gas velocity dispersion of a rotating disc depends on the area integrated by the spectroscopic observations. We thus defined three redshift groups as in Sect. 4.2 for this analysis: z < 0.075, 0.075 < z < 0.125, and 0.125 < z. In Fig. 18, we present the estimated inclination angle i as a function of various gas velocity measurements for the DPS and the NBCS. The NBCS is represented by the gas velocity dispersion σ_{gas} (see Sect. 4.3.1). For the DPS, we display σ_{single} from the single Gaussian approximation (Sect. 4.3.2), Δv_{DP} from the stacking procedure (Sect. 2.2.2) and σ_{close} and σ_{far} as described in Sect. 4.3.1. For galaxies with a redshift $z > 0.075$, we see a clear correlation in the NBCS between σ_{gas} and the galaxy inclination i. This correlation between σ_{gas} and i can be explained by a rotating disc. In contrast, we do not find any dependencies between the displayed velocities of the DPS and i in any redshift range. The absence of such a correlation for the DPS disfavours the rotating (main-) disc scenario.

4.3.4. Tully-Fisher and Faber-Jackson relations

The velocities measured in galaxies are tightly correlated to their size. This relation was first discovered by Faber & Jackson (1976) for the stellar velocity dispersion and the absolute magnitude of elliptical galaxies (FJR). They concluded that the luminosity L of a galaxy is consistent with the relation $L \propto \sigma_*^4$. In parallel, a good relation between the full-width at 20% of the maximum of the HI profile, corrected to the inclination of the galaxy, and the galaxy size was found by Tully & Fisher (1977) for spiral galaxies. This Tully-Fisher relation (TFR) is usually understood as the self-regulation of star formation in the disc (e.g. Silk 1997).

The parameters of these relations have been later measured with higher accuracy. Here, we used for the FJR: $\log(\sigma_*/\mathrm{km\,s^{-1}}) = -0.90 \pm 0.12 + (0.29 \pm 0.02)\ \log_{10}(M_*/\mathrm{M_\odot})$, measured by Gallazzi et al. (2006). For the TFR, we use: $\log_{10}(v_{rot}/\mathrm{km\,s^{-1}}) = -0.69 + (0.27 \pm 0.01)\ \log_{10}(M_*/\mathrm{M_\odot})$, measured by Avila-Reese et al. (2008), where v_{rot} is the rotation velocity, calculated as in Catinella et al. (2005) and Aquino-Ortíz et al. (2018): $v_{rot} = W/[2 \sin i]$, where i is the inclination angle (see Eq. 5) and W the difference between the 10th and the 90th percentile of the velocity measurements. Since we do not have spatially resolved information on galaxy kinematics, we approximated from a Gaussian shaped emission lines the 10th and the 90th percentile as $W = 2.56\sigma$ (This is close to the full-widths half maximum of a Gaussian at 2.36σ). We calculated v_{rot} for the TFR using σ_{gas} for the CS and the NBCS (see Sect. 4.3.1) and σ_{single}, σ_{close} and σ_{far} for the DPS (see Sect. 4.3.1 and 4.3.2). We take the stellar mass $\log(M_*/M_\odot)$ measured by Kauffmann et al. (2003) for the TFR and FJR. In the case where we display only one of the DP (the close or the far peak), we approximated the fraction of the stellar mass for each peak as $\log(f_{1,2}\, M_*/M_\odot)$. We assumed $f_{1,2}$, the mass fraction of each peak, to be the same fraction as the total emission line flux of the stacked lines. This is a rough approximation but would be our best guess to assume each peak corresponds to one component of a hidden merger.

In Fig. 19 (resp. 20), we present the TFR for LTG (resp. S0) of the DPS, the CS and the NBCS. We find good agreement for LTG of the CS and the NBCS with the parameters for the TFR found by Avila-Reese et al. (2008). We find that, for the LTGs of the DPS, the rotation velocity calculated with σ_{single} does not follow the TFR. We measure v_{rot} to be higher than expected for the measured masses. We find a good agreement using σ_{close} whereas rotation velocities calculated with σ_{far} are shifted towards lower velocities. For S0 galaxies, we observe the same velocity shifts as shown in Fig. 20. S0s and LTGs have a similar behaviour: σ_{single} is offset with respect to the NBCS distribution considering the two peaks as individual galaxies following this distribution. In both TFRs, we find some outliers with extreme v_{rot} values. By individual inspection, we find these velocities to be the result of a small inclination and/or very broad peak component.

In Fig 21, we show the FJR (M_* vs σ_*) for elliptical and S0 galaxies. As a reference, we used the best fit from Gallazzi et al. (2006) as a dashed line. We find good agreement for elliptical galaxies of the DPS, CS and the NBCS. For S0 galaxies, we find

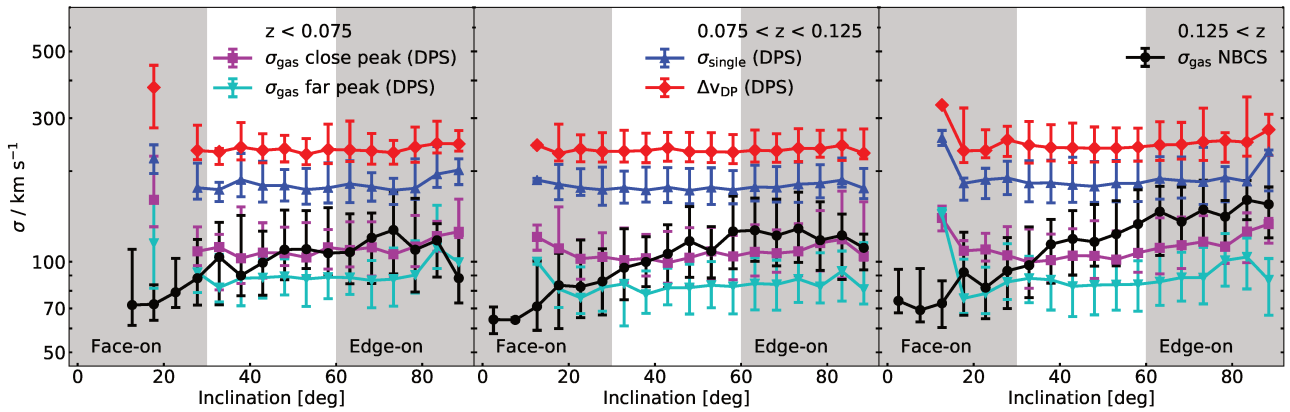

Fig. 18. Influence of the inclination on the velocity dispersion. We show different velocity dispersion distributions as a function of the galaxy inclination for different groups of redshift. We only show LTG and S0 galaxies for which we can compute the inclination using Meert et al. (2015). For the DPS, we show ΔV with red dots, $\sigma_{\rm single}$ of the single Gaussian approximation in blue (see sect. 4.3.2) and in magenta (resp. cyan) the σ of the emission line component which is closer (resp. offset) to the stellar velocity in units of σ. We show the $\sigma_{\rm gas}$ for the NBCS with black dots. All data points represent the medians in the inclination intervals and the error bars the 16th to 84th percentiles.

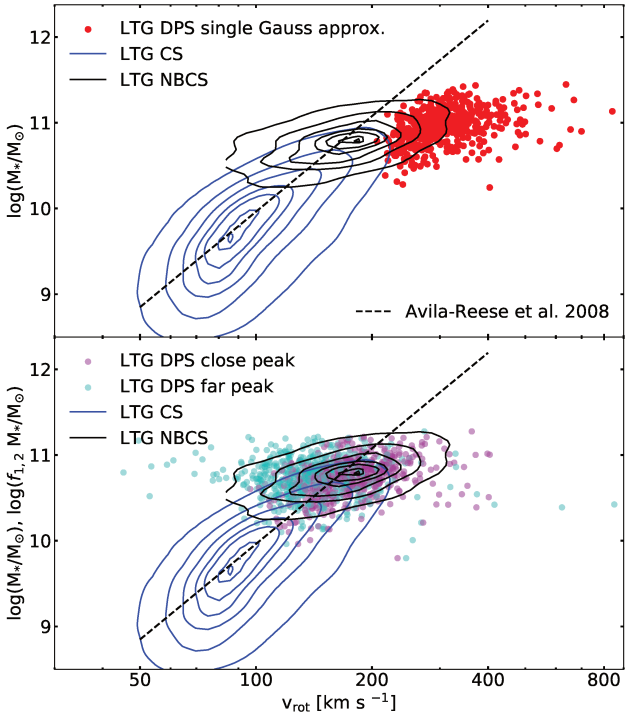

Fig. 19. Tully-Fisher relation (TFR) for LTGs. We compute the rotational gas velocity $v_{\rm rot}$ for the NBCS and CS (black and blue contour lines) using the gas velocity dispersion $\sigma_{\rm gas}$ (see Sect. 4.3.1). For the DPS, we use the $\sigma_{\rm single}$ of the single Gaussian approximation in the top panel. In the second panel, we show the TFR for the close and far peak-components of the DPS (see Sect. 4.3.1). The stellar masses are computed by Kauffmann et al. (2003). We show the best fit computed by Avila-Reese et al. (2008) as a dashed line.

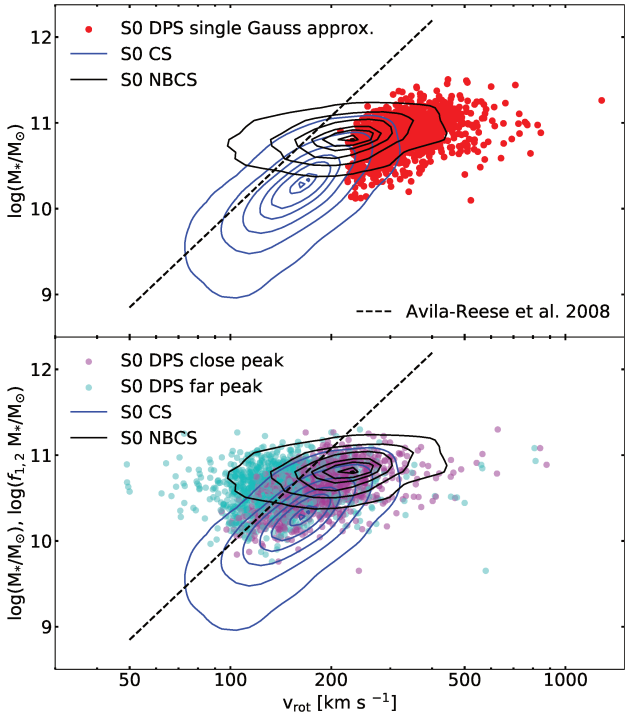

Fig. 20. Same as Fig. 19, but for S0 galaxies. The dashed line corresponds to the best fit of Avila-Reese et al. (2008).

in the NBCS and the CS systematically lower σ_*, whereas the DPS shows velocities agreeing with those of elliptical galaxies with the same stellar mass. This is in agreement with the result discussed in Fig. 15 that the stellar velocity dispersion is larger for the DP galaxies, supporting again a large system composed of the superposition of two systems.

4.4. Morphology and galaxy environment

We studied the environment of the DP galaxies with the galaxy group catalogue provided by Yang et al. (2007)[3] and Saulder et al. (2016). Yang et al. (2007) is a halo-based group finder algorithm, determining the group masses and identifying each member of groups using the redshift. About 90% of the DPS and the NBCS are covered by this catalogue. Saulder et al. (2016) calibrated a group finder algorithm with simulation data providing a

[3] We used the galaxy group catalogue compiled on the SDSS DR 7 available under: https://gax.sjtu.edu.cn/data/Group.html

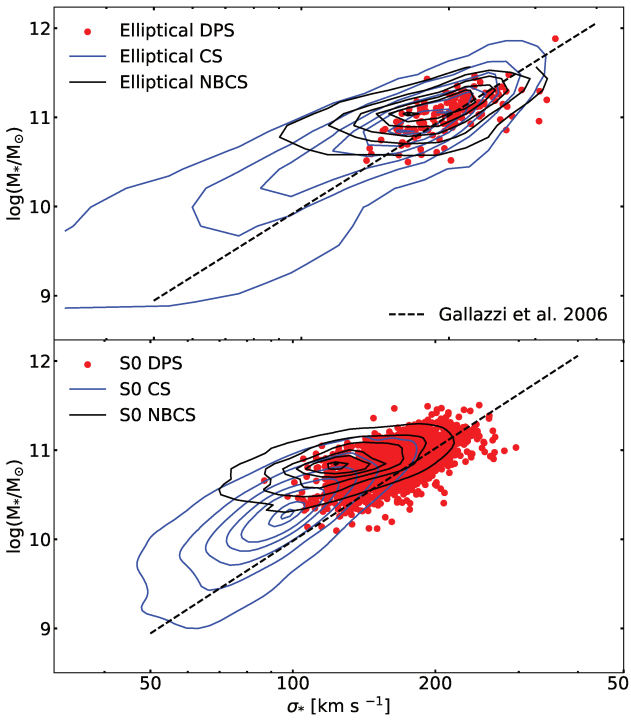

Fig. 21. Faber-Jackson relation for elliptical and S0 galaxies using the stellar velocity dispersion taken from Chilingarian et al. (2017) on the x-axis and the stellar masses computed by Kauffmann et al. (2003) on the y-axis. We show the best fit computed by Gallazzi et al. (2006) in dashed lines.

higher sensitivity to different kinds of galaxy groups up to a redshift of z < 0.11 (47% of the DPS and NBCS). In this redshift range, they cover 97% (resp. 98%) of the DPS (resp. NBCS).

We used galaxy groups sizes as discussed in Blanton & Moustakas (2009): a poor group holds 2 to 4 members, a rich group 5 to 9 and a cluster more than 10. With Yang et al. (2007), we find 64% (resp. 66%) of the DPS (resp. NBCS) to be isolated, 19% (resp. 17%) in poor groups, 3% (resp. 4%) in rich groups and 4% (resp. 4%) in clusters. To compare this result with Saulder et al. (2016), we looked at the fraction for galaxies with redshift z < 0.11 and find similar fractions as above. Using Saulder et al. (2016), we find 45% (resp. 45%) of the DPS (resp. NBCS) to be isolated, 34% (resp. 33%) in poor groups, 11% (resp. 12%) in rich groups and 9% (resp. 12%) in clusters. We detect fewer isolated galaxies in comparison to Yang et al. (2007), which is due to the higher sensitivity of group identification.

In Table D.3, we present the fractions of the environmental classification for the morphological types (see Sect. 3.2). Analysing group properties such as number of group members, distance to the closest neighbour or the velocity dispersion of a galaxy group, we only find a difference between the DPS and the NBCS for elliptical galaxies (Saulder et al. 2016). In the DPS (resp. NBCS), we find 23% (resp. 41%) of the elliptical galaxies to be situated in a dense environment (rich groups or clusters), whereas 72% (resp. 58%) are situated in less dense environments (isolated galaxies or poor groups).

S0 galaxies are usually observed more abundant in clusters than in the field (Dressler 1980), but this is not the case here. In the DPS and the NBCS, we find about 80% of the S0 galaxies to be situated in less dense environments. We do not find any differences in the fraction of isolated S0 galaxies selected in the DPS and the NBCS, but we clearly see that most of the selected S0 galaxies are isolated. Even though we find an excess of S0 galaxies and a lack of LTGs in the DPS in comparison to the NBCS (see Sect. 3.2), we do not find any connection between the galaxy environment and the morphological type.

Dressler et al. (1997) first observed an increase of S0 galaxies over elliptical fraction in groups from z ∼ 0.5 till today, while the spiral fraction before z ∼ 0.5 corresponds to the S0 fraction observed today. This supports the view that spirals evolve into S0 galaxies due to their environment (Fasano et al. 2000). This has been supported by subsequent observational works (e.g. Wilman et al. 2009). However, this is not the case here as 70% of the DP-S0 galaxies are isolated according to Yang et al. (2007), (or 50% for z < 0.11 according to Saulder et al. (2016)), and the behaviour of S0 and LTG are not significantly different in the DPS in terms of excitation mechanisms and dynamics. This apparently contradicts the work of Gao et al. (2018), based on photometric decomposition, who found that the bulges of spirals and S0s are intrinsically different and thus spirals are probably not the progenitors of S0s.

4.5. Non-parametric morphological diagnostics

To further investigate the properties of the different morphological galaxy types, we computed photometric diagnostics for the DPS and NBCS. We used the python package STATMORPH[4], which calculates non-parametric morphological diagnostics of galaxy images (e.g. CAS-statistics or the Gini coefficient), as well a fit of a 2D Sérsic profile (Rodriguez-Gomez et al. 2019). Here, we tested our galaxy samples using CAS-statistics composed by concentration (C), asymmetry (A) and smoothness (S), the shape-asymmetry (A_S), the Gini-coefficient, the second moment of the galaxy's brightest regions M_{20} and the Sérsic index n. For an exact definition and description of these diagnostics, see Rodriguez-Gomez et al. (2019) and references therein. We applied STATMORPH to the r-band 62″ × 62″ Legacy Survey snapshots (Dey et al. 2019).

The CAS-statistics were introduced by Conselice (2003) to distinguish between different morphological types. As discussed in Sect. 4.2, we find for some sub-samples of the DPS a higher concentration, accompanied by a higher central SFR, in comparison to the NBCS. However, we do not find any differences in asymmetry or smoothness between the DPS and the NBCS.

To automatically recognise ongoing or past mergers, Pawlik et al. (2016) introduced the shape asymmetry (A_S), which specifically detects galaxies with low-surface-brightness tidal features. We observe higher A_S for galaxies classified as mergers than for other types (as expected), but we find for all sub-samples and redshift ranges similar distributions for the DPS and NBCS.

Abraham et al. (2003) applied the Gini coefficient on galaxy imaging in order to determine the galaxy morphology. The Gini coefficient quantifies the inhomegeneity (or 'inequality' when applied to human populations) with which a galaxy's light is distributed. Lotz et al. (2004) combined the Gini coefficient with the second moment of the galaxy's brightest regions M_{20} to be able to distinguish between merger and non-merger galaxies. We present this diagnostic in Fig. 22. Galaxies with an ongoing merger process are located on the left of the Gini-M_{20} diagram, which is marked by a purple line (Lotz et al. 2008). In post coalescence stages, the merger would migrate back to the right where two populations are located: in the upper right part elliptical, S0 and Sa galaxies are located, whereas in the lower right

[4] https://statmorph.readthedocs.io

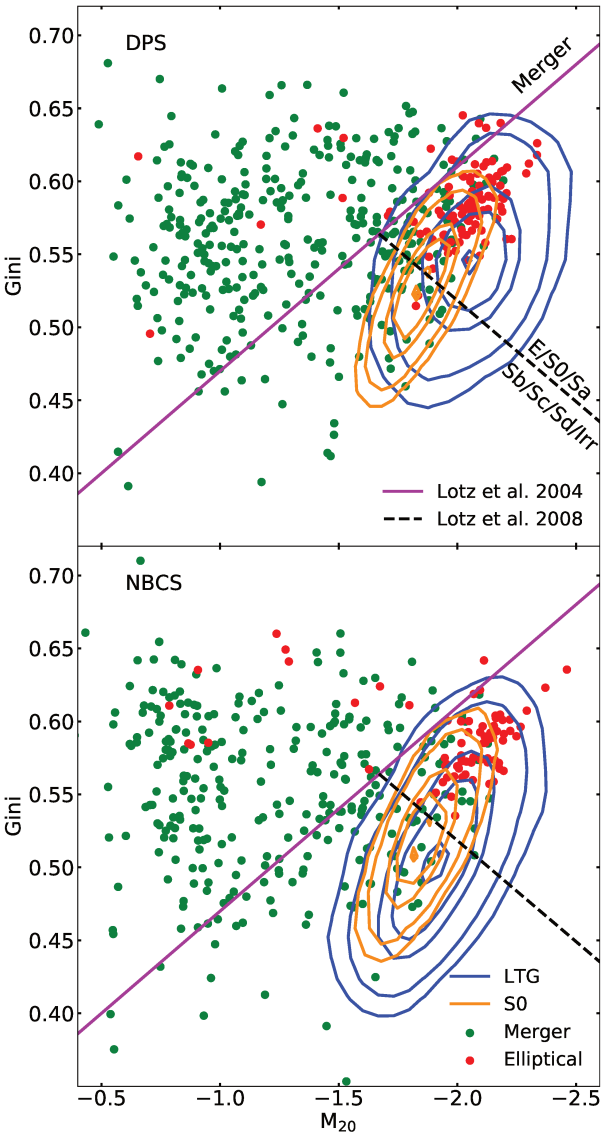

Fig. 22. Gini vs M_{20} coefficients for the DPS (*top panel*) and the NBCS (*lower panel*). Blue (resp. orange) contours represent galaxies classified as LTG (resp. S0) and red (resp. green) dots denote elliptical (resp. merger) galaxies (See the classification in Sect. 3.2). The purple line separates galaxies classified as merger on the left hand side and galaxies associated with a Hubble type on the right hand side (Lotz et al. 2004). The lower black dashed line divides elliptical, S0 and Sa galaxies from later types namely Sb, Sc and Irr (Lotz et al. 2008).

part irregular and spiral galaxies, of type Sb, Sc, Sd, or Irr, are located Lotz et al. (2008). These two regions are separated by a black dashed line. Using hydrodynamical simulations, this diagnostic combined with asymmetry is sensitive to merger timescales of $\sim 200 - 400$ Myr for major disc merger and 60 Myr for minor mergers (Lotz et al. 2010b).

Galaxies of the DPS and the NBCS, classified as merger or elliptical, show good agreement between their classification and their position on the Gini-M_{20} diagram (Fig. 22). Galaxies classified as S0 are spread over the region of early and late Hubble types with similar distributions between the DPS and the NBCS. This diagnostic diagram indicates a difference for LTG of the DPS in comparison to the NBCS: we observe that LTGs of the

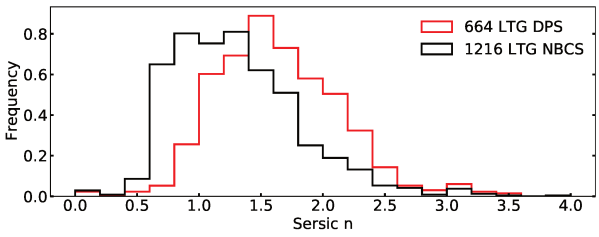

Fig. 23. Distribution of Sérsic indices, computed by STATMORPH (Rodriguez-Gomez et al. 2019) for the Legacy survey *r*-band images (Dey et al. 2019), of LTGs of the DPS (red line) and NBCS (black line). The areas under the histograms are normalised to unity.

DPS are mainly (63 %) situated in the region associated with earlier Hubble type galaxies, whereas LTGs of the NBCS are mainly situated in the region of later Hubble types (only 35 % in the earlier Hubble type region). One might think that Sa galaxies are over-represented in the DPS. However, with respect to the full sample, we detect 10 % of the DPS and 11 % of the NBCS classified as Sa galaxies. We only find 6 % of the DPS that are classified as Sb-d, whereas 19 % of the NBCS are of this type. Hence, there is no Sa excess but a deficit of Sb-d galaxies. In Appendix C, we find Sb-d of the DPS to be the only morphological sub-sample that shows larger stellar masses (~ 0.2 dex in $\log(M_*/M_\odot)$) in comparison to LTG galaxies of the NBCS. Additionally, we find the highest difference in extinction of about 0.3 mag in the *V* band. We furthermore detect a significant excess in star formation in the centre: for Sb-d of the DPS (resp. NBCS), we find a median $SFR_{fibre}/SFR_{total} = 0.59^{+0.30}_{-0.31}$ (resp. $SFR_{fibre}/SFR_{total} = 0.31^{+0.20}_{-0.16}$).

The shift towards earlier Hubble types of LTGs of the DPS, in comparison to the NBCS, is also supported by the measured Sérsic index, presented in Fig. 23. By comparing the Sérsic index of the DPS with those of the NBCS, we only find a discrepancy for LTGs, all other subsets show similar distributions. This indicates, that LTG of the DPS tend to have larger bulges in comparison to the LTGs of the NBCS.

Interestingly, Nevin et al. (2019) tested the position of simulated minor and major mergers in the Gini-M_{20} diagram (see their Fig. 7) and found that most minor mergers and about half of the major mergers lie below the purple line, and mainly in the ETG/S0/Sa region (above the black dashed line). This corresponds to the trend discussed in Lotz et al. (2008): post-coalescence galaxies are more concentrated in their light distribution, while tidal features vanish.

In Appendix B, we follow Nevin et al. (2019), who developed a supervised Linear Decomposition Analysis (LDA) in order to compute the predictor coefficients $LD1_{major}$ and $LD1_{minor}$, defined to identify major and minor mergers. To get comparable results, we restricted our analysis to $z < 0.075$. We find in cases, such as LTG and S0 galaxies, slightly higher merger rates for the DPS in comparison to the NBCS. This result somehow supports a merging scenario, while it is compatible with the fact DP galaxies might be dominated by post-coalescence mergers that would escape such analysis targeting on-going mergers. This result is compatible with the results discussed above based on the Gini-M_{20} diagram.

4.6. Summary

We have studied different parameters derived from observations to compare the DPS with the NBCS. The NBCS is defined to

have the same redshift and stellar mass distributions as the DPS (see Sect. 2.3).

We find the following similar properties:

- Distributions of absolute magnitudes, stellar ages, metallicities, specific star formation ratio and [OIII]λ5008 emission line luminosities are identical.
- According to their colour-colour and their specific star formation-stellar mass diagrams, most of DPS and NBCS galaxies follow the star forming main sequence, only a few exhibit a quenched SF and some are located in the red sequence.
- Double-AGN behave as NBCS-AGN with respect to star formation: there is no significant central excess.
- If one considers that each peak corresponds to a component, the DPS and NBCS follow the Tully-Fisher relation.
- Elliptical galaxies from DPS and NBCS follow the Faber-Jackson relation.
- The same environment statistics are found for the DPS and the NBCS. Most of S0s are isolated, and the S0s excess observed in the DPS is not due to environment.

We detect the following differences:

- There is an excess of S0s (resp. a deficit of LTGs) in the DPS with respect to the NBCS.
- According to the Gini-M_{20} diagram, there appears to also be an excess of Sa galaxies in the DPS compared to the NBCS.
- LTG galaxies display higher Sérsic indices in the DPS compared to those in the NBCS.
- Galaxies classified as LINER are less common in the DPS in comparison to the NBCS.
- DPS galaxies show slightly higher absolute luminosities in the $H_\alpha\lambda$6565 emission line.
- Double-SF galaxies exhibit a central starburst stronger than SF galaxies from the NBCS.
- Double-COMP, -LTG and -S0 galaxies also have such an excess but less significant.
- Double-COMP are more likely SF galaxies, according to the [OII]λ3728 / [OIII]λ5008 line ratio, and to the detection rate of the high-ionisation [NeV]λ3426 emission line at $z > 0.2$.
- There is slightly more extinction (0.25 mag in V) in DPS galaxies than in their NBCS counterparts.
- All DPS velocity estimators are independent of the inclination, while we do detect a correlation for the NBCS.
- At given stellar masses, stellar velocity dispersions are larger for the DPS than for the NBCS.
- The gas velocity dispersion estimator of the close peak component of the DPS is compatible with velocity dispersions measured for the NBCS, whereas the far peak component of the DPS is not.
- With a single Gaussian approximation, the LTG and S0 galaxies from the DPS are offset from the NBCS TF relation.
- S0 galaxies from the DPS are shifted on the FJ relation from the NBCS.

5. Discussion

In Sect. 5.1, we argue that S0 galaxies detected as gas-rich DP galaxies belong to a star-forming population identified in previous works. In Sect. 5.2, we discuss how our non-parametric analysis revealed that LTG are dominated by Sa galaxies in the DPS. In Sect. 5.3, we propose that the DP galaxies sample is a minor merger sequence which could explain the different results discuss in Sect. 4.6. In Sect. 5.4, we discuss here different observations, which are compatible with the characteristics of the DPS described as a minor merger sequence. In Sect. 5.5, we compare the known properties of the DPS galaxies with respect to those of minor and major mergers. To present a complete discussion, we discuss further explanations of the observation of DP in Sect. 5.6 and find that these only apply to a few galaxies in our sample.

5.1. Star-forming S0s

S0 galaxies are usually described as disc galaxies, which have exhausted their gas content (e.g. Somerville & Davé 2015) and are proposed as a parallel Hubble sequence (van den Bergh 1976; Kormendy & Bender 2012). However, it has been known for several decades that some S0s are not forming stars but host large amounts of HI gas (e.g. Kennicutt 1989). In these early observations of HI-gas-rich S0 galaxies (e.g. van Woerden et al. 1983; Knapp et al. 1984, 1985; Krumm et al. 1985; van Driel et al. 1988), inner and outer rings were already detected, and analysed in simulations (e.g. Athanassoula & Bosma 1985; Buta & Combes 1996). The HI gas has often an Hα − [NII]-counterpart (e.g. Pogge & Eskridge 1993). Observations have shown indeed that about 85% of S0 galaxies host optical ionised gas (e.g. Macchetto et al. 1996; Sarzi et al. 2006) and 72% of those are isolated (Katkov et al. 2015). Kannappan et al. (2009) identified a blue sequence of SF S0 galaxies in the low-mass range that might be fading mergers, while massive S0s, with $M > 2 \times 10^{11}\,M_\odot$, belong to the red sequence, but up to 2% of these massive S0 are SF. In the blue S0 sequence, they identify central blue colour gradients, which are interpreted as reminiscent of mergers (e.g. Kannappan 2004; Kewley et al. 2006a). Xiao et al. (2016) find about 8% of an S0 sample exhibits central star formation. They also found that the majority of these SF S0 galaxies have a stellar mass below $10^{10.6} M_\odot$. Tous et al. (2020) did not find such a mass separation. In their study of these two S0 populations composed of SF and quiescent galaxies, they found that SF S0 galaxies avoid high-galaxy density and that their SFR and spectral characteristics are entirely similar to those seen in LTGs.

Numerous observations show further evidence of various tidal disturbances in the outer parts of S0: outer rings (e.g. Comerón et al. 2014; Sil'chenko et al. 2018), polar rings (e.g. van Gorkom et al. 1987; Whitmore et al. 1990), circum-nuclear polar rings (e.g. Sil'chenko & Afanasiev 2004; Chilingarian et al. 2009; Sil'chenko 2016), counter-rotations (e.g. Katkov et al. 2013, 2014; Ilyina et al. 2014; Katkov et al. 2015, 2016; Pizzella et al. 2018) and cylindrical rotation (e.g. Molaeinezhad et al. 2019). In Katkov et al. (2014, 2015), Proshina et al. (2019), and Sil'chenko et al. (2019), the authors discuss the origin of this counter-rotating gas and argue that S0s might accrete gas probably from filaments or from minor mergers. In parallel, numerous works have shown that S0s can be produced by galaxy mergers including major mergers (Bekki 1998; Querejeta et al. 2015; Tapia et al. 2017; Eliche-Moral et al. 2018) as well as minor mergers (Bournaud et al. 2005; Bekki & Couch 2011).

Here, we clearly detect intermediate-mass S0 galaxies in the mass range $3 \times 10^{10} - 3 \times 10^{11}\,M_\odot$ with optical ionised gas, including a large fraction of star forming galaxies. Beside their optical morphology, their kinematic behaviour is similar to those of LTGs. We find similar distributions for LTGs and S0 galaxies in the TFR in Sect. 4.3.4. We argue that the close peak might represent the central galaxy, while the far peak might correspond to a smaller companion or to the result of a recent gas accretion.

5.2. Non-parametric merger identification

In the Sect. 4.5, we compute several non-parametric diagnostics such as CAS-statistics, the shape asymmetry A_s, the Gini and M_{20} coefficients and the Sérsic index n to investigate different approaches of merger identification.

Morphological asymmetry is more prevalent in galaxies within close pairs (Patton et al. 2016). Moreover, SF is enhanced in close pairs with small differences in line-of-sight velocities (Patton et al. 2011, 2013). We studied galaxy asymmetries in the DPS, relying on the parameters of Patton et al. (2016). We do not find any asymmetry difference between the DPS and the NBCS nor any connection between SF and asymmetry. In a scenario where the central SF enhancement is due to a merging process, the absence of a significant asymmetry in the DPS would favour later stages of merging processes or mergers hidden inside the fibre. Pawlik et al. (2016) introduced the shape asymmetry to identify later stages of merger in comparison to the asymmetry. We do not find any difference between the DPS and the NBCS using this diagnostics.

We conducted a merger selection based on the Gini-M_{20} disgnostics, proposed by Lotz et al. (2004, 2008) to separate mergers from non-mergers and to distinguish between late and early Hubble types. We find good agreements with the predictions for S0, merger and elliptical galaxies of the DPS and the NBCS. LTGs of the DPS reveal a systematic effect: they are situated in the region of earlier Hubble types in comparison to LTGs of the NBCS (see Fig. 22). This is in agreement with the fact that we find a tendency towards higher Sérsic index n for LTGs of the DPS in comparison to the NBCS, supporting the idea of a sequence of galaxies thickening towards S0. Last, this is in agreement with the trend discussed in Appendix B with the small positive bias for minor and major mergers observed in the predictor coefficient distributions, as defined by Nevin et al. (2019). These authors also show that numerous simulated (major and minor) mergers lie in the non-merger regions of the Gini-M_{20} diagram.

Comparing all non-parametric methods, designed to detect merger rates, we do not find a direct relation between on-going mergers and DP structure at $z < 0.075$. Even though, these diagnostics were developed to detect late and post-coalescence stages of mergers (Pawlik et al. 2016; Lotz et al. 2008, 2010b,a; Nevin et al. 2019), we might see an even later stage, where traces such as fading tidal features are already quite weak and double nucleus beyond spatial resolution. Nevin et al. (2019) defined post-coalescence when the two galactic nuclei are separated by less than 1 kpc, which correspond to the SDSS resolution at $z \leq 0.03$. Indeed as the DP feature is based on the central 3″spectra, it is probable that the discussed diagnostics are not sensitive.

5.3. S0s as a part of the minor merger sequence

Walker et al. (1996) found that in 1:10 minor mergers, the discs are not destroyed but evolve to an earlier Hubble type, while a core of 45% of the satellite initial mass can reach the central kpc in 1 Gyr. This scenario might account for our DPS: high stellar velocity dispersions, two gas components and a similar kinematic behaviour for the different morphological types. This is supported by numerous hydrodynamical simulations. Bournaud et al. (2005) showed that intermediate mergers with 1:4 to 1:10 mass ratio can produce S0 galaxies. A similar situation was observed in GALMER simulations (Chilingarian et al. 2010a). Hence, while it is now well-known that S0s can be formed by minor and major mergers depending on the orientation and kinematics, Bournaud et al. (2007) studied the evolution of galaxies due to repeated minor mergers, as expected in the hierarchical growth of galaxies. Multiple sequential mergers feed the main progenitor, and gradually change its morphology from a spiral to an elliptical-like system. In addition, this is compatible with the work of van Dokkum et al. (2015) who proposed a two-channel evolution scheme, to account for the evolution of mass-size relation: they first grow inside-out with gas accretion and gas-rich minor mergers, until they quench, and continue to grow by dry minor mergers. Cappellari (2013) proposed a similar modelling to account for the evolution of slow and fast rotators, as further discussed in Cappellari (2016). This scenario is fully compatible with the properties of Sa and S0 galaxies and such a sequential gas-rich minor merger sequence accounts for the main properties of the DPS galaxies, identified here.

The increased central star formation and enhanced central extinction are also well accounted for by minor mergers and galaxy–galaxy interactions (e.g. Li et al. 2008; Ellison et al. 2011a). Using hydrodynamical simulations, Mapelli et al. (2015) produced rejenuvated S0 galaxies and a central SF enhancement with minor mergers with gas-rich galaxies. More generally, this work is compatible with the results of Li et al. (2008), who find that the majority of galaxies with high SSFR have a companion or exhibit tidal features.

5.4. Support from other observations

Studies of S0s performed with planetary nebulae provide characteristics comparable with our findings on the TF relation. With a spectroscopic and kinematic analysis of planetary nebulae in six S0 galaxies, Cortesi et al. (2013) found that S0s are supported by random motions in addition to their rotating discs. S0 galaxies lie about 1 magnitude below the TFR for spiral galaxies while their spheroids lie 1 magnitude above the FJR for elliptical galaxies. This supports previous findings on these S0 characteristics (Bedregal et al. 2006; Rawle et al. 2013), which we observe in the DPS for S0s but also for LTGs. Davis et al. (2016) also observed a break for high velocities in the TF relation, which they interpret as an additional baryonic mass present in the central part.

Similarly to Kannappan et al. (2009), Bait et al. (2017) and Fraser-McKelvie et al. (2018) identified two separate populations of S0 galaxies. Beside old, massive and metal rich galaxies with a bulge older than the disc (probably due to an inside-out quenching), they discuss less massive and more metal poor population having bulges with more recent star formation than their disc. They might have undergone a bulge rejuvenation (or disc fading), or compaction. They argued that environment is not playing a major role, and proposed a faded spiral scenario, which forms low mass S0s while other processes such as mergers form the more massive S0s. As we only detect massive S0s, this is compatible with our findings. We have a population of massive star-forming galaxies, which are evolving through different stages of mergers. S0 galaxies represent 36% of the whole DP population, they are not faded. Beside their morphology, we cannot disentangle them from LTGs.

5.5. Minor versus major mergers

As discussed in Bournaud et al. (2005), intermediate mass mergers with ratio 1:4 to 1:10 produce Sa to S0 galaxies, while equal mass mergers produce mainly ellipticals (e.g. Barnes & Hernquist 1991), and 1:3-1:4 can produce S0-like systems (e.g. Bekki 1998; Eliche-Moral et al. 2018). Last, the scenario of single mi-

nor mergers, with mass ratio larger than 1:10, produces spiral galaxies, while sequential multiple minor mergers can also lead to Sa/S0 galaxies (Bournaud et al. 2007).

On the one hand, the fact that the two peaks have typical intensity ratio in the range 1−3 might favour the idea of two galaxy nuclei with progenitors with 1:1 to 1:4 mass ratios. However, the absence of differences in the rate of morphological mergers between DPS and NBCS is not expected if the majority were such major mergers, as well as the absence of any differences in the distribution of shape-asymmetry and asymmetry. Major mergers can produce large starbursts (e.g. Barnes & Hernquist 1991), even though this is not always the case (e.g. Di Matteo et al. 2007). However, Hani et al. (2020) found that strong enhancements of SFR are dominated by major mergers. They estimated that a starburst of $50\,M_{\odot}\,\mathrm{yr}^{-1}$ has four times higher chances to occur in a major merger than in a minor merger. We have here 1.3 % of the sample with a SFR larger than $50\,M_{\odot}\,\mathrm{yr}^{-1}$.

On the other hand, as discussed above multiple sequential gas-rich minor mergers and/or gas accretion might also produce the DPS galaxies (e.g. Walker et al. 1996). They could also account for the excess of S0 galaxies and the prevalence of Sa galaxies in LTG, as well as relatively morphologically regular DPS galaxies (Mazzilli-Ciraulo et al., in prep.). The intensity ratio of the two peaks (between 1 and 3) can also be biased by the excitation of the AGN triggered by a merger (Maschmann et al., in prep.).

As discussed in Appendix C, the 0.2 dex higher typical stellar masses of DPS galaxies, their 0.25 mag typical excess extinction in V and their central enhancement of star formation for Sb-d galaxies, all in comparison to the NBCS, suggest a past merger scenario for them. A visual inspection of the selected galaxies reveals that they are not dominated by edge-on or strongly inclined galaxies. However, Sb-d galaxies constitute 6 % of the DPS (19 % of the NBCS).

As discussed by Hani et al. (2020) and references therein, minor mergers are expected much more numerous than major ones, for example Kaviraj (2014) estimated that 40% of SF observed in local spirals is directly triggered by minor mergers. In addition, major mergers are known to trigger stronger SF than their minor counterparts. The distributions of $\mathrm{SFR_{fibre}}$ estimated in the SF-DPS galaxies peak between 2 and $10\,\mathrm{M_{\odot}\,yr^{-1}}$ and is about a factor of 2 larger than for the NBCS. In numerical simulations, Hani et al. (2020) found an SFR enhancement of a factor two in $10.0 \leq \log(\mathrm{M_*/M_{\odot}}) \leq 11.4$ SF post-merger galaxies.

Elliptical galaxies of the DPS are situated in the star forming main sequence (See Sect. 4.2), whereas their counterparts of the NBCS are quenched. We quantify this in Appendix C: elliptical DP galaxies show a 4 times higher SFR in comparison to single peaked elliptical galaxies. We furthermore find that elliptical galaxies with a DP have on average a 3 Gyr younger stellar population in comparison with those showing a single peak. This is consistent with the detection of molecular gas in star forming early type galaxies by Combes et al. (2007), who conclude that the molecular gas might has been accreted from the environment and shows properties rather independent from the old, pre-existing stellar component. Such a recent gas accretion might explain the emission line shape and the ongoing star formation that we detect.

DP galaxies have numerous characteristics of post-mergers with enhanced central star formation and extinction. The nature of the DP feature is still elusive, and could correspond to gas clumps as well as to relics of two galaxy nuclei. We argue that DPS galaxies, most of which exhibit an ordinary morphology, are more likely to be linked to gas-rich minor mergers or gas accretion than to major mergers, which would impact more strongly their morphologies. Indeed, we do detect the same number of morphological mergers in the DPS and NBCS. The sequential multiple minor merger scenario accounts for the S0 morphological excess clearly detected in the DPS, while we cannot exclude that a few of these DP galaxies originate from major mergers.

5.6. Alternatives

Supermassive black holes hosted in galaxy centres are expected to have a significant feedback during the AGN phase (Fabian 2012). This effect is measured to be stronger in massive galaxies (Somerville & Davé 2015; Zhang et al. 2018), than in smaller galaxies dominated by star formation feedback. Galaxy collisions are usually thought to trigger AGN feedback (Di Matteo et al. 2005). Gas outflow are found to be associated to emission line asymmetries (Heckman et al. 1981; Whittle 1985). This is studied on large data samples with fitting procedures using single- and double-Gaussian functions in for example Greene & Ho (2005) and Woo et al. (2016). Using observations based on spectroscopic integral field units, Karouzos et al. (2016) observed AGN driven outflow components with velocities between 300 and $600\,\mathrm{km\,s^{-1}}$ with velocity dispersion up to $800\,\mathrm{km\,s^{-1}}$. In the study on major mergers, Rupke & Veilleux (2013) have shown that galaxies with a QSO have the highest projected outflow velocities of at least $1450\,\mathrm{km\,s^{-1}}$. In the system F08572+3915:NW, they found velocities up to $3350\,\mathrm{km\,s^{-1}}$. Galaxies without an AGN still reach projected velocities up to $1000\,\mathrm{km\,s^{-1}}$. They concluded that QSOs play a key role in accelerating gas outflows. Beside these extreme velocities, an outflow with low projected velocities of several hundred $\mathrm{km\,s^{-1}}$ has been observed in NGC 5929 (Riffel et al. 2014).

In order to discuss an AGN outflow creating emission lines with a DP structure, we selected galaxies with a broader off-centred emission line component. Therefore, these galaxies have one peak component associated with the stellar velocity, computed by Chilingarian et al. (2017) and a second peak component more offset in units of $\sigma_{1,2}$ (as discussed in Sect. 4.3.1). Furthermore, we demanded the second peak component to show a velocity dispersion larger than $200\,\mathrm{km\,s^{-1}}$ which is similar to lower velocity dispersion of the outflow component found by Karouzos et al. (2016). We thus selected 68 galaxies showing a broad off-centred component as described in the discussed literature above. We show an example in the upper panel of Fig. 1.

Using the non-parametric emission line for the BPT classification (see Sect. 3.1), we find only 1% of these outflow candidates to be classified as SF galaxies. We find 50% to be classified as AGN, 24% as COMP and 13% as LINER. Even though we find a connection to AGN activity for outflow candidates, these galaxies make only about 1% of the DPS. The lack of sensitivity to AGN outflow candidates can be explained by the amplitude criteria $1/3 < \mathrm{A_1/A_2} < 3$ applied in the selection procedure (see Sect. 2.2). Outflow components show mostly very broad component with a lower amplitude described as wings (e.g Heckman et al. 1981; Whittle 1985; Greene & Ho 2005). These types of asymmetries are systematically filtered out in this work.

We also discussed an outflow scenario to explain off-centred weak [OIII]λ5008 in Maschmann & Melchior (2019). In summary, we find evidence for AGN-driven gas outflow in some galaxies, but in comparison to the large sample of DP galaxies we conclude that this scenario provides well-suited arguments only for a small fraction of them.

6. Conclusions

We identified double-peak emission line galaxies with an automated procedure. They are quite rare as they constitute 0.8% of the RCSED/SDSS catalogue. We compared the DP galaxies with their counter-parts from the no-bias control sample and find several significant differences. There is an excess of S0 galaxies, which cannot be accounted for by the environment. The S0-DP galaxies correspond to the star-forming S0 galaxies identified in isolated environments as discussed in Tous et al. (2020). In parallel, the Gini-M_{20} diagram reveals that LTG are mainly Sa galaxies in the DPS with respect to the LTG of the NBCS. Similarly, the DP LTG exhibit a larger Sérsic index than their NBCS counterparts.

On the one hand, we find that LTG and S0 galaxies behave similarly on the TF relation but are off-centred towards large velocity dispersions. On the other hand, if two gas components are considered, we show that the close component behaves as expected while the far peak is offset and might correspond to a smaller component or a large gas clump. Other results further support this scenario: (1) the absence of any dependency on the galaxy inclination, (2) larger stellar velocity dispersions, (3) a systematic central enhancement of star formation and (4) a central enhancement of the extinction.

We argue that this double-peak sample constitutes a sequence of multiple sequential minor mergers, which could explain the similar behaviour observed for the different morphological types. It is a sequence in the sense that the impact of sequential minor mergers is to increase the size of the bulge, leading to larger fractions of S0 galaxies, while the majority of disc galaxies are Sa. It is difficult to disentangle gas-rich minor mergers from gas accretion, but both will have similar effects. The absence of an excess of proper morphological mergers supports the view that the impact is small, typical of minor mergers. The specificity of these DP galaxies is that the spectroscopic signature is inside the 3″ SDSS-fibre, hence, it is somehow a post-coalescence stage not detected in morphological studies. Last, this sample also constitutes a time sequence of mergers as their spread in redshift gathers galaxies observed with resolution between 1 kpc and 12 kpc.

Acknowledgements. This work is based on the master thesis of DM. We acknowledge Françoise Combes, Anaëlle Halle, Barbara Mazzilli-Ciraulo and Anton Afanasiev for fruitful discussions. We thank the anonymous referee for suggestions on further investigating in non-parametric morphological diagnostics and enlarging the discussion on the merger rate, which supported our analysis and made it more solid. We thank Ivan Zolotukhin for his support in the early stage of this work. DM thanks Gabriele Gramelsberger, Dawid Kasprowicz, Lisa Schüttler, Daniel Wenz, Lukas Böhres and Frederic Kerksieck for supporting this work and for constructive discussions on software structure. We thank David Patton for providing the asymmetry parameter for SDSS galaxies and Helena Domínguez-Sánchez and Kanak Saha for helping with the morphological classification. We also thank Marina Trevisan for nice feedback on the discussion. IC is supported by Telescope Data Center at Smithsonian Astrophysical Observatory. IC and IK acknowledge the Russian Science Foundation grant 19-12-00281 and the Program of development of M.V. Lomonosov Moscow State University for the Leading Scientific School "Physics of stars, relativistic objects and galaxies". Rene Brun and Fons Rademakers, ROOT - An Object Oriented Data Analysis Framework, Proceedings AIHENP'96 Workshop, Lausanne, Sep. 1996, Nucl. Inst. & Meth. in Phys. Res. A 389 (1997) 81-86. See also http://root.cern.ch/. Funding for the Sloan Digital Sky Survey IV has been provided by the Alfred P. Sloan Foundation, the U.S. Department of Energy Office of Science, and the Participating Institutions. SDSS-IV acknowledges support and resources from the Center for High-Performance Computing at the University of Utah. The SDSS web site is www.sdss.org. SDSS-IV is managed by the Astrophysical Research Consortium for the Participating Institutions of the SDSS Collaboration including the Brazilian Participation Group, the Carnegie Institution for Science, Carnegie Mellon University, the Chilean Participation Group, the French Participation Group, Harvard-Smithsonian Center for Astrophysics, Instituto de Astrofísica de Canarias, The Johns Hopkins University, Kavli Institute for the Physics and Mathematics of the Universe (IPMU) / University of Tokyo, the Korean Participation Group, Lawrence Berkeley National Laboratory, Leibniz Institut für Astrophysik Potsdam (AIP), Max-Planck-Institut für Astronomie (MPIA Heidelberg), Max-Planck-Institut für Astrophysik (MPA Garching), Max-Planck-Institut für Extraterrestrische Physik (MPE), National Astronomical Observatories of China, New Mexico State University, New York University, University of Notre Dame, Observatário Nacional / MCTI, The Ohio State University, Pennsylvania State University, Shanghai Astronomical Observatory, United Kingdom Participation Group, Universidad Nacional Autónoma de México, University of Arizona, University of Colorado Boulder, University of Oxford, University of Portsmouth, University of Utah, University of Virginia, University of Washington, University of Wisconsin, Vanderbilt University, and Yale University. The Legacy Surveys (http://legacysurvey.org/) consist of three individual and complementary projects: the Dark Energy Camera Legacy Survey (DECaLS; NOAO Proposal ID # 2014B-0404; PIs: David Schlegel and Arjun Dey), the Beijing-Arizona Sky Survey (BASS; NOAO Proposal ID # 2015A-0801; PIs: Zhou Xu and Xiaohui Fan), and the Mayall z-band Legacy Survey (MzLS; NOAO Proposal ID # 2016A-0453; PI: Arjun Dey). DECaLS, BASS and MzLS together include data obtained, respectively, at the Blanco telescope, Cerro Tololo Inter-American Observatory, National Optical Astronomy Observatory (NOAO); the Bok telescope, Steward Observatory, University of Arizona; and the Mayall telescope, Kitt Peak National Observatory, NOAO. The Legacy Surveys project is honoured to be permitted to conduct astronomical research on Iolkam Du'ag (Kitt Peak), a mountain with particular significance to the Tohono O'odham Nation.

References

Abazajian, K. N., Adelman-McCarthy, J. K., Agüeros, M. A., et al. 2009, ApJS, 182, 543
Abraham, R. G., van den Bergh, S., & Nair, P. 2003, ApJ, 588, 218
Acker, A., Köppen, J., Samland, M., & Stenholm, B. 1989, The Messenger, 58, 44
Aquino-Ortíz, E., Valenzuela, O., Sánchez, S. F., et al. 2018, MNRAS, 479, 2133
Athanassoula, E. & Bosma, A. 1985, ARA&A, 23, 147
Avila-Reese, V., Zavala, J., Firmani, C., & Hernández-Toledo, H. M. 2008, AJ, 136, 1340
Bait, O., Barway, S., & Wadadekar, Y. 2017, MNRAS, 471, 2687
Baldwin, J. A., Phillips, M. M., & Terlevich, R. 1981, PASP, 93, 5
Balogh, M. L., Schade, D., Morris, S. L., et al. 1998, ApJ, 504, L75
Barnes, J. E. & Hernquist, L. E. 1991, ApJ, 370, L65
Bedregal, A. G., Aragón-Salamanca, A., & Merrifield, M. R. 2006, MNRAS, 373, 1125
Begelman, M. C., Blandford, R. D., & Rees, M. J. 1980, Nature, 287, 307
Bekki, K. 1998, ApJ, 502, L133
Bekki, K. & Couch, W. J. 2011, MNRAS, 415, 1783
Blanton, M. R. & Moustakas, J. 2009, ARA&A, 47, 159
Bond, J. R., Kofman, L., & Pogosyan, D. 1996, Nature, 380, 603
Bothun, G. D. & Dressler, A. 1986, ApJ, 301, 57
Bournaud, F., Jog, C. J., & Combes, F. 2005, A&A, 437, 69
Bournaud, F., Jog, C. J., & Combes, F. 2007, A&A, 476, 1179
Brinchmann, J., Charlot, S., White, S. D. M., et al. 2004, MNRAS, 351, 1151
Buta, R. & Combes, F. 1996, Fund. Cosmic Phys., 17, 95
Calistro Rivera, G., Williams, W. L., Hardcastle, M. J., et al. 2017, MNRAS, 469, 3468
Cappellari, M. 2013, ApJ, 778, L2
Cappellari, M. 2016, ARA&A, 54, 597
Catinella, B., Haynes, M. P., & Giovanelli, R. 2005, AJ, 130, 1037
Catinella, B., Kauffmann, G., Schiminovich, D., et al. 2012, MNRAS, 420, 1959
Chilingarian, I. V., Di Matteo, P., Combes, F., Melchior, A. L., & Semelin, B. 2010a, A&A, 518, A61
Chilingarian, I. V., Katkov, I. Y., Zolotukhin, I. Y., et al. 2018, ApJ, 863, 1
Chilingarian, I. V., Melchior, A.-L., & Zolotukhin, I. Y. 2010b, MNRAS, 405, 1409
Chilingarian, I. V., Novikova, A. P., Cayatte, V., et al. 2009, A&A, 504, 389
Chilingarian, I. V. & Zolotukhin, I. Y. 2012, MNRAS, 419, 1727
Chilingarian, I. V., Zolotukhin, I. Y., Katkov, I. Y., et al. 2017, ApJS, 228, 14
Combes, F., Young, L. M., & Bureau, M. 2007, MNRAS, 377, 1795
Comerford, J. M., Gerke, B. F., Newman, J. A., et al. 2009, ApJ, 698, 956
Comerford, J. M., Gerke, B. F., Stern, D., et al. 2012, ApJ, 753, 42
Comerford, J. M., Nevin, R., Stemo, A., et al. 2018, ApJ, 867, 66
Comerford, J. M., Pooley, D., Barrows, R. S., et al. 2015, ApJ, 806, 219
Comerford, J. M., Schluns, K., Greene, J. E., & Cool, R. J. 2013, ApJ, 777, 64
Comerón, S., Salo, H., Laurikainen, E., et al. 2014, A&A, 562, A121
Condon, J. J. 1992, ARA&A, 30, 575
Conselice, C. J. 2003, ApJS, 147, 1
Cortesi, A., Merrifield, M. R., Coccato, L., et al. 2013, MNRAS, 432, 1010
Cui, J., Xia, X. Y., Deng, Z. G., Mao, S., & Zou, Z. L. 2001, AJ, 122, 63

Davis, T. A., Greene, J., Ma, C.-P., et al. 2016, MNRAS, 455, 214
De Propris, R., Liske, J., Driver, S. P., Allen, P. D., & Cross, N. J. G. 2005, AJ, 130, 1516
Deane, R. P., Paragi, Z., Jarvis, M. J., et al. 2014, Nature, 511, 57
Dey, A., Schlegel, D. J., Lang, D., et al. 2019, AJ, 157, 168
Di Matteo, P., Combes, F., Melchior, A. L., & Semelin, B. 2007, A&A, 468, 61
Di Matteo, T., Springel, V., & Hernquist, L. 2005, Nature, 433, 604
Domínguez, A., Siana, B., Henry, A. L., et al. 2013, ApJ, 763, 145
Domínguez Sánchez, H., Huertas-Company, M., Bernardi, M., Tuccillo, D., & Fischer, J. L. 2018, MNRAS, 476, 3661
Dressler, A. 1980, ApJ, 236, 351
Dressler, A., Oemler, Augustus, J., Couch, W. J., et al. 1997, ApJ, 490, 577
Drory, N., MacDonald, N., Bershady, M. A., et al. 2015, AJ, 149, 77
Eliche-Moral, M. C., Rodríguez-Pérez, C., Borlaff, A., Querejeta, M., & Tapia, T. 2018, A&A, 617, A113
Elitzur, M., Asensio Ramos, A., & Ceccarelli, C. 2012, MNRAS, 422, 1394
Ellis, S. C., Driver, S. P., Allen, P. D., et al. 2005, MNRAS, 363, 1257
Ellison, S. L., Nair, P., Patton, D. R., et al. 2011a, MNRAS, 416, 2182
Ellison, S. L., Patton, D. R., Mendel, J. T., & Scudder, J. M. 2011b, MNRAS, 418, 2043
Ellison, S. L., Patton, D. R., Simard, L., & McConnachie, A. W. 2008, AJ, 135, 1877
Ellison, S. L., Patton, D. R., Simard, L., et al. 2010, MNRAS, 407, 1514
Faber, S. M. & Jackson, R. E. 1976, ApJ, 204, 668
Fabian, A. C. 2012, ARA&A, 50, 455
Fasano, G., Poggianti, B. M., Couch, W. J., et al. 2000, ApJ, 542, 673
Fisher, R. A. 1954, Statistical methods for research workers; 20th ed. (Edinburgh: Oliver and Boyd)
Fraser-McKelvie, A., Aragón-Salamanca, A., Merrifield, M., et al. 2018, MNRAS, 481, 5580
Fu, H., Myers, A. D., Djorgovski, S. G., et al. 2015, ApJ, 799, 72
Gallazzi, A., Charlot, S., Brinchmann, J., & White, S. D. M. 2006, MNRAS, 370, 1106
Gao, H., Ho, L. C., Barth, A. J., & Li, Z.-Y. 2018, ApJ, 862, 100
Ge, J.-Q., Hu, C., Wang, J.-M., Bai, J.-M., & Zhang, S. 2012, ApJS, 201, 31
Genzel, R., Tacconi, L. J., Rigopoulou, D., Lutz, D., & Tecza, M. 2001, ApJ, 563, 527
Gilli, R., Vignali, C., Mignoli, M., et al. 2010, A&A, 519, A92
Goulding, A. D., Pardo, K., Greene, J. E., et al. 2019, ApJ, 879, L21
Green, P. J., Myers, A. D., Barkhouse, W. A., et al. 2010, ApJ, 710, 1578
Greene, J. E. & Ho, L. C. 2005, ApJ, 627, 721
Hani, M. H., Gosain, H., Ellison, S. L., Patton, D. R., & Torrey, P. 2020, MNRAS, 493, 3716
Heckman, T. M., Miley, G. K., van Breugel, W. J. M., & Butcher, H. R. 1981, ApJ, 247, 403
Helou, G., Soifer, B. T., & Rowan-Robinson, M. 1985, ApJ, 298, L7
Hogg, D. W., Blanton, M., Strateva, I., et al. 2002, AJ, 124, 646
Ilyina, M. A., Sil'chenko, O. K., & Afanasiev, V. L. 2014, MNRAS, 439, 334
Kannappan, S. J. 2004, ApJ, 611, L89
Kannappan, S. J., Guie, J. M., & Baker, A. J. 2009, AJ, 138, 579
Karouzos, M., Woo, J.-H., & Bae, H.-J. 2016, ApJ, 819, 148
Katkov, I. Y., Kniazev, A. Y., & Sil'chenko, O. K. 2015, AJ, 150, 24
Katkov, I. Y., Sil'chenko, O. K., & Afanasiev, V. L. 2013, ApJ, 769, 105
Katkov, I. Y., Sil'chenko, O. K., & Afanasiev, V. L. 2014, MNRAS, 438, 2798
Katkov, I. Y., Sil'chenko, O. K., Chilingarian, I. V., Uklein, R. I., & Egorov, O. V. 2016, MNRAS, 461, 2068
Kauffmann, G., Heckman, T. M., White, S. D. M., et al. 2003, MNRAS, 341, 33
Kaviraj, S. 2014, MNRAS, 440, 2944
Kennicutt, Robert C., J. 1989, ApJ, 344, 685
Kewley, L. J., Dopita, M. A., Sutherland, R. S., Heisler, C. A., & Trevena, J. 2001, ApJ, 556, 121
Kewley, L. J., Geller, M. J., & Barton, E. J. 2006a, AJ, 131, 2004
Kewley, L. J., Geller, M. J., Jansen, R. A., & Dopita, M. A. 2002, AJ, 124, 3135
Kewley, L. J., Groves, B., Kauffmann, G., & Heckman, T. 2006b, MNRAS, 372, 961
Knapp, G. R., van Driel, W., Schwarz, U. J., van Woerden, H., & Gallagher, J. S., I. 1984, A&A, 133, 127
Knapp, G. R., van Driel, W., & van Woerden, H. 1985, A&A, 142, 1
Kohandel, M., Pallottini, A., Ferrara, A., et al. 2019, MNRAS, 487, 3007
Kormendy, J. & Bender, R. 2012, ApJS, 198, 2
Koss, M., Mushotzky, R., Treister, E., et al. 2012, ApJ, 746, L22
Koss, M. J., Blecha, L., Bernhard, P., et al. 2018, Nature, 563, 214
Koss, M. J., Glidden, A., Baloković, M., et al. 2016, ApJ, 824, L4
Krumm, N., van Driel, W., & van Woerden, H. 1985, A&A, 144, 202
Laigle, C., Pichon, C., Arnouts, S., et al. 2018, MNRAS, 474, 5437
Lee, K.-G., Krolewski, A., White, M., et al. 2018, ApJS, 237, 31
Li, C., Kauffmann, G., Heckman, T. M., Jing, Y. P., & White, S. D. M. 2008, MNRAS, 385, 1903
Liu, X., Civano, F., Shen, Y., et al. 2013, ApJ, 762, 110
Liu, X., Shen, Y., Strauss, M. A., & Greene, J. E. 2010, ApJ, 708, 427
Liu, X., Shen, Y., Strauss, M. A., & Hao, L. 2011, ApJ, 737, 101
Lotz, J. M., Davis, M., Faber, S. M., et al. 2008, ApJ, 672, 177
Lotz, J. M., Jonsson, P., Cox, T. J., & Primack, J. R. 2010a, MNRAS, 404, 590
Lotz, J. M., Jonsson, P., Cox, T. J., & Primack, J. R. 2010b, MNRAS, 404, 575
Lotz, J. M., Primack, J., & Madau, P. 2004, AJ, 128, 163
Macchetto, F., Pastoriza, M., Caon, N., et al. 1996, A&AS, 120, 463
Mapelli, M., Rampazzo, R., & Marino, A. 2015, A&A, 575, A16
Maschmann, D. & Melchior, A.-L. 2019, A&A, 627, L3
Meert, A., Vikram, V., & Bernardi, M. 2015, MNRAS, 446, 3943
Mendenhall, W. & Sincich, T. 2011, A Second Course in Statistics: Regression Analysis (Pearson Education)
Mo, H. J., Mao, S., & White, S. D. M. 1998, MNRAS, 295, 319
Molaeinezhad, A., Zhu, L., Falcón-Barroso, J., et al. 2019, MNRAS, 488, 1012
Müller-Sánchez, F., Comerford, J. M., Nevin, R., et al. 2015, ApJ, 813, 103
Nevin, R., Blecha, L., Comerford, J., & Greene, J. 2019, ApJ, 872, 76
Nevin, R., Comerford, J., Müller-Sánchez, F., Barrows, R., & Cooper, M. 2016, ApJ, 832, 67
Nevin, R., Comerford, J. M., Müller-Sánchez, F., Barrows, R., & Cooper, M. C. 2018, MNRAS, 473, 2160
Osterbrock, D. E. & Ferland, G. J. 2006, Astrophysics of gaseous nebulae and active galactic nuclei
Patton, D. R., Ellison, S. L., Simard, L., McConnachie, A. W., & Mendel, J. T. 2011, MNRAS, 412, 591
Patton, D. R., Qamar, F. D., Ellison, S. L., et al. 2016, MNRAS, 461, 2589
Patton, D. R., Torrey, P., Ellison, S. L., Mendel, J. T., & Scudder, J. M. 2013, MNRAS, 433, L59
Pawlik, M. M., Wild, V., Walcher, C. J., et al. 2016, MNRAS, 456, 3032
Petrosian, V. 1976, ApJ, 210, L53
Pfeifle, R. W., Satyapal, S., Manzano-King, C., et al. 2019, ApJ, 883, 167
Pimbblet, K. A., Smail, I., Kodama, T., et al. 2002, MNRAS, 331, 333
Pizzella, A., Morelli, L., Coccato, L., et al. 2018, A&A, 616, A22
Pogge, R. W. & Eskridge, P. B. 1993, AJ, 106, 1405
Proshina, I. S., Kniazev, A. Y., & Sil'chenko, O. K. 2019, AJ, 158, 5
Querejeta, M., Eliche-Moral, M. C., Tapia, T., et al. 2015, A&A, 579, L2
Rawle, T. D., Lucey, J. R., Smith, R. J., & Head, J. T. C. G. 2013, MNRAS, 433, 2667
Riffel, R. A., Storchi-Bergmann, T., & Riffel, R. 2014, ApJ, 780, L24
Rodriguez-Gomez, V., Snyder, G. F., Lotz, J. M., et al. 2019, MNRAS, 483, 4140
Rupke, D. S. N. & Veilleux, S. 2013, ApJ, 768, 75
Salim, S. 2014, Serbian Astronomical Journal, 189, 1
Salim, S., Lee, J. C., Janowiecki, S., et al. 2016, ApJS, 227, 2
Salim, S., Rich, R. M., Charlot, S., et al. 2007, ApJS, 173, 267
Sanders, D. B. & Mirabel, I. F. 1996, ARA&A, 34, 749
Sarron, F., Adami, C., Durret, F., & Laigle, C. 2019, A&A, 632, A49
Sarzi, M., Falcón-Barroso, J., Davies, R. L., et al. 2006, MNRAS, 366, 1151
Saulder, C., van Kampen, E., Chilingarian, I. V., Mieske, S., & Zeilinger, W. W. 2016, A&A, 596, A14
Schawinski, K., Thomas, D., Sarzi, M., et al. 2007, MNRAS, 382, 1415
Schiminovich, D., Wyder, T. K., Martin, D. C., et al. 2007, ApJS, 173, 315
Schirmer, M., Diaz, R., Holhjem, K., Levenson, N. A., & Winge, C. 2013, ApJ, 763, 60
Schneider, D. P., Richards, G. T., Hall, P. B., et al. 2010, AJ, 139, 2360
Shimwell, T. W., Tasse, C., Hardcastle, M. J., et al. 2019, A&A, 622, A1
Sil'chenko, O., Kostiuk, I., Burenkov, A., & Parul, H. 2018, A&A, 620, L7
Sil'chenko, O. K. 2016, AJ, 152, 73
Sil'chenko, O. K. & Afanasiev, V. L. 2004, AJ, 127, 2641
Silk, J. 1997, ApJ, 481, 703
Sil'chenko, O. K., Moiseev, A. V., & Egorov, O. V. 2019, ApJS, 244, 6
Smith, K. L., Shields, G. A., Bonning, E. W., et al. 2010, ApJ, 716, 866
Somerville, R. S. & Davé, R. 2015, ARA&A, 53, 51
Strateva, I., Ivezić, Ž., Knapp, G. R., et al. 2001, AJ, 122, 1861
Tammour, A., Gallagher, S. C., & Richards, G. 2015, MNRAS, 448, 3354
Tapia, T., Eliche-Moral, M. C., Aceves, H., et al. 2017, A&A, 604, A105
Tous, J. L., Solanes, J. M., & Perea, J. D. 2020, MNRAS[arXiv:2005.09016]
Tremonti, C. A., Heckman, T. M., Kauffmann, G., et al. 2004, ApJ, 613, 898
Tully, R. B. & Fisher, J. R. 1977, A&A, 54, 661
van den Bergh, S. 1976, ApJ, 206, 883
van Dokkum, P. G., Nelson, E. J., Franx, M., et al. 2015, ApJ, 813, 23
van Driel, W., van Woerden, H., Gallagher, J. S., I., & Schwarz, U. J. 1988, A&A, 191, 201
van Gorkom, J. H., Schechter, P. L., & Kristian, J. 1987, ApJ, 314, 457
van Woerden, H., van Driel, W., & Schwarz, U. J. 1983, in IAU Symposium, Vol. 100, Internal Kinematics and Dynamics of Galaxies, ed. E. Athanassoula, 99–104
Vergani, D., Garilli, B., Polletta, M., et al. 2018, A&A, 620, A193
Walker, I. R., Mihos, J. C., & Hernquist, L. 1996, ApJ, 460, 121
Wang, J.-M., Chen, Y.-M., Hu, C., et al. 2009, ApJ, 705, L76
Wang, L., Gao, F., Duncan, K. J., et al. 2019a, A&A, 631, A109
Wang, M. X., Luo, A. L., Song, Y. H., et al. 2019b, MNRAS, 482, 1889
White, R. L., Becker, R. H., Helfand, D. J., & Gregg, M. D. 1997, ApJ, 475, 479
Whitmore, B. C., Gilmore, D. M., & Jones, C. 1993, ApJ, 407, 489
Whitmore, B. C., Lucas, R. A., McElroy, D. B., et al. 1990, AJ, 100, 1489
Whittle, M. 1985, MNRAS, 213, 1
Willett, K. W., Lintott, C. J., Bamford, S. P., et al. 2013, MNRAS, 435, 2835
Wilman, D. J., Oemler, A., J., Mulchaey, J. S., et al. 2009, ApJ, 692, 298
Woo, J.-H., Bae, H.-J., Son, D., & Karouzos, M. 2016, ApJ, 817, 108
Woo, J.-H., Urry, C. M., Lira, P., van der Marel, R. P., & Maza, J. 2004, ApJ, 617, 903
Xiao, M.-Y., Gu, Q.-S., Chen, Y.-M., & Zhou, L. 2016, ApJ, 831, 63
Yang, X., Mo, H. J., van den Bosch, F. C., et al. 2007, ApJ, 671, 153
Yip, C.-W., Szalay, A. S., Wyse, R. F. G., et al. 2010, ApJ, 709, 780
Zhang, H., Zaritsky, D., Werk, J., & Behroozi, P. 2018, ApJ, 866, L4

Table A.1. Contingency table for galaxy types

Type	DPS	NBCS	P-value
SF	2534(44.7%)	2811(54.8%)	1.66e-25
COMP	2153(38.0%)	1226(23.9%)	1.13e-56
AGN	630(11.1%)	687(13.4%)	3.27e-04
LINER	174(3.1%)	308(6.0%)	1.56e-13
LTG	914(16.1%)	1539(30.0%)	2.90e-66
ETG	167(2.9%)	134(2.6%)	2.93e-01
S0	2027(35.8%)	1009(19.7%)	2.11e-78
Merger	589(10.4%)	487(9.5%)	1.23e-01

Notes: We present the fraction of BPT and morphological classification for the DPS and the NBCS and the corresponding p-value.

Appendix A: Statistical significance of contingency tables

In Sect. 3.1 and 3.2, we identified some differences between the DPS and the NBCS. Due to the number of different categories, it is difficult to quantitatively conclude how significant these differences are. Therefore, we used Fisher's exact test (Fisher 1954) to check some selected categories and evaluate a p-value to determine how significant the differences between the DPS and the NBCS are. The p-value represents the probability that the measured fraction of one galaxy type is originating from the same parent sample

From the BPT classification, we used the SF, COMP, AGN and LINER categories. For the DPS, we use the non-parametric fit (see Sect. 3.1). For the morphological classification, we examined LTG, elliptical, S0 and galaxy mergers.

For Fisher's exact test, we took the number of the above mentioned categories c_{DPS} and c_{NBCS} of each sample and consider the objects which are not in this category as the counterpart $\bar{c}_{DPS,NBCS}$. We calculated the p-value following (Fisher 1954) as:

$$p_c = \frac{\binom{c_{DPS}+c_{NBCS}}{c_{DPS}}\binom{\bar{c}_{DPS}+\bar{c}_{NBCS}}{\bar{c}_{DPS}}}{\binom{n_{DPS}+n_{NBCS}}{c_{DPS}+\bar{c}_{DPS}}} \quad (A.1)$$

where n_{DPS} and n_{NBCS} are the total numbers of objects in the samples and $\binom{a}{b}$ denotes the binomial coefficient.

In Table A.1, we present the different classification with their percentage of occurrence and the corresponding p-value. For a sub-sample with a p-value smaller than 0.05, we consider the two parent samples as significantly different. From this table, we can conclude that the lack of SF or LINER and the excess of COMP galaxies in the DPS is significant. Also the fraction of LTG and S0 galaxies are significantly different for the two samples. We also find that the two samples show very similar fractions of galaxy merger and elliptical galaxies.

Appendix B: Non-parametric merger indicators

It is challenging to identify late merger stages directly from imaging observations, since merging signatures are depend strongly on the mass ratio and the initial conditions. As discussed in Sect. 4.5, the combination of Gini-M_{20} diagnostics is a powerful tool (Lotz et al. 2008), but which is strongly modulated by time (Lotz et al. 2010b,a). A promising method to achieve a higher sensitivity to detect a larger range of minor and major merger stages was proposed by Nevin et al. (2019), using a supervised Linear Decomposition Analysis (LDA). As input, they used non-parametric imaging predictors such as the CAS-statistics, the Gini and M_{20} coefficients and the shape asymmetry (A_S) computed by STATMORPH (Rodriguez-Gomez et al. 2019). Using hydodynamical simulations of galaxy merger with different mass ratios, they reached a high accuracy of 85 % (resp. 81 %) and a precision of 97 % (resp. 94 %) for major (resp. minor) merger scenarios.

Nevin et al. (2019) focused on galaxies such as those observed with the SDSS MaNGA survey (Drory et al. 2015), whose average redshift is $\langle z \rangle \sim 0.03$. To keep a statistically significant sample, we restricted the merger identification analysis on subsets of the DPS and the NBCS with $z < 0.075$. We used the predictor inputs computed by STATMORPH as described in Sect. 4.5 and computed the predictor coefficients $LD1_{major}$ and $LD1_{minor}$ for major and minor mergers as described in Nevin et al. (2019):

$$\begin{aligned} LD1_{major} = & -0.81 + 0.69\,\mathrm{Gini} + 3.84\,C + 5.78\,A + 13.14\,A_S \\ & - 3.68\,\mathrm{Gini}\times A_S - 6.5\,C\times A_S - 6.12\,A\times A_S \end{aligned}$$

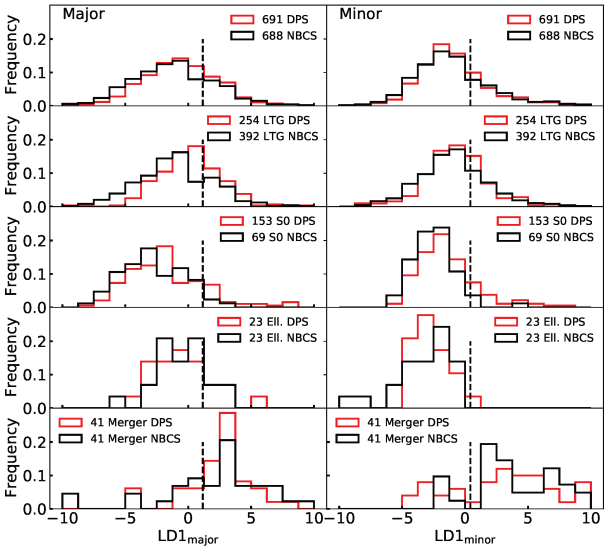

Fig. B.1. Distribution of predictor coefficients $LD1_{major}$ on the left panels and $LD1_{minor}$ on the right panels (Nevin et al. 2019) for galaxies with $z < 0.075$. We mark the decision boundary for $LD1_{major}$ (resp. $LD1_{minor}$) with black dashed lines at > 1.16 (resp. > 0.42). We show the DPS in red lines and NBCS in black lines. We show all galaxies in the top panels and present LTG, S0, elliptical and merger galaxies in the lower panels respectively.

Table B.1. Merger rate estimation using $LD1_{major}$ and $LD1_{minor}$

Type	DPS		NBCS	
	major	minor	major	minor
total	26.9%	18.5%	25.1%	21.1%
LTG	31.5%	18.9%	24.5%	20.4%
S0	15.7%	11.8%	4.3%	1.4%
Elliptical	21.7%	4.3%	21.7%	0.0%
Merger	78.0%	70.7%	75.6%	87.8%

Notes: We present the computed major and minor merger rate using the predictor coefficients $LD1_{major}$ and $LD1_{minor}$ for galaxies with $z < 0.075$ of the DPS and the NBCS (Nevin et al. 2019). The distributions are shown in Fig. B.1. We present also the merger rates for different morphological types (See Sect. 3.2).

$$\mathrm{LD1_{minor}} = -0.87 + 8.64\,\mathrm{Gini} + 14.22\,C + 5.21\,A + 2.53\,A_S - 20.33\,\mathrm{Gini}\times C - 4.32\,A\times A_S$$

We standardised the predictor inputs: we subtracted the mean for each predictor and divide it by the standard deviation. To compute the means and the standard deviations, we used all the galaxies we want to test, meaning the DPS and the NBCS. To separate mergers and non-mergers, the decision boundary for $\mathrm{LD1_{major}}$ (resp. $\mathrm{LD1_{minor}}$) is > 1.16 (resp. > 0.42).

Since we only considered galaxies with a redshift of $z < 0.075$, we classify only 23 elliptical and 41 merger galaxies of the DPS and the NBCS, which is due to the redshift distribution of these sub-samples (see Fig. 8). This makes it difficult to conclude on the measured merger rate of these two sub-samples.

In Fig. B.1, we show the predictor coefficients $\mathrm{LD1_{major}}$ and $\mathrm{LD1_{minor}}$ for different morphological types of the DPS and the NBCS and display the decision boundary for each predictor as a black dashed line. We present the merger rates for DPS and the NBCS and different morphological classifications in Table B.1. In comparison to the merger rate found in Sect. 3.2, we indeed find a slightly higher major merger rate of 27 % for the DPS and 25 % for the NBCS and a slightly higher minor merger rate of 19 % for the DPS and 21 % for the NBCS. This diagnostic is also in good agreement with the merger selection based on Domínguez Sánchez et al. (2018)(See Sect. 3.2): visual merger are classified as major merger with a rate of 78 % (DPS) and 76 % (NBCS) using the LDA-method.

LTGs, which are detected at lower redshift in the DPS and the NBCS, build up the largest sub-sample with 254 of the DPS and 392 of the NBCS. We find indeed a higher major-merger rate of 32 % for the DPS in comparison to the NBCS with 25 %, whereas we find a slightly lower minor-merger rate for the DPS of 19 % in comparison to 21 % for the NBCS. For S0 galaxies, we find a higher major (16 %) and minor (12 %) merger rate for the DPS in comparison to the NBCS (4 % and 1 % respectively).

In our merger scenario for double-peak emission line galaxies (see Sect. 6), we do not find the expected merger rates using the LDA-method. This may be explained by DPS galaxies being past the coalescence phase, while the method developed by Nevin et al. (2019) is not sensitive to faded and later stages of mergers.

Appendix C: Characteristic parameter distributions

As discussed in Sect. 4.2, we detect higher SFRs inside the SDSS fibre for the DPS in comparison to the NBCS. We find comparable total SFRs and about the same stellar mass distribution. As discussed in Sect. 4.1, we detect more extinction for the DPS in comparison to the NBCS with an excess of about 0.25 mag in the V band. We furthermore find comparable stellar ages for the DPS and the NBCS, comparable time scales and about the same stellar and gas metallicities.

With respect to the morphological classifications, we detect significant differences between the DPS and the NBCS in two subsamples, namely Sb-d and elliptical galaxies. Sb-d galaxies of the DPS show higher mean stellar masses ($\sim$ 0.2 dex in $\log(M_*/M_\odot)$) and extinction ($\sim$ 0.3 mag in V) than Sb-d galaxies of the NBCS (Fig. C.1). Furthermore, we detect a significant excess of SF in the centre of DP Sb-d galaxies. We detect $\mathrm{SFR_{fibre}/SFR_{total}} = 0.59^{+0.30}_{-0.31}$ for Sb-d of the DPS and $\mathrm{SFR_{fibre}/SFR_{total}} = 0.31^{+0.20}_{-0.16}$ for the NBCS. In the case of elliptical galaxies, we detect a 4 times higher SFR in the DPS in comparison to their NBCS counterpart (Fig. C.1). This is consistent with the fact that elliptical DP galaxies are situated in the main star forming sequence, whereas elliptical galaxies of the NBCS are associated with the quenched red sequence (see Sect. 4.2). Assuming a single stellar population, we find that elliptical galaxies with a DP have on average a 3 Gyr younger stellar population in comparison with those showing a single peak. Similarly, assuming an exponential declining star formation history, we detect two times larger time scales for DP elliptical galaxies.

Appendix D: Additional material

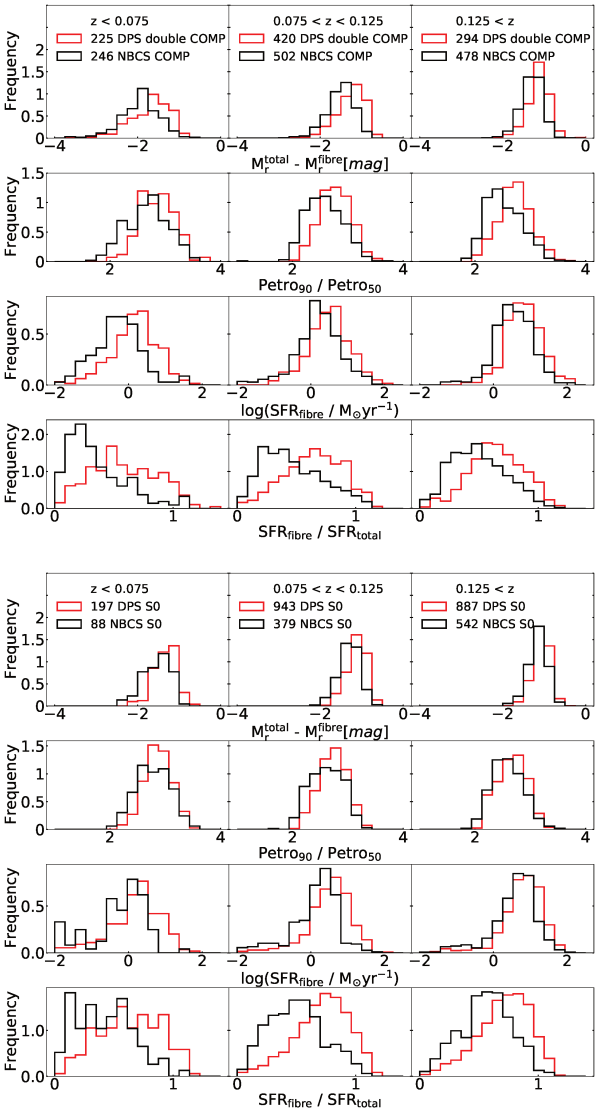

Fig. D.1. Comparison of absolute r-band magnitude, Petrosian radii and ($\mathrm{SFR_{fibre}}$) and ($\mathrm{SFR_{total}}$) as in Fig. 13, but with DP galaxies classified as COMP in both peak components (red) and galaxies of the NBCS classified as COMP (black) in the upper panels and galaxies classified as S0s in the lower panel.

Table D.1. Fraction of cross match for different BPT and morphological types

BPT - class	LTG	Elliptical	S0	Merger	Uncertain	Total
DP- sample						
SF	326(12.9%)	54(2.1%)	990(39.1%)	266(10.5%)	898(35.4%)	2534
COMP	431(20.0%)	69(3.2%)	715(33.2%)	208(9.7%)	730(33.9%)	2153
AGN	103(16.3%)	24(3.8%)	204(32.4%)	77(12.2%)	222(35.2%)	630
LINER	29(16.7%)	13(7.5%)	53(30.5%)	22(12.6%)	57(32.8%)	174
Uncertain	25(14.5%)	7(4.1%)	65(37.8%)	16(9.3%)	59(34.3%)	172
No-bias Control sample						
SF	873(31.1%)	23(0.8%)	539(19.2%)	245(8.7%)	1131(40.2%)	2811
COMP	388(31.6%)	41(3.3%)	266(21.7%)	116(9.5%)	415(33.8%)	1226
AGN	177(25.8%)	29(4.2%)	129(18.8%)	80(11.6%)	272(39.6%)	687
LINER	76(24.7%)	38(12.3%)	56(18.2%)	35(11.4%)	103(33.4%)	308
Uncertain	25(26.0%)	3(3.1%)	19(19.8%)	11(11.5%)	38(39.6%)	96
Control sample						
SF	18510(22.6%)	120(0.1%)	5328(6.5%)	5934(7.2%)	52173(63.6%)	82065
COMP	1123(23.8%)	76(1.6%)	1229(26.0%)	360(7.6%)	1933(40.9%)	4721
AGN	331(20.4%)	46(2.8%)	418(25.8%)	138(8.5%)	690(42.5%)	1623
LINER	122(22.8%)	56(10.4%)	106(19.8%)	49(9.1%)	203(37.9%)	536
Uncertain	71(15.2%)	4(0.9%)	64(13.7%)	43(9.2%)	285(61.0%)	467

Notes: This is a cross match of Tables 4 and 5. We present the fraction of each morphological type for all different subsets classified with the BPT diagram in Sect. 3.1. For the DPS we show the BPT-classification using the non-parametric fit. We present these fractions for the DPS, the NBCS and the CS. All rows add up to unity.

Table D.2. Fraction of cross match for different BPT and morphological types

BPT - class	LTG	Elliptical	S0	Merger	Uncertain
DP- sample					
SF	326(35.7%)	54(32.3%)	990(48.8%)	266(45.2%)	898(45.7%)
COMP	431(47.2%)	69(41.3%)	715(35.3%)	208(35.3%)	730(37.1%)
AGN	103(11.3%)	24(14.4%)	204(10.1%)	77(13.1%)	222(11.3%)
LINER	29(3.2%)	13(7.8%)	53(2.6%)	22(3.7%)	57(2.9%)
Uncertain	25(2.7%)	7(4.2%)	65(3.2%)	16(2.7%)	59(3.0%)
Total	914	167	2027	589	1966
No-bias Control sample					
SF	873(56.7%)	23(17.2%)	539(53.4%)	245(50.3%)	1131(57.7%)
COMP	388(25.2%)	41(30.6%)	266(26.4%)	116(23.8%)	415(21.2%)
AGN	177(11.5%)	29(21.6%)	129(12.8%)	80(16.4%)	272(13.9%)
LINER	76(4.9%)	38(28.4%)	56(5.6%)	35(7.2%)	103(5.3%)
Uncertain	25(1.6%)	3(2.2%)	19(1.9%)	11(2.3%)	38(1.9%)
Total	1539	134	1009	487	1959
Control sample					
SF	18510(91.8%)	120(39.7%)	5328(74.6%)	5934(91.0%)	52173(94.4%)
COMP	1123(5.6%)	76(25.2%)	1229(17.2%)	360(5.5%)	1933(3.5%)
AGN	331(1.6%)	46(15.2%)	418(5.9%)	138(2.1%)	690(1.2%)
LINER	122(0.6%)	56(18.5%)	106(1.5%)	49(0.8%)	203(0.4%)
Uncertain	71(0.4%)	4(1.3%)	64(0.9%)	43(0.7%)	285(0.5%)
Total	20157	302	7145	6524	55284

Notes: This is a cross match of Tables 4 and 5. We present the fraction of each subset classified with the BPT diagram in Sect. 3.1 for all different morphological type specified in Sect. 3.2. For the DPS we show the BPT-classification using the non-parametric fit. We present these fractions for the DPS, the CS and the NBCS. All columns add up to unity.

Table D.3. Galaxy environment

	LTG	S0	Elliptical	Merger	Uncertain	LTG	S0	Elliptical	Merger	Uncertain
Yang et al. (2007)			DPS					NBCS		
isolated	59.7 %	68.6 %	56.3 %	54.0 %	63.4 %	65.7 %	67.6 %	47.8 %	58.1 %	67.9 %
poor group	24.3 %	16.6 %	29.3 %	25.0 %	16.0 %	21.0 %	15.0 %	25.4 %	25.9 %	13.3 %
rich group	5.0 %	2.4 %	6.0 %	3.6 %	2.8 %	4.6 %	3.9 %	11.2 %	3.3 %	3.4 %
cluster	6.1 %	2.4 %	3.0 %	4.2 %	3.3 %	4.5 %	2.2 %	10.4 %	4.5 %	3.4 %
unknown	4.8 %	10.1 %	5.4 %	13.2 %	14.5 %	4.2 %	11.4 %	5.2 %	8.2 %	12.0 %
Yang et al. (2007) (z < 0.11)			DPS					NBCS		
isolated	54.8 %	65.2 %	50.9 %	43.6 %	62.5 %	62.8 %	66.9 %	39.1 %	48.3 %	65.1 %
poor group	28.1 %	23.0 %	34.3 %	33.3 %	20.2 %	22.4 %	20.1 %	28.7 %	32.8 %	15.1 %
rich group	5.1 %	2.8 %	8.3 %	6.7 %	3.6 %	5.8 %	6.1 %	14.9 %	5.0 %	6.0 %
cluster	7.7 %	4.6 %	3.7 %	9.3 %	6.8 %	6.2 %	4.7 %	13.8 %	9.5 %	6.6 %
unknown	4.4 %	4.4 %	2.8 %	7.1 %	7.0 %	2.9 %	2.3 %	3.4 %	4.5 %	7.2 %
Saulder et al. (2016) (z < 0.11)			DPS					NBCS		
isolated	38.2 %	51.1 %	35.2 %	36.4 %	44.0 %	43.5 %	48.8 %	27.6 %	33.3 %	45.7 %
poor group	37.0 %	29.2 %	38.0 %	31.1 %	33.0 %	32.8 %	31.7 %	29.9 %	38.8 %	31.1 %
rich group	12.7 %	9.5 %	11.1 %	13.8 %	9.5 %	11.1 %	10.5 %	20.7 %	11.4 %	10.6 %
cluster	10.7 %	6.7 %	12.0 %	8.9 %	10.0 %	11.0 %	8.1 %	20.7 %	11.9 %	9.8 %
unknown	1.5 %	3.4 %	3.7 %	9.8 %	3.6 %	1.5 %	0.9 %	1.1 %	4.5 %	2.8 %

Notes: Fraction of galaxies in different environments from Yang et al. (2007) and Saulder et al. (2016)

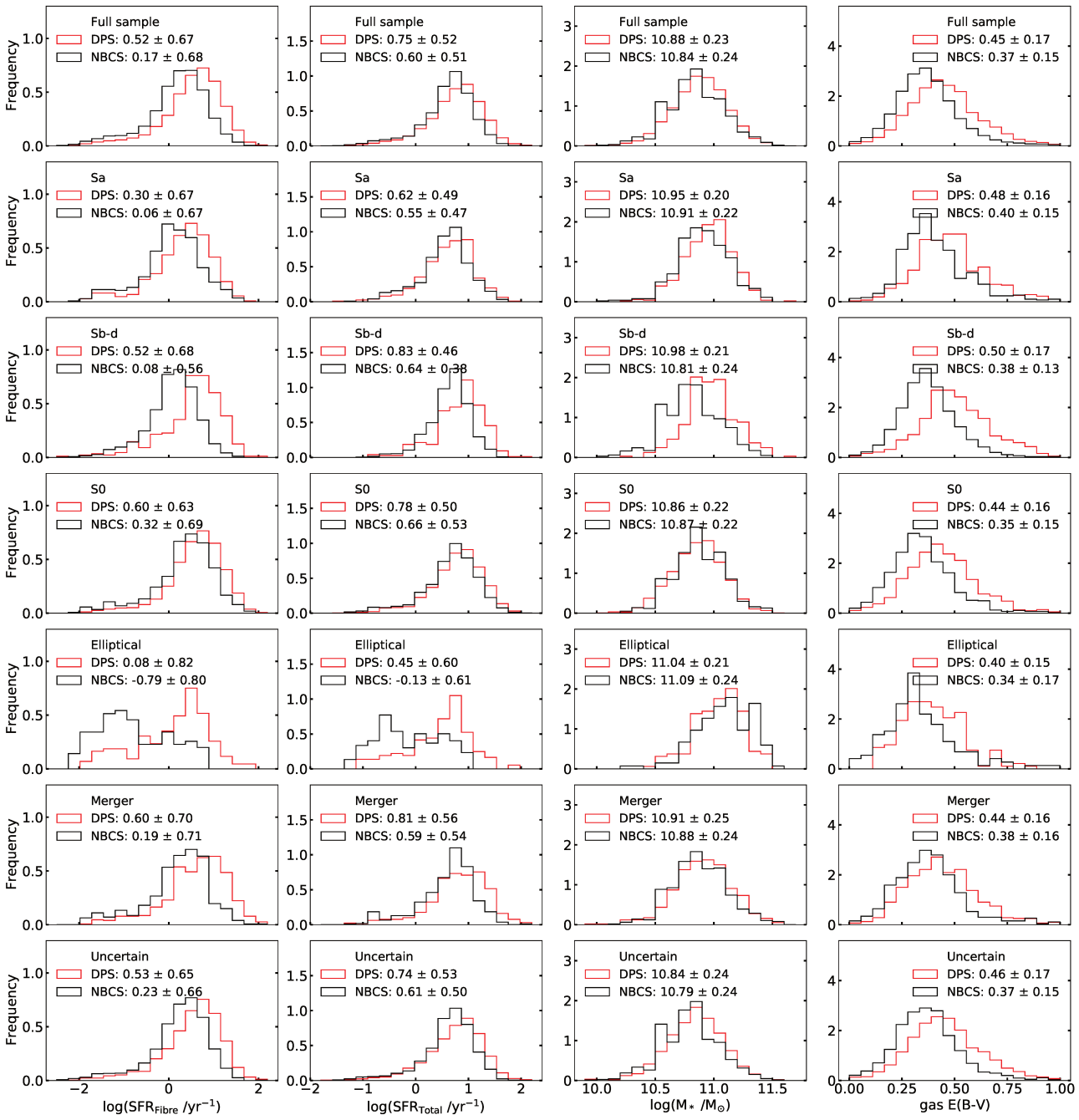

Fig. C.1. Each column presents distributions of different parameters of the DPS (red) and the NBCS (black). We show different morphological classifications in each row: in the top row the full samples, followed by Sa, Sb-d, S0s, elliptical, merger and galaxies without classification (see Sect. 3.2). From left to right: the first column shows the star formation rate inside the 3″ SDSS fibre (SFR_{fibre}), the second column the total star formation rate (SFR_{Total}) (Brinchmann et al. 2004) and the third column the stellar mass M_* (Kauffmann et al. 2003). In the last column, we present the extinction computed with the Balmer decrements Hα/Hβ (Domínguez et al. 2013). We use the non-parametric emission line fit to estimate emission line fluxes taken from Chilingarian et al. (2017). We display the mean and the standard deviation for each distribution.

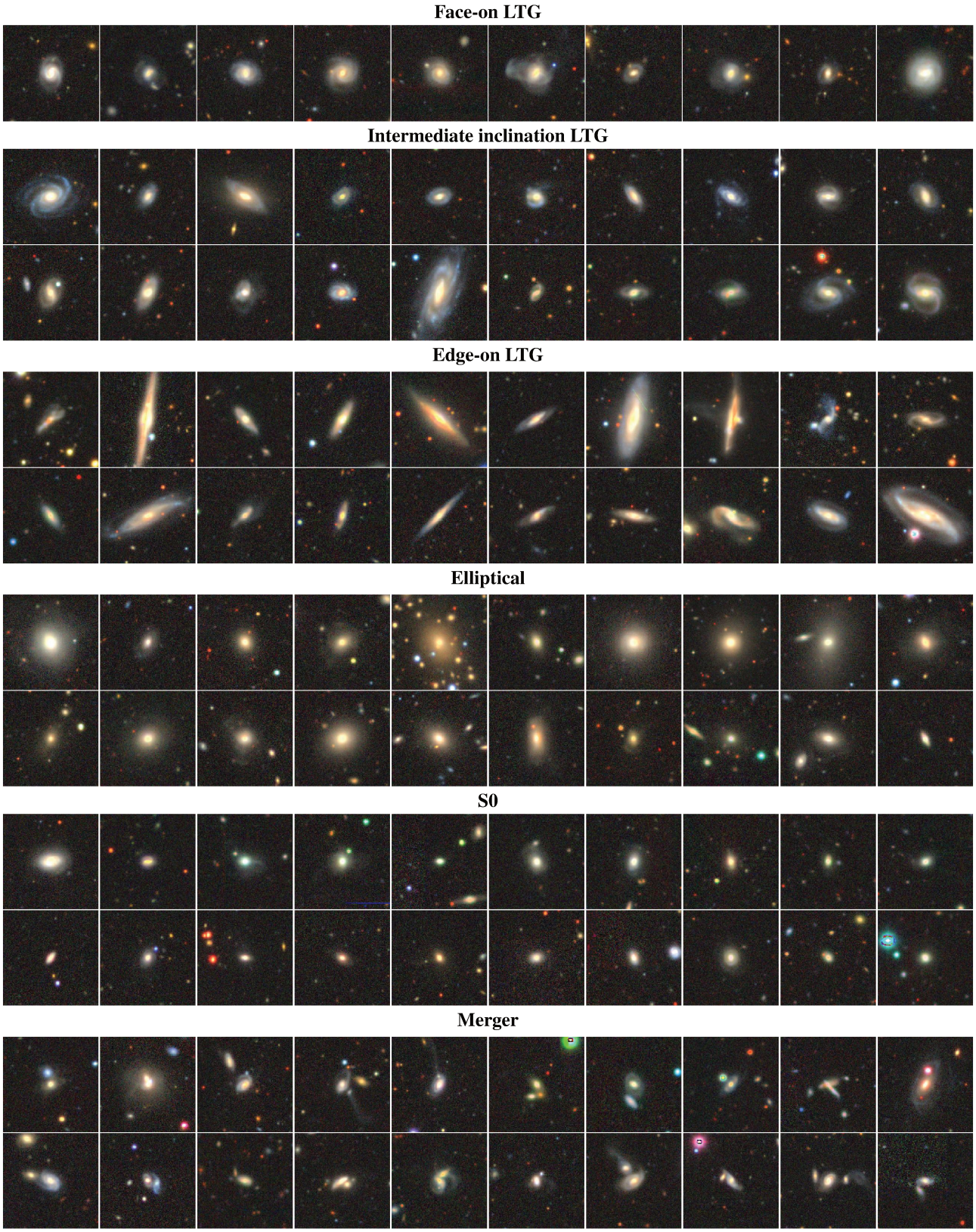

Fig. D.2. 62″ × 62″ Legacy Survey snapshots (Dey et al. 2019) of 20 random galaxies of each morphological type, described in Sect. 3.2 (all 10 are shown for Face-on LTGs).

CHAPTER 3

Double-peak emission lines in modelled and simulated galaxies

Observations of double-peak (DP) emission-line galaxies can already provide important insights on their possible origin. With follow-up observation providing higher resolution one can in some cases even pinpoint the underlying mechanism of an observed DP signature. However, a basic understanding of these mechanisms also requires that they can be reproduced numerically. By doing so, one can refine theories more precisely, explore further possibilities and find more aspects to discuss in observations. To get a better understanding of fundamental kinematic mechanisms that can create a DP emission-line signature, I analysed DP signatures created with axisymmetric disc models and galaxy simulations. This work is gathered in a journal article which is accepted to A&A (Maschmann et al. 2022a).

I computed synthetic SDSS-like spectroscopic emission-line observations from disc models and simulations and searched for DP signatures from all directions using a grid of observation angles. I then tested from which direction I can detect a DP emission line using a single and a double-Gaussian fit. The simulations were taken from the GalMer database which provides simulations of isolated galaxies and a large number of different merger constellations. Considering a pure rotating disc, a central DP emission-line signature mostly depends on the maximal velocity of the rotation curve. This is determined by the mass and concentration of the stellar bulge. Furthermore, in simulated galaxies, a bar signature can create a DP signature when viewed parallel to the major maxis of the bar. This can be even observed in galaxies with less prominent bulges like Sb galaxies.

Galaxy mergers produce DP emission-lines at close encounters and in the moment of their final coalescence. Major mergers, which show a strongly perturbed morphology during the merger form a central gaseous disc at about 1 Gyr after the final coalescence from in-falling gas. This disc can be observed as a DP emission line. At this point the morphology does not show large tidal features anymore. Minor mergers, on the other hand, only show a DP signature up to 350 Myr after the final coalescence. Furthermore, there is no correlation between the direction from where we observe a DP and the galaxy orientation.

Comparing these scenarios with the findings of observed DP emission-line galaxies, major mergers are unlikely to be the predominant mechanism, since these show mostly elliptical and only few S0 morphologies. Furthermore, at the discussed late merger stage, the enhanced star

formation is most likely faded. Bars and minor mergers, on the other hand, are both known to produce a central star-formation enhancement and therefore fit the observation quite well.

Astronomy & Astrophysics manuscript no. output
December 14, 2022

The origin of double-peak emission-line galaxies: Rotating discs, bars, or galaxy mergers?

Daniel Maschmann[1,2], Anaëlle Halle[1], Anne-Laure Melchior[1], Francoise Combes[1,3], Igor V. Chilingarian[4,5]

[1] Sorbonne Université, LERMA, Observatoire de Paris, PSL university, CNRS, F-75014, Paris, France
e-mail: Daniel.Maschmann@observatoiredeparis.psl.eu, anaelle.halle@observatoiredeparis.psl.eu
[2] Steward Observatory, University of Arizona, 933 N Cherry Ave,Tucson, AZ 85721, USA
[3] Collège de France, 11, Place Marcelin Berthelot, F-75005, Paris, France
[4] Center for Astrophysics – Harvard and Smithsonian, 60 Garden St. MS09, Cambridge, MA, 02138, USA
[5] Sternberg Astronomical Institute, M.V. Lomonosov Moscow State University, 13 Universitetsky prospect, Moscow, 119991, Russia

Received 26 July 2022/ accepted 1 December 2022

ABSTRACT

Emission lines with a double-peak (DP) shape, detected in the centre of galaxies, have been extensively used in the past to identify peculiar kinematics such as dual active galactic nuclei (AGNs), outflows, or mergers. With a more general approach considering a large DP galaxy sample selected from the Sloan Digital Sky Survey (SDSS), a connection to minor merger galaxies with ongoing star formation was suggested. To gain a better understanding of different mechanisms creating a DP signature, in this paper, we explore synthetic SDSS spectroscopic observations computed from disc models and simulations. We show how a DP signature is connected to the central part of the rotation curve of galaxies, which is mostly shaped by the stellar bulge. We, furthermore, find that bars can create strong DP emission-line signatures when viewed along their major axis. Major mergers can form a central rotating disc in late post-coalescence merger stages (1 Gyr after the final coalescence), which creates a DP signature. Minor mergers tend to show a DP feature with no correlation to the galaxy inclination within 350 Myr after the final coalescence. Comparisons of these scenarii with observations disfavour major mergers, since they show predominantly elliptical and only a few S0 morphologies. Furthermore, at such a late merger stage, the enhanced star formation is most likely faded. Bars and minor mergers, on the other hand, can be compared quite well with the observations. Both observations coincide with increased star formation found in observations, and minor mergers in particular do not show any dependency with the observation direction. However, observations resolving the galaxy kinematics spatially are needed to distinguish between the discussed possibilities. More insight into the origin of DP will be gained by a broader comparison with cosmological simulations. The understanding of the DP origin can provide important tools to study the mass growth of galaxies in future high redshift surveys.

Key words. galaxies: kinematics and dynamics, galaxies: interactions, galaxies: evolution, Methods: numerical, techniques: spectroscopic

1. Introduction

The evolution of galaxies involves dynamical processes such as galaxy mergers whose frequency remains difficult to measure over cosmic time. Studies based on photometry may for example not always be efficient at identifying these processes, while kinematics may be misleading. Mergers have been extensively studied using simulations (e.g. Toomre & Toomre 1972; Athanassoula & Bosma 1985; Hernquist & Mihos 1995; Bournaud et al. 2005b; Di Matteo et al. 2007; Lotz et al. 2010) and observations (e.g. Combes et al. 1994; Bergvall et al. 2003; Lotz et al. 2004; De Propris et al. 2005; Ellison et al. 2008, 2013), resulting in a good understanding on how galaxy mergers can fuel star formation, trigger active galactic nuclei (AGNs), and transform the morphology of galaxies.

Especially studies dealing with different stages of a galaxy merger rely on an accurate identification of mergers. Interacting galaxies can be identified through their projected separation (De Propris et al. 2005; Ellison et al. 2008; Patton et al. 2011). Major mergers in an early phase of their coalescence show strong tidal features and can be identified though their perturbed morphology (e.g. Lotz et al. 2004). After the final coalescence, tidal features and perturbations gradually fade and it becomes increasingly difficult to correctly distinguish between post-merger galaxies and isolated galaxies. From hydrodynamical simulations, major (resp. minor) mergers can be identified after $\sim$ 200 – 400 Myr (resp. 60 Myr) using photometric diagnostics (Lotz et al. 2010). Using a combination of several photometric classifiers to a linear discriminant analysis, Nevin et al. (2019) succeeded in identifying galaxy mergers over a merger timescale of 2 Gyr. Including stellar kinematics measured with integrated field spectroscopic observations, Nevin et al. (2021) increased the detection sensitivity for post-coalescence mergers. However, it remains challenging to apply these techniques to observations and identify post-coalescence mergers.

As predicted in Begelman et al. (1980), the two supermassive black holes of the progenitors of a merger should eventually merge in the course of the coalescence. Previous to this event, the two nuclei are expected to stay at a separation > 1 kpc for $\sim$ 100 Myr. When both nuclei are AGNs, it is possible to observe this phenomenon using a telescope providing high enough resolution. Such dual AGNs were observed using an X-ray observation (Komossa et al. 2003), radio observations (Maness et al. 2004; Rodriguez et al. 2006), and long-slit spectroscopy, revealing a double-peak (DP) signature (Gerke et al. 2007). The

connection between the kinematic footprint and a dual AGN was further discussed in Comerford et al. (2009a). Systematic studies on DP emission-line AGNs using additional high resolution observations were able to distinguish between dual AGNs, AGN-driven outflows, or rotating discs (Comerford et al. 2011; Comerford & Greene 2014; Comerford et al. 2015, 2018; Müller-Sánchez et al. 2015; Nevin et al. 2016).

In general, a DP emission-line profile traces multiple line-of-sight velocities. AGNs are compact and bright sources and therefore dual AGNs, moving at two different velocities, are particularly interesting to study late stages of mergers. Ge et al. (2012) built up a DP-galaxy sample, also including non-AGNs and gathered 3 030 galaxies, of which only 30 % are classified as AGNs. These DP emission-line signatures can have various causes: a compact rotating disc, gas outflow or inflow, two nuclei, or the alignment of two galaxies inside the line of sight. In Maschmann et al. (2020) (hereafter M20), 5 663 DP emission-line galaxies were selected using an automated selection procedure. Interestingly, only 14 % were found to be AGNs. Different scenarii were discussed to explain the origin of DP emission lines and a recent minor merger was favoured as the underlying process. As these results are particularly relevant for this work, the main findings are explained in detail in Sect. 2.1. On the one hand, it is still challenging to conclude on the origin of DP emission lines for an individual galaxy, relying only on one optical spectrum and a snapshot. On the other hand, a merger scenario becomes increasingly likely if one finds different characteristics in the two emission-line components (Maschmann & Melchior 2019). Using integrated field spectroscopy, Mazzilli Ciraulo et al. (2021) detected two galaxies aligned inside the line of sight, creating a DP emission line. In a recent study, the molecular gas content of DP galaxies selected from above the main star-forming sequence was studied in Maschmann et al. (2022). Twenty percent of the DP galaxies show the same kinematic feature in the CO emission line distribution which traces the molecular gas, indicating a highly concentrated gas reservoir. Furthermore, in nearly all galaxies, a central star formation enhancement was found, and 50 % of the sample was identified as visual mergers or showed tidal features. Taking into account that the observed galaxies have a significantly larger molecular gas reservoir than expected for galaxies situated above the main sequence, the most plausible explanation of the DP emission line profile was found to be a recent minor merger which funnelled gas into the central regions and fuels a compact star-formation region.

To better understand the observed DP emission-lines, in this paper we use models and simulations of galaxies. We investigate possible origins of DP emission lines in this work and determine under which conditions a DP signature may be detected in isolated galaxies, ongoing mergers, and post-mergers. More precisely, we seek to identify DP emission lines in the conditions of observations with a Sloan Digital Sky Survey (SDSS)-like 3″ spectroscopic fibre observations centred on the brightest region of the targeted system. We study the connection between identified DP signatures in the line of sight and the kinematic processes inside the observed systems.

In Sect. 3, we describe axisymmetric models of disc galaxies and then study numerical simulations of such galaxies in which non-axisymmetric patterns, especially bars (in the central regions of interest), form. In Sect. 4, we characterise major- and minor-merger simulations and identify under which circumstances a DP emission line can be detected. We then discuss in Sect. 5 the found results in the context of past work on DP emission line galaxies and conclude in Sect. 6. In this work, a cosmology of $\Omega_m = 0.3$, $\Omega_\Lambda = 0.7$, and $h = 0.7$ is assumed.

2. Observations of double-peak emission-line galaxies in the SDSS

The focus of this work is to determine the origin of DP emission-line profiles. To accomplish this, we analyse synthetic emission-line spectra from galaxy models and galaxy simulations. To frame this analysis in the context of observations, we here recapitulate the results of M20 and summarise the most important sample characteristics of their assembled DP galaxy sample. We then select three redshift values in order to represent the redshift distribution of the DP sample found in M20 and describe how to detect DP profiles in synthetic emission-line spectra.

2.1. Double-peak detection in M20

The selection procedure of M20 is divided into multiple stages which make use of emission-line parameters provided by the Reference Catalogue of Spectral Energy Distribution (RCSED) (Chilingarian et al. 2017). In a first step, galaxies with a high enough signal-to-noise ratio of S/N > 10 in either the Hα or the [OIII]λ5008 emission lines were selected. Then, galaxies with emission-lines which are better described by a non-parametric fit than by a single-Gaussian fit were selected and all emission-lines with a S/N > 5 were stacked. The resulting emission-line profile was fitted by both a single and a double-Gaussian function. Relying on an F-test of the two fits, an amplitude ratio threshold of the two double-Gaussian components, and a minimal threshold in velocity difference $\Delta v_{\rm DP} > 3\delta v$, with δv the SDSS bin-width of 69 km s^{-1}, 7 479 DP-candidates were selected. In a second stage, each emission line was individually fitted with a single and a double-Gaussian fit. The double-Gaussian fit is restrained to the parameters found from the stacked emission line, however, the parameters can still vary within their uncertainties. All emission lines with a S/N > 5 were flagged as a DP emission line if they satisfy the following conditions: (1) the reduced chi-square value of the double-Gaussian fit must be smaller than the value for the single Gaussian fit, (2) the double-Gaussian amplitude ratio A_1/A_2 must fulfil the condition $1/3 < A_1/A_2 < 3$, and (3) each of the double-Gaussian emission-line component must be detected with at least S/N > 3. In a third stage, galaxies were selected with a DP in their strongest emission lines, resulting in a final sample of 5 663 DP galaxies.

In order to compare the selected DP sample to galaxies with only a single peaked (SP) emission-line profile, a no-bias-control-sample was selected with the same emission-line S/N properties, redshift distribution and stellar mass distribution as the DP sample. Analysing the morphology of these two samples, the same visual merger rate was found between DP and SP galaxy. However, DP galaxies are more likely to be classified as S0 galaxies (36 %) in comparison to SP galaxies (20 %). Furthermore, DP galaxies classified as spiral galaxies tend to have larger bulges and are more likely classified as Sa or Sb galaxies whereas SP galaxies tend to be classified as Sc and Sd. A detailed analysis of the spectroscopic kinematics revealed a significant higher stellar velocity dispersion in DP galaxies in comparison to SP galaxies. A correlation between the galaxy inclination and the gas kinematics was found for SP galaxies, but not for DP galaxies. DP galaxies also deviate from the Tully-Fisher relation in contrast to SP galaxies. When considering each individual fit component of the DP sample, however, a good agreement with the Tully-Fisher relation is found. Considering star-forming galaxies, a central star-formation enhancement was found for DP galaxies but not for SP galaxies. Conclusively, these observations agree in particular with a model of repetitive minor merg-

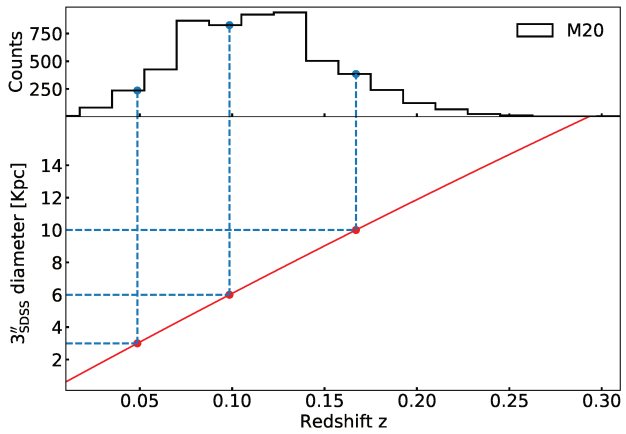

Fig. 1. Redshift distribution of the DP galaxy sample (M20) (top panel) and the conversion curve between redshift and the fibre diameter in kpc of the SDSS 3″ (red curve in the bottom panel). We mark with blue dashed line the three representative redshifts and corresponding fibre diameters: $z = 0.05$, $z = 0.1$, and $z = 0.17$ corresponding to a fibre diameter of 3, 6, and 10 kpc, respectively.

ers which effectively transport gas into the central regions and drive bulge growth as described in Bournaud et al. (2007).

2.2. SDSS spectroscopic measurements at different redshifts

The spectroscopic observation in the SDSS is taken within a 3″ region centred on the brightest spot of a galaxy (Abazajian et al. 2009). Hence, this spectrum probes the central 0.6 kpc in low redshift galaxies at $z = 0.01$ and 30 kpc for the most distant spectroscopic observations in the SDSS at about $z = 0.55$. In the latter case, the SDSS spectrum probes roughly the entire galaxy, whereas for a nearby galaxy the spectroscopic measurement probes only the very centre. In Fig. 1, we show the redshift distribution of the DP galaxy sample of M20 and a conversion curve between the fibre diameter and the redshift. The DP sample has a median redshift of $z = 0.11$ and 99 % of the sample has a redshift of $z < 0.22$. Only 57 galaxies are situated at higher redshift up to a value of $z = 0.34$. In order to represent this distribution, we select three representative redshift values: $z = 0.05$, $z = 0.1$, and $z = 0.17$, corresponding to a fibre diameter of 3, 6, and 10 kpc, respectively. In the following, we analyse simulated SDSS spectral observations of analytical models and galaxy simulations with these three fibre diameters.

2.3. Double-peak detection in synthetic emission-line spectra

In order to test whether a computed emission-line profile from an axisymmetric model or a galaxy simulation shows a DP feature, we develop a detection algorithm similar to M20. In a first step, we convolve the produced line-of-sight velocity profiles with the mean instrumental broadening of 61 km s^{-1} (M20) from the SDSS spectral detector, and compute the resulting signal with the SDSS bin-width of $\delta v = 69$ km s^{-1}. We then fit a single- and a double-Gaussian function to the velocity profile and select DP galaxies satisfying the following criteria: (1) χ^2_ν(single) > χ^2_ν(double), (2) $1/3 < A_1/A_2 < 3$, and (3) $\Delta v_{DP} = |\mu_2 - \mu_2| > 3\,\delta v$. χ^2_ν(single) (resp. χ^2_ν(double)) is the reduced chi-square computed for the single (resp. double) Gaussian fit, A_1 and A_2 are the amplitudes of the two Gaussian functions in the double-Gaussian fit, and Δv_{DP} is the velocity difference between the blue and red-shifted component. In a first step of selection of DP candidates in M20, an F-test was used. However, this was mostly motivated to distinguish a DP from a SP profile in the case of a noisy spectra. Since we do not include noise in our synthetic emission-line profiles, we only use the chi-square ratio as such a selection criterion.

Table 1. Mass and length parameters for the Sa galaxy.

M_{gas}	$M_{*\,disc}$	$M_{*\,bulge}$	M_{DM}	$[2.3 \times 10^9 M_\odot]$
4	40	10	50	
a_{gas}	h_{gas}	$a_{*\,disc}$	$h_{*\,disc}$	$b_{*\,bulge}$	b_{DM}	[kpc]
5	0.2	4	0.5	0.2-3	10	

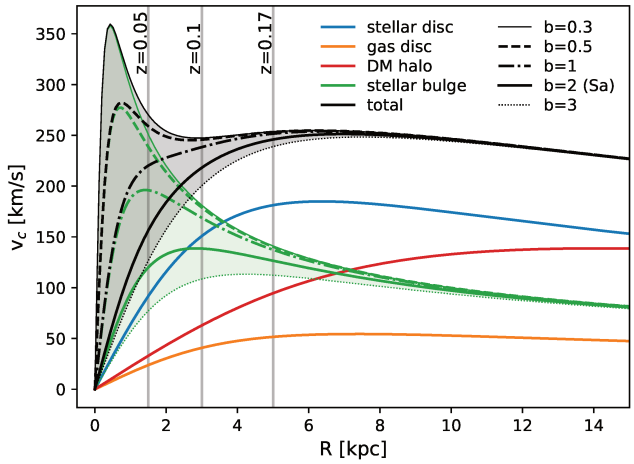

Fig. 2. Rotation curves of a disc galaxy for different characteristic radii of the stellar bulge. We show with coloured lines the contribution of each component, and in black the total rotation curve. In blue (resp. orange), we show the contributions of the stellar (resp. gaseous) disc, described by Miyamoto-Nagai density profiles. With a green (resp. red) line, we show the contributions of the stellar bulge (resp. dark-matter halo), described by Plummer density profiles. We show with different line styles the contribution of the bulge and the total rotation curve for bulges with different characteristic radii b. A characteristic bulge radius $b = 2$ (thick solid green and black lines) corresponds to the fiducial Sa galaxy. Vertical grey lines are plotted at the radii of the simulated fibre for the redshifts $z = 0.05$, 0.1, and 0.17.

3. Rotating discs

Double-peaked emission lines can be due to the rotation of discs. In order to investigate when such a detection of DP is possible, we first construct an idealised galaxy model with an axisymmetric rotating gas disc. We modify the rotation curve of the model by varying the mass concentration of a stellar bulge and study the resulting gas line-of-sight velocity distribution. We also study the effect of a change in the concentration of the gas density profile. Using simulations of isolated galaxies, we then investigate how the presence of a bar may impact the detection of a DP signature.

3.1. Axisymmetric models

The model, for its fiducial set of parameters, reproduces an Sa galaxy. Potential-density pairs are used for all four components. The gas and stellar discs each have a Miyamoto-Nagai density

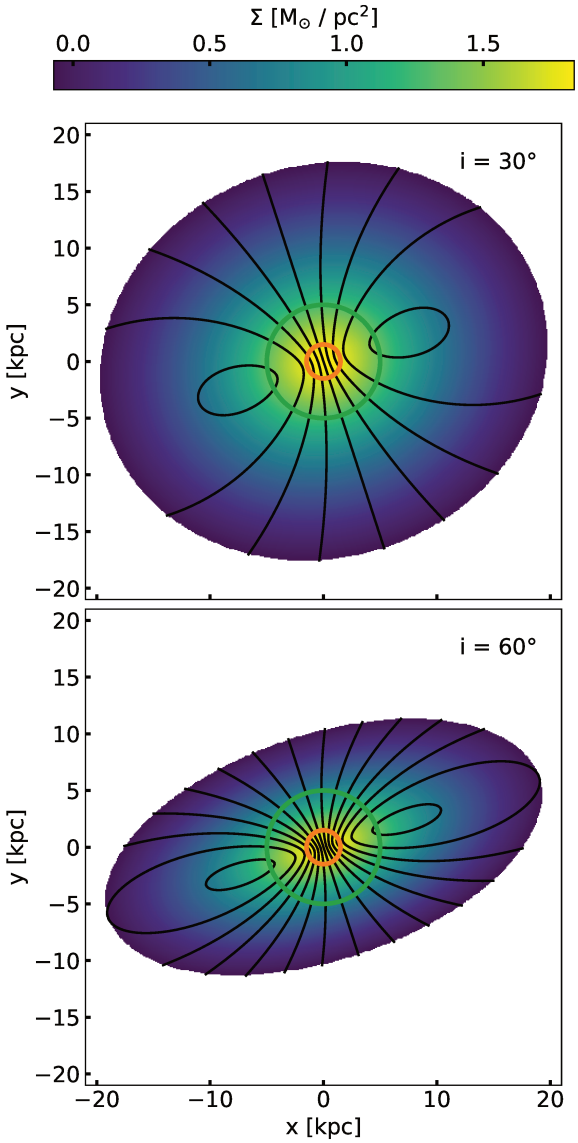

Fig. 3. Gaseous disc model at two different inclinations. We show 2D projections of a Miyamoto-Nagai density profile as described in Equation 1 at an inclination of $i = 30°$ (top panel) and $i = 60°$ (bottom panel). Both discs are turned by a position angle of 20°. The colour-bar indicates the surface density. With black lines, we indicate iso-velocity curves, with velocity values separated by 30 km s^{-1} (with a value of 0 km s^{-1} on the minor axes). With an orange (resp. green) circle, we show the area observed by a 3″ spectroscopic fibre at a redshift of $z = 0.05$ (resp. $z = 0.17$). The more inclined the disc, the smaller the distance of equidistant velocity lines and thus the steeper the velocity gradient probed by the spectroscopic fibre.

profile (Miyamoto & Nagai 1975):

$$\rho_d(R,z) = \left(\frac{h^2 M}{4\pi}\right) \frac{aR^2 + (a+3\sqrt{z^2+h^2})(a+\sqrt{z^2+h^2})^2}{\left[a^2+(a+\sqrt{z^2+h^2})^2\right]^{\frac{5}{2}}(z^2+h^2)^{\frac{3}{2}}}, \quad (1)$$

where M is the total mass of the disc, a is a radial scale length, and h is a vertical scale length. The stellar bulge and the dark-matter halo each have a Plummer profile (Binney & Tremaine 1987, pag. 42):

$$\rho_s(r) = \left(\frac{3M}{4\pi b^3}\right)\left(1+\frac{r^2}{b^2}\right)^{-\frac{5}{2}}, \quad (2)$$

where M is the total mass of the component and b a characteristic radius. The profile parameters for the four components are given in Table 1, for an Sa galaxy.

The rotation curve is shown on Fig. 2 (thick black curve for an Sa), with the detail of the contributions of the different components. The individual contribution of each disc component is $\sqrt{R\frac{\partial\Phi_d}{\partial R}\Big|_{z=0}}$ with Φ_d the gravitational potential of the disc component:

$$\Phi_d(R,z) = -\frac{GM}{\sqrt{R^2+(a+\sqrt{z^2+h^2})^2}}, \quad (3)$$

and the individual contribution of each spherical component (stellar bulge or dark-matter halo) is $\sqrt{r\frac{\partial\Phi_s}{\partial r}}$ with r the spherical radius and Φ_s the gravitational potential of the spherical component:

$$\Phi_s(r) = -\frac{GM}{\sqrt{r^2+b^2}}. \quad (4)$$

The rotation curve is then obtained as the square root of the quadratic sum of the four contributions. For such an Sa galaxy, the bulge dominates the rotation curve in the central parts, creating a steep rise of the rotation curve at small galactocentric radii (see the thick green curve representing the bulge contribution on Fig. 2).

3.1.1. Emission-lines of a fiducial Sa galaxy

Figure 3 shows the mass surface density of the gas disc of this Sa galaxy for two different disc inclinations. Iso-velocity curves with values spaced by 30 km/s are over-plotted, starting at 0 km/s on the minor axes. The line-of-sight velocity V is such that:

$$V = V_{\rm rot}\cos\phi\sin i, \quad (5)$$

with $V_{\rm rot}$ the rotation velocity (obtained from the rotation curve, assuming a zero gas velocity dispersion), ϕ is the azimutal angle in the disc plane ($\phi = 0\,[\pi]$ on the major axis), and i is the inclination of the disc with respect to the line of sight ($i = 0$ for a face-on disc). The larger the inclination of the disc, the larger the amplitude in line-of-sight velocity: for $i = 30°$ the iso-velocity contours have extreme values of -120 and 120 km/s (closed iso-contours near the major axis) while for $i = 60°$, the smallest and largest values are -210 and 210 km/s. The distribution of line-of-sight velocities is thus wider for larger inclinations, and the number of iso-velocity curves encompassed by a given fibre size is larger, as can be seen from the two represented fibres, of diameters 3 and 10 kpc.

The fraction of gas observed with a line-of-sight velocity V, that is the line-of-sight-velocity spectrum, can be computed following Wiklind et al. (1997), as:

$$\frac{{\rm d}M}{{\rm d}v}(V) = \int_0^{R_{\rm max}} \frac{\Sigma_{\rm gas}(R)R{\rm d}R}{V_{\rm rot}(R)\sqrt{1-\left(\frac{V}{V_{\rm rot}(R)\sin i}\right)^2}\sin i} \quad (6)$$

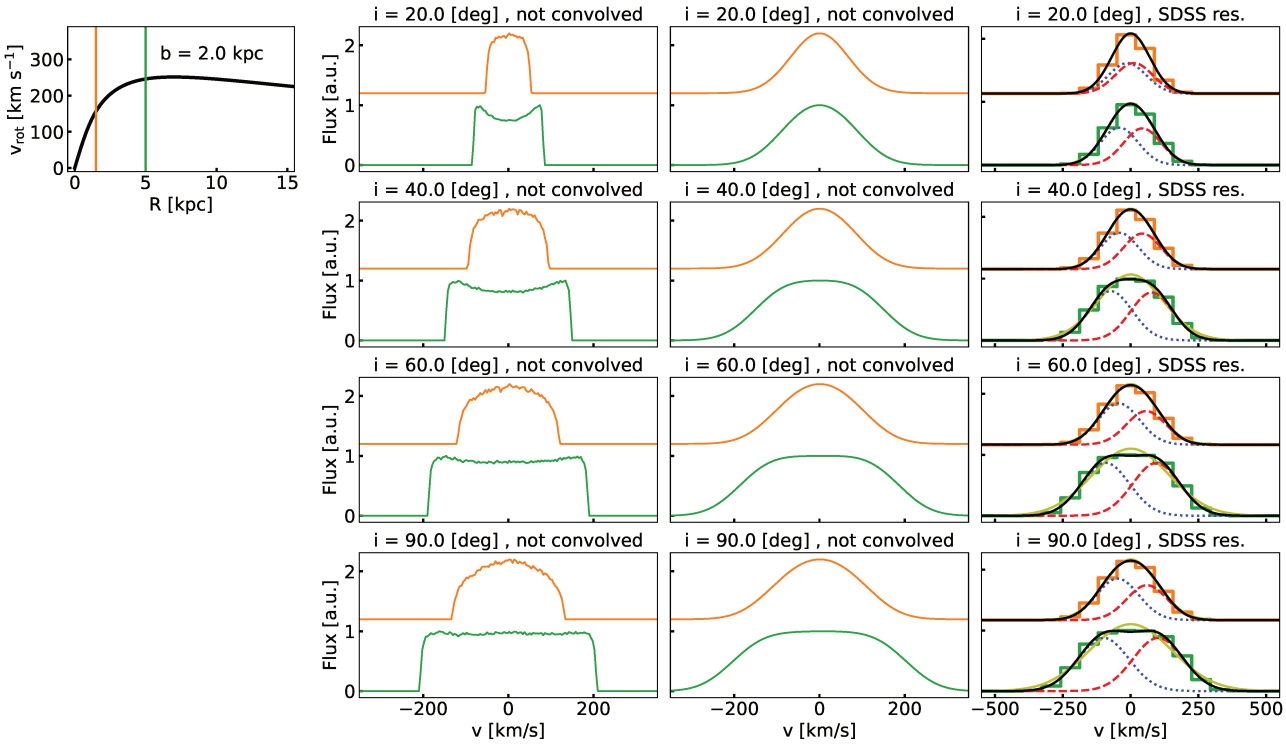

Fig. 4. Emission-line profiles of gaseous-disc model observed at different inclinations. On the top left, we show a rotation curve calculated by a model including a stellar and gaseous disc, a stellar bulge, and a dark-matter halo, parametrised as summarised in Table 1 with $b = 2.0$ kpc. We compute the emission-line profiles observed within a 3″ spectroscopic fibre for two redshift values: $z = 0.05$ and $z = 0.17$. The region probed by these observations are marked by orange and green line, respectively. For the emission-line profiles we also show the two spectroscopic observations in green and orange, with an off-set to the observation of $z = 0.05$ (orange spectra) to show them above the observation of $z = 0.17$ (green spectra). In the second column from the left, we show the measured line of sight velocity as described by Equation 6. In the third column from the left, we show the observed spectra convolved by the SDSS mean instrumental broadening of 61 km s^{-1}. On the rightmost column, we show this signal binned to the detector resolution of the SDSS with a bin-width of 69 km s^{-1}. We fitted a single and a double-Gaussian function to the observations presented by yellow and black lines, respectively. For the double-Gaussian function we show its blueshifted (resp. redshifted) component by dotted blue (resp. dashed red) lines. The different rows show different values of inclination as indicated in the titles.

where the integration goes from $R = 0$ to a maximum galactocentric radius $R_{\rm max}$ (corresponding to the simulated SDSS fibre, for example), and $\Sigma_{\rm gas}(R)$ is the gas surface density. In particular, a double-horn profile can be found for a constant $V_{\rm rot}$ (see Wiklind et al. (1997)). However, the formula is only approximate when applied for a radius $R_{\rm max}$ smaller than the disc size, with an error increasing with inclination. We thus use simulated models of gas discs with Miyamoto-Nagai density profiles, setting the rotation velocity from the modelled rotation curve, and we measure the line-of-sight velocity of gas inside the different fibres for different inclinations.

We simulate the detection of double peaks for this Sa galaxy with the fibres of diameters 3 and 10 kpc for four different inclinations of the disc in Fig. 4. The spectra obtained with Eq. 6 and shown on the second column from the left are, as explained in Sect. 2.3, convolved with the mean instrumental broadening of 61 km s^{-1} from the SDSS spectral detector (the result of this convoion is shown in the third column from the left), and then binned with the SDSS bin-width of $\delta v = 69$ km s^{-1}. The spectra are broader for higher inclinations because of the $\sin i$ term in Eq. 5. For fixed gas density-profile and rotation curve, the shape of the spectra depends on the fibre size. For the small fibre, encompassing the beginning of the rise of the rotation curve, the spectra are single-peaked. However, a 'double-horn' structure, with a central dip and sharp vertical limits at terminal velocities, appears for the larger fibre size. When viewing the disc edge-on, the double-horn shape changes to a box-like shape. This is due to the fraction of the disc moving perpendicular to the observer and which is only covered at an edge-on perspective. The instrumental broadening significantly alters the emission-line shape: for example the maxima of a horn are made closer to the centre of the spectrum, making the spectra single-peaked for low inclinations, and the steepness of the edges is reduced. The result of the binning is shown on the rightmost column, with both a Gaussian fit and a double-Gaussian fit. For the latter fit, the two components are shown in blue and red. Using the three criteria of Sect. 2.3, a double-peak is identified only for $z = 0.17$ (10 kpc diameter fibre) for an inclination of 90°. The difference of velocities of the two peaks $\Delta v_{\rm DP}$ is too small in the other cases for a double-peak to be identified according to our criteria.

Depending on the amount of dust within the line of sight, the signal of each gas particle decreases. As shown by Baes & Dejonghe (2000) and Baes et al. (2000), this can cause a significant decrease in the intensity at 0 km s^{-1} and alter the emission line shape. This effect would favour a DP structure and might lead to a higher DP detection rate. However, the inclusion of this effect is not straightforward. The estimation of dust extinction strongly depends on the wavelength (Fitzpatrick 1999) and factors such as the dust-to-gas mass ratio (Bohlin et al. 1978) and the metallicity (Salim & Narayanan 2020). In practice this means that for

the simple galaxy models chosen in this work it would be difficult to select a certain set of extinction models. In addition, since we are interested in the qualitative question of how different mechanisms can cause DP signatures, we do not include dust extinction in this work.

3.1.2. Effect of total mass concentration on the emission-lines

For a given (non-zero) disc inclination and a given fibre size, the detection of a double-peak is favoured by a combination of a gas density profile and a rotation curve such that more gas is probed at large line-of-sight velocities than at small velocities (corresponding to gas on the minor axis of the disc). In order to show the effect of the shape of the rotation curve, which depends on the total mass concentration, we now keep a constant gas density profile, constant stellar disc, and dark-matter halo profiles, but change the steepness of rising of the rotation curve by varying the concentration of the stellar bulge. The effect of this change is visible on Fig. 2, in which the scale length of the bulge spans from 0.3 kpc to 3 kpc (decreasing the mass concentration of the bulge and hence also of the galaxy). The rotation curve rises monotonously in the first 5 kpc for large scale lengths (low mass concentrations) while it peaks very near the centre of the galaxy for small scale lengths (high mass concentrations).

The difference of velocity of the two peaks obtained by the fitting procedure of Sect. 2.3, $\Delta v_{\rm DP}$, is represented (colour-coded) for different bulge scale-lengths and disc inclinations on the three panels of Fig. 5, with one panel per redshift (fibre size). The part of the rotation curves encompassed by the fibres can be seen on Fig. 2, while on the sub-panels of Fig. 5 at the left of each main panel, we represent the ratio of the maximal velocity value inside the fibre to the maximal velocity in the rotation curve. Double peaks are identified with our criteria in the non-hatched regions of the panels of Fig. 5. At a given bulge scale-length, $\Delta v_{\rm DP}$ increases with inclination because of the broadening of the velocity distribution. At fixed inclination, $\Delta v_{\rm DP}$ increases with the concentration of the bulge (with decreasing bulge scale-length), with a steepness of the increase more pronounced for a small fibre. For the most mass concentrated galaxy models with a high rotation curve peak close to the centre of the galaxy, a double-peak is thus detected at small inclinations 40° for all redshifts. At a given mass concentration (bulge scale-length), the threshold inclination for the double-peak detection generally increases with decreasing redshift (fibre size), with no detection for scale-lengths > 0.7 kpc for the smallest redshift and for scale-lengths > 1.1 kpc (resp. > 2.7 kpc) for the intermediate (resp. highest) redshift.

3.1.3. Effect of gas-disc concentration on the emission-lines

The shape of the spectra and the double-peak detection depend on the gas density-profile, which we qualitatively show on Fig. 6, varying only the scale-length of the gas density profile. Because of the relative small mass of the gas component in this galaxy model with respect to the other components, changing the gas profile concentration alters very little the total rotation curve, as can be seen on the left column of the figure. For a less concentrated profile (a larger scale-length), the spectra indicate steeper horn features but also a higher intensity in the centre since at an inclination of 80° more gas is probed close to a zero line-of-sight velocity. Using the three criteria of Sect. 2.3, a DP is identified for $z = 0.17$ (10 kpc diameter fibre) for scale lengths of 5 kpc (Sa fiducial model), while the gas of the profile with a scale length of 2 kpc is too concentrated for a DP detection. At a scale length of 12 kpc, we do not detect a DP as the concentration at 0 km s^{-1} is leading to a more single-Gaussian shape. With the smallest fibre size, we do not detect any DP signatures. However, we observe the largest Δv value for the smallest scale-length of 2 kpc with $\Delta v = 117\,\mathrm{km\,s^{-1}}$. For a scale length of 5 kpc (resp. 12 kpc), we find $\Delta v = 106\,\mathrm{km\,s^{-1}}$ (resp. $\Delta v = 103\,\mathrm{km\,s^{-1}}$). This is not a strong trend but it shows that for higher central gas concentrations we can see a larger contribution of the rotation in small fibres.

3.2. N-body simulations of isolated disc galaxies

The kinematic signature of emission lines is a direct probe of the gas distribution inside the spectroscopic observation area. In reality, gas is found in clumps, discs, rings, spiral arms, and bars. Such structures deviate significantly from a model of an axisymmetric disc with a simple density profile such as described in Sect. 3.1. In order to explore how DP signatures can be found in more realistic isolated galaxies, we here analyse simulated isolated disc galaxies. We make use of the simulations database GalMer, which is described in detail in Chilingarian et al. (2010). This database is designed to systematically explore galaxy mergers with various initial orbital parameters, galaxy inclinations, and galaxy types. To understand how galaxies evolve in isolation in comparison to the interactions, this database provides isolated galaxy simulations for each morphological type. The reading and analysis of the outputs of the simulations is based on the visualisation software GalaXimView[1].

3.2.1. Simulation design

We here explore the evolution of isolated Sa and Sb galaxies. In Sect. 4, we further explore major-merger (giant + giant) and minor-merger (giant + dwarf) systems. The simulated isolated galaxies are giant galaxies and we thus refer to them as gSa and gSb. DP emission lines are mostly found in S0 and spiral galaxies of the type Sa and Sb. In the GalMer database, S0 galaxies are designed without a gaseous disc since this galaxy type is usually observed with an exhausted gas content (e.g. Somerville & Davé 2015). The gSa and gSb galaxies considered here consist of rotating gas and stellar discs, a non-rotating stellar bulge, and a non-rotating dark-matter halo. The initial conditions of simulations are modelled with the same density profiles as the axisymmetric models described in Sect. 3.1: disc components are described by a Miyamoto-Nagei density profile and the stellar bulge and dark-matter halo by a Plummer density profile. Velocities are set by the method of Hernquist (1993). The discs components have initial Toomre parameters of $Q = 1.2$.

The simulation code is described in detail in Di Matteo et al. (2007). It uses a Tree algorithm for the computation of the gravitational forces (Barnes & Hut 1986) and smoothed particle hydrodynamics (Lucy 1977; Gingold & Monaghan 1982) for the gas with individual smoothing lengths. The gas is considered as isothermal with a temperature $T_{\rm gas} = 10^4$K. To emulate star formation, hybrid particles, corresponding initially to pure gas particles with a stellar fraction of 0, are gradually changed into stellar particles following a star formation law described in Mihos & Hernquist (1994). Once the gas fraction drops below 5 %, a hybrid particle is converted into a stellar particle. During the star-formation process, the total mass of the hybrid particle is

[1] https://vm-weblerma.obspm.fr/~ahalle/galaximview/

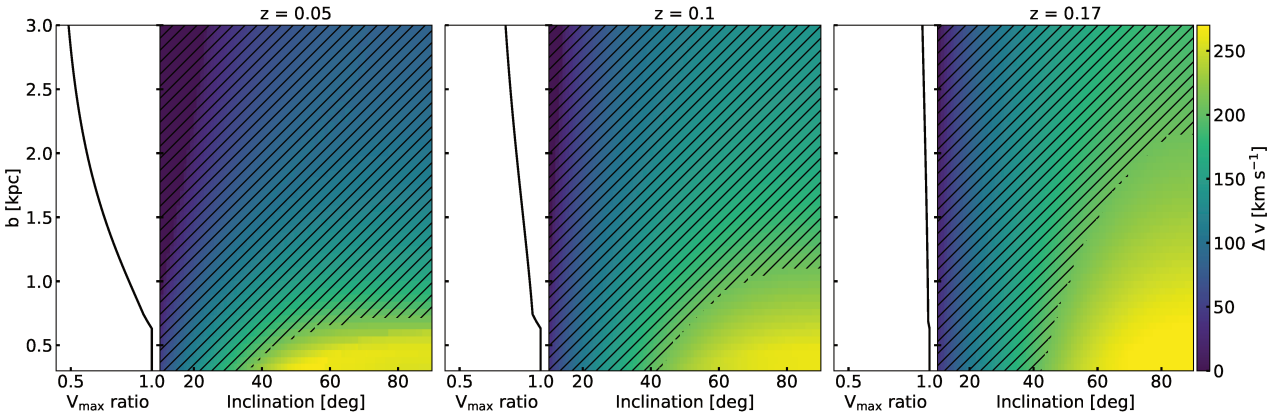

Fig. 5. Scans of DP detections for different inclinations and bulge concentrations of a modelled galaxy. Following Eq. 6, we computed the line-of-sight velocity profile as a function of inclination and the characteristic radius of the bulge b. We perform the DP selection procedure described in Sect. 2.3. We show from left to right the results for a redshift $z = 0.05$, $z = 0.1$, and $z = 0.17$, respectively. In each of the three panels, we show the Δv resulting from the double-Gaussian fit with the colour coding. We mark the parameter combinations where we do not detect a DP profile with black hatches. On the left side of each panel, we show the ratio between the maximal velocity value inside the spectroscopic fibre and the maximal velocity found in the entire rotation curve.

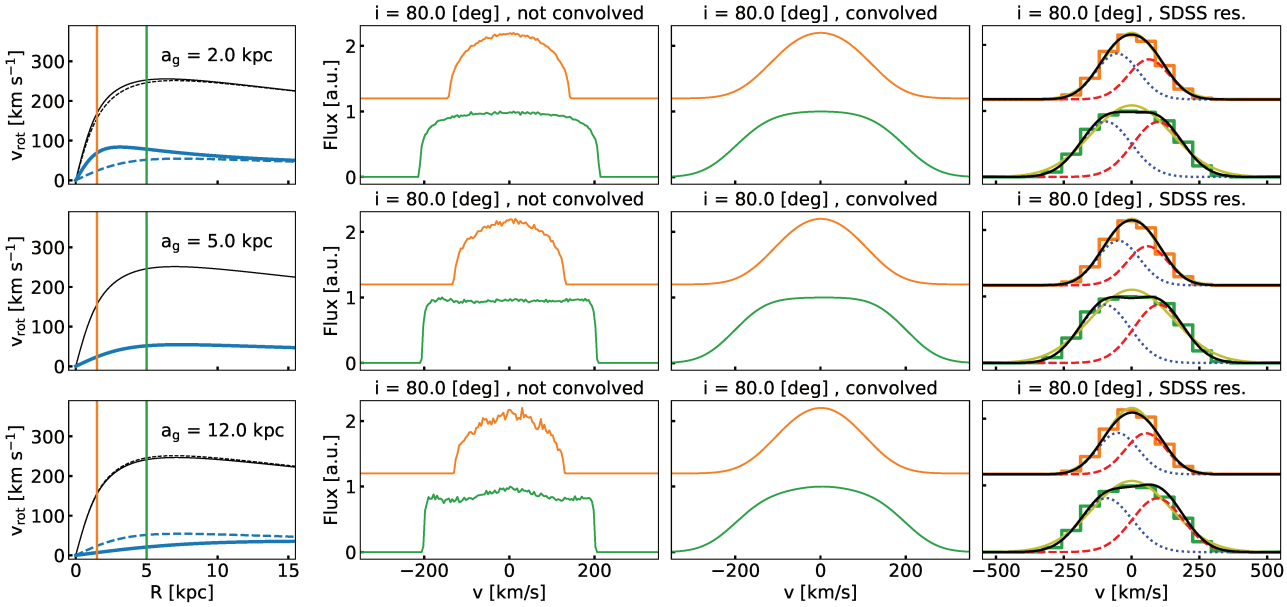

Fig. 6. Emission-line profiles of gaseous-disc models with different scale-lengths, with a disc inclination of 80°. On the left columns, we show the total rotation curves (black) and gas disc contribution (blue) in solid lines and the reference $a_{\rm gas} = 5$ kpc (middle panel) in dashed lines for the top and bottom plots. For a description of the other panels, see the caption of Fig. 4.

constant. There is no feedback from AGN, but there is stellar mass loss, and energy re-injected in the ISM by supernovae, cf Chilingarian et al. (2010). Time integration is performed with a leapfrog integrator with a time-step $\Delta t = 5{\times}10^5$yr and snapshots are output every 5×10^7yr. The simulations are carried out for a time-span of 3 or 3.5 Gyr. The initial parameters for gSa and gSb galaxies are given in the Appendix A, Table A.1. Isolated galaxies are simulated with a total number of 480 000 particles and a softening length of $\epsilon = 200$ pc. The same softening length is used for giant-dwarf interaction simulations while a softening length of $\epsilon = 280$ pc is used for giant-giant interactions (See Sect. 4).

3.2.2. Characterisation of the structure of the galaxies

In order to conduct a systematic analysis of simulated galaxies, we compute at each simulation step the following characteristic values: the position and the velocity of the centre of baryonic mass (COM), the half-mass radius $r_{1/2}$, and the spin vector of the stellar particles. We calculate the COM from the baryonic particles (gas + stars). Therefore, we compute a 3D histogram with a bin-width of 1 kpc and select the bin containing the highest mass. We then calculate the position and the velocity of the COM of the particles inside this bin. For each COM, we calculate the $r_{1/2}$, describing the radius containing half of the baryonic mass of a galaxy. The spin vector of each galaxy is estimated by calculating the angular-momentum vector of the stellar par-

ticles which are outside the $r_{1/2}$ but within a radius < 15 kpc. In bulge-dominated galaxies with a large central velocity dispersion, the spin vector, computed with all particles, would not weigh sufficiently the rotation of the outer disc. Hence, a spin vector, calculated only with the outer particles, provides a better approximation of the disc orientation. As it will be discussed in Sect. 4, during a violent merger with complex geometry and kinematics, this vector does not have any meaningful direction and is only considered as a point of reference. In the following, spectroscopic observations are computed from an observer perspective, orientated with a polar angle θ and an azimuthal angle ϕ defined with respect to the spin vector and to a reference vector in the plane orthogonal to it for ϕ. When the spin vector truly defines a disc plane, $\theta = 0°$ (resp $\theta = 90°$) corresponds to a face-on (resp. edge-on) observation. The inclination angle i is thus $i = \theta$ for $\theta \in [0, 90°]$ and $180° - \theta$ for $\theta \in [90°, 180°]$.

3.3. Double-peak signatures from bars

The initial conditions of the simulated galaxies are computed with the exact same models as discussed in Sect. 3.1. However, one important aspect is a velocity dispersion which is not included in the line-of-sight velocity distribution with the previous models. Comparisons between a simulated gSa galaxy and an axisymmetric model lead to the same DP detection dependencies. For low inclinations (nearly face-on), we find larger emission-line profiles than in the axisymmetric model, which is due to the contribution of the velocity dispersion. The additional velocity dispersion broadens the emission-line profile and we can therefore detect a DP signature at lower inclinations. As visualised in Fig. 5, we detect a DP signature for inclinations larger than 70° using the axisymmetric model with a parametrisation of the fiducial gSa galaxy. For the initial conditions of a simulated gSa galaxy, we detect a DP signature for inclinations larger than 50°, due to the contribution of the velocity dispersion.

The simulated galaxies undergo a rapid evolution in the first 0.5-1 Gyr. Gas condensates into thin and dense structures and clumps, spiral arms, and a stellar bar are formed. These features however vanish after at least 1 Gyr. We observe a homogenisation of the disc with no arm structure while most of the gas has fallen into the centre. This high central gas concentration is then dominated by velocity dispersion and no DP emission-line structure can be observed any more. This likely unrealistic evolution stage is favoured by the low supernovae feedback and absence of AGN feedback in the simulations. From observations we know that about two thirds of disc galaxies are barred (e.g. Eskridge et al. 2000; Menéndez-Delmestre et al. 2007). However, this does not imply that bars have a long life time. In fact, bars can be weakened or destroyed (Bournaud et al. 2005a), but with a high gas fraction they can be re-formed (Bournaud & Combes 2002). Relying on cosmological simulations, the bar fraction is expected to be constant at about 66% for massive spiral galaxies ($M_* \geq 10^{10.6} M_\odot$) over a redshift range of $z = 0 - 1$ (Zhao et al. 2020).

Gas clumps, spiral arm structures, and turbulence in the simulations lead to some minor fluctuations of the DP detection. A stellar bar, however, is significantly changing the DP detection: we find strong Δv values of more than 300 km s^{-1} when observing parallel to the bar at an inclination of $\theta = 60°$. Observations of a gSa galaxy with a characteristic bar structure is shown in Fig. 7, after an evolution of 250 Myr from the initial axisymmetric condition. We define the observation angles in the top and show the 2D-projection of the observed gas in the middle panels: on the left, the disc is seen parallel to the bar and on the right, perpendicular to the bar. On the bottom panels, we show the spectroscopic observation of the gas for the two cases. We find a strong DP feature in the observation taken parallel to the bar but no DP signature in the one observed perpendicular to the bar. This is due to the fact that when observing perpendicular to the bar, the majority of the gas is moving also perpendicular to the line-of sight. Hence, we do not probe a large velocity gradient. In comparison to that, when observing parallel to the bar, we measure gas moving alongside the line of sight due to its streaming motion along the bar.

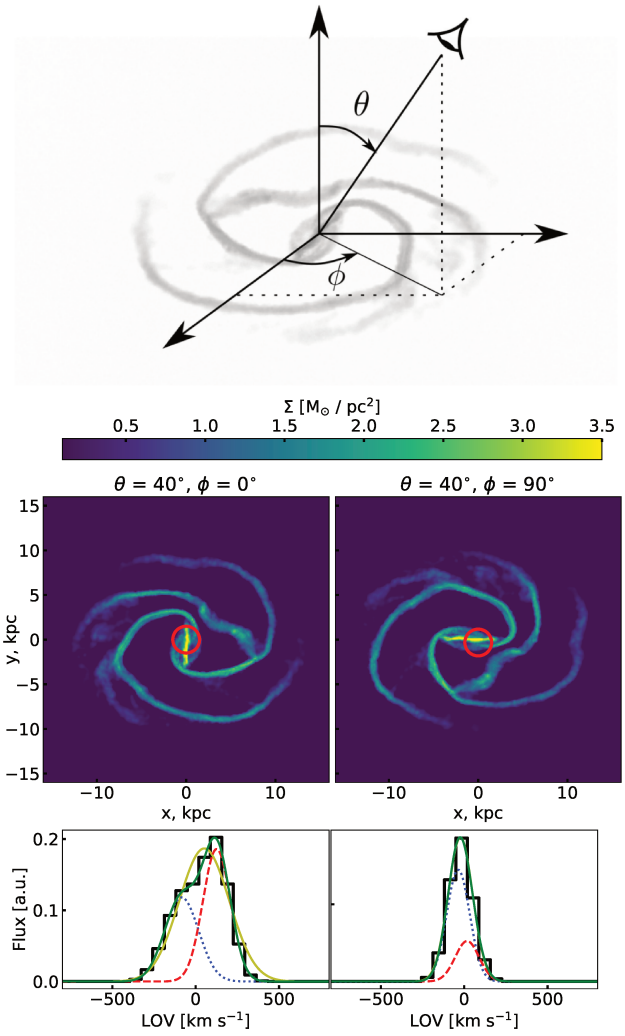

Fig. 7. Observation of an isolated barred galaxy. On the top panel, we show the gas distribution in the 3D space and define the definition of the observation angles ϕ and θ. On the middle panel, two 2D projections are shown for an inclination of $\theta = 40°$. On the left (resp. right) we show an azimuth of $\phi = 0°$ (resp. $\phi = 90°$) which corresponds to an observation parallel (resp. perpendicular) to the bar. With red circles, we mark a 3″ spectral fibre observation situated at a redshift of $z = 0.05$. On the bottom panels, we show the gas emission line line-of-sight distribution inside the fibre. We fitted a double and single Gaussian function to the emission lines.

In order to compute from which observation angles one can find a DP signature, we systematically place the observer on a sphere around the galaxy with the COM as its centre. We choose a uniform sampling of the sphere so that each observation covers

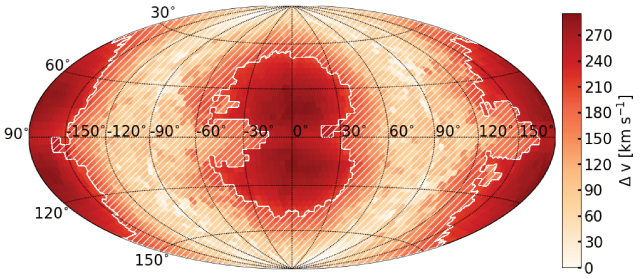

Fig. 8. Δv values measured at different observation angles with a double-Gaussian fit at a redshift $z = 0.05$. Each individual measurement covers a solid angle of 0.013 sr and the colour code indicates the measured Δv value. We choose the Hammer-projection to represent the observation points on the surface. The longitudes represent the azimuth angle ϕ which is measuring the observation angle relative to the central bar of the galaxy. $\phi = 0°$ and $\phi = \pm 180°$ correspond to an observation parallel to the bar and an azimuth angle $\phi = \pm 90°$ to an observation perpendicular to the bar. The latitudes represent the inclination of the observer. At an inclination of $\theta = 90°$ the galaxy is observed edge-on whereas at $\theta = 0°$ and $\theta = 180°$ one sees the galaxy face-on.

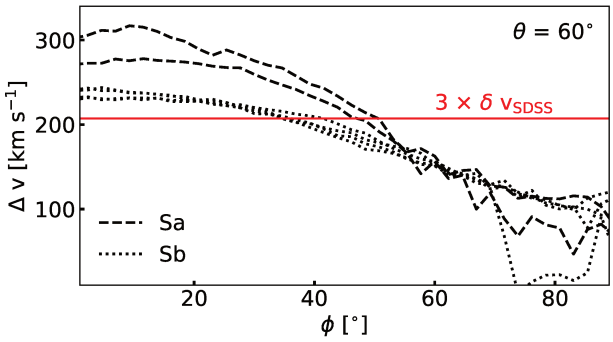

Fig. 9. Δv values from a double-Gaussian fit at different azimuth angles ϕ. We define ϕ as the azimuth angle with respect to the bar as visualised in Fig. 7. We computed spectroscopic observations at a fixed inclination of $\theta = 60°$ and at a redshift of $z = 0.05$

. We show all snapshots of gSa and gSb simulations, which indicate a bar. With a red line we show the value of three times the bin-width of the SDSS. A Δv larger than this value is one criteria for a DP detection (see Sect. 2.3).

a solid angle of 0.013 sr. In Fig. 8, we show a scan of all observation angles observed at $z = 0.05$ for the gSa galaxy exhibiting a bar which is visualised in Fig. 7. We indicate the Δv computed from the double-Gaussian fit with a colour code and mark the angular positions that do not exhibit a DP signature with white hatches. We show the full map (here and in other figures) but note that in the absence of any attenuation, the map contains redundant information: the value at θ and ϕ is the same as the value at $180° - \theta$ and $\phi + 180°$ (modulo 360°). If DP signatures originated from uniform rotation, a DP would be observed at all azimuth angles with a strong inclination of $60° < \theta < 120°$ as we found in Sect. 3.1. However, this is not the case: we see a strong DP signature when observing parallel to the bar ($\phi \sim 0°$ and $\phi \sim \pm 180°$) and single-peak signatures when observed perpendicular to it. Furthermore, we do not see the highest Δv values when observing fully edge-on ($\theta = 90°$) but at a lower inclination of $\theta \sim 75°$. This is due to the fact that when observing fully edge-on along the bar direction, the spectroscopic measurement probes as well gas, at the ends of the bar or elsewhere in the disc, moving perpendicular to the observer and contributing to the line-of-sight velocity distribution at $v = 0\,\mathrm{km\,s^{-1}}$. This makes the two Gaussian functions of the double-Gaussian fit shift closer together and the Δv become smaller. In contrast to that, when observing at a smaller inclination, the observation fibre of 3 kpc in diameter (seen at a redshift of $z = 0.05$) will mostly probe gas with a motion along the bar direction. This gas moves at the highest velocity parallel to the line of sight and only a small contribution of gas moving perpendicular is measured. This leads to a strong DP feature.

This effect can be seen on further galaxy examples. In Fig. 9, we have included all snapshots of gSa and gSb simulations which have a bar. We have determined the Δv value for a constant inclination of $\theta = 60°$ and for azimuth values between $\phi = 0°$ (parallel to the bar) and $\phi = 90°$ (perpendicular to the bar). The spectroscopic observations are evaluated within a spectroscopic fibre of a diameter of 3 kpc, corresponding to a SDSS fibre at redshift $z = 0.05$. For observations with an angle ϕ up to $\sim 40°$, we find Δv values exceeding three times the SDSS bin-width ($3 \times \delta v_{\mathrm{sdss}}$), the definition threshold for a DP signature (see Sect. 2.3). We find higher Δv values for snapshots of the gSa galaxy in comparison to the gSb galaxy, because of the more massive stellar bulge of the gSa galaxy, resulting in a deeper gravitational potential and thus in faster rotation in the centre. For all observations, the Δv value drops below the threshold of $3 \times \delta v_{\mathrm{sdss}}$ when observing perpendicular to the bar. This means that gas motion created by bars can indeed be at the origin of a strong DP feature. Furthermore, as a bar seen parallel to the line of sight is difficult to identify as such in galaxy images, the fraction of DP galaxies in observational studies may show a deficit of bars while bars are in fact the origin of a part of the double peaks.

We can compute the DP fraction f_{DP} as the fraction of directions from which a DP signature is observed. When observing at a redshift $z = 0.05$, the mean DP fraction is $f_{\mathrm{DP}} = 0.24$. This fraction drops to a mean value of $f_{\mathrm{DP}} = 0.2$ at redshift $z = 0.1$. As the fibre covers a larger part of the galaxy, more gas at lower velocities is included in the line-of-sight measurements, diluting the DP signature. However, at $z = 0.17$ we detect a mean DP fraction $f_{\mathrm{DP}} = 0.24$. This DP feature is partly originating from the bar and partly from a rotating disc. The latter effect becomes significant only at higher redshift as a larger part of the rotating disc is included in the line-of-sight velocity measurement.

4. Mergers and post-mergers

In the previous section, we showed that a DP signature can be the result of a rotating disc or a bar. However, in the course of a galaxy merger, two gas components can fall into the gravitational potential well of the interacting system with different line-of-sight velocities. This, in turn, can be observed as DP emission lines in a central spectroscopic observation. Late stages of post-coalescence major mergers are known to mostly form elliptical galaxies (e.g. Steinmetz & Navarro 2002). However, the expelled gas during a merger can be re-accreted and form a disc (e.g. Barnes 2002; Robertson et al. 2006; Lotz et al. 2008; Puech et al. 2009). Merger events can cause a contraction of a gas disc which then forms a central rotating star-formation site (Dekel & Burkert 2014). Such a nuclear disc can have a DP emission-line signature. Since a single minor merger is not expected to cause radical morphological transformations, we examine, besides major mergers, also the possibility of how a minor merger

can funnel gas into the central region and create a DP emission-line signature.

In order to explore a DP signature which is related to galaxy mergers, we here explore major mergers with a mass-ratio of 1:1 (giant + giant) and minor mergers with a mass ratio of 1:10 (giant + dwarf). As discussed in M20, DP signatures are mostly associated with spiral galaxies of type Sa and Sb and S0 galaxies. At high redshift, it is difficult to distinguish an elliptical galaxy of e.g. Hubble type E6 from a S0 or Sa galaxy. This motivates merger scenarii leading to earlier Hubble types. We thus select from the GalMer database the major-merger simulations gSa + gSa and gSb + gSb. For minor-merger simulations, we explore gSa + dSb and gSa + dSd. We evaluate possible DP signatures of the selected merger simulations from all directions, in the same way as in Sect. 3.3, for all three representative SDSS spectroscopic fibre diameters at redshift $z = 0.05$, $z = 0.1$, and $z = 0.17$ (see Sect. 2.2).

We consider major-merger simulations between two galaxies of the same type, leading to an equal contribution of gas in the resulting system. Even though we selected dwarf galaxies for the minor-merger simulations with the highest gas fraction compared to the giant gSa galaxy, the resulting gas mass ratio is still of 1:10 to 1:5 (see Table A.1). In order to identify two Gaussian components in an emission line as a DP signature, an amplitude ratio of at least three is necessary (See Sect. 2.3). However, dwarf galaxies have a significant lower metallicity than giant galaxies (Tremonti et al. 2004), which in fact leads to a stronger emission-line signal (e.g. Wolfire et al. 2010; Bolatto et al. 2013; Kewley et al. 2019). Since we aim to clarify quantitatively how a minor merger can generate a DP signature through internal kinematic processes, we multiply the signal from the giant galaxy by a factor of 0.5. The choice of this factor is purely empirical, since it results in a DP detection with two Gaussian components inside the line of sight. However, if one aims to obtain a more complete picture of the contributions of different gas populations in galaxy mergers, an accurate calibration of a radiative transfer would be necessary.

4.1. Merger simulation parameters

The GalMer database provides major and minor galaxy merger simulations. Major mergers are simulated with a total particle number of N_{tot} = 240 000 (120 000 + 120 000) particles, while minor mergers have N_{tot} = 528 000 (480 000 + 48 000), i.e. 4 times more particles for a giant galaxy than in a major merger, in order to resolve the dwarf galaxy (Chilingarian et al. 2010). Thus, the softening length for major mergers is $\epsilon = 280$ pc, and $\epsilon = 200$ pc for minor mergers. The initial conditions for each galaxy are set in the same way as for isolated galaxies described in Sect.3.2.1 with initial parameters for the different galaxy types summarised in Table A.1. The two galaxies are initially set at a distance of 100 kpc with an orbit characterised by the orbital angular momentum **L**. Giant-giant mergers simulations are carried out either with a direct-direct configuration in which the spins of both galaxies have a positive projection on the orbital spin (unit vector aligned with the orbital angular momentum), or with a retrograde-retrograde configuration, where the orbital spin is flipped. For the giant-dwarf mergers, simulations are carried out either with a direct-retrograde configuration as shown in Fig. 10, or with a retrograde-direct configuration. In the giant-giant mergers, the disc plane of one galaxy is always initially in the orbital plane while the other one has an inclination i_2 with respect to the plane (see Fig. 10). The giant-dwarf configuration is more generic: both discs are inclined with respect to the orbital plane (see Fig. 10) A detailed description of the orbital parameters for the GalMer database is given in Chilingarian et al. (2010). In the Tables A.2, we summarise the orbital parameters used in this work.

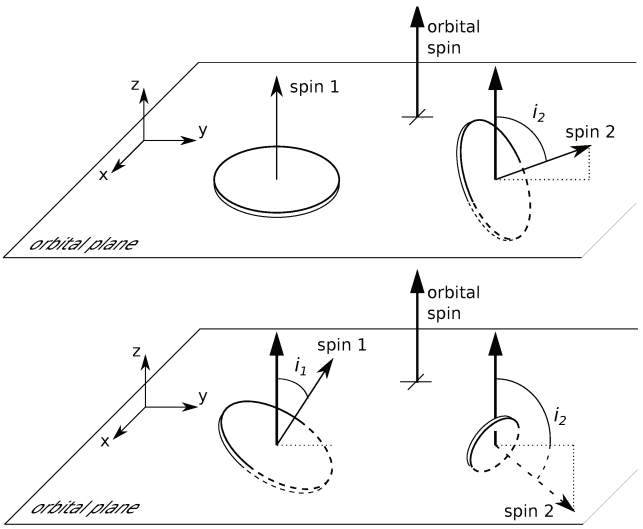

Fig. 10. Visualisation of merger orbits. Top: Initial configuration of a direct-direct merger between two giant galaxies. In the retrograde-retrograde configuration, the orbital spin is flipped. The inclination i_2 is set to 0, 45, 75, or 90°. Galaxy 1 has a spin of coordinates $(0, 0, 1)$, and galaxy 2, $(0, \sin i_2, \cos i_2)$. Bottom: Initial configuration of a direct-retrograde merger between a giant and a dwarf. In the retrograde-direct configuration, the orbital spin is flipped. The giant galaxy has an inclination $i_1 = 33°$ and the dwarf galaxy, $i_2 = 130°$. Galaxy 1 has a spin of coordinates $(0, \sin i_1, \cos i_1)$, and galaxy 2, $(0, \sin i_2, \cos i_2)$. In both panels, dashed lines indicate that patterns are below the orbital plane or behind the discs.

We are interested in DP emission-line signatures during mergers and after coalescence. We, therefore, sort out all fly-by simulations, in which the two galaxies only move away from each other after one single encounter, and retrograde minor mergers (with a retrograde configuration for the giant galaxy), whose final coalescence does not happen during the simulated period. Galaxy mergers with a retrograde orbit last longer in comparison to direct ones (Villalobos et al. 2012; Solanes et al. 2018). As mentioned in Sect. 3.2.1, the simulation design of the GalMer database does not include AGN feedback. This leads to high concentration in the very centre at the end, where almost no rotation is visible in the central gas. Depending on the merger process, the central in-fall of gas can happen with no gas being expelled. In such a situation, we do not see any DP signature and thus such scenarii are not interesting for this work and are sorted out. This happens more frequently in gSa + gSa mergers which is most probably related to the deeper gravitational potential from the final stellar bulge in comparison to gSb + gSb mergers. These selection criteria lead us to a final simulation sample of 16 major-merger simulations (5 gSa + gSa and 11 gSb + gSb) and 11 minor-merger simulations (6 gSa + dSd and 5 gSa + dSb).

4.2. Characterisation of the merger process and DP fraction measurement

To describe the orbit of a galaxy merger, we compute the COM and $r_{1/2}$ of each individual galaxy as described in Sect. 3.2.2. This allows us to compute the distance between the two galax-

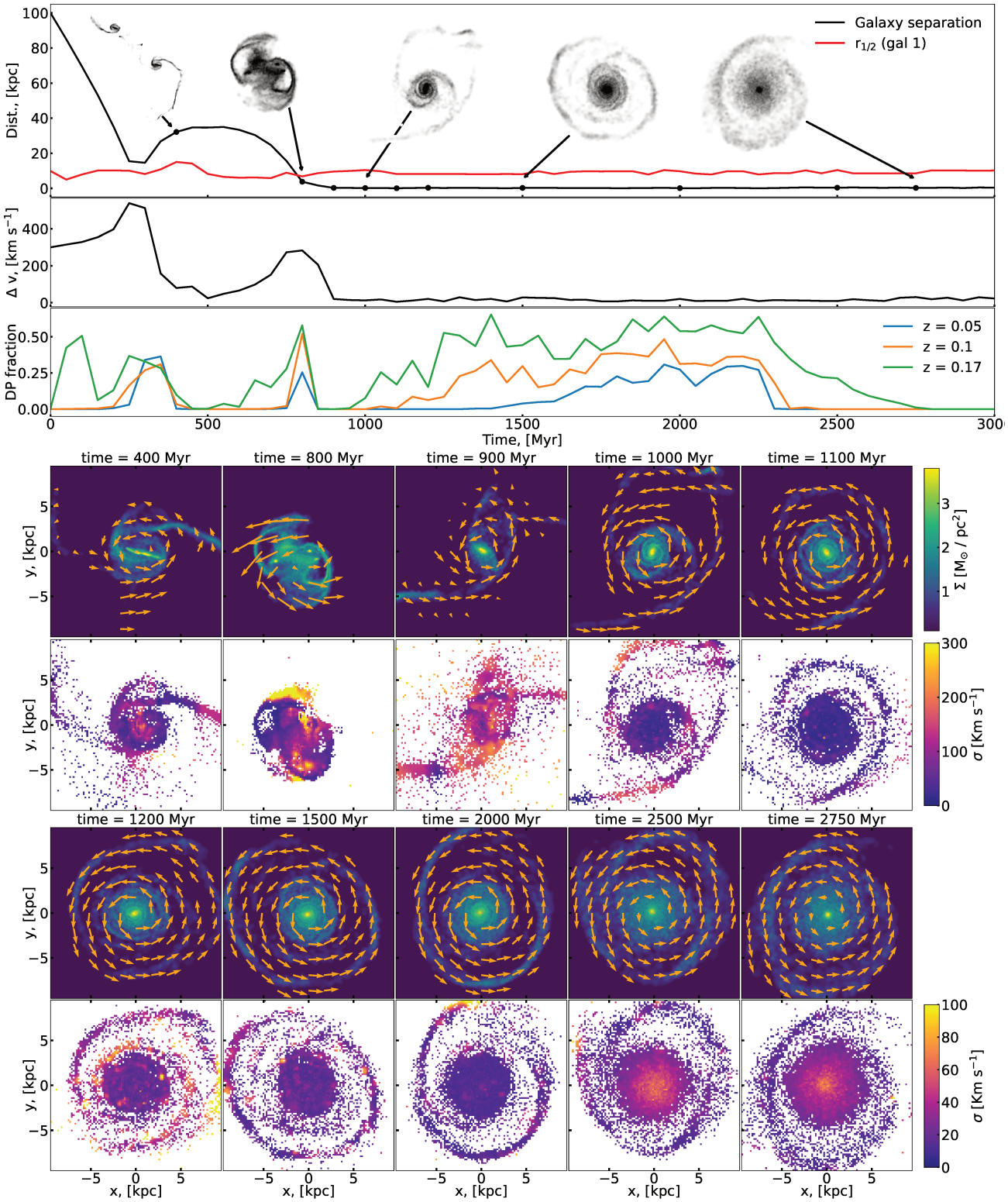

Fig. 11. Visualisation of a major merger process. We show characteristic parameters of the galaxy merger simulation of gSb + gSb with an orbit id 02dir and a merger inclination of 0° (See Sect. 4.1 and Table A.2). On the top panel, we show with a black line the distance between the COM of the two galaxies which corresponds to the distance between the two galaxies. The red line represents the half mass radius $r_{1/2}$ of the first galaxy. In order to illustrate the merger process, we show snapshots of only the gas at different merger stages. Black arrows indicate the exact stage of the merger process. On the second panel, we show the velocity difference between the two COM. On the third panel, we show the DP fraction which corresponds to the fraction of observation angles from which one detects a DP. On the bottom panels, we show zoomed-in observations of the central kiloparsecs of the first galaxy, we display, on the top panels, the 2D projection of the gas surface density Σ observed from a face-on view and the measured velocity dispersion σ on the panels beneath. To illustrate the gas dynamics, we show arrows representing the 2D projected in-plane velocity of the particles.

ies at each simulation step, shown as the black line on the top panel of Fig. 11. The $r_{1/2}$ value of the first galaxy is shown with a red line. In order to visualise the morphology of the gas during the merger, we show snapshots of the gas distribution of some simulation steps and use arrows to mark their position on the evolution of the simulation. In the second panel, we show the velocity difference between the two COMs. With these parameters, we can characterise the merger simulations: we clearly see the first peri-passage after about 250 Myr. This is the point where the velocity difference between the two galaxies is the highest. The two galaxies then recede from each other until the point at about 500 Myr where we see a maximum of their distance and a minimum of their velocity difference. The two galaxies then fall back onto each other and finally merge. We estimate some coalescence time as the time after which the distance between the two galaxies no longer exceeds the half-mass radius $r_{1/2}$ of the first galaxy. The velocity difference is also then dropping to 0.

In order to understand at what merger stage a DP emission line signature can be observed, we scan each simulation step from all directions as described in Sect. 3.3, with a uniform sampling of the sphere. For the major mergers, the origin of this scan is set to the COM of the galaxy whose disc is initially in the orbital plane. For the minor mergers, the origin is set to the COM of the giant galaxy. We also orientate the viewing angle with the spin of these reference galaxies. This provides us a DP fraction at each simulation step, which we show in the third panel from the top in Fig. 11 and B.1. For the gSb galaxies in major-merger simulations, we do not observe any DP emission-line signature in the initial conditions. However, we find for a redshift of $z = 0.17$ a DP fraction of about 0.6 for gSa galaxies which is in good agreement with the DP signatures found for an Sa galaxy with the same parameters using an axisymmetric model in Sect. 3.1, where we find a DP signature for inclinations larger than $\theta = 55°$, which covers about 60 % of a sphere. While the galaxies in major-merger simulations start with the initial parameters described in Sect. 3.1. minor-merger simulations start with already evolved galaxies. Therefore, the initial DP fraction in gSa galaxies is quite different in the initial snapshot of minor-merger simulations.

During the merger process, we always observe a peak of DP fraction during 50-100 Myr after a peri-passage. This phenomenon of two galaxies observed in the act of merging was analysed by Mazzilli Ciraulo et al. (2021) and will be discussed systematically in Halle et al (in prep.). As we know from observations, DP emission line signatures are not significantly more common in visually identified galaxy merger systems (Maschmann et al. 2020). Therefore, we here focus on DP signatures which appear in the post-coalescence phase of major and minor mergers.

4.3. Double-peak signatures in major mergers

Here we discuss systematically at what merger stage we can observe a DP signature. We furthermore discuss the significance of the observation angle and further discuss the morphology of the resulting galaxy.

4.3.1. Central discs in post major mergers

Major mergers are known to show strong morphological perturbations during the merger. In Lotz et al. (2008), the timescale during which a merger is observable from the photometry of equal-mass galaxy mergers was estimated to be of the order of 1.1 – 1.9 Gyr. This timescale can vary due to different orbital parameters which determine when the final coalescence happens. Looking at the exemplary gSb + gSb major merger shown in Fig. 11 and the gSa + gSa major merger in Fig. B.1, there is no DP signature directly after the final coalescence. However, at about 1 Gyr after the final coalescence, an increasing DP fraction is detected.

On the bottom panels of Fig. 11 and B.1, we display 10 snapshots of the central parts of the first galaxy at different simulation steps, marked with black dots in the galaxy separation diagram. We show for each selected time the gas surface brightness and the velocity dispersion. The line of sight is parallel to the spin vector so that discs are seen face-on. Gas motion in the plane is illustrated with orange velocity arrows. During the simulation of the gSb + gSb merger (Fig. 11), we observe a peak in DP fraction in an early phase at 400 Myr, shortly after the first encounter. A second peak is observed at 800 Myr, at the moment of post coalescence. In the snapshot of the central region of the first galaxy at 400 Myr, we identify a bar structure as the origin of the increase in the DP fraction. As discussed in Sect. 3.3, a central bar structure in the gas distribution can create strong DP signatures, especially for small spectroscopic fibre diameters. For the second peak in DP fraction at 800 Myr, we can identify the two galaxies at a separation less than 4 kpc and with a velocity difference of 300 km s^{-1}, creating a DP signature as two gas populations with high Δv are captured inside the spectroscopic fibres. The two galaxies are no longer moving away from each other and this moment marks the final coalescence.

Shortly after this final coalescence, the detection of DP stops abruptly. We observe in these stages a high concentration of gas in the very centre with a strong velocity dispersion which dominates in the observed region. In fact, the strong velocity dispersion is not sufficient to produce a broad emission-line profile which can be identified as a DP. About a few 100 Myr after the final coalescence, a gaseous central disc with a radius smaller than 5 kpc starts to form. In contrast to the strong perturbations during the coalescence the gas starts to settle in the disc and the velocity dispersion decreases. The in-falling gas originates from parts of the tidal tails which gradually fall back onto the galaxy. As the stellar bulge of the post-merger galaxy gradually grows, the rotation curve becomes increasingly steep in the centre. As we know from Sect. 3.1, a steep rotation curve is needed in order to detect a DP signature at lower redshift because e.g. at $z = 0.05$, only the central 3 kpc of the rotation curve is measured. This gradual steepening of the rotation curve explains why we start detecting a DP signature later during post-coalescence in low redshift observations than high redshift ones.

The detected DP signature eventually disappears at about 2500 Myr. At this point, the gas contracts drastically to the very centre and the central part of the disc is dominated by random motion which can be seen as the velocity dispersion increases. As mentioned in Sect. 3.2.1, this is due to low feedback efficiency. It is therefore difficult to say whether such a rapid collapse is realistic or whether a central disc can fall so quickly into the centre. Therefore, in the following, we only consider simulation snapshots up to the moment when we also see a gas distribution that is not contracted below he resolution.

We computed the DP fraction for all selected major-merger simulations and observe a recurring pattern: strong DP detection is observed at close interactions and a gradually increasing DP fraction emerges between 500 and 1000 Myr after the final coalescence. In Fig. 12, we show the DP fraction observed at $z = 0.05$ seen after the final coalescence for all selected major-merger simulations. We see, that for gSb + gSb mergers, a DP

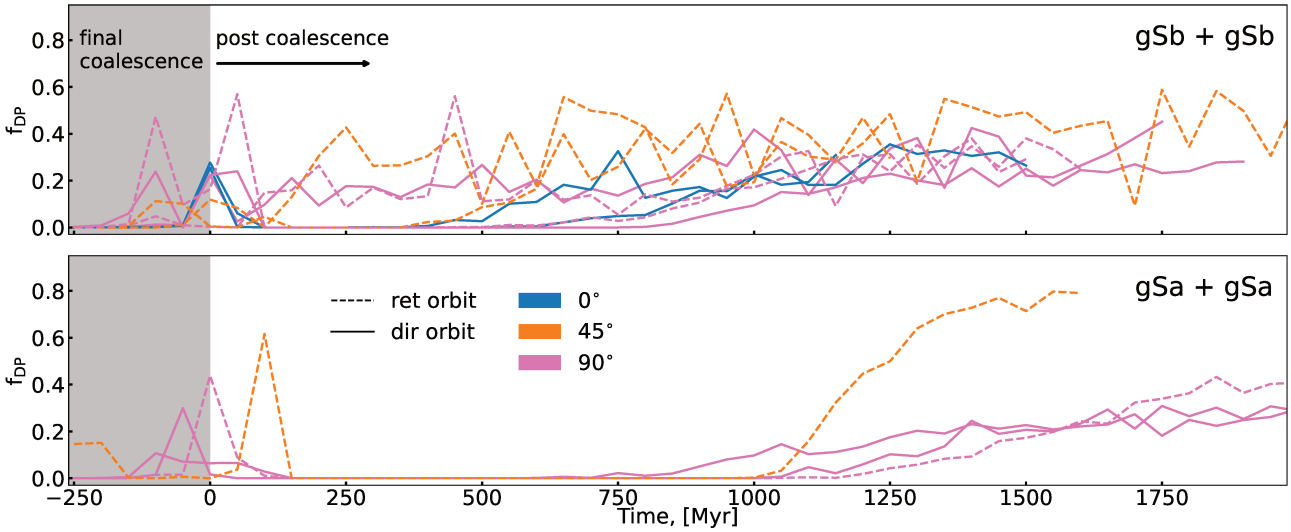

Fig. 12. Evolution of the DP fraction of major-merger simulations after the final coalescence observed at $z = 0.05$. We identify the snapshot in each simulation where the distance between the two galaxies remains below the half mass radius of the first galaxy for the rest of the simulation. We use this snapshot as reference point and show the time starting 250 Myr before this snapshot on the x-axis. On the y-axis, we show the DP fraction f_{DP}. On the top (resp. bottom) panel, we show gSb + gSb (resp. gSa + gSa) simulations. We mark the time before the final coalescence in grey. We mark simulations with an inclination of 0°, 45° and 90° of the second disc (see Fig. 10) with blue, orange and pink lines, respectively. Mergers with direct (resp. retrograde) orbit are presented by solid (resp. dashed) lines.

can be detected between 500 and 1000 Myr after the final coalescence and in some cases we see a DP continuously since the final coalescence. We identify in all these cases a gaseous disc which is progressively formed from gas of the tidal tails falling into the central kiloparsecs of the galaxy. In the post-coalescence phase of the gSa + gSa simulations, we observe an increase in DP fraction but starting 1000 Myr after the final coalescence. This delay is mostly due to the fact that in comparison to gSb + gSb mergers, gSa + gSa mergers stabilise the gas due to a deeper gravitational potential and therefore, the gas takes longer to migrate towards the central region. As can be seen in the appendix in Fig. B.1, the central discs found in post-merger gSa + gSa galaxies are significantly smaller at a radius below 3 kpc in comparison to the discs observed in gSb + gSb simulations. However, this simulation stands out among other gSa + gSa simulations as it shows the smallest disc which we observed in any post-coalescence mergers. This strong concentration leads to a high DP fraction of about 0.8 at the end of the simulation.

The post-coalescence behaviour of the DP fraction is only shown for observations at $z = 0.05$ in Fig. 12. For the observations at $z = 0.1$ and $z = 0.17$, we find a similar evolution of the DP fractions but higher fractions than one can see for the example shown in Fig. 11. In Fig. B.1, however, we see in the late development of the central disc a larger DP fraction for the observation at $z = 0.05$ which only covered the central 3 kpc than for the other redshifts. This is due to the fact, that observations at higher redshift includes gas located outside the central disc and with more random motion, diluting the DP signal. Considering the different merger orbits we discussed here, we do not find any dependence on the orbital geometry of the resulting DP feature.

4.3.2. Angular dependent double-peak emission lines in the post coalescence

To visualise the observation angles from where we mostly observe a DP signature in the post-coalescence phase, we calculated an observation angular depending DP probability p_{DP}. We selected all simulation snapshots 1000 Myr after the final coalescence, which show a DP fraction of at least 0.1. We then calculated a DP probability for each viewing angle as the ratio between the number of DP detections and the number of included snapshots. We did this separately for gSb + gSb and gSa + gSa simulations and further divided them into the three observed redshifts $z = 0.05, 0.1$, and 0.17. This provides maps, presented in Fig. 13, indicating the most favourable observation direction for DP signatures or rule out specific observation angles.

We do not find any DP detections when observing face-on which is expected, as we observe rotating discs in all post-coalescence phases. However, for gSa + gSa simulations we find in some cases a DP signature up to an angle of 20°. For the observations at low redshift ($z = 0.05$), we see for gSb + gSb galaxies that edge-on observations are less favourable to detect a DP than observations at an inclination of about $\theta \sim 60°$. This is due to the same reason as we discussed for DP observations in galaxies with bar signatures in Sect. 3.3: when seen perfectly edge-on, more gas moves perpendicular to the observer. Since we observe only a small part of the velocity gradient in the central 3 kpc at a redshift of $z = 0.05$, this gas moving at a null projected velocity dominates the emission-line profile, and the DP signature produced by the rotation is not detectable anymore. However, at a smaller inclination, significantly less gas moving perpendicular to the observer contributes to the observed spectrum and the rotation footprint dominates. This effect gets weaker at a redshift $z = 0.1$ and disappears at $z = 0.17$ because the spectroscopic fibre probes a larger part of the rotation curve, and a broader emission line profile is observed.

For gSa + gSa merger simulations, we find an even stronger direction dependency. In fact, we see for all three different redshifts a strong DP fraction at inclinations of $30° < \theta < 60°$. This is due to the fact that the central disc is more concentrated in comparison to what we see in gSb + gSb simulations. In such a case, a DP signature gets more diluted when viewed edge-on due to gas moving perpendicular to the line of sight. At redshift $z = 0.05$ and $z = 0.1$, it is furthermore very unlikely to observe

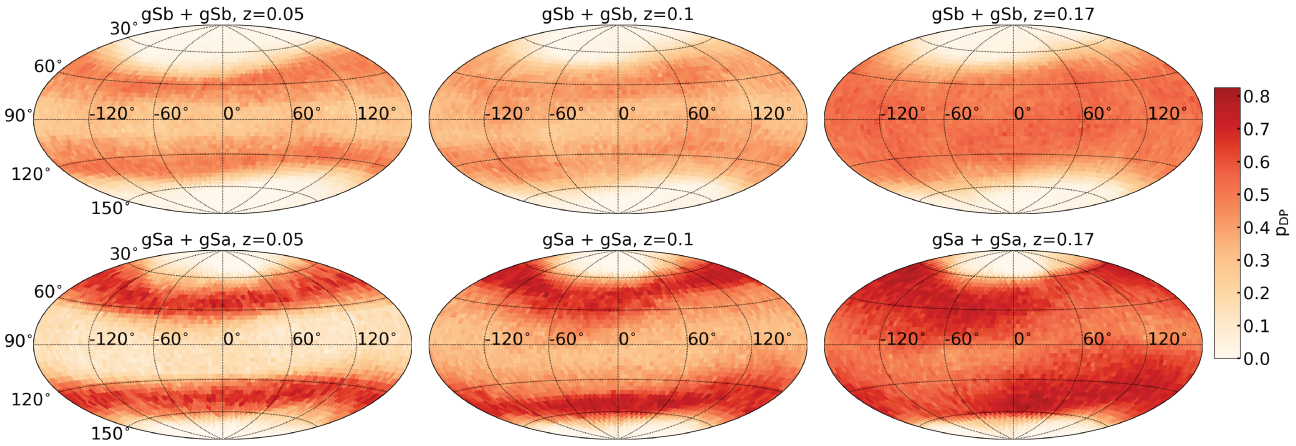

Fig. 13. Direction maps of DP detection probability p_{DP} in post-coalescence major-merger simulations. We present maps of p_{DP} for the three different evaluated redshifts ($z = 0.05, 0.1$ and 0.17) and for the two discussed merger simulations gSb + gSb and gSa + gSa separately. We calculate the probability of each scanned direction from all simulation steps 1000 Myr after the final coalescence that have a DP fraction > 0.1.

a DP signature from an edge-on perspective. Only for a redshift of $z = 0.17$, we start to detect DP signatures from the edge-on view. Since these observations cover a larger surface, gas that is just about to fall back to the central regions is included in the line-of-sight velocity distribution and broadens the emission line.

4.3.3. The morphology of post-coalescence major mergers

One of the central results of M20 is that DP emission-line signatures are more likely found in S0 galaxies and in bulge-dominated disc galaxies. Furthermore, no higher merger rate was found in comparison with single-peak emission-line galaxies at the same redshift and with the same stellar mass distribution. In order to discuss how relevant major mergers are for the discussion on the origin of DP signatures, two aspects are of particular interest when looking at the morphology: (1) do the post-coalescence mergers still show disc components and (2) can tidal features and merger remnants still be identified with photometric observations? In order to test this hypothesis, we computed mock *rgb*-images created with the g', r', and i'-band filters of the galaxies 1000 Myr and 1500 Myr after the final coalescence. The broadband colours are computed from stellar population PEGASE-HR models (Le Borgne et al. 2004) which is implemented in the GalMer database access[2] (Chilingarian et al. 2010). In order to estimate the intensity in each band, light rays are traced along the line of sight and attenuation through dust was included. The dust was modelled as explained in Chilingarian et al. (2010). In Fig. 14 (resp. 15), we show the *rgb*-images for the face-on and edge-on perspective for the gSb + gSb (resp. gSa + gSa) merger simulations. In only some snapshots, we are able to identify small tidal features or a miss-aligned dust-lane that can indicate a recent merger. For the majority of snapshots, we observe a smooth morphology. In the two cases of gSb + gSb galaxies with a collision angle of 0°, we even observe a prominent disc. However, as discussed in Chilingarian et al. (2010), these kinds of orbits are unlikely to happen. For all other simulations, we observe an elliptical galaxy which in some cases still has a disc or has a high ellipticity and is of Hubble type E6 or can be identified as S0, as discussed in Eliche-Moral et al. (2018).

[2] http://galmer.obspm.fr/

4.4. Double-peak signatures in minor mergers

Since minor mergers are discussed to be responsible for a large fraction of observed DP emission-line galaxies in the literature (e.g. M20), we here discuss how such a kinematic signature can originate from a minor merger event. We explore the merger orbits in the same manner as we discussed major mergers (see Sect. 4.3) and discuss their morphology.

4.4.1. Two gas populations detected in one spectra

In order to explore how a minor merger can produce a central DP signature, we compute the directional depending DP fraction of all minor-merger simulations selected in Sect. 4.1. In Fig. 16, we visualise the merger process of a direct (for the giant galaxy) merger encounter between a gSa + dSd and with the orbit-id 3. In comparison to the orbits observed for major-merger simulations (see Sect. 4.3), we observe longer merger timescales for minor mergers until the final coalescence. In fact, retrograde (for the giant galaxy) orbits take, for minor-merger simulations, longer than the simulated time span to reach coalescence. Since we are interested in post-coalescence behaviour of galaxies, we selected 6 gSa + dSd and 5 gSa + dSb simulation with direct orbits.

During the merger process, we can clearly identify the two nuclei of the giant and the dwarf galaxies. During close encounters of the two nuclei, we can observe a DP signature. However, only at the final coalescence, where the nuclei of the dwarf galaxy migrates closer than the half mass radius of the giant galaxy, we clearly see a DP signature with observations of the very centre. In this simulation step, the two nuclei are inside the spectroscopic fibre measurements of the $z = 0.05$ observation. In Fig. 16, we present the 2D projection of two close encounters and the direction maps indicating from which direction one can observe the highest Δv with a double-Gaussian fit to the line-of-sight velocity distribution. In the first encounter at 1400 Myr, the two nuclei are separated by a distance of less than 5 kpc. We observe a DP signature in more than 50 % of the directions at a redshift of $z = 0.17$. This is due to the fact that the 3″ spectroscopic fibre covers the central region of 10 kpc and therefore covers the two nuclei. This is not the case for observations at a redshift of $z = 0.05$ and $z = 0.1$ and the DP fraction for these observations is significantly smaller. In fact for smaller redshift one can only detect a DP when observing from an angle where

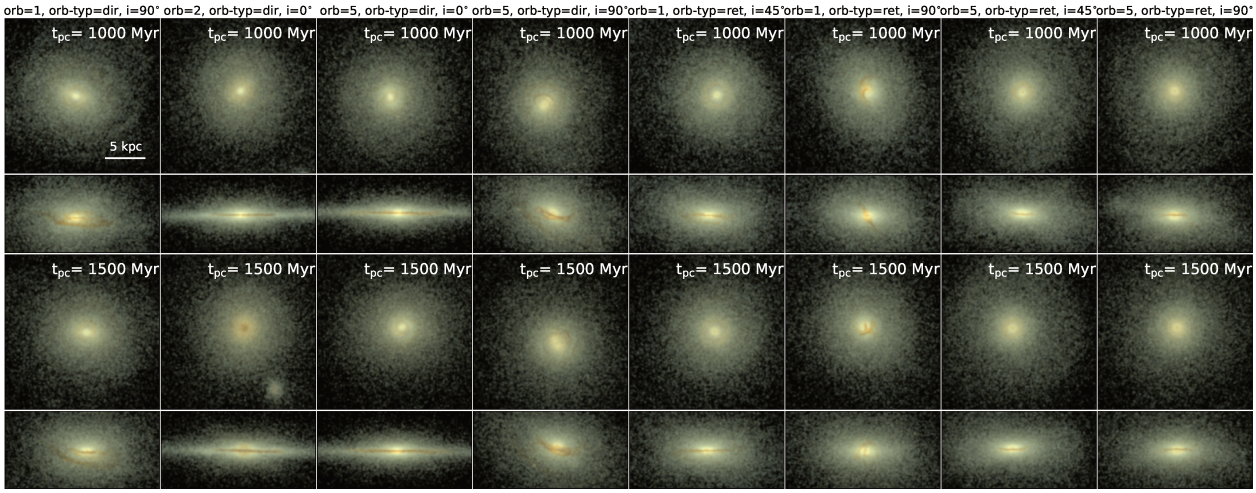

Fig. 14. Mock *rgb* snapshots created with g', r', and i' bands of gSb + gSb merger simulations. The images were produced using the radiative transfer software PEGASE-HR (Le Borgne et al. 2004). We precise the orbital parameters in the title and show below each simulation from the face-on ($40 \times 40\,kpc$, 200×200 pixels) and edge-on ($20 \times 40\,kpc$, 100×200 pixels) perspective at 1000 Myr and 1500 Myr after the final coalescence.

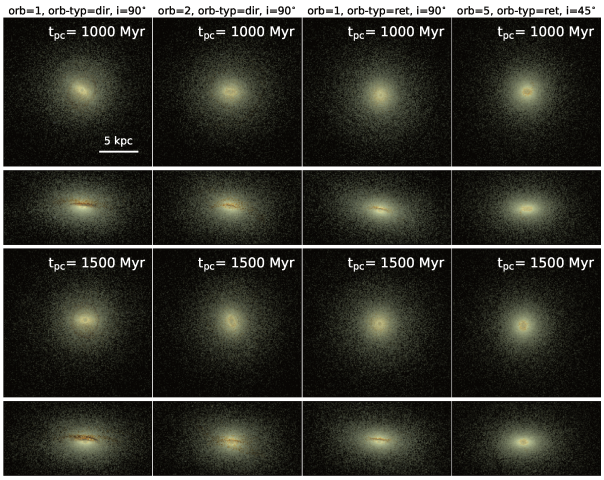

Fig. 15. Same as Fig. 14, but for gSa + gSa simulations.

both nuclei are covered by the fibre. This is shown in the bottom-left panels of Fig. 16, where we only detect a signal of the dwarf galaxy for a small set of observation angles. On the bottom-right panels of Fig. 16, we show the measured Δv for the snapshot where the two nuclei are separated at about 1.5 kpc before finally merging to one nucleus. A spectroscopic observation at a redshift $z = 0.05$ covered both nuclei and a large Δv value of up to $400\,\mathrm{km\,s^{-1}}$ can be observed. For this specific case we also observe a DP for observations nearly face-on with an inclination of $\theta \sim 10°$.

Taking all minor merger observations into account, we can see a clear pattern: at close encounters, we find higher DP fractions. However, for the redshift of $z = 0.05$, the value is largest in the closest configuration directly before the two nuclei finally merge. After the final coalescence, no DP can be detected and no rotating disc as seen in major mergers is formed. In Fig. 17, we show the DP fraction of all minor-merger simulations at the final coalescence observed at different redshifts. As described in Sect. 4.2, the final coalescence is defined by the moment where the COMs of the two galaxies approach each other less than the half mass radius of the giant galaxy without subsequently moving away from each other. For the redshift $z = 0.17$, we observe DP signatures between 50 to 350 Myr after the final coalescence. This is in all cases the moment when the two nuclei are closer than the spectroscopic fibre size. Since for the redshift at $z = 0.1$ and $z = 0.17$ the fibre size is larger we see in these observations a DP signature earlier in the final coalescence. However, the moment of the last detected signature does not depend on the redshift. This is due to the fact that the two nuclei finally merge. By observing the directions of detection of DP at the final detection, we do not see a preferred observation direction and a DP can be seen from a face-on view in some cases.

4.4.2. The morphology of minor mergers at the final coalescence

At the moment of final coalescence in major mergers, one can find high DP fractions similar to minor mergers. However, there is a big difference: major mergers show very strong perturbations at this moment which is easy to identify even at a higher redshift. Minor mergers, on the other hand, are not known to have such a strong impact on the morphology. In Fig. 18, we present the morphology of all the minor-merger simulations after the final coalescence when the largest DP fraction at $z = 0.05$ is measured. In only one case, the two nuclei can be clearly identified from the face-on, although this would only be visible with high-resolution images. In all post-coalescence minor mergers, we see a nearly undisturbed disc structure and it would be difficult to distinguish such a galaxy from an isolated galaxy.

5. Discussion

5.1. Double-peak signatures from rotating discs: isolated galaxy vs. post merger

A spectroscopic observation of an entire rotating gaseous disc is known to describe a double-horn profile, when observed inclined (e.g. Westmeier et al. 2014). However, this is well known for the HI line, measured for an entire galaxy. Ionised gas kine-

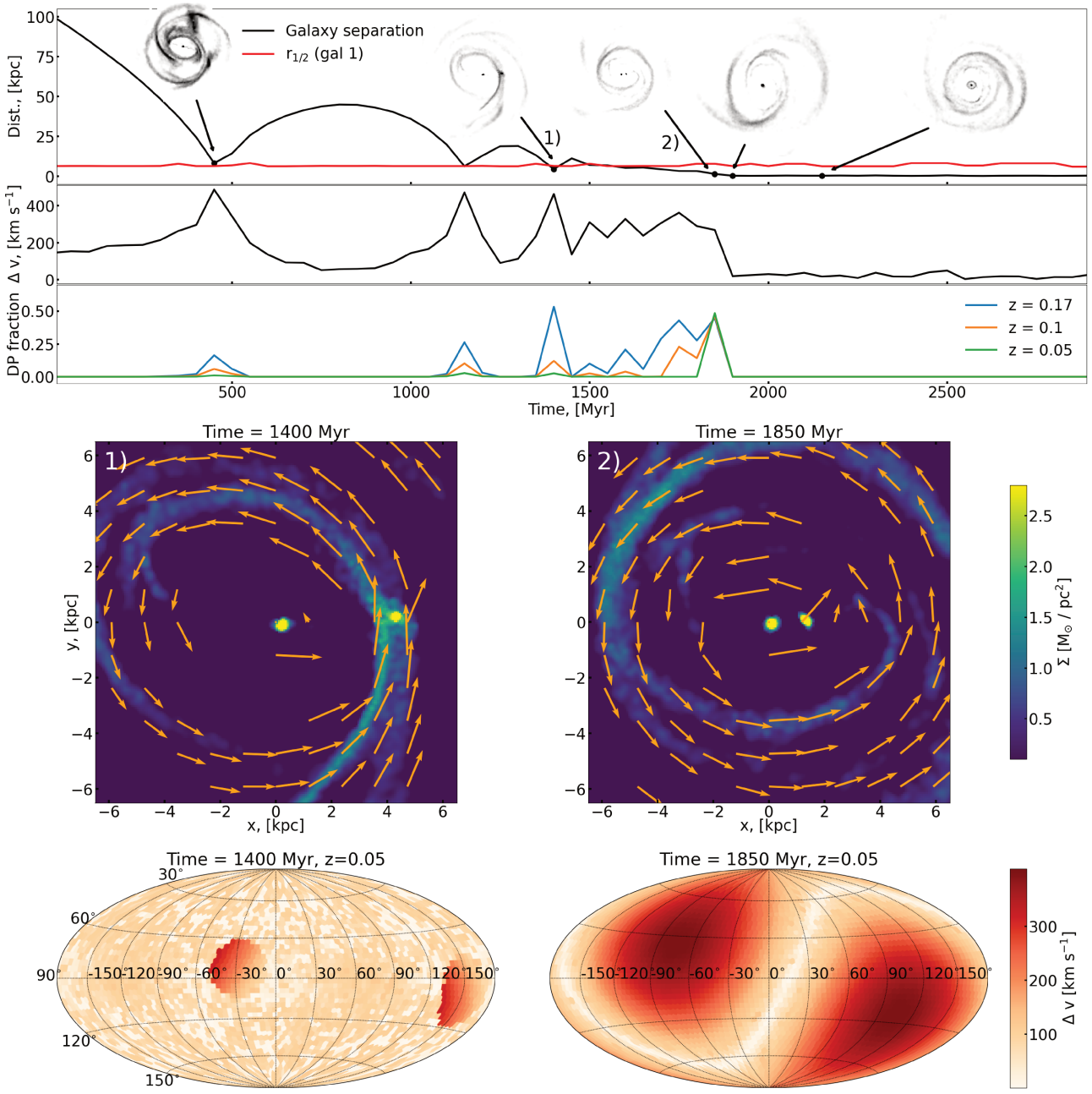

Fig. 16. Visualisation of a minor merger between a gSa + dSd, simulated with the orbit-id 3 and a direct collision. We show the top panels and two 2D projected gas maps in the same manner as described in Fig. 11. We show two specific snapshots: one close encounter and the moment of final coalescence. The two 2D-projected snapshots are indicated with numbers to better assign them to the orbit, shown on the top. On the two bottom panels, we show direction maps and indicate, with colour maps, the Δv measured with the double-Gaussian fit to each observed spectrum.

matics in the centre of a galaxy, on the other hand, traces only an inner small part of the rotation curve. Massive bulges in disc galaxies are known to create a strong velocity gradient in the central region (Sofue & Rubin 2001). Using axisymmetric models of discs with pure rotation, we find that the DP signature primarily depends on the angle of observation: the higher the inclination, the larger the separation of a double-Gaussian fit. Furthermore, we find the strongest DP signatures for high bulge concentrations when only observing the central 3 kpc. This analytical view points out one aspect quite clearly: DP emission lines have a strong connection to the bulges of galaxies. Accordingly, massive or highly concentrated bulges in galaxies can create a sufficient deep gravitational potential to cause high velocity gradients at the centre.

In Sect. 4.3, we find that a centralised disc can be formed in a late stage of a post major galaxy merger. Major mergers generally destroy the disc morphology of the two progenitors and result in an elliptical galaxy as demonstrated in Farouki & Shapiro (1982); Negroponte & White (1983). These findings were further confirmed for dry major mergers (Peschken et al. 2020). For gas rich major mergers however, a disc can be formed in the post merger phase from a gaseous disc that subsequently re-

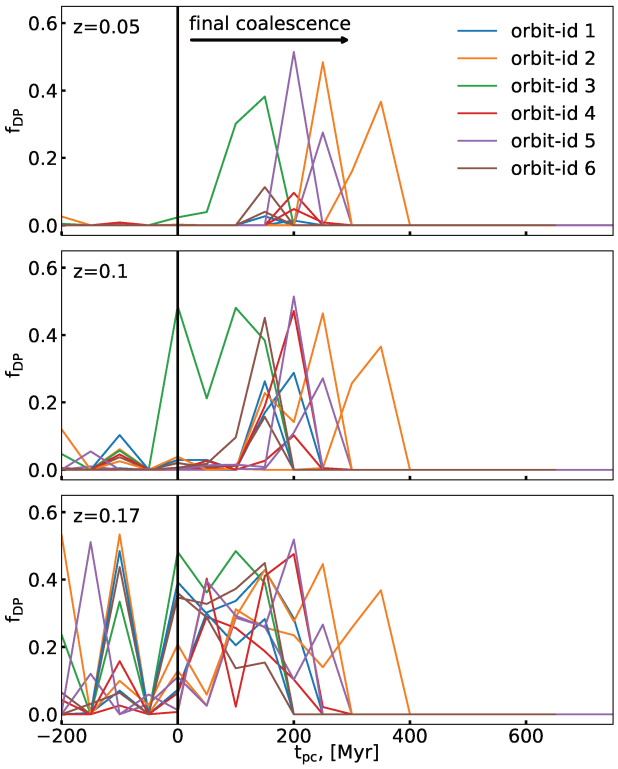

Fig. 17. Double peak fraction observed at different redshifts after the final coalescence of minor-merger simulation. On the *x*-axis, we show the post-coalescence time t_{pc}, starting at the moment of final coalescence. The moment of final coalescence is marked by a black line and the values of DP-fraction are indicated on the *y*-axis. The line colour represents the orbit-id specified in Table A.2.

settles (Governato et al. 2009; Hopkins et al. 2009). In violent major mergers which undergo a phase of ultra-luminous infrared emission, a centralised molecular gas disc was detected in Downes & Solomon (1998). Puech et al. (2009) reported a gas rich disc which might be the result of a collapse of a larger disc or a major merger.

After the final coalescence of a major merger, in-falling gas from tidal tails can form a rotating gaseous disc over long periods of time (Barnes 2002). In the major-merger simulations which we consider in this work, we do see this behaviour: at about 1000 Myr after the final coalescence, gas which was slung far outside the merging system due to tidal tails formed a central disc, which we observe as a double-peak emission line. We do see stronger DP signature for the resulting galaxy of a gSa + gSa galaxy merger in comparison to a gSb + gSb. This is most likely due to the progenitors of the latter having less massive bulges and the resulting rotation curve shows smaller velocities in the centre.

Regarding the morphology of the late stages of major mergers, we observe indeed mostly early type morphologies. Only in mergers with the two discs in the orbital plane do we observe a prominent disc structure in the resulting galaxy. However, besides such mergers, we do not find any dependencies on the orbital geometry of the merger, which was further discussed in Mihos & Hernquist (1996). At the observed stage of post-coalescence, we do not observe strong tidal features in the central kiloparsecs, which is in line with the findings from Lotz et al. (2010). In this work, we only consider visual merger identification similar to e.g. Domínguez Sánchez et al. (2018) or Willett et al. (2013). This is only sensitive to prominent tidal features and perturbations which are detectable in early merger stages. The detection of post-coalescence galaxy mergers are difficult to detect and are often accompanied by large bulges (e.g. Barnes & Hernquist 1991; Barnes 1992) or dual nuclei (e.g. Komossa et al. 2003). However, the presence of large bulges do not give any insight concerning the merger time-scale, and in order to identify dual nuclei, high-resolution observations are needed. By combining multiple imaging predictors to a linear discriminant analysis method, it is possible to correctly identify post-coalescence galaxy mergers as shown with simulated galaxies by Nevin et al. (2019). When including stellar kinematics, observed with integrated-field spectroscopy, the post-coalescence mergers can be even better identified (Nevin et al. 2021). In a similar work on galaxy mergers from cosmological simulations, Bottrell et al. (2022) have shown that accurate identification can also be achieved with neuronal networks, even though they find that the kinematic input has a less significant contribution compared to the imaging input.

For the post coalescence major mergers in this work, we find morphologies indicate a strong ellipticity so that the galaxies can be identified as lenticular galaxies. This was discussed for the same merger simulations in Eliche-Moral et al. (2018). These galaxies can correspond to the excess of DP S0 galaxies, found in M20. However, these configurations of post-major mergers form around 1 Gyr after the final coalescence. The increased star-formation rate associated with a merger has already faded away at this merger stage (Mihos & Hernquist 1996; Di Matteo et al. 2007). Hence, this is in conflict with the increased star-formation rates found for DP galaxies (Maschmann & Melchior 2019; Maschmann et al. 2020, 2022).

5.2. Strong double-peak features in disc galaxies: Bars or minor mergers?

In contrast to major mergers, minor mergers are less violent and the merger morphology is detectable only up to 100 Myr after the final coalescence using photometry (e.g. Lotz et al. 2010). In addition to that, within this timescale an enhance star-formation rate can be induced by the merger (Di Matteo et al. 2007). Considering the excess of S0 and Sa galaxies and the central star formation enhancement found in star-forming DP galaxies (M20), a minor merger can explain the observed characteristics of DP emission-line galaxies. During a close encounter in a minor merger, one can observe a DP signature which is similar to the case discussed in Mazzilli Ciraulo et al. (2021). However, this is not necessarily the final stage of the merger but a superposition of two galaxies aligned with the line of sight. This phenomenon will be addressed in greater detail in Halle et al. (in prep.). In this work, however, we set the focus on how to create a DP signature which cannot be identified though visual inspection. Depending on the merger orbit, the dwarf galaxy can enter from any direction into the central region and we therefore do not detect any directional dependence. In some cases, we even observe a strong DP signature from a face-on perspective. Within 350 Myr, the two nuclei finally merge and no DP signature can be detected anymore. In the merger stage of final coalescence, when we observe the highest DP fraction, we only see weak tidal features in the central kiloparsecs. The two nuclei would be only visible with high resolution imaging or in very nearby galaxies. furthermore, minor mergers are considered to happen more fre-

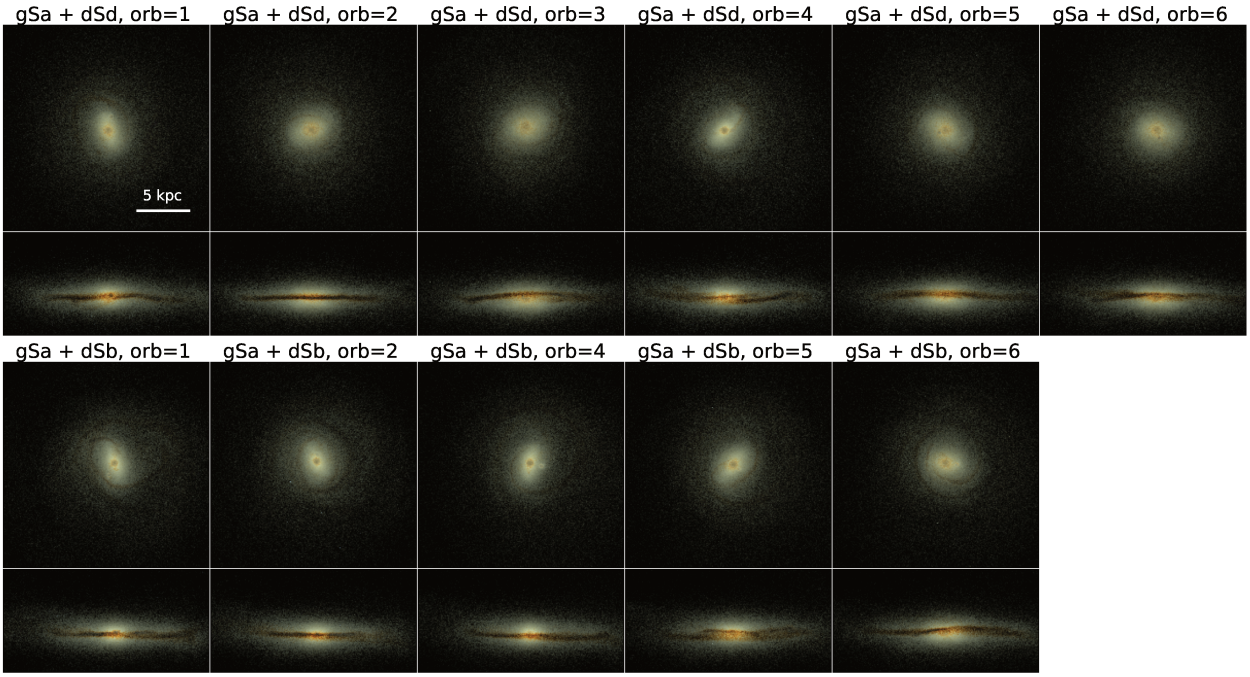

Fig. 18. Mock *rgb*-images of gSa + dSd and gSa + dSb merger simulations computed in the same manner as in Fig. 14

quently than major mergers in the late universe (Conselice et al. 2005; Noeske et al. 2007).

As mentioned in Sect. 5.1, a bar feature in isolated galaxies can also create a DP emission line. In Sect. 3.3, we explore bars in simulated Sa and Sb galaxies and find a DP when viewing from a perspective parallel to the bar. Barred galaxies are considered to be effective in transporting cold gas inwards, leading to central growth and rejuvenation of SF in the central region (Chown et al. 2019). On the one hand, minor mergers can trigger a central star-formation enhancement (e.g. Dekel & Burkert 2014), on the other hand, however, bars are considered to trigger central star bursts more effectively than galaxy-galaxy interactions (Ellison et al. 2011). Therefore, also barred galaxies would be a considerable mechanism to produce a strong DP emission-line signature accompanied by a central star-formation enhancement.

Observing a bar parallel to its major axis can lead to a false classification of a disc galaxy with a symmetric bulge. In fact, M20 finds only 3 % barred galaxy for DP emission-line galaxies. However, the used identification of this galaxy type is favouring less inclined and face-on galaxies as they are detected with a machine-learning algorithm described in Domínguez Sánchez et al. (2018). Thus, a large part of more inclined barred galaxies might be not detected, the bar being hidden due to the viewing angle. In principle, bars can occur in spiral and S0 galaxies. These types make up half of the M20-DP galaxy sample (16 % spiral and 36 % S0 galaxies). By combining a bar fraction from observations and the estimated DP fraction due to a bar, we can estimate whether bars can be responsible alone for the significant increase in DP S0 galaxies observed by M20. We adopt a bar fraction of spiral galaxies of P(bar|spiral) = 0.66 (Eskridge et al. 2000) and for S0 galaxies of P(bar|S0) = 0.46 (Laurikainen et al. 2009). In order to estimate the frequency of S0 and spiral galaxies, we use the same morphological selection of these galaxy types as performed in M20, based on Domínguez Sánchez et al. (2018), for SDSS galaxies. We further restrain the selection to a similar stellar mass and redshift distribution by applying a stellar-mass cut of $M_* \geq 10^{10.5}\,M_\odot$ and a redshift cut of $z \leq 0.2$. This selection results in fractions of P(spiral) = 0.131 and P(S0) = 0.255. The fact that we find more S0 galaxies is due to the selection of galaxies with high stellar masses which is similar to the selection in M20. Since we assume a lower probability of S0 galaxies exhibiting a bar (P(bar|S0)), it is rather unlikely that the factor $\sim$ 2 we see in the ratio between S0 and spiral galaxies in the M20-DP sample can be explained purely by bars. However, this estimation is based on two simplified assumptions: first, that bars in S0 galaxies produce the same DP fraction as in spiral galaxies and second, that the bar fraction is constant for all stellar masses $\geq 10^{10.5}\,M_\odot$, which is not the case (Zhou et al. 2020; Zhao et al. 2020; Roshan et al. 2021). In this paper we address the fundamental question of which mechanisms can cause DP signatures. However, it is difficult to estimate which of these effects is more likely based on idealised simulations and we therefore plan to estimate this question in a future work.

5.3. Resolving double-peak emission lines and the importance of future surveys

Here, we discussed multiple mechanisms which can lead to a DP signature observed in a central spectroscopic observation of a galaxy. However, considering only a central spectrum and a snapshot in the optical light, one cannot conclusively determine the origin of the DP emission line. In order to distinguish between the different mechanisms, discussed here, additional information about a spatial distribution of the kinematic signatures is needed.

As shown in Mazzilli Ciraulo et al. (2021), relying on integrated field spectroscopy with the Mapping Nearby Galaxies at APO (MaNGA, Bundy et al. 2015) survey, one can spatially disentangle two different gas components. In this very case, the central DP signature found in the central 3″ SDSS spectrum, originates from two superposed discs. Long-slit spectroscopic

observations provide a spatial resolution and Comerford et al. (e.g. 2009b, 2011); Müller-Sánchez et al. (e.g. 2015); Nevin et al. (e.g. 2016) and Comerford et al. (2018) succeeded in resolving a dual AGN as the underlying mechanism of a detected DP and distinguished them from other mechanisms such as gas outflows or rotating discs. Therefore, the mechanisms, discussed in this work should be studied in greater detail by means of surveys such as MaNGA, but at the same time the basic understanding of these phenomena should be investigated with further simulations. Cosmological simulations, in particular, offer a special opportunity as they provide a much greater diversity of different merger scenarii, and galaxies are in constant interaction with their environment. Furthermore, the inclusion of AGN feedback allows to even further discuss how DP emission lines are connected to physical processes (Somerville & Davé 2015; Vogelsberger et al. 2020). A complete analysis of SDSS-like spectroscopic observations in cosmological simulations may also provide insight into which underlying process is more likely (e.g. bar signatures or minor merger).

By aiming for a better understanding of the kinematic footprint of gas in galaxies, we might also be able to apply such insights to upcoming surveys. The SDSS only observed galaxies in the late Universe. By using DP emission-line signatures as a tracer to study gaseous discs and galaxy mergers, we can better estimate the merger rate over larger ranges of redshift. This would help us to understand for example how galaxies evolve through mergers and quantify how the star-formation rate is connected to such phenomena. Two upcoming surveys are of special interest for this very task: the VLT 4MOST survey as it probes emission-line galaxies up to a redshift of $z = 1.1$ (Richard et al. 2019) and the EUCLID mission which will provide spectroscopic data for galaxies up to $z \sim 2$ (Laureijs et al. 2011). Spectroscopic observations from the EUCLID mission will not be able to resolve DP signatures due to the insufficient spectral resolution of R=250 at a pixel size of $0.3''$, however, the high imaging resolution of $0.1''$ will enable to probe earlier stages of merger with an unprecedented sample size. Visual galaxy mergers and DP emission-line galaxies can be used as a tool to select promising candidates in the high redshift universe and compare the measured kinematic footprint and merger rate to the ones we know from the late Universe.

6. Conclusions

A double-peak (DP) emission line, observed in the centre of a galaxy is a peculiar feature, as it offers insights into the central kinematic processes. This kinematic footprint has been used to find dual active galactic nuclei (AGN) or AGN-driven gas outflows. In recent studies, a broader search for DP galaxies has been conducted in order to shed light on this phenomenon from a more general perspective. The resulting DP sample showed that AGNs represent only a small subgroup and the majority shows only moderate or no AGN activity. Furthermore, DP galaxies are predominantly S0 or disc galaxies with large bulges and no increased merger rate was observed. Taking into account that star-forming DP galaxies exhibit a central star-formation enhancement, the most plausible explanation would be the observation of a minor merger. However, without followup observations one cannot conclusively determine the underlying mechanism for an individual galaxy.

In order to get a better understanding of the internal kinematic processes creating a DP signatures, we investigated different possibilities in this work. We, therefore, computed synthetic SDSS spectroscopic emission-line observations from disc models and simulations and searched for DP signatures from all directions using a grid of observation angles. With axisymmetric models, we explored from which observation angle and for which rotation curves one can see a DP. To get a more realistic view, we searched in simulations of isolated galaxies from where we can observe a DP signature and found besides a rotation pattern that bars can create a strong DP when observed parallel to the major axis of the bar. We also observed minor and major-merger simulations over the course of their merger process. We found DP signatures during close encounters of two galaxies as two gas components are present inside the spectroscopic observation. Furthermore, after about 1 Gyr after the final coalescence, we see a central rotating disc in post-major mergers which create a distinct DP fraction. This phenomena however, is not detected in minor-merger simulations. However, a strong DP signature is observed within 350 Myr after the final coalescence. For the discussed stages of major and minor merger simulations, the morphology does not give a direct indication of a recent merger.

Using axisymmetric models, we have gained a clear understanding of how the connection between the stellar bulge and the rotation curve can lead to a DP. Massive or highly concentrated bulges can create a strong central velocity gradient such that a DP can be observed at low inclinations of $\theta = 40°$ ($\theta = 0°$ would be face-on). In the context of observed DP galaxies in the SDSS, we must clearly say that late cycles of major mergers are unlikely, as they tend to produce S0 and mainly elliptical morphologies. Moreover, at the merger stage, we discuss here, they have already consumed the majority of their gas for star formation and an enhanced star-formation rate is close to impossible. Minor mergers and bars as a mechanism for DP signatures show great agreement with observations. On the one hand, both are known for central star-formation activity and, on the other hand, both phenomena occur frequently. Although the range in which we can observe a DP in minor mergers is relatively short (about 350 Myr), however, this footprint can be seen from a large range of angles and there is no correlation with the galaxy inclination. These findings show further possibilities of how one can interpret an observed DP emission line. And at the same time it is in line with the observations of which minor mergers were discussed as the most plausible explanation.

In the context of future work on DP emission-line galaxies, we further discussed that using integrated-field spectroscopy can disentangle the underlying mechanisms. Furthermore, the understanding of DP emission lines is a crucial tool for upcoming spectroscopic surveys at high redshift, as they can help to identify galaxy mergers.

Acknowledgements. This work was supported by the *Programme National Cosmology et Galaxies* (PNCG) of CNRS/INSU with INP and IN2P3, co-funded by CEA and CNES. IC's research is supported by the SAO Telescope Data Center. IC acknowledges support from the RScF grant 19-12-00281.

References

Abazajian, K. N., Adelman-McCarthy, J. K., Agüeros, M. A., et al. 2009, ApJS, 182, 543
Athanassoula, E. & Bosma, A. 1985, ARA&A, 23, 147
Baes, M. & Dejonghe, H. 2000, MNRAS, 313, 153
Baes, M., Dejonghe, H., & De Rijcke, S. 2000, MNRAS, 318, 798
Barnes, J. & Hut, P. 1986, Nature, 324, 446
Barnes, J. E. 1992, ApJ, 393, 484
Barnes, J. E. 2002, MNRAS, 333, 481
Barnes, J. E. & Hernquist, L. E. 1991, ApJ, 370, L65
Begelman, M. C., Blandford, R. D., & Rees, M. J. 1980, Nature, 287, 307
Bergvall, N., Laurikainen, E., & Aalto, S. 2003, A&A, 405, 31

Binney, J. & Tremaine, S. 1987, Galactic dynamics
Bohlin, R. C., Savage, B. D., & Drake, J. F. 1978, ApJ, 224, 132
Bolatto, A. D., Wolfire, M., & Leroy, A. K. 2013, ARA&A, 51, 207
Bottrell, C., Hani, M. H., Teimoorinia, H., Patton, D. R., & Ellison, S. L. 2022, MNRAS, 511, 100
Bournaud, F. & Combes, F. 2002, A&A, 392, 83
Bournaud, F., Combes, F., & Semelin, B. 2005a, MNRAS, 364, L18
Bournaud, F., Jog, C. J., & Combes, F. 2005b, A&A, 437, 69
Bournaud, F., Jog, C. J., & Combes, F. 2007, A&A, 476, 1179
Bundy, K., Bershady, M. A., Law, D. R., et al. 2015, ApJ, 798, 7
Chilingarian, I. V., Di Matteo, P., Combes, F., Melchior, A. L., & Semelin, B. 2010, A&A, 518, A61
Chilingarian, I. V., Zolotukhin, I. Y., Katkov, I. Y., et al. 2017, ApJS, 228, 14
Chown, R., Li, C., Athanassoula, E., et al. 2019, MNRAS, 484, 5192
Combes, F., Prugniel, P., Rampazzo, R., & Sulentic, J. W. 1994, A&A, 281, 725
Comerford, J. M., Gerke, B. F., Newman, J. A., et al. 2009a, ApJ, 698, 956
Comerford, J. M. & Greene, J. E. 2014, ApJ, 789, 112
Comerford, J. M., Griffith, R. L., Gerke, B. F., et al. 2009b, ApJ, 702, L82
Comerford, J. M., Nevin, R., Stemo, A., et al. 2018, ApJ, 867, 66
Comerford, J. M., Pooley, D., Barrows, R. S., et al. 2015, ApJ, 806, 219
Comerford, J. M., Pooley, D., Gerke, B. F., & Madejski, G. M. 2011, ApJ, 737, L19
Conselice, C. J., Blackburne, J. A., & Papovich, C. 2005, ApJ, 620, 564
De Propris, R., Liske, J., Driver, S. P., Allen, P. D., & Cross, N. J. G. 2005, AJ, 130, 1516
Dekel, A. & Burkert, A. 2014, MNRAS, 438, 1870
Di Matteo, P., Combes, F., Melchior, A. L., & Semelin, B. 2007, A&A, 468, 61
Domínguez Sánchez, H., Huertas-Company, M., Bernardi, M., Tuccillo, D., & Fischer, J. L. 2018, MNRAS, 476, 3661
Downes, D. & Solomon, P. M. 1998, ApJ, 507, 615
Eliche-Moral, M. C., Rodríguez-Pérez, C., Borlaff, A., Querejeta, M., & Tapia, T. 2018, A&A, 617, A113
Ellison, S. L., Mendel, J. T., Patton, D. R., & Scudder, J. M. 2013, MNRAS, 435, 3627
Ellison, S. L., Nair, P., Patton, D. R., et al. 2011, MNRAS, 416, 2182
Ellison, S. L., Patton, D. R., Simard, L., & McConnachie, A. W. 2008, AJ, 135, 1877
Eskridge, P. B., Frogel, J. A., Pogge, R. W., et al. 2000, AJ, 119, 536
Farouki, R. T. & Shapiro, S. L. 1982, ApJ, 259, 103
Fitzpatrick, E. L. 1999, PASP, 111, 63
Ge, J.-Q., Hu, C., Wang, J.-M., Bai, J.-M., & Zhang, S. 2012, ApJS, 201, 31
Gerke, B. F., Newman, J. A., Lotz, J., et al. 2007, ApJ, 660, L23
Gingold, R. A. & Monaghan, J. J. 1982, Journal of Computational Physics, 46, 429
Governato, F., Brook, C. B., Brooks, A. M., et al. 2009, MNRAS, 398, 312
Hernquist, L. 1993, ApJS, 86, 389
Hernquist, L. & Mihos, J. C. 1995, ApJ, 448, 41
Hopkins, P. F., Cox, T. J., Younger, J. D., & Hernquist, L. 2009, ApJ, 691, 1168
Kewley, L. J., Nicholls, D. C., & Sutherland, R. S. 2019, ARA&A, 57, 511
Komossa, S., Burwitz, V., Hasinger, G., et al. 2003, ApJ, 582, L15
Laureijs, R., Amiaux, J., Arduini, S., et al. 2011, arXiv e-prints, arXiv:1110.3193
Laurikainen, E., Salo, H., Buta, R., & Knapen, J. H. 2009, ApJ, 692, L34
Le Borgne, D., Rocca-Volmerange, B., Prugniel, P., et al. 2004, A&A, 425, 881
Lotz, J. M., Jonsson, P., Cox, T. J., & Primack, J. R. 2008, MNRAS, 391, 1137
Lotz, J. M., Jonsson, P., Cox, T. J., & Primack, J. R. 2010, MNRAS, 404, 575
Lotz, J. M., Primack, J., & Madau, P. 2004, AJ, 128, 163
Lucy, L. B. 1977, AJ, 82, 1013
Maness, H. L., Taylor, G. B., Zavala, R. T., Peck, A. B., & Pollack, L. K. 2004, ApJ, 602, 123
Maschmann, D. & Melchior, A.-L. 2019, A&A, 627, L3
Maschmann, D., Melchior, A.-L., Combes, F., et al. 2022, A&A, 664, A125
Maschmann, D., Melchior, A.-L., Mamon, G. A., Chilingarian, I. V., & Katkov, I. Y. 2020, A&A, 641, A171
Mazzilli Ciraulo, B., Melchior, A.-L., Maschmann, D., et al. 2021, A&A, 653, A47
Menéndez-Delmestre, K., Sheth, K., Schinnerer, E., Jarrett, T. H., & Scoville, N. Z. 2007, ApJ, 657, 790
Mihos, J. C. & Hernquist, L. 1994, ApJ, 437, 611
Mihos, J. C. & Hernquist, L. 1996, ApJ, 464, 641
Miyamoto, M. & Nagai, R. 1975, PASJ, 27, 533
Müller-Sánchez, F., Comerford, J. M., Nevin, R., et al. 2015, ApJ, 813, 103
Negroponte, J. & White, S. D. M. 1983, MNRAS, 205, 1009
Nevin, R., Blecha, L., Comerford, J., & Greene, J. 2019, ApJ, 872, 76
Nevin, R., Blecha, L., Comerford, J., et al. 2021, ApJ, 912, 45
Nevin, R., Comerford, J., Müller-Sánchez, F., Barrows, R., & Cooper, M. 2016, ApJ, 832, 67
Noeske, K. G., Weiner, B. J., Faber, S. M., et al. 2007, ApJ, 660, L43
Patton, D. R., Ellison, S. L., Simard, L., McConnachie, A. W., & Mendel, J. T. 2011, MNRAS, 412, 591
Peschken, N., Łokas, E. L., & Athanassoula, E. 2020, MNRAS, 493, 1375
Puech, M., Hammer, F., Flores, H., Neichel, B., & Yang, Y. 2009, A&A, 493, 899
Richard, J., Kneib, J. P., Blake, C., et al. 2019, The Messenger, 175, 50
Robertson, B., Bullock, J. S., Cox, T. J., et al. 2006, ApJ, 645, 986
Rodriguez, C., Taylor, G. B., Zavala, R. T., et al. 2006, ApJ, 646, 49
Roshan, M., Ghafourian, N., Kashfi, T., et al. 2021, MNRAS, 508, 926
Salim, S. & Narayanan, D. 2020, ARA&A, 58, 529
Sofue, Y. & Rubin, V. 2001, ARA&A, 39, 137
Solanes, J. M., Perea, J. D., & Valentí-Rojas, G. 2018, A&A, 614, A66
Somerville, R. S. & Davé, R. 2015, ARA&A, 53, 51
Steinmetz, M. & Navarro, J. F. 2002, New A, 7, 155
Toomre, A. & Toomre, J. 1972, ApJ, 178, 623
Tremonti, C. A., Heckman, T. M., Kauffmann, G., et al. 2004, ApJ, 613, 898
Villalobos, Á., De Lucia, G., Borgani, S., & Murante, G. 2012, MNRAS, 424, 2401
Vogelsberger, M., Marinacci, F., Torrey, P., & Puchwein, E. 2020, Nature Reviews Physics, 2, 42
Westmeier, T., Jurek, R., Obreschkow, D., Koribalski, B. S., & Staveley-Smith, L. 2014, MNRAS, 438, 1176
Wiklind, T., Combes, F., Henkel, C., & Wyrowski, F. 1997, A&A, 323, 727
Willett, K. W., Lintott, C. J., Bamford, S. P., et al. 2013, MNRAS, 435, 2835
Wolfire, M. G., Hollenbach, D., & McKee, C. F. 2010, ApJ, 716, 1191
Zhao, D., Du, M., Ho, L. C., Debattista, V. P., & Shi, J. 2020, ApJ, 904, 170
Zhou, Z.-B., Zhu, W., Wang, Y., & Feng, L.-L. 2020, ApJ, 895, 92

Appendix A: Initial galaxy parameters

In this section we provide detailed parameters of galaxy simulations of the GalMer project, described in Sect. 3.2.1 and 4.1. Table A.1 summarises the initial parameters of all individual galaxy types used in this work and Table A.2 summarises orbital parameters of the merger simulations.

Table A.1. Initial parameters of simulated galaxies in the GalMer database.

	gSa	gSb	dSb	dSd
$M_{\rm gas}[2.3\times10^9 M_\odot]$	4	4	0.4	0.75
$M_{*\,\rm disc}[2.3\times10^9 M_\odot]$	40	20	2	2.5
$M_{*\,\rm bulge}[2.3\times10^9 M_\odot]$	10	5	0.5	0
$M_{DM}[2.3\times10^9 M_\odot]$	50	75	7.5	7.5
$a_{\rm gas}$ [kpc]	5	6	1.6	2.2
$h_{\rm gas}$ [kpc]	0.2	0.2	0.06	0.06
$a_{*,\rm disc}$ [kpc]	4	5	1.6	1.9
$h_{*,\rm disc}$ [kpc]	0.5	0.5	0.16	0.16
$b_{*,\rm bulge}$ [kpc]	2	1	0.3	-
$b_{\rm DM}$ [kpc]	10	12	3.8	4.7

Notes. The values are taken from Chilingarian et al. (2010).

Table A.2. Orbital parameters for major and minor mergers used in the GalMer database.

orb.id	$r_{\rm ini}$ kpc	$v_{\rm ini}$ 10^2 km s^{-1}	L 10^2 km s^{-1} kpc	spin
		Major merger		
01dir	100	2.	56.6	up
01ret	100	2.	56.6	down
02dir	100	3.	59.3	up
02ret	100	3.	59.3	down
03dir	100	3.7	62.0	up
03ret	100	3.7	62.0	down
04dir	100	5.8	71.5	up
04ret	100	5.8	71.5	down
05dir	100	2.	80.0	up
05ret	100	2.	80.0	down
		Minor merger		
01dir	100	1.48	29.66	up
01ret	100	1.48	29.66	down
02dir	100	1.52	29.69	up
02ret	100	1.52	29.69	down
03dir	100	1.55	29.72	up
03ret	100	1.55	29.72	down
04dir	100	1.48	36.33	up
04ret	100	1.48	36.33	down
05dir	100	1.52	36.38	up
05ret	100	1.52	36.38	down

Notes. The values are taken from Chilingarian et al. (2010).

Appendix B: Merger orbit of major merger galaxies

In this section, an additional figure of a major merger simulation of two gSa galaxies is presented in Fig. B.1. This is supplementary to Fig. 11 which is used to discuss a major merger simulation.

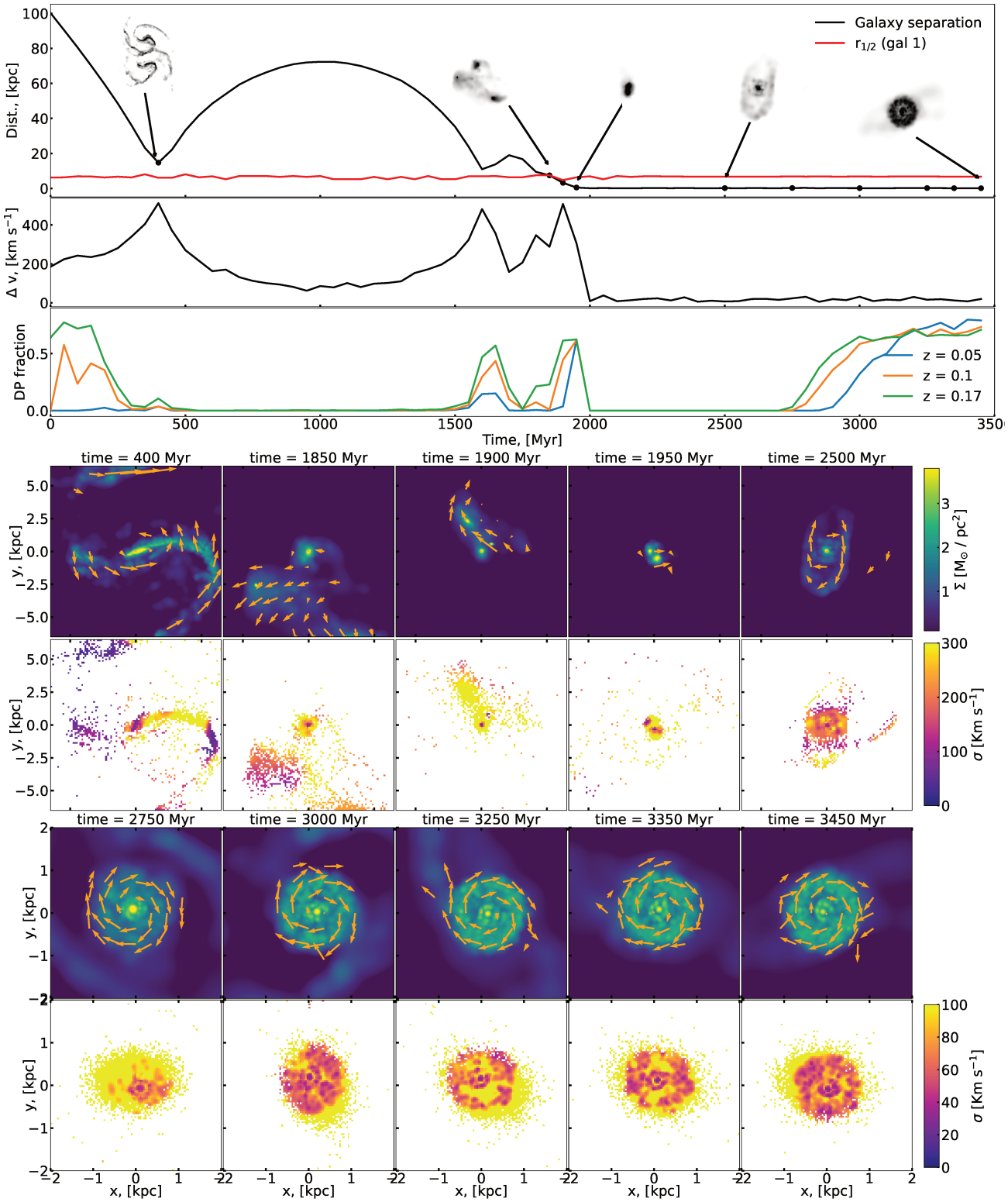

Fig. B.1. Visualisation of a gSa + gSa galaxy merger. The presentation is the same as described in Fig. 11. However, in the bottom panels, presenting the 2D projection of different snapshots, we display the central 4 kpc to better visualise the central disc. The merger process is characterised by an retrograde orbit with the orbit-id 5 and an inclination of 45°.

CHAPTER 4

Molecular gas in double-peak emission-line galaxies

As it was pointed out in the Chapters 1 and 3, there are many different mechanisms that can produce double-peak (DP) emission-lines. However, one can systematically rule out specific scenarios and find statistical arguments in favour of one most probable scenario. From Maschmann et al. (2020), we know that galaxies classified as S0 galaxies or bulge-dominated spiral galaxies are more likely to exhibit DP emission lines. In addition, DP galaxies, classified as star-forming galaxies, exhibit a central star-formation enhancement and the measured gas kinematics deviate from the predicted kinematic behaviour according to the Tully-Fisher relation. Taking all these aspects into account, the most probable scenario is a DP emission-line signature originating from two gas populations inside the fibre which is the result of a minor merger. This scenario was discussed in detail in Chapter 3 using simulations and clearly points out that, merger events can be the cause of a DP. However, to further argue on this scenario, additional observations are needed to provide a new perspective on associated effects such as merger-induced star formation. Therefore, I conducted 2 observational runs with the IRAM 30m telescope located at Pico Veleta in Spain to measure the molecular-gas content of in total 70 DP galaxies.

As discussed in detail in Chapter 1 Sect. 2.3 and 3, galaxy mergers can funnel gas into the galaxy centre and enhance star formation. I, therefore, selected galaxies which are located at least 0.3 dex above the main star-forming sequence (see Chapter 1, Sect. 4.3) and studied their molecular-gas content. I selected 35 DP I observed with the IRAM 30m telescope and 17 DP galaxies from the literature. Even though, the area measured by the IRAM 30m telescope of $23''$ and $12''$ is significantly larger than SDSS spectroscopic measurement of $3''$, it was possible to find in about 19 % of the DP galaxies the exact same DP signature in the molecular gas as found in the SDSS emission-line spectrum. This is an indication that in many galaxies the molecular gas might be highly concentrated in the centre and coincides with the star-formation sites, traced by the ionised gas. In addition to that, a clear central star-formation enhancement is further supporting this scenario. A morphological classification of these galaxies revealed that 50 % show signs of a recent merger or tidal features. Comparison to molecular gas scaling relations from the literature reveals an unusually large molecular gas reservoir but moderate depletion times, expected from their distance to the main sequence. In the Maschmann et al. (2022b) peer reviewed journal article, I describe in detail the molecular gas observations, the subsequent data

analysis, the DP characteristics and finally conclude on the origin of the observed DP signature.

DP galaxies which are situated above the main star-forming sequence are a special population of the DP galaxies, assembled in Maschmann et al. (2020). The characteristics of these galaxies indicate a minor merger event or the accretion of a significant amount of gas in the recent past. Such an event funneled gas into the centre, enhancing star formation and thus lifting the galaxy above the main sequence. Due to their large bulges, the gas in these galaxies is stabilised against gravitational instabilities, reducing the star-formation efficiency. This gas distribution is observed in the form of DP emission-lines.

Astronomy & Astrophysics manuscript no. output
December 11, 2022

Central star formation in double-peak, gas-rich radio galaxies

Daniel Maschmann[1], Anne-Laure Melchior[1], Francoise Combes[1,2], Barbara Mazzilli Ciraulo[1], Jonathan Freundlich[3], Anaëlle Halle[1] and Alexander Drabent[4]

[1] Sorbonne Université, LERMA, Observatoire de Paris, PSL university, CNRS, F-75014, Paris, France
e-mail: Daniel.Maschmann@observatoiredeparis.psl.eu, A.L.Melchior@oobservatoiredeparis.psl.eu
[2] Collège de France, 11, Place Marcelin Berthelot, F-75005, Paris, France
[3] Université de Strasbourg, CNRS, Observatoire astronomique de Strasbourg, UMR 7550, F-67000 Strasbourg, France
[4] Thüringer Landessternwarte, Sternwarte 5, 07778 Tautenburg, Germany

Received 14 September 2021/ accepted 11 May 2022

ABSTRACT

The respective contributions of gas accretion, galaxy interactions, and mergers to the mass assembly of galaxies, as well as the evolution of their molecular gas and star-formation activity are still not fully understood. In a recent work, a large sample of double-peak (DP) emission-line galaxies have been identified from the SDSS. While the two peaks could represent two kinematic components, they may be linked to the large bulges that their host galaxies tend to have. Star-forming DP galaxies display a central star-formation enhancement and have been discussed as compatible with a sequence of recent minor mergers. In order to probe merger-induced star-formation mechanisms, we conducted observations of the molecular-gas content of 35 star-forming DP galaxies in the upper part of the main sequence (MS) of star formation (SF) with the IRAM 30m telescope. Including similar galaxies 0.3 dex above the MS and with existing molecular-gas observations from the literature, we finally obtained a sample of 52 such galaxies. We succeeded in fitting the same kinematic parameters to the optical ionised- and molecular-gas emission lines for ten (19 %) galaxies. We find a central star-formation enhancement resulting most likely from a galaxy merger or galaxy interaction, which is indicated by an excess of gas extinction found in the centre. This SF is traced by radio continuum emissions at 150 MHz, 1.4 GHz, and 3 GHz, all three of which are linearly correlated in log with the CO luminosity with the same slope. The 52 DP galaxies are found to have a significantly larger amount of molecular gas and longer depletion times, and hence a lower star-formation efficiency, than the expected values at their distance of the MS. The large bulges in these galaxies might be stabilising the gas, hence reducing the SF efficiency. This is consistent with a scenario of minor mergers increasing the mass of bulges and driving gas to the centre. We also excluded the inwards-directed gas migration and central star-formation enhancement as the origin of a bar morphology. Hence, these 52 DP galaxies could be the result of recent minor mergers that funnelled molecular gas towards their centre, triggering SF, but with moderate efficiency.

Key words. galaxies: kinematics and dynamics, galaxies: interactions, galaxies: evolution, galaxies: star formation, Methods: observational, techniques: spectroscopic, methods: data analysis

1. Introduction

The evolutionary state of galaxies depends mostly on their growth rate and their efficiency when it comes to transforming gas into stars. Galaxy interactions, smooth accretion of gas, and internal mechanisms such as active galactic nucleus (AGN) feedback all affect the gas content and the SF. Galaxy interactions and mergers are well known to enhance the star-formation rate (SFR) (Bothun & Dressler 1986; Pimbblet et al. 2002). However, while they tend to increase the molecular-gas content (Combes et al. 1994; Violino et al. 2018; Lisenfeld et al. 2019), their effect on the evolution of the neutral hydrogen gas fraction is still an open question. Some studies find little difference in close galaxy pairs (e.g. Zuo et al. 2018; Braine & Combes 1993) or post-merger galaxies (e.g. Ellison et al. 2015) compared to the general population of similar galaxies. Other studies find an enhancement of the atomic gas fraction in recently merged galaxies (Huchtmeier et al. 2008; Ellison et al. 2018) or a deficit in the final stages of merging (Hibbard & van Gorkom 1996). The environment can be also responsible for the final quenching of a galaxy (Balogh et al. 1998). Interactions and mergers can also drive gas towards the centre and hence fuel a nuclear black hole, enhancing AGN activity and feedback (Croton et al. 2006; Springel et al. 2005), which can then influence star formation (SF) in the host galaxy (Barrows et al. 2017; Concas et al. 2017; Woo et al. 2017). In cases of powerful AGNs, the radiation can shut down the SF entirely (Di Matteo et al. 2005; Croton et al. 2006; Cattaneo et al. 2009). Relying on simulations, Sanchez et al. (2021) discussed the fact that two successive minor merger events can quench Milky Way-like galaxies through AGN feedback. Based on the projected distances between galaxies and projected velocities, Ellison et al. (2008) and Patton et al. (2011) conducted studies on large galaxy pairs samples and the associated effects. They found an increase of central SF with decreasing galaxy separation. By extending the pair search with quasi stellar objects and AGNs, Ellison et al. (2011b) found that AGN activity can be triggered by galaxy interactions before the final coalescence.

To explain the overall growth of galaxies over cosmic time, Tacchella et al. (2016b) described a scenario of recurring episodes of gas in-fall and depletion phases. Gas is accreted into a galaxy in large amounts through streams from the surroundings (Dekel et al. 2009) or through minor merger events, causing a contraction of the gas disc with efficient star-formation sites and a central enhancement (Dekel & Burkert 2014). This shifts the galaxy above the star-forming main sequence (MS), before

gas depletion allows the galaxy to descend underneath the MS. Smooth gas accretion from filaments (Bouché et al. 2010; Davé et al. 2011, 2012; Feldmann 2013; Lilly et al. 2013; Dekel et al. 2013; Peng & Maiolino 2014; Dekel & Burkert 2014) can explain that most galaxies on the MS exhibit a disc morphology (Förster Schreiber et al. 2006; Genzel et al. 2006, 2008; Stark et al. 2008; Daddi et al. 2010; Wuyts et al. 2011) and that star-forming galaxies at $z = 1 - 2$ experience long, sustained star-formation cycles (Daddi et al. 2005, 2007; Caputi et al. 2006).

The occurrence of double-peak (DP) emission lines in spectra of galaxies can have different causes, amongst which are galaxy mergers. As predicted by Begelman et al. (1980), galaxy mergers lead at one point to the final coalescence of the supermassive black holes of their progenitors. Earlier stages of this scenario have been reported many times in the form of a dual AGN (e.g. Genzel et al. 2001; Koss et al. 2016, 2018; Goulding et al. 2019). Such galaxy mergers can be identified through kinematic signatures with spectroscopic observations. Post-coalescence mergers can create two separated gas populations, which can be observed as DP emission lines. This has been studied in works focusing on AGN (e.g. Comerford et al. 2009; Liu et al. 2011; Koss et al. 2012; Liu et al. 2013; Comerford et al. 2013; Fu et al. 2015). DP signatures were found to be related to merging processes in Comerford et al. (2018) and Maschmann & Melchior (2019). In a recent study, Mazzilli Ciraulo et al. (2021) succeeded in resolving two independent kinematic components using integrated field spectroscopy of a DP emission-line galaxy and identified two galaxies in the process of merging, superimposed in a projection along the line of sight.

In order to discuss the nature of DP emission-line galaxies, Maschmann et al. (2020) (hereafter M20) developed an automated selection procedure and found 5663 DP galaxies, including non-AGN galaxies. A systematic search for DP emission-line galaxies was also conducted by Ge et al. (2012) and also included non-AGN galaxies such as star-forming or composite galaxies. M20 relied on reduced spectra provided by the value-added Reference Catalogue of Spectral Energy Distributions (RCSED) (Chilingarian et al. 2017) and compared them to single-peaked galaxies with the same emission-line signal-to-noise (S/N) properties and redshift and stellar mass distributions. They found that most of the DP galaxies are massive star-forming galaxies characterised by a central enhancement of their SFR. In addition, they exhibit a large bulge with a Sersic index larger than for the single-peaked galaxy comparison sample. While this configuration could result from repetitive minor mergers, as discussed by Bournaud et al. (2007), it could also correspond to a rotating inner structure. However, as discussed in detail in Mazzilli Ciraulo et al. (2021), integrated field spectroscopy is needed to identify two individual gas components and conclusively identify galaxy mergers. In this work, we studied statistical properties of a sub-sample of 52 galaxies with SDSS spectra.

We explored the most extreme part of this DP sample, focusing on DP galaxies located more than 0.3 dex above the MS. We performed new molecular-gas observations at the IRAM 30m telescope and completed the sample with existing molecular-gas observations from the literature. We studied the relation between the molecular-gas content and the star-formation activity. In order to test possible biases due to dust, we also used the radio continuum emission, extensively studied as a tracer of SF (Condon 1992; Bell 2003; Schmitt et al. 2006; Murphy et al. 2011). We also relied on the kinematics to explore the possible connection between the ionised and molecular gas. We used these combined analyses to probe the relation between galaxy merging and star-formation mechanisms.

This paper is organised as follows. In Sect. 2, the sample is defined with a description of the CO observations performed at the IRAM 30m telescope and the data selection from the literature. In Sect. 3, we describe the emission-line fitting and the characteristics of the galaxy sample. We analyse the sample in Sect. 4 with different star-formation tracers and calculate the molecular-gas content. We also present the Kennicutt-Schmidt relation and explore the connection between the CO luminosity and radio continuum emission. Lastly, we discuss our results in Sect. 5 and present the conclusion in Sect. 6. A cosmology of $\Omega_m = 0.3$, $\Omega_\Lambda = 0.7$ and $h = 0.7$ is assumed in this work.

2. Data

We focused on a sample of 52 DP galaxies lying more than 0.3 dex above the MS and gather a few comparison galaxy samples. In Sect. 2.1, the 52-galaxy sample is presented. We discuss the M20 selection of 35 galaxies in Sect. 2.1.1, their observation in CO at the IRAM 30m telescope in Sect. 2.1.2, and the selection of 17 additional galaxies with CO observations available from the literature in Sect. 2.1.3. In Sect. 2.2, different comparison galaxy samples obtained from existing CO and SFR measurements are described. Lastly, in Sect. 2.3, all the galaxies of the different samples are displayed with respect to their distance from the MS as a function of their stellar mass. In Sect. 2.4, the different samples are cross-identified with existing radio-continuum surveys.

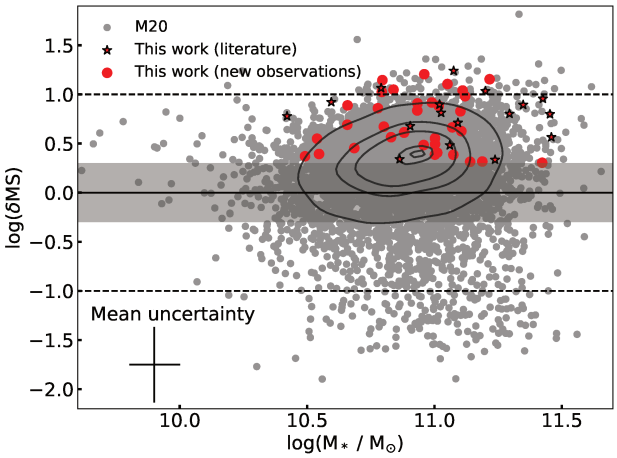

Fig. 1. Offset from MS for all CO samples as a function of stellar mass (M_*) using the parametrisation of the MS found by Speagle et al. (2014). The shaded area marks the 0.3 dex and the dashed lines the ±1 dex scatter. We used the SFR computed by Brinchmann et al. (2004) and the stellar mass from Kauffmann et al. (2003). We show the M20 sample with grey dots and mark the DP sample (definition in Sect. 2.1) with red circles and stars. Circles represent galaxies with new CO observations and stars represent galaxies for which we obtained the CO measurements from the literature. The contour lines show the density of the M20 sample. In the bottom left, we show the mean uncertainties.

2.1. Sample of 52 DP galaxies 0.3 dex above the MS

The main sample of this work consists of M20 DP galaxies lying more than 0.3 dex above the MS, observed during two observing runs with the IRAM 30m telescope in April and December 2020.

2.1.1. Selection of M20 DP galaxies 0.3 dex above the MS

We computed the SFR of the MS $SFR_{MS} = SFR(MS; z, M_*)$, as parametrised by Speagle et al. (2014), at the redshifts z and stellar masses M_* for the DP galaxies of M20 and computed their offset from the MS as $\delta MS = SFR/SFR_{MS}$ using the SFR computed by Brinchmann et al. (2004) and the stellar masses from Kauffmann et al. (2003). The MS is estimated from observations with a typical scatter of $\delta MS \sim 0.3$ dex (e.g. Noeske et al. 2007; Rodighiero et al. 2011; Whitaker et al. 2012; Schreiber et al. 2015). To target galaxies with increased star-formation activity in comparison to the MS, we thus selected galaxies that are located at least $\delta MS = 0.3$ dex above the MS. With this criterion, we aimed to focus our work on galaxies with ongoing SF, which can either be recently induced by galaxy interaction or gas accretion (e.g. Bothun & Dressler 1986; Pimbblet et al. 2002) or be the remainder of a faded starburst event (Schawinski et al. 2009; French et al. 2015). We selected 35 DP galaxies, which we observed with the IRAM 30m telescope. These galaxies correspond to the red dots of Fig. 1, in which the whole parent M20 sample is shown via grey dots.

2.1.2. IRAM-30m observations of the selected M20 galaxies

We observed the 35 DP galaxies during two observing runs from the 21 to the 24 April 2020 and from the 23 to the 29 December 2020 with the IRAM 30m telescope at Pico Veleta in Spain. Galaxies with a redshift of $z < 0.144$ could be observed simultaneously in the CO(1-0) and CO(2-1) lines, and five galaxies at higher redshift were only observable in CO(1-0) at the time. The mean emission-line wavelengths were $\sim$ 3 mm for the CO(1-0) line and $\sim$ 1.5 mm for the CO(2-1) line. Thick clouds and snow prevented us from observing for 1.5 nights during the first run and two nights during the second run, but we were able to observe all proposed galaxies during the remaining time under excellent conditions.

The galaxies were observed using the broad-band EMIR receiver, tuned in single-band mode with a total bandwidth of 3.715 GHz per polarisation. This allowed us to observe an average velocity range of 11 140 km s^{-1} for the CO(1-0) line and 5 570 km s^{-1} for the CO(2-1) line. The Wobbler switching mode was used to carry out the observations and the backends WILMA and FTS were used in parallel with a channel width of 2 MHz and 0.195 MHz, respectively.

We pointed, on average, one hour at each galaxy and reached noise levels between 0.1 and 1.8 mK (main-beam temperature), smoothed over 60 km/s. Focus measurements were performed at the beginning of the night and at dawn, as well as pointing measurements every two hours. The temperature scale we use here is main-beam temperature, and the beam size is $\lambda/D = 22''$ at 2.8 mm and $12''$ at 1.4 mm wavelength with an average beam efficiency of $\eta_{mb} = T_A^*/T_{mb} = 0.76$ and 0.56, respectively. The observation data were reduced using the CLASS/GILDAS software. We transformed the observed main-beam temperature into units of spectral flux density by using the IRAM-30m-antenna factor of 5 Jy/K, in order to compare our observations with other CO samples.

2.1.3. Inclusion of galaxies with CO data from the literature

In order to enlarge our sample, we further selected DP galaxies lying more than 0.3 dex above the MS from published CO observations. An emission-line fit conducted using the method described in M20 is shown in Fig. 3 for DP-8[1], one of the 35 galaxies taken from M20. For galaxies from the literature, we performed a simplified DP selection procedure compared to the one of M20, especially with no emission line stacking nor multiple selection stages. Our present algorithm consists of a simultaneous fit of multiple emission lines and selection criteria but we finally rely on a visual inspection, to exclude some noisy spectra but also to enlarge the selection to galaxies with strongly perturbed gas kinematics making emission lines deviate from pure double-Gaussian profiles. The identification of DP emission-line galaxies in literature samples is hence as follows. The best-fitting stellar continuum template provided by Chilingarian et al. (2017) is first subtracted from the SDSS spectrum to obtain the pure emission-line spectrum. Then, we fit single and double-Gaussian functions to the emission lines Hβ, [OIII]λ4960, [OIII]λ5008, [OI]λ6302, [NII]λ6550, Hα, [NII]λ6585, [SII]λ6718, and [SII]λ6733 simultaneously. We also use a global velocity of μ (resp. μ_1 and μ_2 for the double-Gaussian fit) and a Gaussian standard deviation σ (resp. σ_1 and σ_2) for all emission lines but keep the individual emission-line amplitudes as free parameters. We also include the spectral instrumental broadening σ_{inst} in the fitted σ for each observed emission line individually in order to obtain the observed Gaussian velocity dispersion $\sigma_{obs} = \sqrt{\sigma_{inst}^2 + \sigma^2}$. We pre-select galaxies that are selected by the F-test criterion, with an emission-line separation $\Delta v = |\mu_1 - \mu_2|$ of at least 200 km s^{-1} and an amplitude ratio of the [OIII]λ5008 or Hα line to be between 1/3 and 3, as described in detail in M20.

We select 17 DP galaxies from the literature. These include 11 galaxies observed with the Combined Array for Research in Millimeter-wave Astronomy (CARMA) by Bauermeister et al. (2013), three ultra-luminous infrared galaxies (ULIRG) observed with the 14m telescope of the Five College Radio Astronomy Observatory (FCRAO) observed by Chung et al. (2009), two galaxies observed with the IRAM 30m telescope as part of the COLD GASS survey (Saintonge et al. 2011, 2017), and one galaxy observed by Solomon et al. (1997), which is known as Arp 220. We found an ALMA-CO(1-0) observation for this galaxy in the ESO archives[2]. With the high spatial resolution of 37 pc, Scoville et al. (2017) succeeded in precisely locating the two nuclei and studying their nuclear gas discs. We extract the molecular-gas observations from the exact same location as the 3″ SDSS fibre and also from the entire galaxy. We note that the majority of the molecular gas coincides with the two nuclei of Arp 220. However, these two nuclei are strongly obscured by dust, and the SDSS 3″ fibre observation is centred about 4″ north of the two nuclei (Scoville et al. 2017).

We thus gather a DP galaxy sample with CO observations of 52 galaxies lying more than 0.3 dex above the MS: the 35 galaxies from M20 for which we present new CO observations and the 17 galaxies selected from the literature. This sample is presented in Table 1 with characteristic measurements such as the redshift, stellar mass, SFR, radio-continuum fluxes, galaxy size, and inclination. In Sect. 2.2, we further discuss the total DP detection rate for each public CO galaxy sample included in this work.

[1] We note that the continuum of the [OI]λ6302 line shows a small dip. This is most likely due to the fact that, for the stellar continuum fit, the emission lines are masked and structures close to the emission lines cannot be accurately modelled. Since we fit all emission lines simultaneously with the same kinematic parameters, this has no effect on the emission-line fit.

[2] `http://archive.eso.org/scienceportal`

Table 1. Characteristics of DP galaxy sample.

ID	SDSS Designation	z	$\log(M_*/M_\odot)$	SFR	$F_{150\,MHz}$	$F_{1.4\,GHz}$	$F_{3\,GHz}$	D_{25}	i
				$M_\odot\ yr^{-1}$	mJy	mJy	mJy	arcsec	°
DP-1[a]	J153457.21+233013.3	0.0181	10.9	4.7	-	316.1	242.8	90.8	-
DP-2	J143117.98+075640.7	0.0269	11.0	7.7	-	5.8	3.1	65.8	66
DP-3	J142129.76+050423.6	0.0271	10.5	3.9	-	5.4	2.8	82.2	61
DP-4	J130702.99+130429.3	0.0274	10.5	3.5	-	5.0	2.3	61.6	58
DP-5	J141721.07+265126.8	0.0367	11.1	13.4	-	21.0	10.6	60.9	-
DP-6	J141916.59+261755.0	0.0368	11.1	7.4	-	9.7	8.1	59.7	50
DP-7	J160457.92+140815.3	0.0372	10.5	5.8	-	2.6	1.8	43.5	51
DP-8	J143713.73+143954.5	0.0379	10.9	10.1	-	9.1	5.4	25.2	-
DP-9	J141238.95+273740.7	0.0386	10.7	9.3	-	2.7	1.6	44.6	64
DP-10	J090007.20+600458.1	0.0390	11.0	43.5	8.5	4.8	2.9	38.5	52
DP-11	J132357.46+120233.3	0.0390	11.0	7.3	-	4.1	-	41.4	56
DP-12	J135309.67+143920.9	0.0405	11.2	7.4	-	18.0	3.9	47.0	-
DP-13[b]	J020359.16+141837.3	0.0427	10.9	12.3	-	-	3.3	47.4	62
DP-14	J105716.67+283230.0	0.0457	10.9	10.4	8.4	1.6	1.8	43.7	56
DP-15	J113507.51+295327.7	0.0462	11.0	7.2	15.2	3.3	2.8	49.6	-
DP-16	J145415.59+254121.3	0.0479	10.8	24.8	-	3.3	1.9	25.3	48
DP-17[b]	J091954.54+325559.8	0.0490	10.4	9.1	36.4	22.3	7.8	65.8	-
DP-18	J094142.69+283555.6	0.0538	11.1	7.5	10.7	2.8	2.0	45.2	58
DP-19[c]	J233455.24+141731.1	0.0621	11.0	21.5	-	-	1.7	27.5	-
DP-20	J120854.47+472833.3	0.0677	10.7	17.0	7.2	2.4	-	19.6	36
DP-21	J134316.22+524742.5	0.0690	11.1	36.7	6.0	5.1	2.8	27.1	46
DP-22	J110428.21+560131.4	0.0702	11.0	10.5	15.8	4.7	2.6	33.1	42
DP-23	J110746.31+552633.3	0.0715	10.9	25.2	6.9	2.9	1.2	25.2	-
DP-24[d]	J121346.08+024841.5	0.0731	10.6	17.5	-	24.6	17.0	4.5	-
DP-25[d]	J102142.79+130656.1	0.0763	11.1	19.8	-	16.4	7.1	19.4	-
DP-26	J120437.97+525717.2	0.0815	10.9	22.4	10.4	5.2	1.4	31.0	-
DP-27[c]	J221938.11+134213.9	0.0835	11.1	11.7	-	-	-	33.4	-
DP-28	J114325.16+505154.7	0.0844	11.0	28.0	10.1	4.0	2.1	22.6	39
DP-29	J131943.32+515255.8	0.0902	11.1	18.5	18.8	4.1	2.2	23.2	61
DP-30	J114050.50+561335.3	0.1065	10.8	43.7	6.9	1.1	-	19.3	-
DP-31[d]	J135609.99+290535.1	0.1087	11.2	55.8	13.1	10.7	5.2	20.1	-
DP-32	J150439.86+501100.4	0.1124	10.8	15.2	7.8	1.5	-	15.0	45
DP-33	J150911.71+482041.2	0.1194	10.8	12.7	5.6	1.9	-	18.2	40
DP-34	J124406.54+503940.3	0.1211	10.8	23.7	8.4	2.0	-	13.2	-
DP-35	J130704.53+485845.5	0.1230	11.2	80.6	8.7	1.7	1.2	13.8	39
DP-36	J130847.69+504259.8	0.1244	11.0	35.6	8.7	3.5	-	14.6	29
DP-37	J143616.57+554822.0	0.1400	11.1	63.8	11.5	2.1	1.2	12.2	-
DP-38	J135705.89+523532.3	0.1437	11.1	36.5	5.4	2.8	1.0	19.0	-
DP-39	J113703.72+504420.7	0.1601	10.8	47.1	4.8	1.0	-	15.3	61
DP-40	J141803.61+534104.0	0.1638	11.1	65.9	10.9	2.2	1.0	14.1	39
DP-41[c]	J100518.63+052544.2	0.1657	10.8	47.1	-	-	-	9.8	-
DP-42[c]	J105527.19+064015.0	0.1731	11.0	44.1	-	-	-	11.9	-
DP-43[c]	J091426.24+102409.6	0.1762	11.5	61.5	-	1.1	-	9.8	-
DP-44[c]	J114649.18+243647.7	0.1767	11.1	106.1	-	-	-	6.7	-
DP-45[c]	J134322.28+181114.1	0.1781	11.3	67.7	-	-	-	10.0	-
DP-46	J144017.35+563503.7	0.1801	11.4	19.3	5.3	1.6	-	19.3	21
DP-47[c]	J223528.64+135812.7	0.1830	11.4	88.2	-	-	0.0	15.7	-
DP-48	J110333.10+475932.7	0.1906	11.0	21.1	6.5	1.4	-	9.9	42
DP-49[c]	J002353.97+155947.9	0.1918	11.3	54.6	-	-	-	13.6	-
DP-50	J143211.77+495535.8	0.1938	10.7	11.4	3.1	1.5	-	9.8	-
DP-51[c]	J092831.94+252313.9	0.2830	11.2	25.4	-	-	-	14.8	-
DP-52[c]	J132047.14+160643.7	0.3124	11.5	64.9	-	-	-	10.2	-

Notes. DP emission-line galaxy sample consisting of 52 galaxies, observed in CO and lying more than 0.3 dex above the MS. We conducted CO observations for 35 galaxies and mark observations from the literature for the remaining 17. We note galaxies taken from Solomon et al. (1997) with the footnote *a*, from Saintonge et al. (2017) with *b*, from Bauermeister et al. (2013) with *c*, and from Chung et al. (2009) with *d*. We show the SDSS designation, redshift, stellar mass (Kauffmann et al. 2003), and SFR (Brinchmann et al. 2004). Radio fluxes at 150 MHz are taken from Shimwell et al. (2019), those at 1.4 GHz are taken from White et al. (1997), and those at 3 GHz are taken from (Lacy et al. 2020). D_{25} is the optical diameter at the 25 mag isophote taken from the NASA/IPAC Extra galactic Database (NED)[a]. We used the radii computed from the SDSS *r*-band observation or, if available, from a photometric B-band observation. We further present the galaxy inclination calculated from a 2D Sérsic profile fit, as described in detail in Sect. 3.2.2.

[a] https://ned.ipac.caltech.edu/

2.2. Comparison samples

In order to discuss the peculiarities of our DP sample of 52 galaxies, we assembled complementary galaxy samples from existing CO observations in the literature at different redshifts, star-forming activities, and evolutionary states. For each of these galaxy samples, we performed single and double-Gaussian fits to the SDSS emission-line spectra, when available, as described in Sect. 2.1.3, and present an overview of the DP fractions in Table 2. The DP galaxies lying more than 0.3 dex above the MS have been included in the DP sample of 52 galaxies, as discussed in Sect. 2.1.3.

2.2.1. Sample from the COLD GASS survey

We use 213 CO(1-0) detected galaxies from the final COLD GASS sample (Saintonge et al. 2011, 2017), observed with the IRAM 30m telescope with M_* greater than $M_* > 10^{10}\,M_\odot$ and $0.025 < z < 0.050$. These constraints exclude the COLD GASS low extension, which is composed of galaxies of $10^9\,M_\odot < M_* < 10^{10}\,M_\odot$. We discarded these galaxies since they have an M_* of about $\sim 1-2$ dex smaller than the discussed DP sample. Due to their smaller gravitational potential, these galaxies play a different role in terms of merger-induced SF. The selected sample represents the local galaxy population, since it was selected randomly out of the complete parent sample of the SDSS within the ALFALFA footprint. We find 13 galaxies to be identified with a DP and include the two that are situated more than 0.3 dex above the MS in our present DP sample (Sect. 2.1.3).

2.2.2. M sample

To characterise galaxies that are scattered around the MS at higher redshift ($z = 0.5-3.2$), we composed a CO-detected sample, which is a part of the sample used in Tacconi et al. (2018). This sample is associated with the MS at higher redshift and we name it the M sample. The purpose of this sample is to compare the molecular-gas content and scaling relations of gas depletion time and molecular-gas fractions of DP galaxies with galaxies associated with the MS. We gathered 51 MS galaxies from the PHIBSS1 survey (Tacconi et al. 2013) observed with the IRAM Plateau de Bure Interferometer (PdBI) in CO(3-2) at two redshift groups, $z = 1-1.5$ and $z = 2-2.5$, 87 MS galaxies from the PHIBSS2 survey (Tacconi et al. 2018; Freundlich et al. 2019) observed with NOEMA in CO(2-1) or (3-2) at $z = 0.5-2.7$, nine MS galaxies at $z = 0.5-3.2$ observed by with IRAM PdBI in CO(2-1) or (3-2) (Daddi et al. 2010; Magdis et al. 2012), six MS galaxies from the *Herschel*-PACS Evolutionary Probe (PEP) survey (Lutz et al. 2011) observed with the IRAM PdBI in CO(2-1) at redshift $z = 1-1.2$ (Magnelli et al. 2012), and eight MS gravitationally lensed galaxies observed with the IRAM PdBI in CO(3-2) at $z = 1.4-3.2$ (Saintonge et al. 2013, and references therein). As shown in Fig. 2, this sample is scattered around the MS with some outliers of up to δMS = 1 dex. Contrary to the sample used in Tacconi et al. (2018), we discuss the COLD GASS sample, the EGNOG and ULIRG samples separately, and exclude all sub-samples of galaxies situated above the MS. We composed the M sample with 161 galaxies. Even though this sample lies at higher redshift than our DP sample, it allows us to discuss underlying mechanisms accounting for deviation from the scaling relations found by Tacconi et al. (2018) and which contribute to various stages of cosmic evolution. Due to their high redshifts, we do not have optical spectra of the M sample galaxies and are thus unable to estimate their DP fraction.

2.2.3. Sample from the EGNOG survey

We used 31 CO(1–0) or (3–2) galaxies detected above the MS from the EGNOG survey (Bauermeister et al. 2013) at redshift $z = 0.06-0.5$. These galaxies are mainly characterised by star-formation enhancement and show starbursts in some cases. We have SDSS spectra for 26 of these galaxies and find 11 galaxies exhibiting a DP, which we select in our present DP sample (discussed in Sect. 2.1.3). To discuss the remaining single-peaked (SP) galaxies of this sample, we gather them in the SP-EGNOG sample. The DP galaxies of the EGNOG sample are similar to the present DP sample ones in terms of SFR (Brinchmann et al. 2004), M_* (Kauffmann et al. 2003), and redshift. One main difference is the absence of radio continuum observations for the most part of this sample.

2.2.4. ULIRG sample

To compare our galaxies with the brightest infrared (IR) galaxies, we assembled a sample of ultra luminous infrared galaxies (ULIRG) with existing CO detections performed with the IRAM 30m and the FCRAO 14m telescope. These galaxies exhibit a starburst or are identified as strong quasars. We selected 18 ULIRGs detected in CO(1-0), (2-1) or (3-2) at $z = 0.2-0.6$ with far-IR luminosities of $\log(L_{FIR}/L_\odot) > 12.45$ (Combes et al. 2011), 15 ULIRGs detected in CO(2-1), (3-2), or (4-3) at $z = 0.6-1.0$ with $\log(L_{FIR}/L_\odot) > 12$ (Combes et al. 2013), 27 ULIRGs detected in CO(1-0) at $z = 0.04-0.11$ with $L_{FIR} = 0.24-1.60\,10^{12}\,L_\odot$ (Chung et al. 2009), and 37 CO(1-0) detected ULIRGs at $z < 0.3$ with $L_{FIR} = 0.29-3.80\,10^{12}\,L_\odot$ (Solomon et al. 1997). We identify three DP galaxies out of eight SDSS galaxies published by Chung et al. (2009), which are also part of our present sample (defined in Sect. 2.1.3). One DP galaxy out of the eight SDSS galaxies in Solomon et al. (1997) is Arp 220, part of our present DP sample. This provides us 93 ULIRGs, enabling us to compare our DP sample with strong IR and radio sources.

2.2.5. Low-SF sample

To study the difference between star-forming galaxies and galaxies at late stages of a starburst, or even with quenched SF, we gathered a low-SF sample. Therefore, we used 11 galaxies from Schawinski et al. (2009), which were CO(1-0)-detected with the IRAM 30m telescope. These galaxies are early-type galaxies at a redshift of $0.05 < z < 0.10$, currently undergoing the process of quenching or showing late-time SF. We further selected 17 CO(1-0) and (2-1) detected post-starburst galaxies with little ongoing SF ($\sim 1 M_\odot\,yr^{-1}$) at $0.01 < z < 0.12$ (French et al. 2015), four of which are exhibiting DP emission lines in the SDSS spectra. We added 15 bulge-dominated, quenched galaxies with large dust lanes detected in CO(1-0) and (2-1) with the IRAM 30m telescope at $0.025 < z < 0.133$ (Davis et al. 2015), three of which have DP emission line in the SDSS spectra. Finally, we added two quenched massive spiral galaxies at $z \sim 0.1$ detected in CO(1-0) with the IRAM 30m telescope (Luo et al. 2020). The low-SF sample therefore consists of 38 galaxies, creating a well-suited counterpart to MS and above-MS galaxies.

Table 2. DP rates in samples from the literature.

Sample	Size	SDSS spectrum	confirmed DP
EGNOG	31	27	11(35 %)
COLD GASS	213	213	13(6 %)
ULIRG	97	18	4(4 %)
Low SF	47	47	7(15 %)

Notes. To determine the DP rate, we show, for each sample the size, the number of galaxies with an SDSS spectra and the number of galaxies with confirmed DP emission lines. We do not show the MEGAFLOW or the M sample as they do not have SDSS spectra.

2.2.6. MEGAFLOW sample

We aim to discuss our observations with respect to recent NOEMA observations conducted by Freundlich et al. (2021). In a pilot programme of the MusE GAs FLOw and Wind (MEGAFLOW) survey, they measured CO(3-2) and (4-3) detection limits for six galaxies at $z = 0.6-1.1$ with confirmed inflows and outflows in the circumgalactic medium, to test the quasi-equilibrium model and the compaction scenario describing the evolution of galaxies along the MS, implying a tight relation between SF activity, the gas content, and inflows and outflows. This sample will help us discuss different mechanisms of compaction due to filaments or merger-driven inflows, increasing both the molecular-gas content and the star-formation efficiency, which is discussed in Sect. 5.3.

2.2.7. Fraction of DP galaxies in the comparison samples

Forty-three DP galaxies have been idenfied in the EGNOG, COLD GASS, ULIRG, and low-SF samples. Table 2 shows the fraction of DP galaxies in each sample. The M and the MEGAFLOW samples are not part of the SDSS and it is not possible to derive a DP fraction for them. Furthermore, only 19 % of the ULIRG sample is covered by the SDSS, which makes it difficult to estimate a DP fraction. As described in Sect. 2.1.3, only galaxies situated more than 0.3 dex above the MS have been selected for the present DP sample, restricting us to 17 galaxies. Hence, the remaining 26 DP galaxies are excluded from the subsequent analysis of the DP sample.

2.3. Distributions of M_* and distance to the MS for all samples

Figure 2 displays the location of the galaxies from all the samples with respect to the MS, as defined in Sect. 2.1. The estimated uncertainty of SFR_{MS} is 0.2 dex (Speagle et al. 2014). We used the SFR estimates provided by Brinchmann et al. (2004) and the M_* provided by Kauffmann et al. (2003) for our DP sample, the SF-EGNOG sample, the COLD GASS sample, and the low-SF sample, if available. We estimate a mean uncertainty of 0.1 dex for M_* for all these samples. For the SFR measurement, the average uncertainties are 0.3 dex for the DP sample, 0.15 dex for the SF-EGNOG sample, 0.45 dex for the low-SF sample, and 0.4 dex for the COLD GASS sample. The high mean uncertainties for the latter two samples are mainly influenced by quenched galaxies, as they show large SFR uncertainties (Brinchmann et al. 2004). For the M and the MEGAFLOW samples, we used SFR and M_* values provided in the literature. An estimate of the mean uncertainties is 0.25 and 0.2 dex for the SFR and M_*, respectively (Tacconi et al. 2018; Freundlich et al. 2019, 2021). For the ULIRG sample, we used a literature M_* estimate if available and computed the SFR from the L_{FIR} following Kennicutt (1998). The uncertainties for the SFR and M_* are 0.2 and 0.15 dex, respectively, as discussed in Genzel et al. (2015). However, many of these galaxies are known to host powerful AGNs, which can contribute substantially to the IR flux. Furthermore, the aperture effects and possible contribution of companions can also lead to a systematic overestimation of both the SFR and the stellar mass (Sanders & Mirabel 1996). Since we cannot quantify systematic uncertainties, we used these estimates with caution.

Table 3. Number of available radio measurements for CO samples.

Sample	CO	150 MHz	1.4 GHz	3 GHz
DP sample	52	26 (50 %)	41 (79 %)	32 (62 %)
SP-EGNOG	13	1 (8 %)	5 (38 %)	3 (23 %)
M sample	161	3(1.9 %)	0(0 %)	0(0 %)
COLD GASS	204	16 (8 %)	40 (20 %)	28 (14 %)
ULIRG	93	41 (44 %)	52 (56 %)	72 (77 %)
Low SF	38	21 (55 %)	11 (29 %)	8 (21 %)

Notes. We present the number of available radio-continuum measurements in all three radio frequencies used in Fig. 9. The percentages do not represent the radio detection rates, since not all samples are located in the observed footprints of the used radio surveys.

We find that the M sample, the majority of the COLD GASS sample, the MEGAFLOW sample, and parts of the low-SF sample are situated within the MS. We observe that parts of the COLD GASS and low-SF samples are shifted below the MS. As expected due to their high-IR luminosities, we find the ULIRG sample to be located far above the MS, and in some cases it exceeds 2 dex. Since their SFR is estimated using L_{FIR}, it is possible that in some cases non-stellar gas heating from the AGN dominates the IR emission, biasing the SFR estimate as shown in Ciesla et al. (2015). We find the DP and EGNOG samples situated in the same environment: in the upper MS or above with high stellar masses of $\sim 10^{11}$ M_*, and below the ULIRG sample.

2.4. Radio continuum for all samples

To discuss the star-forming activity based on synchrotron emission, we cross-matched the different samples with radio-continuum observation catalogues at 150 MHz, 1.4 GHz, or 3 GHz. These measurements would also be sensitive to the contribution of a possible hidden AGN. We thus selected galaxies observed by the LOFAR Two-metre Sky Survey (LoTSS) at 150 MHz (see Shimwell et al. (2019) for DR1), the Faint Images of the Radio Sky at Twenty-Centimeters (FIRST) at 1.4 GHz (White et al. 1997) or the Very Large Array Sky Survey (VLASS) at 3 GHz (Lacy et al. 2020). We used the integrated radio flux measured for each source. We used the LoTSS DR2 (early access) fluxes as the DR2 offers a larger coverage of SDSS DR7 footprint than the DR1. One can note that the DP galaxies covered by LOFAR observations have been detected.

We include radio measurements at 150 MHz provided by the LoTSS DR2 (see for DR1 Shimwell et al. 2019) and at 3 GHz taken from the VLASS (Lacy et al. 2020). We used the 1.4 GHz observations from the FIRST survey (White et al. 1997) or the NVSS (Condon et al. 1998). In Table 3, we present the fraction of available radio measurements for the different samples. We had early access to the LoTSS DR2, which does not cover the entire northern hemisphere. We thus can only take into account galaxies that are within the observed footprint. We compute the

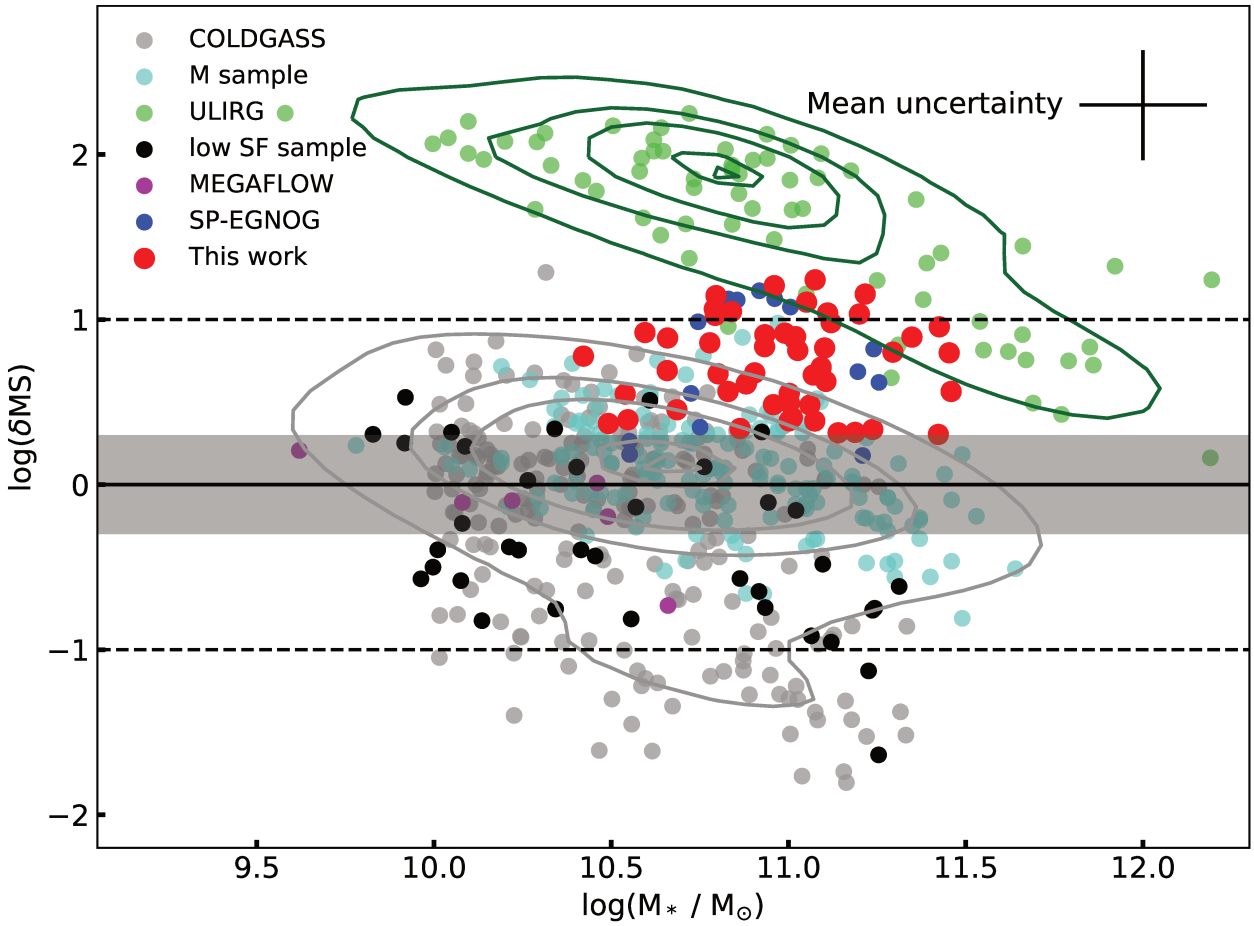

Fig. 2. Offset from MS as in Fig. 1. We show the DP sample with red dots, the SP-EGNOG sample with blue dots, the COLD GASS sample with grey dots, the low-SF sample with black dots, the ULIRG sample with green dots, the M sample with turquoise dots, and the MEGAFLOW sample with magenta dots. The literature samples are introduced in Sects. 2.2.1-,2.2.6 and a detailed description of the MS is given in Sect. 2.3. We show contour lines for the ULIRG sample in green and for the COLD GASS sample combined with the M sample in grey. In the top right, we show the mean uncertainties of all samples and discuss the individual uncertainties for each sample in the text.

radio luminosity as

$$\left(\frac{L_\nu}{W\,Hz^{-1}}\right) = \frac{36\pi \times 10^{18}}{(1+z)^{1+\alpha}} \left(\frac{F_\nu}{Jy}\right)\left(\frac{D_L}{Mpc}\right)^2, \quad (1)$$

where F_ν is the integrated radio-continuum flux at the observed frequency, D_L the luminosity distance, and α the spectral index (Condon et al. 2019). We calculated the spectral index using two radio measurements, ν_1 and ν_2, at two different frequencies:

$$\alpha = \frac{\log(F_{\nu_1}/F_{\nu_2})}{\log(\nu_1/\nu_2)}. \quad (2)$$

We preferred to use the radio measurements at 150 MHz and 1.4 GHz if available, otherwise we used a combination with the 3 GHz measurement. For galaxies where we only have a single measurement, we use $\alpha = -0.7$ (Condon et al. 2019) as an approximation.

3. Data analysis

In Sect. 3.1, we describe the fit applied to the CO emission lines. A combined fit, performed on optical and molecular-gas spectra, enabled us to identify ten DP galaxies with identical kinematic parameters, suggesting a compact molecular-gas configuration. For the remaining galaxies, a single-, a double-, and a triple-Gaussian function are fitted, and the best-fit is selected in order to accurately measure the emission-line integral. In Sect. 3.2, the CO luminosity and the aperture-corrected gas mass are computed. In Sect. 3.3, the characteristics of the DP sample are compared with the literature samples: namely, the BPT diagram, the morphology, and environment and the galaxy inclination. In Sect. 3.4, the SFR measured for the entire galaxy and only the SDSS 3″ fibre are compared.

3.1. CO line fitting

The SDSS 3″ fibre only probes the central few kpc of a galaxy in comparison to the IRAM 30m CO(1-0) beam of 23″ which covers roughly the entire galaxy at a redshift $z > 0.05$. So, these two measurements probe not only different types of gas, but also different regions of the galaxy. However, in a scenario where a merger event, a galaxy interaction, or the accretion of a large amount of gas have funnelled the gas into the central region fuelling the SF, we would expect the molecular gas to follow sim-

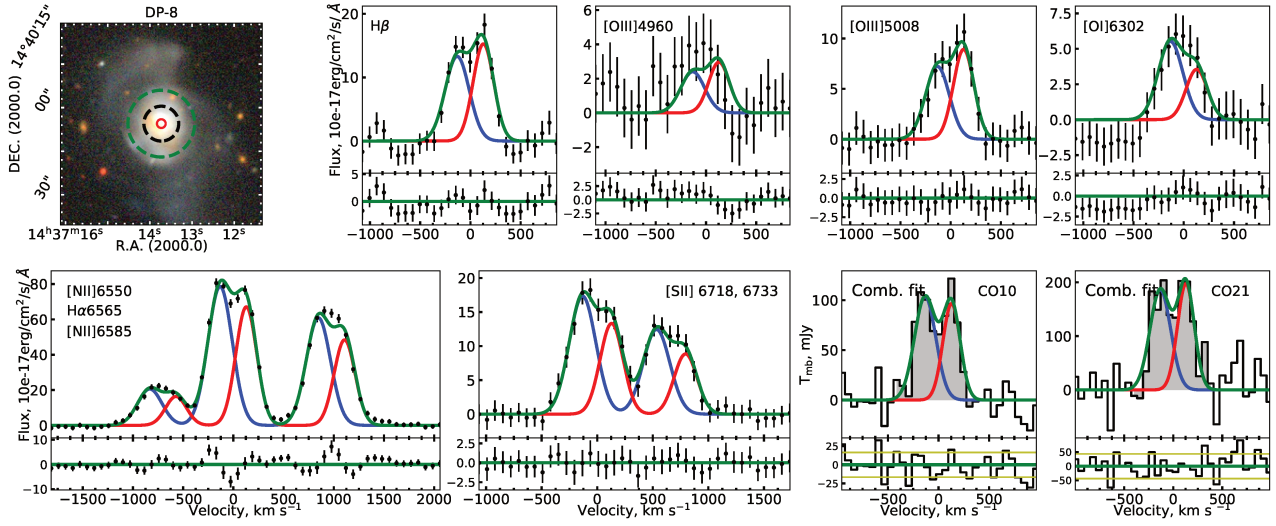

Fig. 3. Example of combined emission-line fit for DP-8. We show the Legacy survey snapshot in the top left panel, with a red circle for the SDSS 3″ fibre and dashed green (resp. black) circles for the FWHM of the CO(1-0) (resp. CO(2-1)) beam of the IRAM 30m telescope. The top row displays, next to the snapshot, the Hβ, [OIII]λ4960, [OIII]λ5008, and [OI]λ6302 emission lines. The bottom row displays the [NII]λ6550, Hα, [NII]λ6585, [SII]λ6718, and [SII]λ6733 emission lines, and two CO emission lines: CO(1-0) and CO(2-1). We show the double-Gaussian fit with the blueshifted (resp. redshifted) component in blue (resp. red) and the total fitted function in green. For each line, we show the residuals below. We display the RMS level in yellow for the CO lines, estimated beside the lines. The x-axis measures the deviations from the velocity calculated using the redshift. For the Hα line and the [NII]λ6550, 6585 doublet, we display the lines with respect to the expected Hα line velocity, and, for the [SII]λ6718, 6733, with respect to the [SII]λ6718 line velocity.

ilar kinematics to the ionised gas, with the latter tracing these star-forming regions. Such a scenario would motivate a combined fit approach, where we would expect similar kinematics in the molecular- and ionised-gas measurements.

3.1.1. Combined fit of ionised- and molecular-gas spectra

We tested to see if the same kinematic parameters can be fitted for the ionised-gas and molecular-gas emission lines. Therefore, the same Gaussian kinematic parameters $\mu_{1,2}$ and $\sigma_{1,2}$ obtained from the optical ionised-gas emission lines (as described in Sect. 2.1.3) are fixed for the CO lines' fit. Thus, only the emission-line amplitudes are fitted. Then, we checked if the ratios, between the blueshifted and redshifted Gaussian fit components, A_b/A_B, for the CO and the Hα emissions are compatible within $3\,\sigma$. In order to test the significance of the fitted components, we also computed the RMS outside the CO emission lines and checked if the residuals of the performed fit exceed three times the RMS value. If this is the case, a significant deviation from the residuals would indicate a molecular-gas component that cannot be represented by the velocity distribution found in the ionised gas. In addition, we demanded that each of the two fit components have a signal-to-noise ratio of at least 3. Secondly, if these criteria were met, we adopted this fit and flagged the CO line to indicate a successful combined fit.

When available, we first check the CO(2-1) spectra since this observation probes a smaller region than the CO(1-0) observation. Therefore, if we do not manage to perform a combined fit in the CO(2-1) line, we do not fit the CO(1-0) with this approach. In four galaxies, we only succeeded in fitting a combined fit in the CO(2-1) line and not in the CO(1-0) line. We finally find ten (19 %) galaxies with a successful combined fit and show, in Fig. 3, an example of combined fit results with all included lines for DP-8.

3.1.2. Individual CO emission-line fits

In order to estimate the CO emission lines of those galaxies where the combined fit approach failed, we fitted these spectra individually. To accurately model clumpy line shapes, we fitted each emission line with a single-, a double-, and a triple-Gaussian function and selected the best fit through an F-test, as performed for the ionised-gas emission-line fit in Sect. 2.1.3. This allows us to also model complex line shapes such as a double horn or asymmetric emission lines. To further provide a uniform estimation for the entire DP sample, we performed a single-Gaussian fit for each emission line. This allows us to compare, for example, the full width at half maximum (FWHM) value of each galaxy. In Fig. A.1, we show all results with only the Hα line and the [NII]λ6550, 6585 doublet and the CO lines. We mark a successful combined fit with a flag in each molecular emission line. The CO fit results are presented in Tables B.1 and B.2.

3.2. CO luminosity and H_2 mass

To derive the total H_2 mass, we first compute the intrinsic CO luminosity with the velocity integrated transition line flux $F_{CO(J\rightarrow J-1)}$ and calculate

$$\left(\frac{L'_{CO(J\rightarrow J-1)}}{K\,km\,s^{-1}\,pc^2}\right) = \frac{3.25\times10^7}{(1+z)}\left(\frac{F_{CO(J\rightarrow J-1)}}{Jy\,km\,s^{-1}}\right)\left(\frac{\nu_{rest}}{GHz}\right)^{-2}\left(\frac{D_L}{Mpc}\right)^2, \quad (3)$$

where ν_{rest} is the rest CO line frequency and D_L the luminosity distance (Solomon et al. 1997). We can thus derive the total

molecular-gas mass including a correction of 36 % for interstellar helium using

$$M_{H_2} = \alpha_{CO}\, L'_{CO(J\rightarrow J-1)}/r_{J1},, \quad (4)$$

where the mass-to-light ratio α_{CO} denotes the CO(1-0) luminosity-to-molecular-gas-mass conversion factor, and $r_{J1} = L_{CO\,(1\rightarrow 0)}/L_{CO\,(J\rightarrow J-1)}$ is the CO line ratio.

3.2.1. Conversion factor

The conversion factor estimated for the Milky Way and nearby star-forming galaxies with similar stellar metallicities to the Milky Way, including a correction for interstellar helium, is $\alpha_G = 4.36 \pm 0.9\,M_\odot/(K\,km\,s^{-1}\,pc^2)$ (Strong & Mattox 1996; Abdo et al. 2010). As discussed in Wolfire et al. (2010) and Bolatto et al. (2013), the CO conversion factor depends on the metallicity. We use a mean value for the correction established by Genzel et al. (2012) and Bolatto et al. (2013) and adopted by Genzel et al. (2015), Tacconi et al. (2018), and Freundlich et al. (2021):

$$\alpha_{CO} = \alpha_G \sqrt{0.67 \times \exp(0.36 \times 10^{8.67-\log Z}) \times 10^{-1.27\times(8.67-\log Z)}}, \quad (5)$$

where $\log Z = 12 + \log(O/H)$ is the gas-phase metallicity on the Pettini & Pagel (2004) scale, which we can estimate from the stellar mass using

$$\log Z = 8.74 - 0.087 \times (\log(M_*) - b)^2, \quad (6)$$

with $b = 10.4 + 4.46 \times \log(1+z) - 1.78 \times (\log(1+z))^2$ (see Genzel et al. (2015) and references therein). The gas-phase metallicity can be estimated using optical emission-line ratios, as discussed in Pettini & Pagel (2004). However, the SDSS central 3″ spectral observation is only covering the central part of the galaxy, depending on the redshift. Here, we use Equation 6 in order to obtain an estimate for the entire galaxy selection and to be consistent with previous works (Genzel et al. 2015; Tacconi et al. 2018; Freundlich et al. 2021). Furthermore, this approach enables us to compute the gas-phase metallicity for galaxies with no available spectral measurements. We find a mean conversion factor for the DP sample of $\alpha_{CO} = 3.85 \pm 0.08\,M_\odot/(K\,km\,s^{-1}\,pc^2)$, which is similar to the conversion factor we find for the EGNOG sample (of $3.86 \pm 0.09\,M_\odot/(K\,km\,s^{-1}\,pc^2)$), the low-SF sample ($3.86 \pm 0.12\,M_\odot/(K\,km\,s^{-1}\,pc^2)$), or the COLD GASS sample ($3.84 \pm 0.10\,M_\odot/(K\,km\,s^{-1}\,pc^2)$). For the ULIRG sample, we find a slightly higher conversion factor of $\alpha_{CO} = 4.00 \pm 0.39\,M_\odot/(K\,km\,s^{-1}\,pc^2)$. In case we do not have the stellar mass of a galaxy, we use the mean stellar mass of the sample to compute the conversion factor and then the molecular-gas mass. This estimation is adapted for MS galaxies (e.g. Tacconi et al. 2018) and might be overestimated in comparison with the conversion factor of $\alpha_{CO} = 0.80\,M_\odot/(K\,km\,s^{-1}\,pc^2)$ for ULIRGs discussed in Solomon et al. (1997), and we therefore use this conversion for these galaxies. The molecular-gas mass of the three ULIRGs which we adapted for our DP sample from Chung et al. (2009) are calculated using Equation. 5 in order to keep a consistent molecular-gas-mass estimate.

To compare the calculated molecular-gas masses, we need to assume the line ratio r_{J1}. In Genzel et al. (2015), Tacconi et al. (2018), and Freundlich et al. (2021), a line ratio of $r_{21} = 0.77$ and $r_{31} = 0.5$ was assumed, which is used here for the M sample. For the ULIRG sample, we choose ratios of $r_{21} = 0.83$, $r_{31} = 0.52$, and $r_{41} = 0.42$, which are empirically motivated by recent observations (see Genzel et al. (2015) and references therein).

3.2.2. Aperture correction

The closest galaxies that we observed are not entirely covered by the CO(1-0) 22″ beam, resulting in an incomplete measurement of the molecular gas. To account for the gas content outside the telescope beam, we perform an aperture correction following Lisenfeld et al. (2011). Relying on CO maps of local spiral galaxies (Nishiyama et al. 2001; Regan et al. 2001; Leroy et al. 2008), these authors assume an exponential distribution function of the CO gas. Hence, we first define the scale and geometry of each galaxy. To approximate the apparent galaxy size, we extract the optical radius at the 25 mag isophote r_{25} (see Table 1). As discussed in Lisenfeld et al. (2011), we can assume $r_e/r_{25} = 0.2$ where r_e is the CO scale length. We measure the galaxy inclination using the minor-to-major axial ratio b/a estimated from a 2D Sérsic profile fit using the photometric diagnostic software STATMORPH[3] (Rodriguez-Gomez et al. 2019). We compute the inclination i as

$$\cos i = \sqrt{\frac{(b/a)^2 - q_0^2}{1 - q_0^2}}, \quad (7)$$

where q_0 describes the intrinsic axial ratio of an edge-on observation and is set to $q_0 = 0.2$ (Catinella et al. 2012; Aquino-Ortíz et al. 2018). For galaxies classified as mergers, we set the inclination to 0°, since we cannot identify their orientation with a Sérsic profile. Lastly, following Lisenfeld et al. (2011), the aperture correction factor is computed as

$$f_a = \pi r_e^2 \left\{ \int_0^\infty dx \int_0^\infty dy \exp\left(-\ln(2) \left[\left(\frac{2\,x}{\Theta_B} \right)^2 + \left(\frac{2\,y\cos(i)}{\Theta_B} \right)^2 \right] \right) \exp\left(-\frac{\sqrt{x^2+y^2}}{r_e} \right) \right\}^{-1}, \quad (8)$$

where Θ_B is the FWHM of the observation beam. We carry out the integration numerically.

We present the aperture correction factors and the corrected molecular-gas masses in Table B.3. We set the correction factor to 1 for galaxies that are observed using interferometry since we have accurate molecular-gas-mass measurements. We measure a mean correction factor for the DP sample of $f_a = 1.27$. We present the CO luminosities, the molecular-gas mass, and the aperture correction in Table B.3.

3.3. DP sample characteristics

The properties of the DP galaxies are discussed here. These include their position on the BPT diagram (Sect. 3.3.1), their morphology and their environment (Sect. 3.3.2), and their inclination (Sect. 3.3.3).

3.3.1. BPT diagram

We use the BPT diagnostic diagram (Baldwin et al. 1981) to classify our galaxy samples based on optical emission-line ratios: [OIII]λ5008/Hβ on the y-axis and [NII]λ6585/Hα on the x-axis. Relying on the criteria empirically found by Kewley et al.

[3] https://statmorph.readthedocs.io

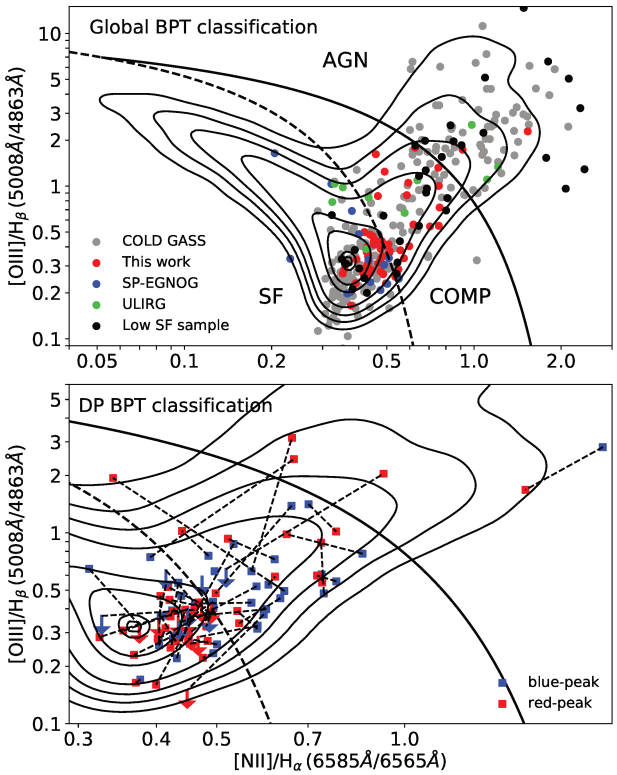

Fig. 4. BPT diagrams to classify our galaxy samples into different galaxy types based on ionised-gas emission-line ratios (Kewley et al. 2006). The black solid line separates AGN and COMP galaxies and the dashed black line star-forming galaxies from COMP galaxies. In the *top* panel, we show galaxies of all samples with existing SDSS spectra. We use Gaussian or non-parametric emission-line fits, in case of a non-Gaussian emission-line shape, provided by Chilingarian et al. (2017). In the *bottom* panel, we show, for each galaxy of the DP sample, the blueshifted and redshifted peaks represented by blue and red squares, respectively, and connect them by a black dashed line. In comparison to the *top* panel, we zoomed into the region where we detect DP galaxies, to resolve both components. For galaxies with one of the needed emission lines below 3 σ, we indicate the emission-line ratio limits with arrows. In both panels, we show contour lines representing galaxies of the RCSED catalogue which have a S/N > 3 in all required emission lines.

(2006), we differentiate between SF galaxies, AGN, and composite (COMP) galaxies, which are characterised by both mechanisms: SF and AGN. In the top panel of Fig. 4, we show the position on the BPT diagram of the DP, COLD GASS, SP-EGNOG, and low-SF samples. Depending on which function fits the data better, we use the Gaussian or the non-parametric emission-line estimate provided by Chilingarian et al. (2017). For the DP sample, for example, we used the latter, which gives us a global estimation of the entire emission line. In order to characterise each emission-line component individually, we classify each of them separately. We present both classifications in the lower panel of Fig. 4 and list their classifications in Table 4. We also show the classification using the non-parametric fit. In order to unambiguously classify each emission-line component, the Hβ and [OIII]λ5008 lines must be detected, with an S/N > 3, at least, which is not always the case, as for DP-45 and DP-51. However, using the non-parametric fit we are able to classify DP-51.

Using the non-parametric fit, we classify 56 % of the DP sample as SF, 37 % as COMP, and 4 % as AGNs. The DP sample is dominated by SF galaxies, which is consistent with the fact that the DP sample was selected 0.3 dex above the MS. When each emission-line component is considered individually, nine galaxies (17 %) have their two components classified differently. In particular, we find seven SF + COMP, one SF + AGN, and one COMP + AGN. However, we do not find any trend in molecular-gas mass, morphological type, or success of combined fit for these peculiar galaxies.

We classify galaxies of all samples, if possible, with the BPT diagram and build up SF-COMP sub-samples of all galaxies classified as SF or COMP, and an active galaxy sample for those classified as AGNs. For the ULIRG sample, we use classifications provided in the literature since we have SDSS spectra of ten galaxies enabling a detailed BPT classification. We classify all Low Intensity Narrow Emission-line Regions (LINER), Seyfert galaxies, and quasars as an AGN sub-sample. Galaxies of the ULIRG sample show large fractions of strong radio galaxies, we thus do not select any SF-COMP sub-sample for them since we are not able to correctly characterise their AGN contribution. This classification allows us to test the radio flux as a tracer of molecular gas in SF galaxies and to discuss the behaviour of AGN galaxies.

3.3.2. Morphology and galaxy environment

To further characterise the evolutionary state of the galaxies, we visually inspect the legacy survey images (Dey et al. 2019) and categorise them as mergers if we see an optical perturbation, as late-type galaxies (LTG) if we can identify a spiral disc, or as S0 if we can identify a disc with the bulge dominating the shape. The results found by Domínguez Sánchez et al. (2018), using a machine-learning-based classification discussed in M20, inspired this classification.

We also flag LTG and S0 galaxies that have tidal features, since this can be the sign of a recent merger or interaction. In Table 4, we present the morphological type of each galaxy of the DP sample.

We find 27 % to be classified as LTG, 38 % as S0 galaxies, and 35 % as mergers. We also find 13 % to be either S0 galaxies or LTG with notable tidal features. A close examination of all DP LTGs reveals that they are all bulge-dominated and Sa types. In order to compare the obtained merger fraction to the one of single-peaked emission-line galaxies, we select 1000 single-peak galaxies from Maschmann et al. (2020) that are situated at 0.3 dex above the MS, and we classify them in the exact same way. This sample of single-peaked emission-line galaxies was selected with the same S/N ratio thresholds of the Hα and O[III]λ5008 emission lines and following the same redshift and stellar mass distribution as the DP galaxy sample of Maschmann et al. (2020). For this galaxy sample, we find only 10 % mergers and 14 % galaxies with tidal features. It is not straightforward to compare these two galaxy samples. On the one hand, we selected four ULIRGs for the DP sample from the literature, which are all mergers, and on the other hand, galaxies with unusually high SFR values were selected for our CO observations, introducing a bias. However, we find 48 % of the DP sample to show either a visual merger or tidal features, which is about twice as much as we find for single-peak emission-line galaxies.

To discuss the fact that we see more bulge-dominated galaxies in the DP sample, we perform a morphological classification of other nearby galaxies samples. Using the Legacy Survey images, we can classify the SP-EGNOG, the COLD GASS, and

the low-SF samples in the exact same way as for the DP sample without adding a bias of resolution due to larger redshifts to this classification. The SP-EGNOG sample shows a very similar distribution of stellar masses and SFR as discussed in Sect. 2.3. We also find a very similar morphological composition of 30 % LTG, 40 % S0, and 10 % mergers. The remaining 20 % are at redshift 0.5 and thus not classifiable with the Legacy Survey images. Interestingly, we also find the LTG galaxies of the SP-EGNOG sample to be bulge-dominated and Sa type. Furthermore, we detect fewer mergers but identify 25 % of the LTG and S0 galaxies to have tidal features. In order to compare the DP sample to the literature galaxies, we classify the galaxies of the COLD GASS sample that are situated more than 0.3 dex above the MS. These galaxies have a mean stellar mass of $\log(M_*/M_\odot) = 10.5$, which is 0.5 dex smaller than the mean stellar mass of the DP sample. We find 63 % of LTGs, 18 % of S0 galaxies, and 18 % of galaxy mergers. The LTGs exhibit smaller bulges which are of type Sb or Sc. The low-SF sample, in contrast, consists of only 13 % LTGs and 18 % mergers. However, we find 68 % to be classified as bulge-dominated galaxies (i.e. S0 or elliptical galaxies). While the merger rates are not discriminant, the low-SF sample is dominated by early-type galaxies partly quenching explaining their low SFR, while the COLD GASS sample hosts more disc-like galaxies with smaller bulges than the DP sample.

To discuss the impact of the environment, we identify the associated group galaxies using Saulder et al. (2016) for galaxies at $z < 0.11$, and Yang et al. (2007) for galaxies at $z > 0.11$. In Saulder et al. (2016), galaxy groups were identified using a group-finding algorithm that was calibrated with cosmological simulations. The group-finding algorithm in Yang et al. (2007) is a halo-based friends-of-friends finding algorithm. Both algorithms provide the number of galaxies in the group and we can measure the projected distance to the closest neighbour. In Table 4, we present the environment parameters for each DP galaxy.

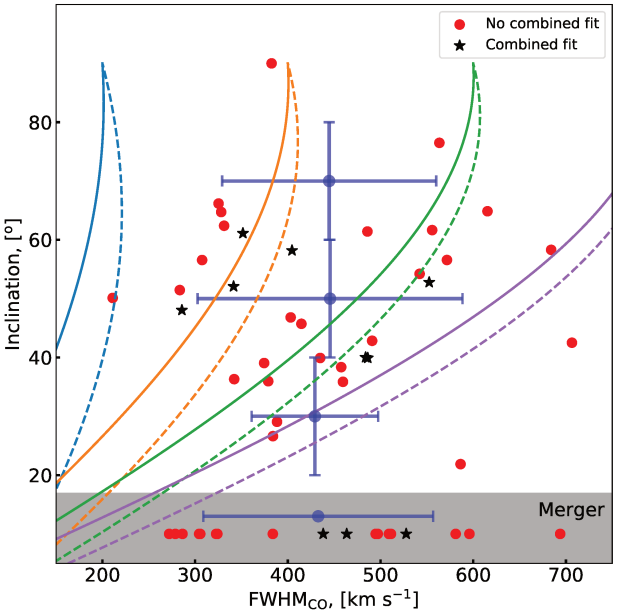

Fig. 5. Values of CO FWHM (x-axis) for different galaxy inclinations i (y-axis) of the DP sample. Black stars (resp. red dots) are galaxies for which we succeeded (resp. fail) in applying a combined line fit (see Sect. 3.1). Since it is not possible to measure the inclination of galaxy mergers, we show their FHWM values separately in the grey area at the bottom of the plot. Mean values of the FWHM and standard deviations are displayed with blue error bars for three groups of different inclinations and for the merger sub-sample. The curves show the relation between FWHM and inclination obtained for the estimate of Eq. 9 for a rotating disc, with v_{rot} = 100, 200, 300, and 400 km/s for the blue, orange, green, and purple curves, respectively, and with gas velocity dispersions of 10 and 40 km/s for solid and dashed lines.

3.3.3. Relation between inclination and kinematics

A rotating disc creating different velocity measurements within the line of sight of a galaxy can create a double-horn or double-peak signature (e.g. Westmeier et al. 2014). In such a scenario, we may expect to see at least a correlation between the galaxy inclination and the FWHM of the CO emission lines. We therefore performed a single-Gaussian fit to the CO emission lines and compare the measured FWHM to the galaxy inclination i, as estimated in Sect. 3.2.2. We use the CO(2-1) line since it has a higher S/N in comparison to the CO(1-0) line in the DP sample. For galaxies with no CO(2-1) observations, we use the CO(1-0) line. The beam sizes of the CO(1-0) and CO(2-1) observations are different (23″ and 12″ , respectively) for the 35 galaxies observed at the IRAM-30m telescope and for the 17 galaxies obtained from the literature, measured with different telescopes and beam sizes. Given the DP galaxies' redshift distributions, the CO emission lines are not measured on uniform scales. However, as described in Sect. 3.2.2, most measurements include the majority of the molecular gas. The relation between the CO FWHM and the galaxy inclination for the DP sample is displayed in Fig.5. The mean values and the standard deviation of the CO FWHM for groups of different inclinations are shown. Galaxies classified as mergers are presented separately, since the Sérsic profile fit to the r-band image does not necessarily represent the disc orientation of the galaxies. Inclinations are gathered in three groups: $20° < i < 40°$, $40° < i < 60°$, and $60° < i < 80°$. Galaxies for which we succeeded in applying a combined line fit are indicated as black stars (see Sect. 3.1).

We are not able to find any trend or correlation between the measured FWHM and the galaxy inclinations. A large scatter is, however, expected even in the case of rotating discs, depending on the mass concentration of the galaxies and also on the velocity dispersion of the molecular gas. A rotation curve rises all the more steeply as mass is concentrated, leading to a dependency of the measured velocities on the mass concentration for a given stellar mass (for typical massive galaxies whose mass is dominated by baryonic matter in their central parts). As the CO gas emission tends to be concentrated, the corresponding velocity measurements may probe only a part of the rising of the rotation curve. A more concentrated stellar bulge will thus likely lead to a larger detected FWHM of the CO emission lines. To illustrate this effect, in Fig. 5 we show a few curves corresponding to different measured rotation velocities, representing measurements for a varying mass concentration at fixed stellar mass, and with two different molecular-gas velocity-dispersion values. We use the simple estimate:

$$\mathrm{FWHM_{CO}} = 2.35\sigma \cos i + 2v_{rot} \sin i, \quad (9)$$

corresponding to the expected width of a double-horn velocity profile widened by a gas-velocity dispersion σ for a disc rotating at v_{rot} with an inclination of i. The first term corresponds to the contribution of the velocity of the gas in the orthogonal direction to the disc plane, and the second term corresponds to the disc's in-plane gas velocity, dominated by rotation. We also do not find different effects between galaxies with and without a successful combined fit. The rotation velocity of disc galaxies depends

Table 4. Characteristics of observed galaxies.

ID	Morphology	BPT_1	BPT_2	BPT_t	Comb. fit	N_G	D_N
							kpc
DP-1[a]	Merger	agn	agn	agn	0	$2^{\dagger}$	$334^{\dagger}$
DP-2	LTG	comp	sf	comp	0	$3^{\dagger}$	$269^{\dagger}$
DP-3	LTG	comp	comp	comp	1	$1^{\dagger}$	-
DP-4	LTG	sf	sf	sf	1	$2^{\dagger}$	$117^{\dagger}$
DP-5	Merger	comp	comp	comp	1	$4^{\dagger}$	$27^{\dagger}$
DP-6	LTG	comp	sf	comp	0	$12^{\dagger}$	$61^{\dagger}$
DP-7	LTG	sf	sf	sf	0	$13^{\dagger}$	$115^{\dagger}$
DP-8	Merger	comp	comp	comp	1	$1^{\dagger}$	-
DP-9	LTG	sf	sf	sf	0	$1^{\dagger}$	-
DP-10	LTG	comp	comp	comp	1	$3^{\dagger}$	$64^{\dagger}$
DP-11	S0	sf	sf	sf	0	$2^{\dagger}$	$313^{\dagger}$
DP-12	Merger	comp	comp	comp	0	$20^{\dagger}$	$15^{\dagger}$
DP-13[b]	LTG	sf	sf	sf	0	$1^{\dagger}$	-
DP-14	LTG	comp	comp	comp	0	$2^{\dagger}$	$146^{\dagger}$
DP-15	Merger	sf	sf	sf	1	$1^{\dagger}$	-
DP-16	S0 + T	sf	sf	sf	1	$6^{\dagger}$	$174^{\dagger}$
DP-17[b]	Merger	comp	comp	comp	0	$6^{\dagger}$	$161^{\dagger}$
DP-18	S0	sf	sf	sf	0	$4^{\dagger}$	$138^{\dagger}$
DP-19[c]	LTG + T	comp	sf	sf	1	$3^{\dagger}$	$85^{\dagger}$
DP-20	S0 + T	sf	sf	sf	0	$3^{\dagger}$	$399^{\dagger}$
DP-21	S0	comp	sf	sf	0	$2^{\dagger}$	$104^{\dagger}$
DP-22	S0		agn	agn	0	$3^{\dagger}$	$707^{\dagger}$
DP-23	Merger	comp	sf	sf	0	$3^{\dagger}$	$651^{\dagger}$
DP-24[d]	Merger	comp	comp	comp	0	$8^{\dagger}$	$129^{\dagger}$
DP-25[d]	Merger	comp	comp	comp	0	$4^{\dagger}$	$7^{\dagger}$
DP-26	Merger	comp	sf	comp	0	$4^{\dagger}$	$42^{\dagger}$
DP-27[c]	LTG	sf	sf	sf	0	$1^{\dagger}$	-
DP-28	S0 + T	sf	sf	sf	0	$1^{\dagger}$	-
DP-29	S0	comp	agn	comp	0	$2^{\dagger}$	$370^{\dagger}$
DP-30	Merger	comp	comp	comp	0	$1^{\dagger}$	-
DP-31[d]	Merger	comp	comp	comp	0	$1^{\dagger}$	-
DP-32	S0	sf	sf	sf	0	1^{+}	-
DP-33	S0 + T	sf	sf	sf	1	1^{+}	-
DP-34	Merger	sf	sf	sf	0	1^{+}	-
DP-35	LTG	comp	sf	sf	0	2^{+}	303^{+}
DP-36	S0	sf	sf	sf	0	1^{+}	-
DP-37	Merger	sf	sf	sf	0	1^{+}	-
DP-38	Merger	sf	sf	sf	0	-	-
DP-39	LTG + T	sf	sf	sf	0	1^{+}	-
DP-40	S0	sf	sf	sf	1	1^{+}	-
DP-41[c]	S0	sf	sf	sf	0	-	-
DP-42[c]	S0	sf	sf	sf	0	1^{+}	-
DP-43[c]	Merger	sf	sf	sf	0	1^{+}	-
DP-44[c]	S0	comp			0	1^{+}	-
DP-45[c]	S0				0	1^{+}	-
DP-46	S0 + T	comp	comp	comp	0	1^{+}	-
DP-47[c]	S0	sf	sf	comp	0	1^{+}	-
DP-48	S0	sf	sf	sf	0	1^{+}	-
DP-49[c]	Merger	comp	sf	sf	0	1^{+}	-
DP-50	Merger	sf	agn	comp	0	-	-
DP-51[c]	S0			sf	0	-	-
DP-52[c]	LTG	sf	sf	comp	0	-	-

Notes. Column 2 shows the morphological classification based on visual inspection. Galaxies that show tidal features are indicated with a '+ '. We also show the BPT classification of the blueshifted and redshifted components in columns 3 and 4, respectively. In column 5, we show the total BPT classification using the non-parametric fit. In column 6, we indicate if we succeeded in performing a combined fit using a 1. We display the number of galaxies N_G associated in the same group in column 7 and the distance to the closest neighbour in column 8. We preferred to use Saulder et al. (2016), which is denoted with a † and, for galaxies at $z > 0.11$, we used Yang et al. (2007), denoted with a +. The denotations *a*, *b*, and *c* are the same as in Table 1.

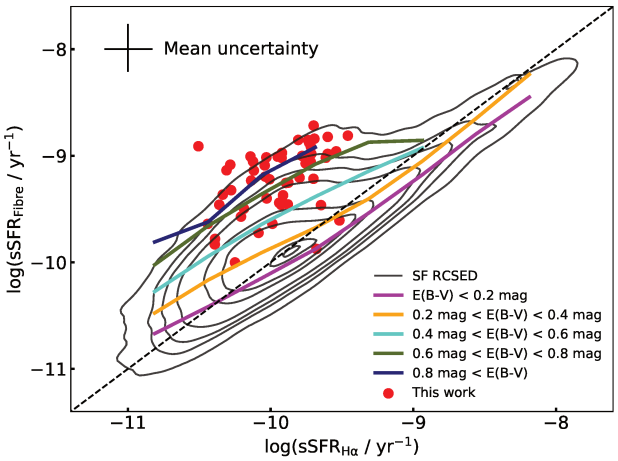

Fig. 6. Comparison of sSFR estimate inside the SDSS 3″ fibre. On the x-axis, we show the sSFR estimated from extinction corrected Hα luminosities ($SFR_{H\alpha}$), and on the y-axis, we show the sSFR inside the fibre (SFR_{fibre}) estimated by Brinchmann et al. (2004). The DP sample is marked with red circles, and the galaxies with an S/N> 10 in the Hα line of the RCSED catalogue (Chilingarian et al. 2017) are marked with black contour lines. We also show the median of groups of different gas extinction E(B-V), computed following Equation (11), with solid thick lines. The black dashed line denotes $SFR_{H\alpha} = SFR_{fibre}$. The black error bar is the mean estimated uncertainty of the SFR, including stellar mass uncertainties.

on galaxy mass (Tully & Fisher 1977), but by taking their stellar mass into account, we were still not able to detect any trend. These findings are in agreement with results on ionised-gas velocity dispersions and galaxy inclination of a larger DP sample (M20).

3.4. Star formation

To compute the extinction-corrected luminosity of the Hα emission line, we used the following Calzetti (2001):

$$L_{int}(H\alpha) = L_{obs}(H\alpha)\, 10^{0.4\kappa(H\alpha)E(B-V)}, \quad (10)$$

where $L_{int}(H_\alpha)$ is the intrinsic and $L_{obs}(H_\alpha)$ the observed Hα luminosity. $\kappa(H_\alpha)$ is the reddening curve parametrised by Calzetti et al. (2000) at the Hα rest-frame wavelength, and E(B-V), the colour excess, is computed as

$$E(B-V) = 1.97 \log_{10}\left[\frac{(H\alpha/H\beta)_{obs}}{2.86}\right], \quad (11)$$

following Momcheva et al. (2013) and Domínguez et al. (2013). The dust extinction estimate is based on the assumption of an intrinsic Hα/Hβ ratio of 2.86, appropriate for a temperature of $T = 10^4$ K and an electron density of $n_e = 10^2 cm^{-3}$ for a case B recombination (Osterbrock & Ferland 2006). We can thus compute the Hα-based SFR as $SFR(H\alpha) = 7.9 \times 10^{-42} \times L_{int}(H\alpha)$ following Kewley et al. (2002).

We compute the $SFR_{H\alpha}$ inside the SDSS 3″ fibre for both emission-line components of the DP sample and the total emission-line luminosity using the non-parametric emission-line fit provided by Chilingarian et al. (2017). To assess the quality of this estimate, we compare the $SFR_{H\alpha}$ estimate to the SFR estimate of the SDSS fibre SFR_{fibre} provided by Brinchmann et al. (2004), which is based on an emission-line modelling to avoid creating biases in the SFR estimated from the emission lines as a function of metallicity or stellar mass. This approach also takes the diffuse emission inside a galaxy into account. In Fig. 6, we show the specific star formation rate sSFR = SFR / M_* inside the 3″ fibre using the stellar mass estimate (Kauffmann et al. 2003), considering the $SFR_{H\alpha}$ on the x-axis and the SFR_{fibre} on the y-axis. We present galaxies from the RCSED catalogue with an S/N > 10 in the Hα emission line with black contours and show the mean values of groups of different extinction E(B-V) computed following Eq. 11. We show the DP sample with red dots using the SFR estimate with the non-parametric emission-line fit to account for the entire system. We find the $sSFR_{H\alpha}$ to be underestimated of around 1 dex in comparison with the $sSFR_{fibre}$ for the DP sample. This systematic effect correlates with the measured dust extinction. We observe a mean value of $E(B-V) = 0.66 \pm 0.19$ mag for the DP sample, which is in agreement with the observed offset for SF galaxies of the RCSED with comparable gas-extinction values. Although we corrected the Hα luminosity for extinction, strong dust obscuration can shield parts of the optical light from star-formation sites. This phenomenon was discussed in greater detail in Sanders & Mirabel (1996) and references therein. To calculate the SFR correctly, the estimate of the Hα luminosity has to be combined with IR estimates as performed e.g. in Pancoast et al. (2010). This means that the calculated $SFR_{H\alpha}$ for both components is systematically underestimated but still provides an estimate enabling us to compare the SF contribution of both components.

Besides the SFR_{fibre}, Brinchmann et al. (2004) estimated the SFR_{total} for the entire galaxy, enabling us to test if SF is concentrated in the central parts of the galaxy or is equally distributed in the disc. In Fig. 7, we show the ratio of $\mathcal{R} = SFR_{fibre}/SFR_{total}$ for the DP sample, the EGNOG sample, the COLD GASS sample, and the low-SF sample. We also show subsets of BPT classifications as discussed in Sect. 3.3.1. This diagnostic method is only meaningful for galaxies at lower redshift since the 3″ SDSS fibre covers the entire galaxy at higher redshift. We thus exclude the galaxies of $z \sim 0.5$ of the EGNOG sample from this study. We also do not show galaxies of the M sample or the ULIRG sample, since these galaxies have either no SDSS spectral observation or do not show any difference between fibre and total SFR due to their high redshift. We note that the SFR_{total} is calculated using star-formation history modelling, which relies on a first estimate of SFR_{fibre} from Brinchmann et al. (2004). This can result in an SFR_{total} estimate smaller than the SFR_{fibre}, creating ratios slightly greater than one.

For the DP and SP-EGNOG samples, we find a tendency towards a ratio of 1 ($\mathcal{R}_{DP} = 0.81 \pm 0.25$ and $\mathcal{R}_{SP-EGNOG} = 0.77 \pm 0.32$, respectively). The galaxies of the DP sample with a successful combined fit (see Sect. 3.1) show an even higher mean ratio of $\mathcal{R}_{DP} = 0.90 \pm 0.19$, indicating that the majority of their SF is happening in the centre. In contrast to that, we find the opposite effect with no central enhancement of SF for galaxies of the COLD GASS sample ($\mathcal{R}_{COLD\ GASS} = 0.27 \pm 0.24$). The low-SF sample exhibits a very broad distribution ($\mathcal{R}_{low\ SF} = 0.48 \pm 0.26$). Given the measurement uncertainties, we can observe that the DP and the SP-EGNOG samples are clearly biased in favour of large values of $\mathcal{R}$, in particular with respect to the COLD GASS sample.

4. Results

In Sect. 4.1, the ionised- and molecular-gas kinematics measured in single apertures are compared. Sect. 4.2 is focused on the correlation between the molecular gas and the radio continuum. The position of all samples on the Kennicutt-Schmidt relation are dis-

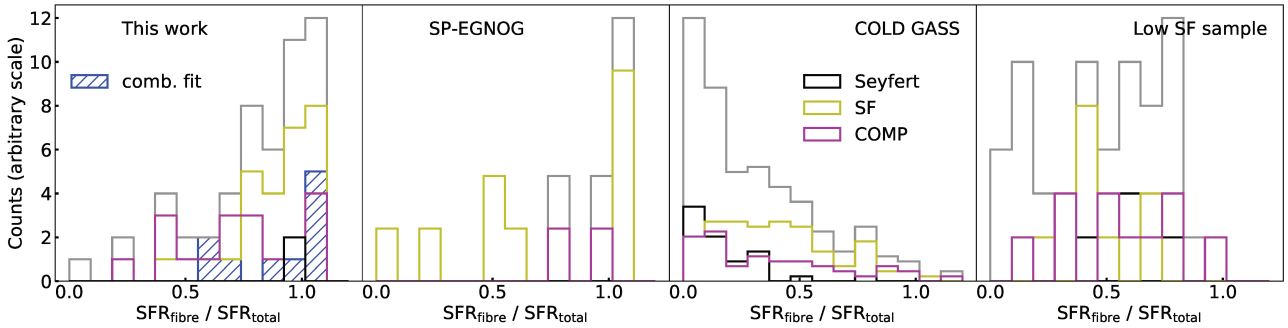

Fig. 7. Ratio of SFR inside the 3″ SDSS fibre SFR_{fibre} and the total SFR SFR_{total} (Brinchmann et al. 2004). We show this relation for galaxies processed by Brinchmann et al. (2004), which are, from left to right, the DP galaxies, 14 galaxies of the SP-EGNOG survey, 161 galaxies of the COLD GASS sample, and 74 galaxies of the low-SF sample. Subsets of BPT classification of SF are in yellow, those of COMP are in magenta, those of AGNs are in black, and those of the total histogram are in grey. For the DP sample, the subset of galaxies with successful combined fit is indicated with a hatched blue histogram. The scales of the histograms are in arbitrary units.

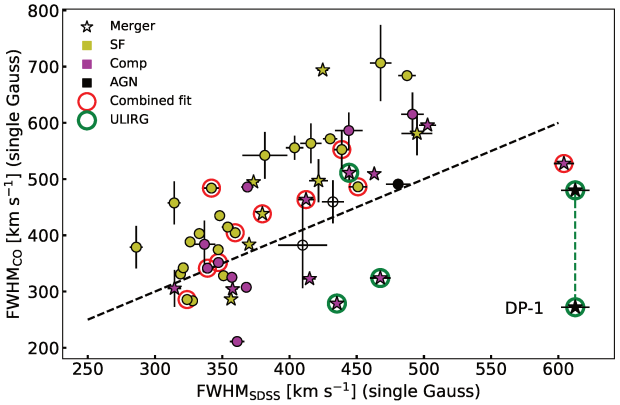

Fig. 8. Comparison of FWHMs of ionised- and molecular-gas emission lines, estimated from a single-Gaussian function for the DP sample galaxies. The FWHMs of the ionised-gas emission lines (x-axis) measured inside the 3″ SDSS fibre are estimated by Chilingarian et al. (2017). The FWHMs of the CO line (x-axis) are measured as described in Sect. 3.3.3. The black dashed line denotes $y = x$. Error bars are estimated from the single-Gaussian line fitting. Stars indicate galaxies classified as mergers. The markers are coloured according to the BPT classification (See Sect. 3.3.1): SF in yellow, COMP in magenta and AGN in black. We mark galaxies for which we succeed in applying a combined line fit (see Sect. 3.1) by red circles. The four ULIRGs of the DP sample are marked with green circles. For the galaxy DP-1, the CO-FWHM is estimated both inside the 3″ SDSS fibre and for the entire galaxy, and the two points are connected with a green dashed line.

cussed in Sect. 4.3. Lastly, the variation of the molecular-gas fraction and depletion time with redshift and with the relative distance to the MS are studied in Sect. 4.4.

4.1. Kinematical arguments: Mergers, rotating discs, and outflows

Since the measurements of ionised and molecular gas used in this work do not originate from the same area, we compare the FWHM values of the ionised gas and the CO lines in Fig. 8. We show the uncertainties with error bars estimated from the fit. Their size can be in some cases smaller than the marker, which is due to high S/N values.

We find that the CO FWHM values are, on average, larger than those of the ionised gas. This can be explained since the CO measurement probes a larger area. For a typical rotation curve rising with radius before reaching a plateau, the widths of the emission lines depend on the part of the rotation curve encompassed by the fibre or beam. If the SDSS fibre encompasses a smaller extent of the rising part of the rotation curve than the CO beam, the ionised emission line is expected to be narrower. The width of the ionised-gas emission lines can, however, be similar to the CO ones, even if the ionised gas extends further away than the SDSS fibre, if the galaxy mass is concentrated enough for the SDSS fibre to encompass the beginning of the plateau of the rotation curve.

In Sect. 3.1, we discuss a combined fit that we performed to select galaxies that show similar kinematics in the ionised and molecular gas. These are highlighted in Fig. 8. The majority of these galaxies are situated near the $y = x$ line, except for two galaxies (DP-20 and DP-33) that have CO FWHM values of about 100 km s^{-1} larger than the FWHM estimated for the ionised gas. While they met the selection criteria discussed in Sect. 3.1, they give an idea of the expected scatter. In parallel, many galaxies are very close to the $y = x$ line but do not meet the combined fit criteria due to low S/N values and different double peak ratios.

We also observe galaxies with larger FWHM values for the ionised gas than for the molecular gas. This is expected due to ionised-gas outflows driven by a central AGN. As displayed in Fig. 8, most galaxies classified as composite or AGNs are near the $y = x$ line or below. In particular, for DP-1, which is the resolved (ULIRG) galaxy of the DP sample, we observe that the FWHM of the molecular gas inside the 3″ fibre is more than two times smaller than for the optical spectra. When one integrates over the whole galaxy, the molecular gas is still well below the $y = x$ line. Also, the other galaxies lying below the $y = x$ line, including the two of the four ULIRGs marked with green circles, show a broader ionised-gas velocity distribution. This is not expected to be due to rotation, but it is compatible with AGN outflows, which could account for velocities undetected in CO. Interestingly, while mergers are spread all over Fig. 8, the majority of the galaxies below the $y = x$ line are mergers, suggesting a link between the AGN feedback and the merging process. In contrast to that, we find that the majority of the galaxies classified as SF lie above the $y = x$ line, but fewer of these SF galaxies are classified as mergers.

Table 5. Fit results of L'_{CO} - radio correlation.

Relation	Slope	Intercept	σ	P
$L'_{CO} - L_{150\,MHz}$	0.82 ± 0.06	-9.54 ± 1.39	0.32	0.88
$L'_{CO} - L_{1.4\,GHz}$	0.80 ± 0.05	-8.62 ± 1.03	0.26	0.87
$L'_{CO} - L_{3\,GHz}$	0.87 ± 0.08	-10.01 ± 1.75	0.23	0.83

Notes. Best-fit results for a linear fit of CO luminosties as a function of radio luminosities. We show the slope, the intercept, the scatter σ, and the Pearson coefficient P.

4.2. CO and radio-luminosity correlation

star-formation sites accelerate electrons and positrons in supernova remnants to high energies, emitting synchrotron radiation when interacting with the galaxies magnetic field (e.g. Condon 1992). It is thus possible to directly trace the SF with radio continuum observations, which is a well-established technique at 1.4 GHz (Condon 1992; Bell 2003; Schmitt et al. 2006; Murphy et al. 2011) and has also proven to be valid at 150 MHz, as shown in Calistro Rivera et al. (2017) and Wang et al. (2019). In contrast, electrons and positrons can also be accelerated in relativistic jets of AGN and shock regions as discussed in, for example, Meisenheimer et al. (1989). In extended radio lobes, these high-energy particles interact with the magnetic-field-creating sychrotron emission (see e.g. Krause et al. 2012). Both mechanisms result in a spectrum described by a power law of $S(\nu) \propto \nu^{\alpha}$, where $S(\nu)$ is the radio flux and α the spectral index.

SF depends directly on the molecular-gas reservoir, and thus another way to exploit this connection is the relation between the radio luminosity and L'_{CO}. This relation has been known for a long time using the 1.4 GHz radio continuum, and it dates back to the beginning of CO observations (Rickard et al. 1977; Israel & Rowan-Robinson 1984; Murgia et al. 2002). Recently, Orellana-González et al. (2020) quantified this relation as $L'_{CO} = (1.04 \pm 0.02)\, L_{1.4\,GHz} - 14.09 \pm 0.21$ for galaxies at $z < 0.27$ for more than five orders of magnitude of the luminosities. We aimed to test this relation for the selected CO samples by distinguishing between star-forming galaxies and those with AGN contribution.

In Fig. 9, we show the correlation between L'_{CO} and radio luminosity at 150 MHz, 1.4 GHz, and 3 GHz. The average uncertainties of the observed radio fluxes are 7 % at 150 MHz, 5 % at 1.4 GHz, and 11 % at 3 GHz and are indicated by an error bar. We mark active galaxies with dots, SF galaxies with yellow stars, and COMP galaxies with purple stars. We find a good agreement with the empirical correlation found by Orellana-González et al. (2020) for $L_{1.4\,GHz}$ and observe a similar behaviour for the SF-COMP sub-samples at 3 GHz and 150 MHz. We note that galaxies classified as AGNs do not follow such a linear relation. The ULIRG sample especially shows a clear excess in radio luminosity in comparison to other galaxies with comparable L'_{CO} measurements. This might be an indicator that the radio-continuum emission is dominated by the AGN and is thus no longer correlated with the molecular gas. We fit a straight line to all three relations by only using the SF+COMP sub-samples, and we show the fit results in Table 5. For the $L'_{CO} - L_{1.4\,GHz}$ relations, we find a less steep slope (0.80 ± 0.05) than Orellana-González et al. (2020) (1.04 ± 0.02). However, taking the scatter of 0.32 into account, these two estimates are still comparable. Interestingly, we find similar parameters for the $L'_{CO} - L_{150\,MHz}$, the $L'_{CO} - L_{1.4\,GHz}$, and the $L'_{CO} - L_{3\,GHz}$ relations with nearly the exact same slope.

4.3. Kennicutt-Schmidt relation

Figure 10 displays the empirical Kennicutt-Schmidt (KS) relation relating the gas density and SFR through a power law (Schmidt 1959; Kennicutt 1998). On the x-axis, we plot the SFR surface density $\Sigma_{SFR} = SFR/\pi R^2$, and on the y-axis we plot the molecular-gas surface density $\Sigma_{H_2} = M_{H_2}/\pi R^2$, where R is the half-light radius provided in the literature from optical high-resolution images, if available, or computed from a 2D Sérsic profile adjusted to the legacy r-band image as explained in Sect. 3.2.2. In the top panel of Fig. 10, we show the unresolved KS relation. We use the same SFR estimates as used for the MS offset estimate in Sect. 2.3. We plot straight lines of constant depletion times $t_{depl} = M_{H_2}/SFR$ of 0.1, 1, and 10 Gyr. We also mark the MS depletion time of 1.24 Gyr, computed by Tacconi et al. (2018), for the mean redshift ($z = 0.10$) and stellar mass ($\log(M_*/M_\odot) = 11.0$) of the DP sample. We display the mean uncertainties with error bars that include an average surface estimation uncertainty of 0.2 dex (van der Wel et al. 2012).

The DP sample has a mean depletion time of 1.1 ± 0.8 Gyr; for the SP-EGNOG sample, it is 0.7 ± 0.4 Gyr. These are close to the depletion times expected for galaxies situated on the MS. These two samples fill a slight under-density of measurements between the region dominated by nearby galaxies of the COLD GASS sample and the region of the M sample at higher redshifts. The majority of the galaxies of the low-SF sample and the COLD GASS sample follows the same relation as the M sample, but with some galaxies shifted towards lower star-formation efficiencies (with t_{depl} about 10 Gyr).

We marked galaxies classified as AGNs in Sect. 3.3.1 with stars, and, in fact, the majority of galaxies with very high depletion times are classified as AGNs, which is consistent with a scenario where the AGN is quenching ongoing SF (e.g. Shimizu et al. 2015). Nevertheless, some galaxies with large depletion times do not host any detected AGN activity. This might be due to the exhaustion of their gas reservoir or to a hidden AGN. In contrast, all ULIRGs have significantly smaller depletion times of ∼ 0.01 Gyr and show the largest range of Σ_{H_2} measurements. Furthermore, as we discussed in Sect. 2.2, their SFR might be overestimated due to AGN contribution, since it was computed using L_{FIR}, shifting the galaxies towards regions of smaller depletion times.

In the *bottom* panel of Fig. 10, we show the KS relation for the ten DP galaxies with a successful combined fit (see Sect. 3.1). Since we find similar gas distributions between the ionised and the molecular gas, we may assume that the majority of the detected molecular gas (see Sect. 3.1) is situated in the central part of the galaxy, fuelling central SF, as discussed in Sect. 3.4. We show on the y-axis $\Sigma_{SFR\,H\alpha}$, the SFR surface density estimated using the extinction-corrected Hα luminosity of each peak component (see Sect. 3.4). As discussed in Sect. 3.4, this SFR estimate is systematically underestimated by about 1 dex for the DP sample. On the x-axis, we show the individual H_2 mass surface densities $\Sigma_{H_2\,fibre}$, without applying any aperture correction. Both surface densities are calculated for the SDSS 3″ fibre. We also display the mean uncertainties as in the *top* panel. However, no uncertainties for the surface measurements are included, which leads to significantly smaller error bars. We show the redshifted (resp. blueshifted) peak with a red (resp. blue) square and connect them with a dashed line. The three galaxies, which are classified as mergers, are marked with black plus signs. Interestingly, we find these galaxies to be shifted towards higher molecular-gas surface densities than the non-mergers. As discussed in Sect. 3.4, the $SFR_{H\alpha}$ estimates are most likely underestimated, causing a

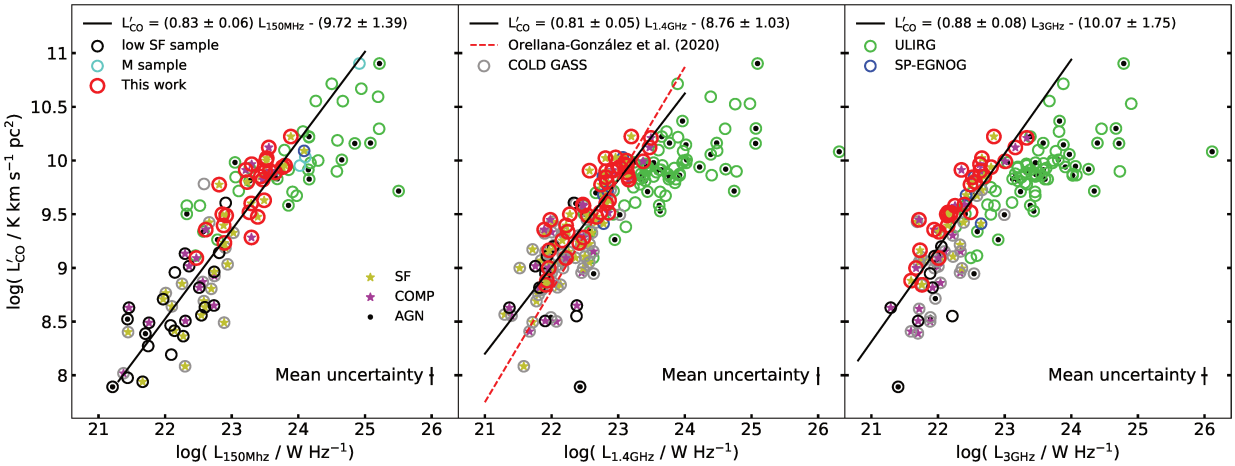

Fig. 9. Correlation between L'_{CO} and radio luminosity at 150 MHz (left panel), 1.4 GHz (middle panel) and 3 GHz (right panel). We show k-corrected radio luminosity following Equation. 1. Circles show the DP (red), EGNOG (blue), ULIRG (green), low-SF (black), COLD GASS (grey), and M samples (turquoise). We mark galaxies that are classified as AGN with a black dot in the centre and use a yellow (resp. purple) star to highlight galaxies classified as SF (resp. COMP). In the middle panel, we show the best fit for nearby galaxies found by Orellana-González et al. (2020) with a red dashed line. We fit a straight line in all three relations to all galaxies classified as SF or COMP and display the best fit with a solid black line. In each panel, we show the average uncertainties in the lower right corner with error bars.

shift towards larger t_{depl} as observed in the *top panel* of Fig. 10. Since the $SFR_{H\alpha}$ is systematically underestimated, we are only able to effectively compare the relative difference in t_{depl} of the two components.

If an evenly distributed rotating gaseous disc were at the origin of a DP structure, we would expect to observe similar SF efficiencies in each component, comparable t_{depl} values, and both components being aligned with the lines of constant t_{depl} in the KS relation. Alternatively, if the DP structure is derived from two different gas populations, two different SF efficiencies would be expected, with two different values of $t_{depl,}$ and thus the two components would not be aligned with the lines of constant t_{depl}. We note that due to the logarithmic scale in Fig. 10, t_{depl} also scales in a logarithmic manner perpendicularly to the lines of constant t_{depl}. Hence, the difference in t_{depl} between the two components is expected the largest for the galaxies near the line of t_{depl} = 10 Gyr and classified as mergers. These galaxies show a difference in t_{depl} between 0.2 and 0.5 Gyr. In parallel, a difference in t_{depl} of up to 0.3 Gyr is estimated for the non-merger galaxies.

These trends suggest that the DP signature can probe two different star-formation sites in the merger galaxies, as well as a central disc of homogeneous SF in the LTG and S0 galaxies. However, taking the uncertainties into account, it is difficult to come to solid conclusions regarding these two scenarios. To correctly classify multiple components in a galaxy, observations with optical integral field spectroscopy and spatially resolved measurements of the molecular gas are needed. Such high-resolution observations might also reveal perturbed merger remnants or contracted gaseous discs in the remaining DP galaxies, for which we fail to perform a combined fit.

4.4. Molecular-gas-mass fraction and depletion time

The evolutionary state of a galaxy is strongly dependent on its SFR relying on the molecular-gas reservoir. We thus characterise the CO samples using the molecular-gas-to-stellar-mass ratio ($\mu_{gas} = M_{H_2}/M_\odot$) and the depletion time ($t_{depl} = M_{H_2}/SFR$). In Fig. 11, we show μ_{gas} and t_{depl} as a function of log(1 + z) for a redshift range of $0 < z < 3$. We present the DP sample, the M sample, the COLD GASS sample, the low-SF sample, the SP-EGNOG sample, the ULIRG sample, and the estimated limits for the MEGAFLOW sample and their estimate obtained through stacking. To discuss the different measurements, we make use of the best-fitting unified scaling relations for μ_{gas} and t_{depl} found by Tacconi et al. (2018):

$$\log(\mu_{gas}) = 0.12 - 3.62\,(\log(1+z) - 0.66)^2 + 0.53\log(\delta MS) - 0.35\log(\delta M_*) + 0.11\log(\delta R) \quad (12)$$

and

$$\log(t_{depl}) = 0.09 - 0.62\log(1+z) - 0.44\log(\delta MS) - 0.09\log(\delta M_*) + 0.11\log(\delta R), \quad (13)$$

where $\delta MS = SFR/SFR_{MS}$ is the distance to the MS, $\delta M_* = M_*/5 \times 10^{10} M_\odot$ is the correction to the fiducial stellar mass of $5 \times 10^{10} M_\odot$, and $\delta R = R_e/R_{0,e}$ is the correction of the effective radius R_e to the average radius of star-forming galaxies of $R_{0,e} = 8.9\text{kpc}(1+z)^{-0.75}(M_*/5\times10^{10}M_\odot)^{0.23}$. In Fig. 11, we show the expected evolution of μ_{gas} and t_{depl} for MS galaxies as a function of redshift and of the mean stellar mass of the DP sample ($M_* = 10^{11} M_\odot$) and the mean size of R_e = 8.3kpc. These relations allow one to visualise how the molecular-gas fraction decreases steeply, since $z \sim 3$; whereas, in parallel, the depletion time slightly increases, showing that ongoing SF depends on the available molecular gas. We find that the M sample is still well described by the empirical line and thus presents the scatter of 0.4 dex for the expected scaling relation. We chose this scaling relation since the majority of the literature samples discussed here (COLD GASS, SP-EGNOG, and parts of the ULIRG and the M samples) were used to obtain this relation that is valid over large parts of cosmic time.

Galaxies of the low-SF sample have a large scatter in μ_{gas} and in depletion time. Some of these galaxies are quenched due to exhausted gas reservoirs or stopped their SF due to AGN activity.

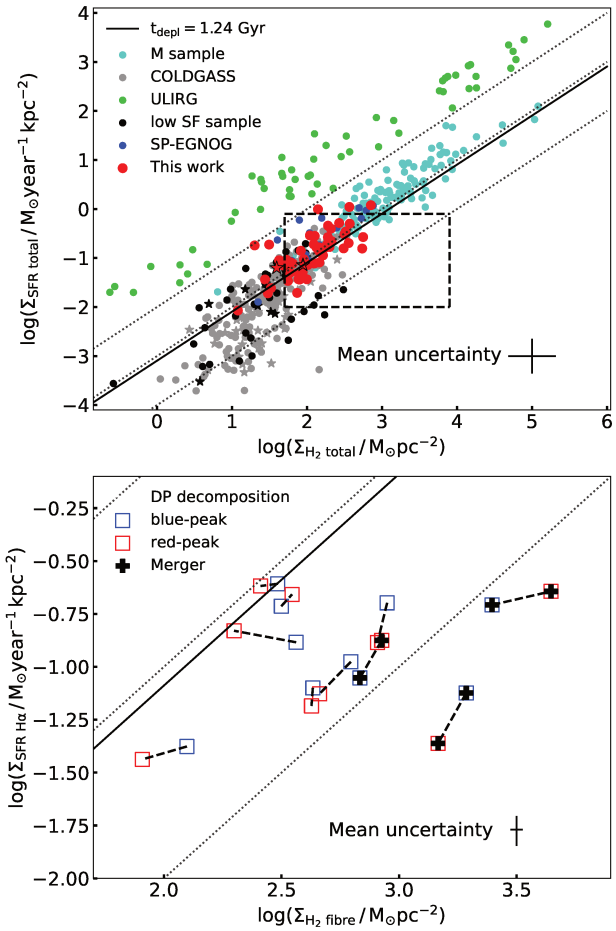

Fig. 10. Kennicutt-Schmidt (KS) relation for CO samples. In the *top* panel, we show the KS relation using the total molecular-gas mass and the SFR of the all of the galaxies, and we normalise both quantities using the half-light radii. The DP sample is indicated with red dots, the EGNOG sample with blue dots, the COLD GASS sample with grey dots, the low-SF sample with black dots, the M sample with turquoise dots, and the ULIRG sample with green dots. Galaxies of the low-SF and COLD GASS samples showing AGN activity are marked with stars (see Sect. 3.3.1). In the *bottom* panel, we show the decomposition of the ten DP galaxies for which we succeeded in performing a combined fit (see Sect. 3.1). We show the decomposition in a zoomed-in image of the *top* panel, which we mark with a dashed box. We display blue (resp. red) squares for the blueshifted (resp. redshifted) component and connect the two components with a black dashed line. We use the SFR estimated by Hα emission of each component and the observed H_2 mass of each component and normalise them to the surface of the 3″ SDSS fibre. The three galaxies, classified as mergers, are marked with black plus signs. In both panels, dotted lines denote the constant t_{depl} of 0.1, 1, and 10 Gyr. The solid black line corresponds to a constant t_{depl} of 1.24 Gyr estimated using Tacconi et al. (2018) for the mean redshift and stellar mass of the DP sample. In both panels, error bars indicate the mean estimated uncertainties. However, in the *lower* panel, uncertainties estimated from the surface measurement are not included.

This allows us to probe a wide range of gas fractions and depletion times. Similar behaviour is also observed for the COLD GASS sample. We find that galaxies with long depletion times of these two samples are dominated by AGNs. In contrast, the ULIRG sample shows a large scatter of gas fractions of 1 to 2 dex and very short depletion times of around 0.01 Gyr, which might also be an effect of the overestimation of the SFRs of this sample. As discussed in Sect. 2.3, their stellar mass can be overestimated due to the presence of strong AGNs. While their possibly underestimated mass fraction of gas μ_{gas} follows the scaling relation, their depletion time, 2 dex below the scaling relation, is probably underestimated.

The DP and SP-EGNOG samples are shifted above the expected gas fraction, indicating an unusually large gas reservoir, but their depletion time is in the expected range at low redshift. We find two of the DP galaxies (DP-17 and DP-24) to be shifted 2 dex over the expected gas fraction. DP-24 is a ULIRG merger selected from Chung et al. (2009) and DP-17 is a major merger galaxy selected from the COLD GASS sample. We thus assume that the high μ_{gas} values are due to an overestimated CO-to-molecular-gas-mass conversion factor (see Sect. 3.2). We also identify three DP galaxies (DP-10, 30, and 44) and one galaxy of the SP-EGNOG (A06) with unexpected small t_{depl} values of $\sim$ 0.1Gyr. We find all of these galaxies to show a large SFR, between 35 and 106 $M_\odot yr^{-1}$.

In Fig. 12, we show μ_{gas} divided by the expected value provided by Equation 12 as a function of their relative distance to the MS (δMS) (left panel) and their stellar mass (right panel). We computed the expected SFR value of the MS (SFR_{MS}) following Speagle et al. (2014). In order to compare these values to the expected scaling relations established by Tacconi et al. (2018), we show black lines indicating the relative deviation of μ_{gas} from the expected value of the MS μ_{gas}(MS). Therefore, we compute μ_{gas}, according to Equation 12, with the fiducial values, despite different δMS (resp. M_*) values for the left (resp. right) panel, while the redshift term is cancelled out. We then divide these values by μ_{gas}(MS), calculated for the same arbitrary redshift, δMS = 1 and the fiducial values. The resulting function for the left panel is $\mu_{gas}/\mu_{gas}(MS) = 0.53 \log(\delta MS)$ and $\mu_{gas}/\mu_{gas}(MS) = -0.35 \log(\delta M_*)$ for the right panel. Dashed lines show the scatter found for the M sample.

We present the same samples as for Fig. 11, but for the MEGAFLOW sample we show the stacked estimates for galaxies with identified outflows and inflows separately. As discussed in Freundlich et al. (2021), gas fraction and depletion times are perfectly compatible with the established values of the MS with a mass-selected sample (Tacconi et al. 2018). This indicates that galaxies with identified accretion may not have a specifically high gas content, which is at odds with the theoretical expectations of the quasi-equilibrium and compaction models where the accretion of gas is seen as a gas replenishment. Galaxies from the M sample are scattered around the expected values on the MS; the same is true for the majority of the COLD GASS galaxies. Some galaxies of the COLD GASS and the low-SF samples are shifted below the MS but with significantly large amounts of molecular gas and large t_{depl} values. As discussed in Sect. 4.3, these outliers are mostly dominated by an AGN. The ULIRG sample exhibits a fraction of molecular gas μ_{gas}, which is expected for their distance to the MS according to Tacconi et al. (2018).

Galaxies from the SP-EGNOG sample are slightly shifted above the expected MS μ_{gas} values (except A06) but is still compatible with the scatter of the MS. For the DP sample galaxies, due to their selection criteria, they belong to the upper MS. Most of them exhibit a larger molecular-gas reservoir than the MS scaling relation found by Tacconi et al. (2018). As explained above, two galaxies (DP-17 and DP-24) are shifted more than 1 dex above the expected value. In contrast to that, we find three galaxies with smaller gas-mass fractions than expected. Interestingly, these galaxies (DP-10, 30, and 44) are the exact same

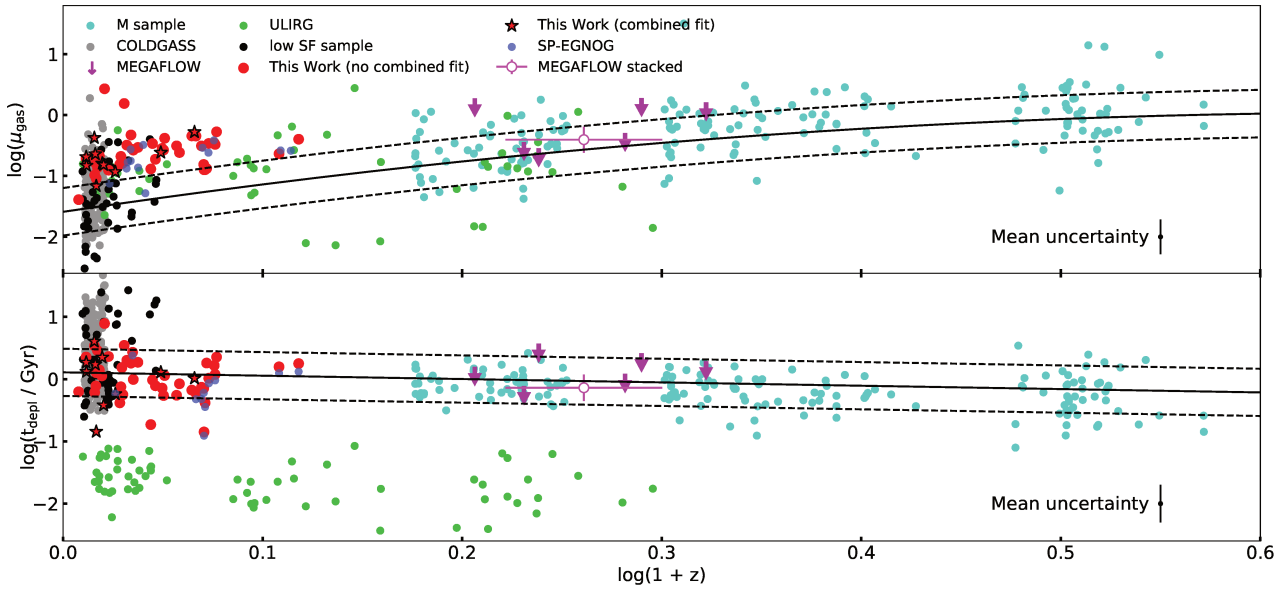

Fig. 11. Gas fraction $\mu_{gas} = M_{H2}/M_*$ (top panel) and depletion time $t_{depl} = M_{H2}/SFR$ (bottom panel) as a function of log(1 + z). We show the observed DP galaxies (red), the EGNOG sample (blue), the COLD GASS sample (grey), the low-SF sample (black), the ULIRG sample (green), the M sample (turquoise), and the detection limits of the MEGAFLOW galaxies (magenta). With an empty circle, we show the estimate based on stacking from Freundlich et al. (2021). The solid black lines represent the scaling relations expected for MS galaxies found by Tacconi et al. (2018), scaled to the mean stellar mass and size of the DP sample ($\log(M_*/M_\odot) = 11.0$ and $R_e = 8.3$kpc). The dashed line marks the scatter of 0.4 dex found for the M sample.

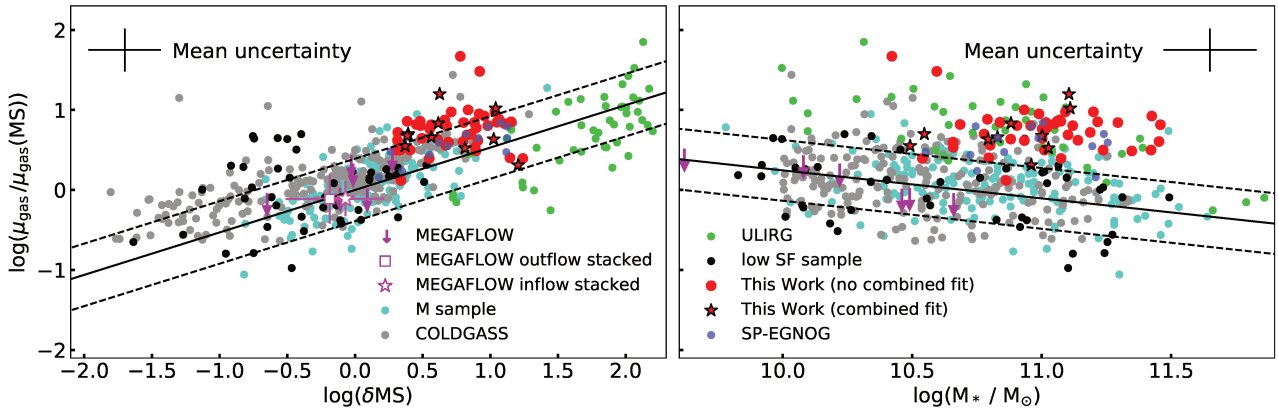

Fig. 12. Gas fractions divided by their average values on the MS $\mu_{gas}/\mu_{gas}(MS)$ as a function of their relative distance to the MS $\delta MS = SFR/SFR_{MS}$ (left panel) and stellar mass M_* (right panel). We use the predicted $\mu_{gas}(MS)$ according to Tacconi et al. (2018) and the parametrisation of SFR_{MS} following Speagle et al. (2014). We show the observed DP galaxies (red), the SP-EGNOG sample (blue), the COLD GASS sample (grey), the low-SF sample (black), the ULIRG sample (green), and the M sample (turquoise). For the MEGAFLOW sample, we show the detection limits of each galaxy (magenta) and, with an empty square (resp. star), the estimate reached by stacking for galaxies identified with an outflow (resp. inflow) (Freundlich et al. 2021). The solid black lines represent the scaling relations found by Tacconi et al. (2018) and the dashed line marks the scatter of 0.4 dex found for the M sample.

galaxies that are shifted to significantly shorter t_{depl} values (see Fig. 11) with strong SFR. This might be an indicator of a late-stage starburst and an almost depleted gas reservoir. For the majority of the DP sample, we see that the expected μ_{gas} values are even higher relatively to their shift above the MS. This means, in parallel, that we observe larger t_{depl} values than we would expect for their distance to the MS. Thus, the gas is not consumed as efficiently as expected, which could be due to recent gas accretion, corresponding to an early-stage starburst. Alternatively, the large bulges characterising the DP galaxies might stabilise the gas and reduce the star-formation efficiency.

In the right panel of Fig. 12, we observe the COLD GASS, low-SF, and M samples to be scattered around the expected values for the MS. However, we observe a strong deviation from the scaling relations for the SP-EGNOG, ULIRG, and DP samples. These samples show larger gas-mass fractions than expected for galaxies of their mass on the MS. The shift above the MS observed for these galaxies might be related to galaxy interactions and mergers that increased their molecular-gas reservoir significantly and fuelled their SF.

5. Discussion

The results are discussed here to account for the properties of the DP sample. Sect. 5.1 is devoted to galaxies that are mainly star-formation dominated with a remarkable radio-continuum-CO correlation. Sect. 5.2 discusses the effect of bars. Sect. 5.3 suggests that DP galaxies are akin to the compaction phase observed after mergers in high-z galaxies.

5.1. Star-formation dominated galaxies

The evolutionary state of galaxies is mostly determined by their growth rate and star-formation efficiency. The relation between SFR and molecular-gas densities is important, since it quantifies the efficiency of the process (see Bigiel et al. (2008) and references therein). In a recent study, Chown et al. (2021) showed that L_{CO} and IR emission at 12 μm describe an even more robust correlation than L_{CO} and SFR. This provides a better estimator to predict the molecular-gas mass for different kinds of galaxies. This is neither significantly affected by the presence of an obscured AGN nor does it rely on a correct choice of the CO-to-H_2 conversion factor.

Ongoing SF is also measurable in the IR regime where dust grains are heated from the ultraviolet light emitted by young stars. As discussed in Sect. 4.2, electrons are accelerated in supernova remnants of massive young stars, emitting synchrotron radiation. The underlying process of these two emissions is SF and the radio-continuum–infrared (RC–IR) correlation has been studied extensively for star-forming galaxies (e.g. Bell 2003; Ibar et al. 2008; Ivison et al. 2010; Smith et al. 2014; Liu et al. 2015). Although the RC–IR correlation has long been known as one of the tightest in galaxy physics, Molnár et al. (2021) emphasised the poor match of IR and radio samples that could bias the calibration. They find a slightly non-linear correlation of slope 1.11 ± 0.01.

In order to extend the RC–IR correlation, Orellana-González et al. (2020) found a 3D connection L_{CO}, $L_{1.4\,GHz}$ and the infrared luminosity L_{IR} for galaxies with a redshift smaller than $z < 0.27$. They excluded quasar-like objects to focus on star-formation activity. To further explore this relation, we tested the correlation between L_{CO} and the radio continuum luminosity at 150 MHz, 1.4 GHz, and 3 GHz. We also find a linear relation for galaxies classified as SF or COMP with the BPT diagram (see Sect. 3.3.1) for all three radio-continuum measurements. We performed a linear fit and find a slightly flatter relation between L_{CO} and $L_{1.4\,GHz}$ than Orellana-González et al. (2020). Furthermore, we find nearly the same slope for the L_{CO}-$L_{150\,MHz}$ relation (0.80 ± 0.06), the L_{CO}-$L_{1.4\,GHz}$ relation (0.79 ± 0.04), and the L_{CO}-$L_{3\,GHz}$ relation (0.87 ± 0.07).

We also find that these linear relations are not valid for the majority of ULIRGs, which are mostly active galaxies such as quasars or AGNs. Galaxies with high-IR luminosities were observed to be nearly all advanced mergers with circumnuclear-starburst and AGN activity (Sanders & Mirabel 1996). Such galaxies might characterise an important stage of quasar formation and powerful radio galaxies, which is compatible with the large offset that the ULIRG sample shows between CO and radio continuum luminosities. To which relative fractions the ongoing starburst and the AGN are contributing to the IR and radio-continuum luminosities is still under debate (e.g. Dietrich et al. 2018).

Hence, the slope for SF and COMP galaxies measured constant over a wide range of radio wavelengths might be an indicator that the underlying process is dominated by SF. This is also in agreement with DP galaxies having comparable depletion times of around 1 Gyr (see Sect. 4.3). In particular, the good agreement between results at 1.4 GHz, 3 GHz, and 150 MHz suggests that the latter observable is a robust tracer for SF (Calistro Rivera et al. 2017; Wang et al. 2019). Hence, the presented DP sample is dominated by SF with no significant AGN contribution, as confirmed by the BPT classification discussed in Sect. 3.3.1. Indeed, only two galaxies (DP-1 and DP-22), respectively a merger and a S0 galaxy, exhibit AGN excitation on the BPT diagram, but they have a high SFR and high molecular-gas content.

5.2. Gas infall due to bars

Bars are well known to effectively transport gas inwards and create a central starburst. The torques they exert may lead to the creation of star-forming rings in the central parts of galaxies or to the accumulation of gas in the very centre (see Buta & Combes (1996) for a review). Sakamoto et al. (1999) showed, using a sample of nearby galaxies, that the central molecular-gas concentration is higher in barred systems than in unbarred galaxies. This leads to a central star-formation enhancement, which they estimated to be larger than $0.1 - 1\,M_{\odot}yr^{-1}$. By comparing barred, unbarred, and interacting systems, Chown et al. (2019) found that cold gas is transported inwards by a bar or tidal interaction, which leads to the growth and rejuvenation of SF in the central region. Ellison et al. (2011a) found that bars are responsible for 3.5 times more triggered central SF than galaxy-galaxy interactions.

However, in our sample, we only find DP-13 and DP-14 to show a dominant bar. As discussed in Sect. 3.3.2, the present sample is characterised by bulge-dominated systems and mergers. This suggests that the central star-formation enhancement and the higher gas concentration we observe are most likely related to galaxy interactions and mergers, as we discuss in the next section.

5.3. Central star formation and compaction phase

As mentioned in Sect. 1, galaxy interactions and galaxy mergers can trigger SF (Bothun & Dressler 1986; Pimbblet et al. 2002). Relying on larger galaxy samples with 10^5 SDSS DR4 galaxy pairs, Li et al. (2008) found a clear star-formation enhancement triggered by galaxy interactions. Based on a systematic search for galaxy pairs in the SDSS DR7, Patton et al. (2011) found evidence for a central starburst induced by galaxy interactions. As discussed in Dekel et al. (2009), the merger mechanism forms steady streams enhancing the growth of the central spheroid, leading to earlier Hubble types. This is a different evolution from one of violent mergers that strongly modify the morphology, and it is in agreement with the hierarchical bulge growth described in Bournaud et al. (2007).

We find that 19 % of the DP sample galaxies show the same kinematic signature in the molecular and ionised gases, indicating that in these galaxies, most of the molecular gas is located in the very central region of radius 3″. We furthermore observe a central star-formation enhancement for the majority of the DP sample and detect a significant gas reservoir. These findings confirm a compact central star-formation site supporting an effective molecular-gas transportation into the galaxy centre. This scenario is reminiscent of the gas-compaction phase suggested for $z = 2 - 4$ galaxies by observations (e.g. Barro et al. 2013, 2017) and simulations (Zolotov et al. 2015; Tacchella et al. 2016a,b) according to which galaxies experience a central enhancement

of SF due to gas contraction at their centres, before inside-out depletion and quenching. This model was further described over large scales of cosmic time by Tacchella et al. (2016b), with repetitive compaction and depletion phases shifting galaxies up and down the MS before finally quenching. Since our galaxies are 0.3 dex above the MS, the central SF enhancement and the similar kinematic distribution in the ionised and molecular gas might be a sign of an ongoing compaction phase. In such a scenario, a recent minor merger, a galaxy interaction or a disc instability funnelled gas into the central parts, initiating SF.

In Sect. 4.4, we find that the DP and SP-EGNOG samples have significantly larger molecular-gas fractions (0.8 dex on average) than main-sequence galaxies of the same mass and redshift ranges studied by Tacconi et al. (2018). This discrepancy can be accounted for by a conversion factor of $\alpha_{\rm CO} = 0.80\,{\rm M}_\odot/({\rm K\,km\,s^{-1}\,pc^2})$ adopted for ULIRGs by Solomon et al. (1997). We also observe a central star-formation enhancement for the SP-EGNOG sample, which is indeed very similar to the DP sample in terms of stellar mass and redshift. In Fig. 12, we observe both samples to be situated between the population of the M sample and the extreme case of the ULIRG sample. Both samples are found to be situated at the upper MS and above (see Sect. 2.3), but they also show an increased molecular-gas-mass fraction with only a slight decrease in depletion time. The galaxies of the MEGAFLOW sample, which are galaxies showing inflows and outflows in the circumgalactic medium, are maintaining their SF as described in the quasi-equilibrium model (Freundlich et al. 2021). These galaxies have SFEs compatible with star-formation efficiencies measured for the MS. The offset of the DP sample, observed in Fig. 12, suggests that large amounts of gas were recently accreted, possibly through a merger event, and were effectively funnelled into the central regions, where we observe the majority of the ongoing SF.

6. Conclusions

We present new observations of the molecular-gas content for 35 DP emission-line galaxies with ongoing SF situated more than 0.3 dex above the MS. We considered, in addition, 17 DP galaxies from existing CO samples matching the same criterion, leading to a sample of 52 galaxies. We tried to fit the same double-Gaussian parameters to the central optical emission lines and to the CO lines integrated over the entire galaxy. We succeeded in finding similar kinematic signatures for these two measurements in ten (19 %) DP galaxies. By comparing the SFR inside the SDSS fibre and in the total galaxy, we find a significant central enhancement of SF for this DP sample. We discuss the possibility of a rotating gaseous disc creating a DP signature. By comparing the emission-line width of the CO gas and the galaxy inclination, we do not find any correlation; however, considering the scatter expected due to galaxy mass concentration or molecular-gas velocity dispersion, the lack of correlation does not allow us to exclude this origin for the observed DP. A deep gravitational potential can in fact be the origin of the DP. This might be the result of a recent minor merger event or galaxy-galaxy interaction that funnelled gas into the central regions. The DP signature might also be the result of cold gas accretion from cosmic filaments, which recently fell into the galaxy centre. These scenarios account for the observed increase of molecular gas and its funnelling into the central region where the majority of the stars are formed. This is also in agreement with the observed excess of dust extinction in the centre.

Such a recently ignited SF is traced by radio-continuum emission at 150 MHz, 1.4 GHz, and 3 GHz all three of which are linearly correlated in log with $L'_{\rm CO}$ with the same slope. This is a signature of synchrotron emission, mostly dominated by SF. Within this interpretation, the possible merger-induced central SF is happening without a simultaneous increase in AGN activity.

Arguments are discussed concerning whether the observed central SF and the large molecular-gas reservoir are the results of a recent merger. Bar structures in galaxies can also effectively migrate gas inwards, which cannot be the case for the presented galaxy samples as it lacks these morphological types. However, we cannot exclude the possibility that we observe gas-rich spiral galaxies with a central molecular disc formed due to large-scale instabilities. In such a scenario, we would observe a central rotating disc that might not be aligned with the host galaxy's orientation. To further probe our findings and to distinguish between rotating-disc and merger-induced central SF, high resolution observations of the molecular and ionised gas would be necessary. A kinematic decomposition of spatially extended gas would enable us to further characterise the dynamics of these systems and draw conclusions on the origin of double-peak emission-line galaxies. In addition, we could also explore spatially resolved SF and compare its efficiency with findings for regular spiral galaxies (Bigiel et al. 2008; Leroy et al. 2008) in order to conclude on the underlying process of SF and galaxy growth.

Acknowledgements. We thank the anonymous referee who helped us to improve our emission line fitting procedure which finally strengthened the arguments in our analysis and discussion. We thank Susanne Maschmann for helpful advise on the English language. This work is based on observations carried out under the two project numbers 198-19 and 166-20 with the IRAM 30m telescope at Pico Veleta in Spain. IRAM is supported by INSU/CNRS (France), MPG (Germany) and IGN (Spain). This paper makes use of the following ALMA data: ADS/JAO.ALMA#2015:1:00113:S.ALMA is a partnership of ESO (representing its member states), NSF (USA) and NINS (Japan), together with NRC (Canada), MOST and ASIAA (Taiwan), and KASI (Republic of Korea), in cooperation with the Republic of Chile. The Joint ALMA Observatory is operated by ESO, AUI/NRAO and NAOJ. Funding for the Sloan Digital Sky Survey IV has been provided by the Alfred P. Sloan Foundation, the U.S. Department of Energy Office of Science, and the Participating Institutions. SDSS-IV acknowledges support and resources from the Center for High-Performance Computing at the University of Utah. The SDSS web site is www.sdss.org. SDSS-IV is managed by the Astrophysical Research Consortium for the Participating Institutions of the SDSS Collaboration including the Brazilian Participation Group, the Carnegie Institution for Science, Carnegie Mellon University, the Chilean Participation Group, the French Participation Group, Harvard-Smithsonian Center for Astrophysics, Instituto de Astrofísica de Canarias, The Johns Hopkins University, Kavli Institute for the Physics and Mathematics of the Universe (IPMU) / University of Tokyo, the Korean Participation Group, Lawrence Berkeley National Laboratory, Leibniz Institut für Astrophysik Potsdam (AIP), Max-Planck-Institut für Astronomie (MPIA Heidelberg), Max-Planck-Institut für Astrophysik (MPA Garching), Max-Planck-Institut für Extraterrestrische Physik (MPE), National Astronomical Observatories of China, New Mexico State University, New York University, University of Notre Dame, Observatário Nacional / MCTI, The Ohio State University, Pennsylvania State University, Shanghai Astronomical Observatory, United Kingdom Participation Group, Universidad Nacional Autónoma de México, University of Arizona, University of Colorado Boulder, University of Oxford, University of Portsmouth, University of Utah, University of Virginia, University of Washington, University of Wisconsin, Vanderbilt University, and Yale University. The Legacy Surveys (http://legacysurvey.org/) consist of three individual and complementary projects: the Dark Energy Camera Legacy Survey (DECaLS; NOAO Proposal ID # 2014B-0404; PIs: David Schlegel and Arjun Dey), the Beijing-Arizona Sky Survey (BASS; NOAO Proposal ID # 2015A-0801; PIs: Zhou Xu and Xiaohui Fan), and the Mayall z-band Legacy Survey (MzLS; NOAO Proposal ID # 2016A-0453; PI: Arjun Dey). DECaLS, BASS and MzLS together include data obtained, respectively, at the Blanco telescope, Cerro Tololo Inter-American Observatory, National Optical Astronomy Observatory (NOAO); the Bok telescope, Steward Observatory, University of Arizona; and the Mayall telescope, Kitt Peak National Observatory, NOAO. The Legacy Surveys project is honoured to be permitted to conduct astronomical research on Iolkam Du'ag (Kitt Peak), a mountain with particular significance to the Tohono O'odham Nation.
LOFAR is the Low Frequency Array designed and constructed by ASTRON. It has observing, data processing, and data storage facilities in several coun-

tries, which are owned by various parties (each with their own funding sources), and which are collectively operated by the International LOFAR Telescope (ILT) foundation under a joint scientific policy. The ILT resources have benefited from the following recent major funding sources: CNRS-INSU, Observatoire de Paris and Université d'Orléans, France; BMBF, MIWF-NRW, MPG, Germany; Science Foundation Ireland (SFI), Department of Business, Enterprise and Innovation (DBEI), Ireland; NWO, The Netherlands; The Science and Technology Facilities Council, UK; Ministry of Science and Higher Education, Poland; The Istituto Nazionale di Astrofisica (INAF), Italy. This research made use of the Dutch national e-infrastructure with support of the SURF Cooperative (e-infra 180169) and the LOFAR e-infra group. The Jülich LOFAR Long Term Archive and the German LOFAR network are both coordinated and operated by the Jülich Supercomputing Centre (JSC), and computing resources on the supercomputer JUWELS at JSC were provided by the Gauss Centre for Supercomputing e.V. (grant CHTB00) through the John von Neumann Institute for Computing (NIC). This research made use of the University of Hertfordshire high-performance computing facility and the LOFAR-UK computing facility located at the University of Hertfordshire and supported by STFC [ST/P000096/1], and of the Italian LOFAR IT computing infrastructure supported and operated by INAF, and by the Physics Department of Turin university (under an agreement with Consorzio Interuniversitario per la Fisica Spaziale) at the C3S Supercomputing Centre, Italy.

References

Abdo, A. A., Ackermann, M., Ajello, M., et al. 2010, ApJ, 710, 133
Aquino-Ortíz, E., Valenzuela, O., Sánchez, S. F., et al. 2018, MNRAS, 479, 2133
Baldwin, J. A., Phillips, M. M., & Terlevich, R. 1981, PASP, 93, 5
Balogh, M. L., Schade, D., Morris, S. L., et al. 1998, ApJ, 504, L75
Barro, G., Faber, S. M., Koo, D. C., et al. 2017, ApJ, 840, 47
Barro, G., Faber, S. M., Pérez-González, P. G., et al. 2013, ApJ, 765, 104
Barrows, R. S., Comerford, J. M., Zakamska, N. L., & Cooper, M. C. 2017, ApJ, 850, 27
Bauermeister, A., Blitz, L., Bolatto, A., et al. 2013, ApJ, 768, 132
Begelman, M. C., Blandford, R. D., & Rees, M. J. 1980, Nature, 287, 307
Bell, E. F. 2003, ApJ, 586, 794
Bigiel, F., Leroy, A., Walter, F., et al. 2008, AJ, 136, 2846
Bolatto, A. D., Wolfire, M., & Leroy, A. K. 2013, ARA&A, 51, 207
Bothun, G. D. & Dressler, A. 1986, ApJ, 301, 57
Bouché, N., Dekel, A., Genzel, R., et al. 2010, ApJ, 718, 1001
Bournaud, F., Jog, C. J., & Combes, F. 2007, A&A, 476, 1179
Braine, J. & Combes, F. 1993, A&A, 269, 7
Brinchmann, J., Charlot, S., White, S. D. M., et al. 2004, MNRAS, 351, 1151
Buta, R. & Combes, F. 1996, Fund. Cosmic Phys., 17, 95
Calistro Rivera, G., Williams, W. L., Hardcastle, M. J., et al. 2017, MNRAS, 469, 3468
Calzetti, D. 2001, PASP, 113, 1449
Calzetti, D., Armus, L., Bohlin, R. C., et al. 2000, ApJ, 533, 682
Caputi, K. I., Dole, H., Lagache, G., et al. 2006, ApJ, 637, 727
Catinella, B., Kauffmann, G., Schiminovich, D., et al. 2012, MNRAS, 420, 1959
Cattaneo, A., Faber, S. M., Binney, J., et al. 2009, Nature, 460, 213
Chilingarian, I. V., Zolotukhin, I. Y., Katkov, I. Y., et al. 2017, ApJS, 228, 14
Chown, R., Li, C., Athanassoula, E., et al. 2019, MNRAS, 484, 5192
Chown, R., Li, C., Parker, L., et al. 2021, MNRAS, 500, 1261
Chung, A., Narayanan, G., Yun, M. S., Heyer, M., & Erickson, N. R. 2009, AJ, 138, 858
Ciesla, L., Charmandaris, V., Georgakakis, A., et al. 2015, A&A, 576, A10
Combes, F., García-Burillo, S., Braine, J., et al. 2011, A&A, 528, A124
Combes, F., García-Burillo, S., Braine, J., et al. 2013, A&A, 550, A41
Combes, F., Prugniel, P., Rampazzo, R., & Sulentic, J. W. 1994, A&A, 281, 725
Comerford, J. M., Gerke, B. F., Newman, J. A., et al. 2009, ApJ, 698, 956
Comerford, J. M., Nevin, R., Stemo, A., et al. 2018, ApJ, 867, 66
Comerford, J. M., Schluns, K., Greene, J. E., & Cool, R. J. 2013, ApJ, 777, 64
Concas, A., Popesso, P., Brusa, M., et al. 2017, A&A, 606, A36
Condon, J. J. 1992, ARA&A, 30, 575
Condon, J. J., Cotton, W. D., Greisen, E. W., et al. 1998, AJ, 115, 1693
Condon, J. J., Matthews, A. M., & Broderick, J. J. 2019, ApJ, 872, 148
Croton, D. J., Springel, V., White, S. D. M., et al. 2006, MNRAS, 365, 11
Daddi, E., Alexander, D. M., Dickinson, M., et al. 2007, ApJ, 670, 173
Daddi, E., Bournaud, F., Walter, F., et al. 2010, ApJ, 713, 686
Daddi, E., Renzini, A., Pirzkal, N., et al. 2005, ApJ, 626, 680
Davé, R., Finlator, K., & Oppenheimer, B. D. 2012, MNRAS, 421, 98
Davé, R., Oppenheimer, B. D., & Finlator, K. 2011, MNRAS, 415, 11
Davis, T. A., Rowlands, K., Allison, J. R., et al. 2015, MNRAS, 449, 3503
Dekel, A., Birnboim, Y., Engel, G., et al. 2009, Nature, 457, 451
Dekel, A. & Burkert, A. 2014, MNRAS, 438, 1870
Dekel, A., Zolotov, A., Tweed, D., et al. 2013, MNRAS, 435, 999
Dey, A., Schlegel, D. J., Lang, D., et al. 2019, AJ, 157, 168
Di Matteo, T., Springel, V., & Hernquist, L. 2005, Nature, 433, 604
Dietrich, J., Weiner, A. S., Ashby, M. L. N., et al. 2018, MNRAS, 480, 3562
Domínguez, A., Siana, B., Henry, A. L., et al. 2013, ApJ, 763, 145
Domínguez Sánchez, H., Huertas-Company, M., Bernardi, M., Tuccillo, D., & Fischer, J. L. 2018, MNRAS, 476, 3661
Ellison, S. L., Catinella, B., & Cortese, L. 2018, MNRAS, 478, 3447
Ellison, S. L., Fertig, D., Rosenberg, J. L., et al. 2015, MNRAS, 448, 221
Ellison, S. L., Nair, P., Patton, D. R., et al. 2011a, MNRAS, 416, 2182
Ellison, S. L., Patton, D. R., Mendel, J. T., & Scudder, J. M. 2011b, MNRAS, 418, 2043
Ellison, S. L., Patton, D. R., Simard, L., & McConnachie, A. W. 2008, AJ, 135, 1877
Feldmann, R. 2013, MNRAS, 433, 1910
Förster Schreiber, N. M., Genzel, R., Lehnert, M. D., et al. 2006, ApJ, 645, 1062
French, K. D., Yang, Y., Zabludoff, A., et al. 2015, ApJ, 801, 1
Freundlich, J., Bouché, N. F., Contini, T., et al. 2021, MNRAS, 501, 1900
Freundlich, J., Combes, F., Tacconi, L. J., et al. 2019, A&A, 622, A105
Fu, H., Myers, A. D., Djorgovski, S. G., et al. 2015, ApJ, 799, 72
Ge, J.-Q., Hu, C., Wang, J.-M., Bai, J.-M., & Zhang, S. 2012, ApJS, 201, 31
Genzel, R., Burkert, A., Bouché, N., et al. 2008, ApJ, 687, 59
Genzel, R., Tacconi, L. J., Combes, F., et al. 2012, ApJ, 746, 69
Genzel, R., Tacconi, L. J., Eisenhauer, F., et al. 2006, Nature, 442, 786
Genzel, R., Tacconi, L. J., Lutz, D., et al. 2015, ApJ, 800, 20
Genzel, R., Tacconi, L. J., Rigopoulou, D., Lutz, D., & Tecza, M. 2001, ApJ, 563, 527
Goulding, A. D., Pardo, K., Greene, J. E., et al. 2019, ApJ, 879, L21
Hibbard, J. E. & van Gorkom, J. H. 1996, AJ, 111, 655
Huchtmeier, W. K., Petrosian, A., Gopal-Krishna, McLean, B., & Kunth, D. 2008, A&A, 492, 367
Ibar, E., Cirasuolo, M., Ivison, R., et al. 2008, MNRAS, 386, 953
Israel, F. & Rowan-Robinson, M. 1984, ApJ, 283, 81
Ivison, R. J., Magnelli, B., Ibar, E., et al. 2010, A&A, 518, L31
Kauffmann, G., Heckman, T. M., White, S. D. M., et al. 2003, MNRAS, 341, 33
Kennicutt, Robert C., J. 1998, ApJ, 498, 541
Kewley, L. J., Geller, M. J., Jansen, R. A., & Dopita, M. A. 2002, AJ, 124, 3135
Kewley, L. J., Groves, B., Kauffmann, G., & Heckman, T. 2006, MNRAS, 372, 961
Koss, M., Mushotzky, R., Treister, E., et al. 2012, ApJ, 746, L22
Koss, M. J., Blecha, L., Bernhard, P., et al. 2018, Nature, 563, 214
Koss, M. J., Glidden, A., Baloković, M., et al. 2016, ApJ, 824, L4
Krause, M., Alexander, P., Riley, J., & Hopton, D. 2012, MNRAS, 427, 3196
Lacy, M., Baum, S. A., Chandler, C. J., et al. 2020, PASP, 132, 035001
Leroy, A. K., Walter, F., Brinks, E., et al. 2008, AJ, 136, 2782
Li, C., Kauffmann, G., Heckman, T. M., Jing, Y. P., & White, S. D. M. 2008, MNRAS, 385, 1903
Lilly, S. J., Carollo, C. M., Pipino, A., Renzini, A., & Peng, Y. 2013, ApJ, 772, 119
Lisenfeld, U., Espada, D., Verdes-Montenegro, L., et al. 2011, A&A, 534, A102
Lisenfeld, U., Xu, C. K., Gao, Y., et al. 2019, A&A, 627, A107
Liu, L., Gao, Y., & Greve, T. R. 2015, ApJ, 805, 31
Liu, X., Civano, F., Shen, Y., et al. 2013, ApJ, 762, 110
Liu, X., Shen, Y., Strauss, M. A., & Hao, L. 2011, ApJ, 737, 101
Luo, Y., Li, Z., Kang, X., Li, Z., & Wang, P. 2020, MNRAS, 496, L116
Lutz, D., Poglitsch, A., Altieri, B., et al. 2011, A&A, 532, A90
Magdis, G. E., Daddi, E., Sargent, M., et al. 2012, ApJ, 758, L9
Magnelli, B., Saintonge, A., Lutz, D., et al. 2012, A&A, 548, A22
Maschmann, D. & Melchior, A.-L. 2019, A&A, 627, L3
Maschmann, D., Melchior, A.-L., Mamon, G. A., Chilingarian, I. V., & Katkov, I. Y. 2020, A&A, 641, A171
Mazzilli Ciraulo, B., Melchior, A.-L., Maschmann, D., et al. 2021, A&A, 653, A47
Meisenheimer, K., Roser, H. J., Hiltner, P. R., et al. 1989, A&A, 219, 63
Molnár, D. C., Sargent, M. T., Leslie, S., et al. 2021, MNRAS, 504, 118
Momcheva, I. G., Lee, J. C., Ly, C., et al. 2013, AJ, 145, 47
Murgia, M., Crapsi, A., Moscadelli, L., & Gregorini, L. 2002, A&A, 385, 412
Murphy, E. J., Condon, J. J., Schinnerer, E., et al. 2011, ApJ, 737, 67
Nishiyama, K., Nakai, N., & Kuno, N. 2001, PASJ, 53, 757
Noeske, K. G., Weiner, B. J., Faber, S. M., et al. 2007, ApJ, 660, L43
Orellana-González, G., Ibar, E., Leiton, R., et al. 2020, MNRAS, 495, 1760
Osterbrock, D. E. & Ferland, G. J. 2006, Astrophysics of gaseous nebulae and active galactic nuclei
Pancoast, A., Sajina, A., Lacy, M., Noriega-Crespo, A., & Rho, J. 2010, ApJ, 723, 530
Patton, D. R., Ellison, S. L., Simard, L., McConnachie, A. W., & Mendel, J. T. 2011, MNRAS, 412, 591
Peng, Y.-j. & Maiolino, R. 2014, MNRAS, 443, 3643
Pettini, M. & Pagel, B. E. J. 2004, MNRAS, 348, L59
Pimbblet, K. A., Smail, I., Kodama, T., et al. 2002, MNRAS, 331, 333
Regan, M. W., Thornley, M. D., Helfer, T. T., et al. 2001, ApJ, 561, 218
Rickard, L. J., Palmer, P., Morris, M., Turner, B. E., & Zuckerman, B. 1977, ApJ, 213, 673

Rodighiero, G., Daddi, E., Baronchelli, I., et al. 2011, ApJ, 739, L40
Rodriguez-Gomez, V., Snyder, G. F., Lotz, J. M., et al. 2019, MNRAS, 483, 4140
Saintonge, A., Catinella, B., Tacconi, L. J., et al. 2017, ApJS, 233, 22
Saintonge, A., Kauffmann, G., Kramer, C., et al. 2011, MNRAS, 415, 32
Saintonge, A., Lutz, D., Genzel, R., et al. 2013, ApJ, 778, 2
Sakamoto, K., Okumura, S. K., Ishizuki, S., & Scoville, N. Z. 1999, ApJ, 525, 691
Sanchez, N. N., Tremmel, M., Werk, J. K., et al. 2021, ApJ, 911, 116
Sanders, D. B. & Mirabel, I. F. 1996, ARA&A, 34, 749
Saulder, C., van Kampen, E., Chilingarian, I. V., Mieske, S., & Zeilinger, W. W. 2016, A&A, 596, A14
Schawinski, K., Lintott, C. J., Thomas, D., et al. 2009, ApJ, 690, 1672
Schmidt, M. 1959, ApJ, 129, 243
Schmitt, H. R., Calzetti, D., Armus, L., et al. 2006, ApJ, 643, 173
Schreiber, C., Pannella, M., Elbaz, D., et al. 2015, A&A, 575, A74
Scoville, N., Murchikova, L., Walter, F., et al. 2017, ApJ, 836, 66
Shimizu, T. T., Mushotzky, R. F., Meléndez, M., Koss, M., & Rosario, D. J. 2015, MNRAS, 452, 1841
Shimwell, T. W., Tasse, C., Hardcastle, M. J., et al. 2019, A&A, 622, A1
Smith, D. J. B., Jarvis, M. J., Hardcastle, M. J., et al. 2014, MNRAS, 445, 2232
Solomon, P. M., Downes, D., Radford, S. J. E., & Barrett, J. W. 1997, ApJ, 478, 144
Speagle, J. S., Steinhardt, C. L., Capak, P. L., & Silverman, J. D. 2014, ApJS, 214, 15
Springel, V., Di Matteo, T., & Hernquist, L. 2005, MNRAS, 361, 776
Stark, D. P., Swinbank, A. M., Ellis, R. S., et al. 2008, Nature, 455, 775
Strong, A. W. & Mattox, J. R. 1996, A&A, 308, L21
Tacchella, S., Dekel, A., Carollo, C. M., et al. 2016a, MNRAS, 458, 242
Tacchella, S., Dekel, A., Carollo, C. M., et al. 2016b, MNRAS, 457, 2790
Tacconi, L. J., Genzel, R., Saintonge, A., et al. 2018, ApJ, 853, 179
Tacconi, L. J., Neri, R., Genzel, R., et al. 2013, ApJ, 768, 74
Tully, R. B. & Fisher, J. R. 1977, A&A, 54, 661
van der Wel, A., Bell, E. F., Häussler, B., et al. 2012, ApJS, 203, 24
Violino, G., Ellison, S. L., Sargent, M., et al. 2018, MNRAS, 476, 2591
Wang, L., Gao, F., Duncan, K. J., et al. 2019, A&A, 631, A109
Westmeier, T., Jurek, R., Obreschkow, D., Koribalski, B. S., & Staveley-Smith, L. 2014, MNRAS, 438, 1176
Whitaker, K. E., van Dokkum, P. G., Brammer, G., & Franx, M. 2012, ApJ, 754, L29
White, R. L., Becker, R. H., Helfand, D. J., & Gregg, M. D. 1997, ApJ, 475, 479
Wolfire, M. G., Hollenbach, D., & McKee, C. F. 2010, ApJ, 716, 1191
Woo, J.-H., Son, D., & Bae, H.-J. 2017, ApJ, 839, 120
Wuyts, S., Förster Schreiber, N. M., Lutz, D., et al. 2011, ApJ, 738, 106
Yang, X., Mo, H. J., van den Bosch, F. C., et al. 2007, ApJ, 671, 153
Zolotov, A., Dekel, A., Mandelker, N., et al. 2015, MNRAS, 450, 2327
Zuo, P., Xu, C. K., Yun, M. S., et al. 2018, ApJS, 237, 2

Appendix A: Spectra

In Fig. A.1, we show all galaxies of the DP sample. We present their $70'' \times 70''$ legacy survey snapshot (Dey et al. 2019), the ionised-gas emission lines' Hα and the [NII]$\lambda 6550, 6585$ doublet, and the CO spectra. Furthermore, we show the fit results as discussed in Sect. 3.1.

Appendix B: Observation tables

In Table B.1 (resp. B.2), we present the parameters for the CO(1-0) (resp. CO(2-1)) line obtained using our fitting procedure described in Sect. 3.1. In Table B.3, we present the CO-to-M_{H_2} conversion factor, the molecular-gas mass, the aperture correction factor, the estimated molecular-gas-mass fraction, and the depletion time.

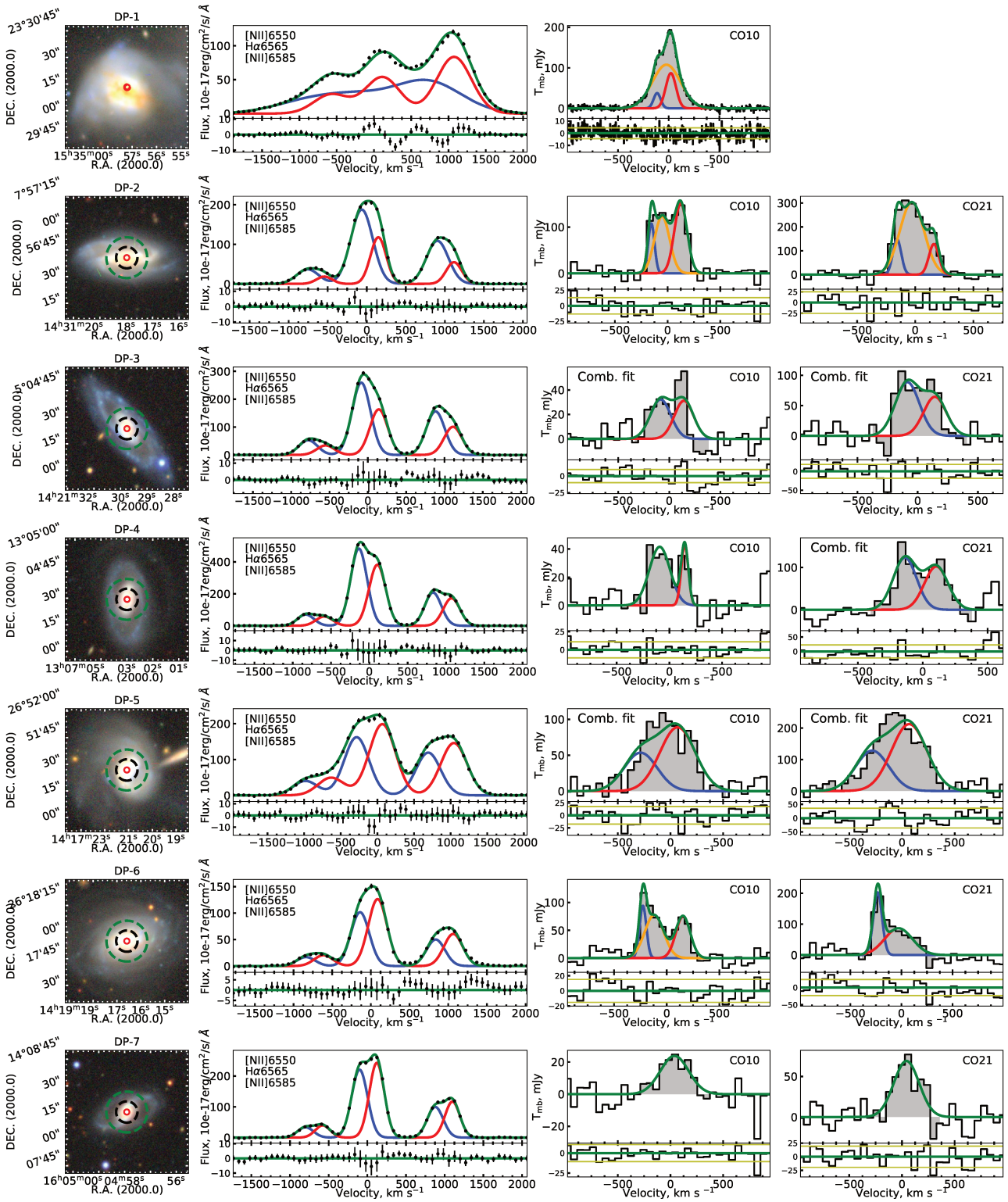

Fig. A.1. Fit results of ionised-gas emission lines and CO(1-0)/CO(2-1) lines. On the left, we show the 70″ × 70″ legacy survey snapshots (Dey et al. 2019) and mark the position of the SDSS 3″ fibre in red and the IRAM CO(1-0) (resp. CO(2-1)) beam of 23″ (resp. 12″) with a green (resp. black) dashed line. For interferometry observations conducted by Bauermeister et al. (2013), we show the beam with a blue ellipse. For DP-24, DP-25, and DP-31, we show the FCRAO CO(1-0) beam of 50″. For DP-1, we extracted a CO(1-0) signal from ALMA interferometry observations for the exact same area as the SDSS 3″ fibre. Next to the snapshots, we show the Hα emission line and the [NII]λ6550/6585 doublet fitted with a double-Gaussian function. On the right hand side, we show the CO(1-0) and the CO(2-1) line, if observed, fitted by a single, a double, or a triple-Gaussian function. In the case of a successful combined fit as described in Sect. 3.1, we indicate this in the top left of the CO panels. For a detailed description of the fitting procedure, see Sect. 3.1.

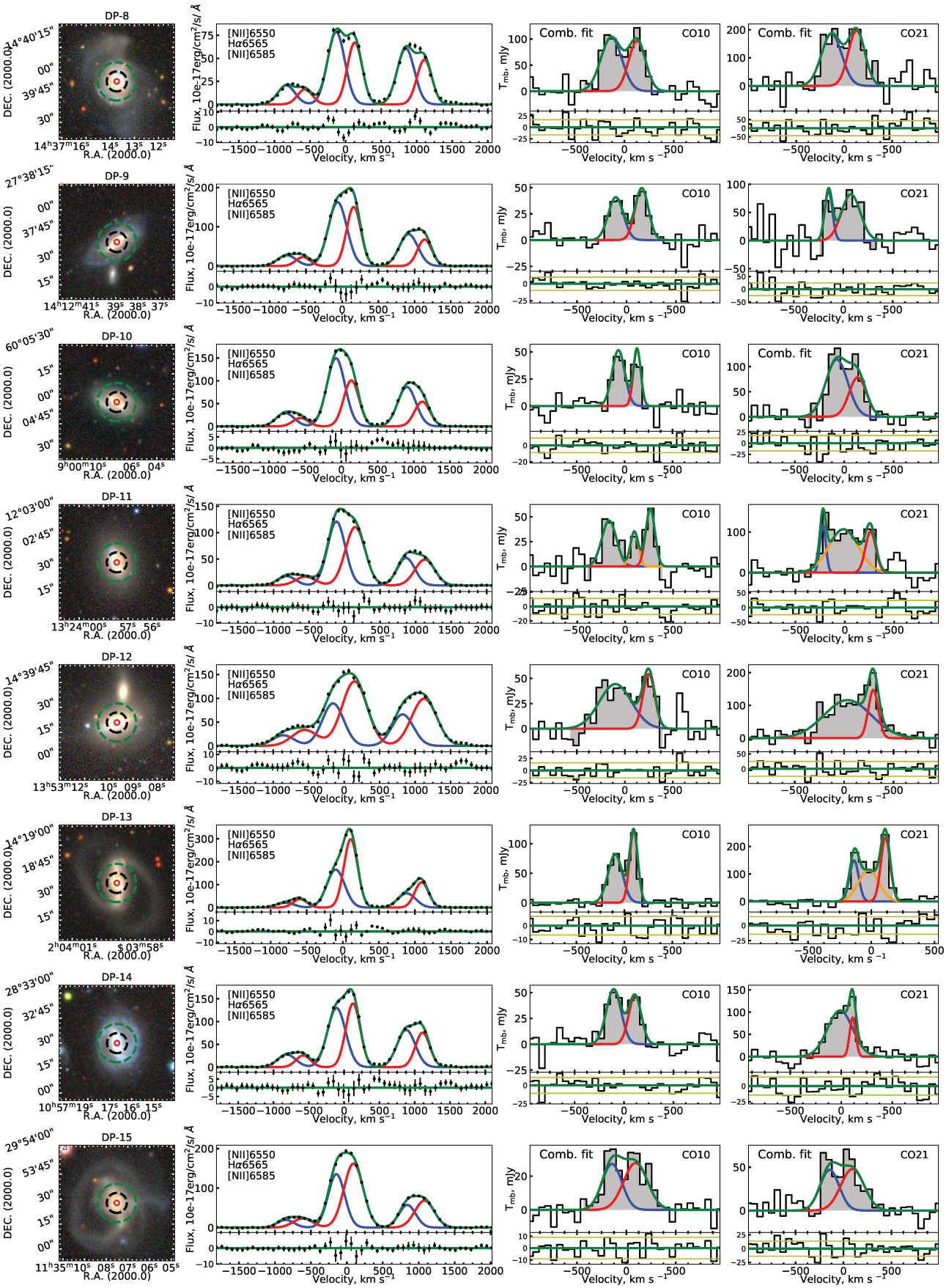

Fig. A.1. Continued.

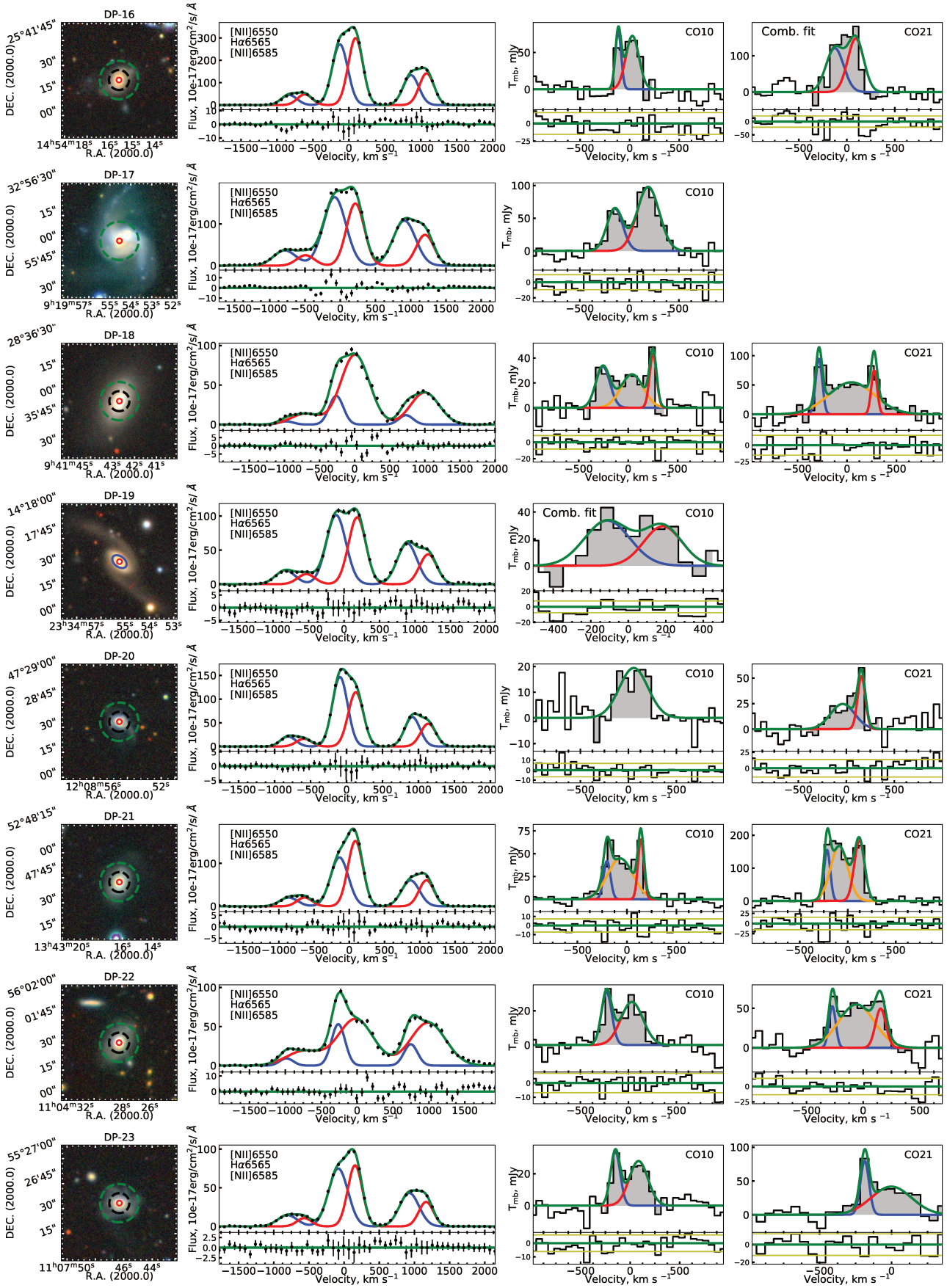

Fig. A.1. Continued.

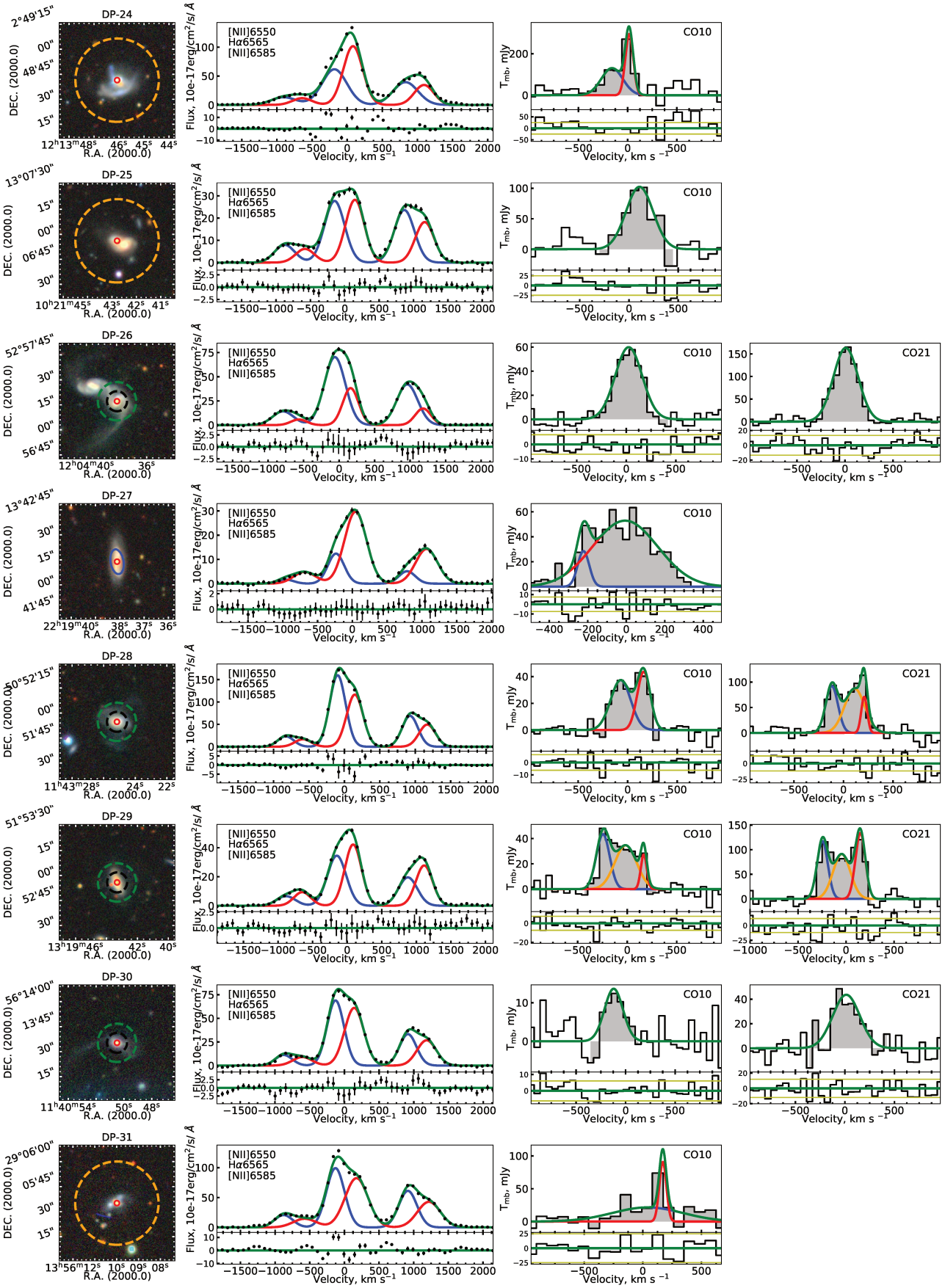

Fig. A.1. Continued.

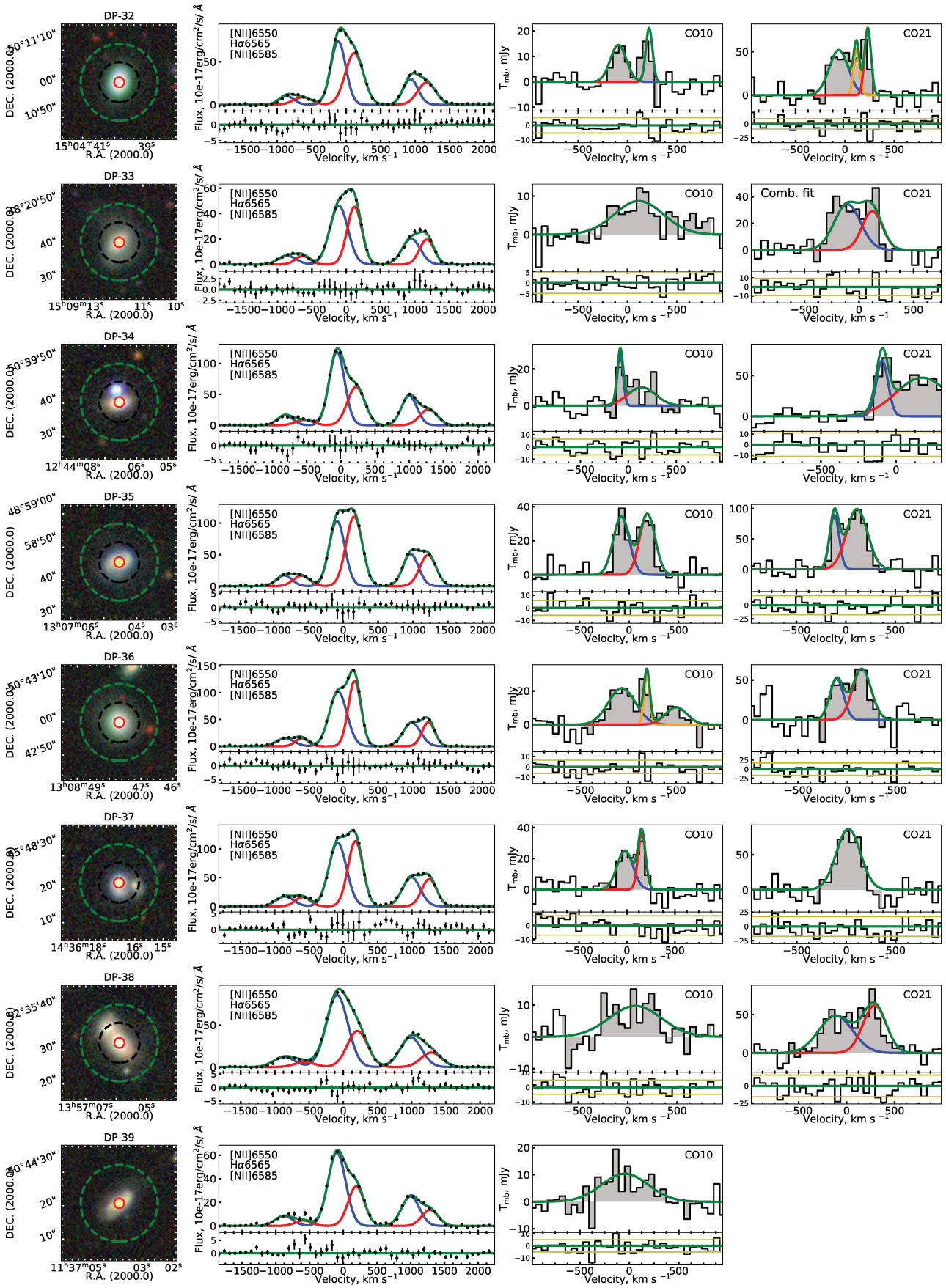

Fig. A.1. Continued.

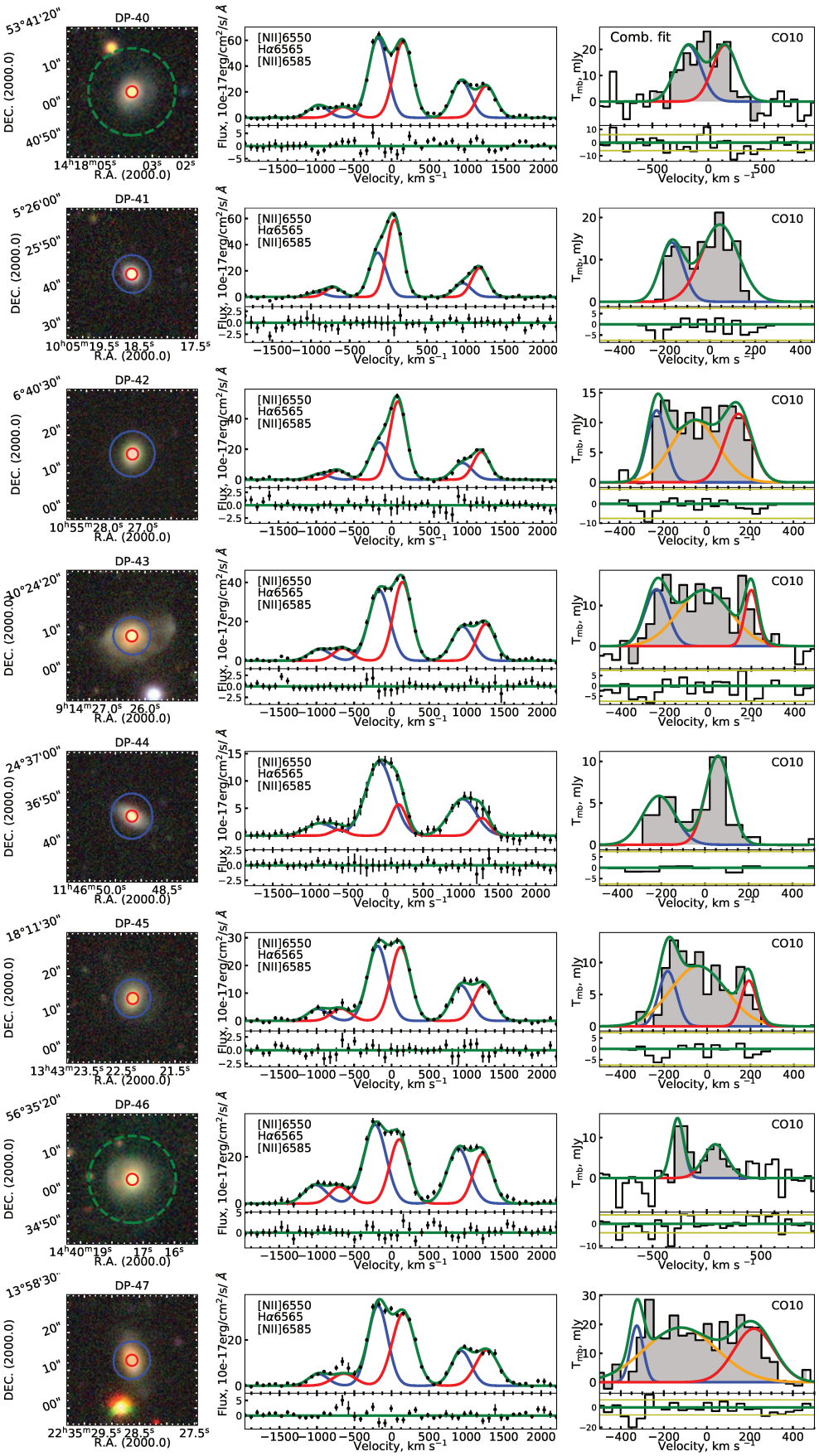

Fig. A.1. Continued.

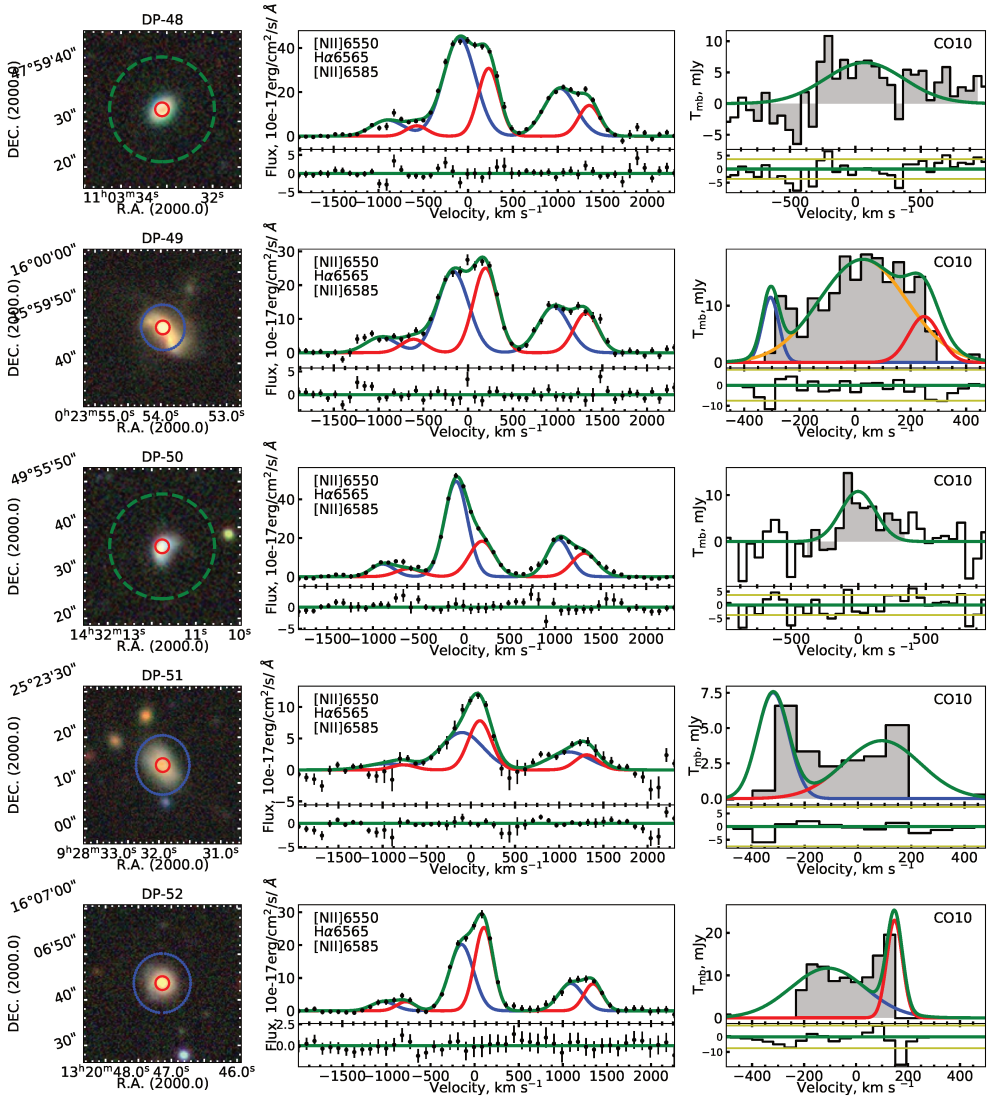

Fig. A.1. Continued.

Table B.1. Observed CO(1-0) line parameters.

ID	Comb. fit	$I_{1\ CO(1-0)}$	μ_1	σ_1	$I_{2\ CO(1-0)}$	μ_2	σ_2	$I_{3\ CO(1-0)}$	μ_3	σ_3
		Jy km s$^-$1	km s$^-$1	km s$^-$1	Jy km s$^-$1	km s$^-$1	km s$^-$1	Jy km s$^-$1	km s$^-$1	km s$^-$1
DP-1[a]	0	3.3 ± 0.1	-113 ± 1	34 ± 1	37.5 ± 0.2	-22 ± 1	138 ± 1	10.9 ± 0.7	21 ± 1	50 ± 1
DP-2	0	8.1 ± 0.1	-154 ± 1	30 ± 1	22.1 ± 0.3	-52 ± 1	71 ± 1	23.1 ± 0.5	124 ± 1	60 ± 1
DP-3	1	8.1 ± 0.4	-85 ± 8	100 ± 4	7.4 ± 0.5	143 ± 11	94 ± 6	-	-	-
DP-4	0	10.3 ± 0.1	-92 ± 1	99 ± 1	3.6 ± 0.2	145 ± 1	33 ± 1	-	-	-
DP-5	1	21.1 ± 1.3	-283 ± 17	157 ± 9	37.6 ± 1.9	67 ± 15	168 ± 8	-	-	-
DP-6	0	7.6 ± 0.2	-225 ± 1	32 ± 1	17.5 ± 0.4	-118 ± 1	90 ± 1	12.9 ± 0.2	155 ± 1	68 ± 1
DP-7	0	8.1 ± 0.2	38 ± 3	134 ± 3	-	-	-	-	-	-
DP-8	1	27.4 ± 1.7	-132 ± 8	105 ± 6	20.8 ± 1.5	129 ± 8	85 ± 6	-	-	-
DP-9	0	7.8 ± 0.2	-108 ± 1	76 ± 1	8.4 ± 0.2	154 ± 1	67 ± 1	-	-	-
DP-10	0	8.6 ± 0.1	-64 ± 1	66 ± 1	5.1 ± 0.2	130 ± 1	38 ± 1	-	-	-
DP-11	0	8.9 ± 0.2	-167 ± 1	76 ± 1	3.7 ± 0.2	95 ± 1	42 ± 1	7.0 ± 0.2	261 ± 1	47 ± 1
DP-12	0	18.7 ± 0.3	-98 ± 2	168 ± 2	8.5 ± 0.2	250 ± 1	62 ± 2	-	-	-
DP-13[b]	0	15.4 ± 0.2	-96 ± 1	74 ± 1	13.3 ± 0.2	96 ± 1	43 ± 1	-	-	-
DP-14	0	10.0 ± 0.3	-104 ± 1	75 ± 2	7.5 ± 0.2	110 ± 1	63 ± 2	-	-	-
DP-15	1	6.8 ± 0.4	-145 ± 11	99 ± 5	8.5 ± 0.5	93 ± 12	121 ± 6	-	-	-
DP-16	0	5.9 ± 0.1	-115 ± 1	30 ± 1	12.1 ± 0.2	27 ± 1	66 ± 1	-	-	-
DP-17[b]	0	13.1 ± 0.2	-146 ± 1	80 ± 1	27.5 ± 0.3	190 ± 1	111 ± 1	-	-	-
DP-18	0	6.0 ± 0.2	-256 ± 2	71 ± 2	7.6 ± 0.3	38 ± 4	112 ± 2	3.8 ± 0.2	250 ± 1	35 ± 2
DP-19[c]	1	10.2 ± 0.6	-112 ± 9	120 ± 6	7.5 ± 0.5	184 ± 8	101 ± 5	-	-	-
DP-20	0	7.3 ± 0.2	54 ± 4	149 ± 3	-	-	-	-	-	-
DP-21	0	3.7 ± 0.2	-201 ± 1	35 ± 1	14.4 ± 0.1	-67 ± 1	128 ± 1	4.9 ± 0.4	141 ± 3	30 ± 1
DP-22	0	4.2 ± 0.3	-227 ± 2	54 ± 2	7.3 ± 0.3	35 ± 4	115 ± 2	-	-	-
DP-23	0	4.2 ± 0.3	-149 ± 3	48 ± 2	6.6 ± 0.4	84 ± 4	94 ± 2	-	-	-
DP-24[d]	0	35.6 ± 0.7	-158 ± 1	108 ± 1	29.6 ± 0.6	16 ± 1	40 ± 1	-	-	-
DP-25[d]	0	35.3 ± 0.4	107 ± 1	137 ± 1	-	-	-	-	-	-
DP-26	0	20.4 ± 0.3	24 ± 1	136 ± 1	-	-	-	-	-	-
DP-27[c]	0	2.1 ± 0.2	-222 ± 1	30 ± 2	22.5 ± 0.3	-6 ± 1	169 ± 2	-	-	-
DP-28	0	9.5 ± 0.3	-70 ± 4	101 ± 3	7.3 ± 0.3	162 ± 2	66 ± 3	-	-	-
DP-29	0	7.3 ± 0.3	-244 ± 2	67 ± 2	9.6 ± 0.1	-15 ± 1	111 ± 2	2.1 ± 0.4	167 ± 5	30 ± 2
DP-30	0	3.2 ± 0.2	-120 ± 5	93 ± 3	-	-	-	-	-	-
DP-31[d]	0	16.2 ± 0.5	40 ± 9	299 ± 3	6.8 ± 2.5	170 ± 2	30 ± 3	-	-	-
DP-32	0	2.9 ± 0.2	-94 ± 4	80 ± 4	1.8 ± 0.2	216 ± 2	33 ± 4	-	-	-
DP-33	0	5.4 ± 0.5	114 ± 13	247 ± 16	-	-	-	-	-	-
DP-34	0	2.1 ± 0.1	-85 ± 1	30 ± 1	3.7 ± 0.2	138 ± 9	144 ± 1	-	-	-
DP-35	0	6.9 ± 0.3	-79 ± 2	80 ± 2	7.0 ± 0.2	185 ± 2	78 ± 2	-	-	-
DP-36	0	7.7 ± 0.3	-66 ± 4	141 ± 3	2.2 ± 0.1	194 ± 1	30 ± 3	2.9 ± 0.2	499 ± 3	112 ± 3
DP-37	0	5.2 ± 0.4	-20 ± 4	82 ± 5	3.6 ± 0.2	154 ± 1	39 ± 5	-	-	-
DP-38	0	6.4 ± 0.3	77 ± 11	262 ± 9	-	-	-	-	-	-
DP-39	0	6.1 ± 0.3	-45 ± 11	235 ± 9	-	-	-	-	-	-
DP-40	1	6.2 ± 0.2	-179 ± 2	113 ± 2	6.1 ± 0.2	148 ± 2	112 ± 2	-	-	-
DP-41[c]	0	1.8 ± 0.2	-169 ± 4	51 ± 4	3.8 ± 0.3	43 ± 4	82 ± 4	-	-	-
DP-42[c]	0	1.3 ± 0.2	-229 ± 5	43 ± 4	2.8 ± 0.6	-54 ± 23	106 ± 4	1.8 ± 0.4	146 ± 11	63 ± 4
DP-43[c]	0	1.9 ± 0.3	-237 ± 6	53 ± 7	4.2 ± 0.6	-16 ± 13	120 ± 7	1.0 ± 0.1	199 ± 2	30 ± 7
DP-44[c]	0	1.1 ± 0.3	-210 ± 15	74 ± 14	1.5 ± 0.2	59 ± 8	55 ± 14	-	-	-
DP-45[c]	0	0.9 ± 0.2	-182 ± 7	41 ± 6	3.0 ± 0.6	-40 ± 21	128 ± 6	0.6 ± 0.3	192 ± 6	35 ± 6
DP-46	0	2.2 ± 0.2	-270 ± 4	58 ± 3	2.3 ± 0.3	78 ± 9	107 ± 3	-	-	-
DP-47[c]	0	1.5 ± 0.1	-325 ± 2	30 ± 1	7.9 ± 0.6	-121 ± 12	167 ± 1	4.3 ± 0.4	219 ± 7	92 ± 1
DP-48	0	4.9 ± 0.5	70 ± 19	299 ± 28	-	-	-	-	-	-
DP-49[c]	0	0.9 ± 0.1	-305 ± 3	30 ± 2	7.2 ± 0.4	27 ± 10	157 ± 2	1.1 ± 0.3	248 ± 9	56 ± 2
DP-50	0	3.5 ± 0.4	-1 ± 12	129 ± 13	-	-	-	-	-	-
DP-51[c]	0	1.1 ± 0.4	-318 ± 14	58 ± 16	1.5 ± 0.5	90 ± 38	144 ± 16	-	-	-
DP-52[c]	0	4.2 ± 0.3	-108 ± 9	143 ± 8	1.7 ± 0.3	148 ± 1	30 ± 8	-	-	-

Notes. Denotations *a*, *b*, *c*, and *d* are the same as in Table 1.We present CO(1-0) fitting parameters from the fitting procedure described in Sect. 3.1. We note if we performed a combined fit using the kinematic parameters from the optical ionised-gas emission lines from the SDSS spectrum with the flag's combined fit. We further present the intensity $I_{CO(1-0)}$, the peak position μ, and the Gaussian σ for each line component.

Table B.2. Observed CO(2-1) line parameters.

ID	Comb. fit	$I_{1\ CO(2-1)}$	μ_1	σ_1	$I_{2\ CO(2-1)}$	μ_2	σ_2	$I_{3\ CO(2-1)}$	μ_3	σ_3
		Jy km s$^-$1	km s$^-$1	km s$^-$1	Jy km s$^-$1	km s$^-$1	km s$^-$1	Jy km s$^-$1	km s$^-$1	km s$^-$1
DP-2	0	13.4 ± 0.2	-156 ± 1	36 ± 1	79.0 ± 0.6	-28 ± 1	103 ± 1	13.7 ± 0.3	160 ± 1	42 ± 1
DP-3	1	22.3 ± 1.0	-85 ± 8	100 ± 4	15.3 ± 1.0	143 ± 11	94 ± 6	-	-	-
DP-4	1	27.9 ± 0.9	-137 ± 4	90 ± 2	23.6 ± 0.9	103 ± 5	91 ± 3	-	-	-
DP-5	1	50.5 ± 3.0	-283 ± 17	157 ± 9	89.7 ± 4.4	67 ± 15	168 ± 8	-	-	-
DP-6	0	21.6 ± 0.2	-232 ± 1	42 ± 1	29.4 ± 0.3	-28 ± 1	135 ± 1	-	-	-
DP-7	0	20.9 ± 0.2	42 ± 1	120 ± 1	-	-	-	-	-	-
DP-8	1	49.3 ± 3.0	-132 ± 8	105 ± 6	42.5 ± 3.1	129 ± 8	85 ± 6	-	-	-
DP-9	0	8.5 ± 0.1	-149 ± 1	38 ± 1	19.8 ± 0.2	76 ± 1	96 ± 1	-	-	-
DP-10	1	31.8 ± 1.3	-75 ± 8	110 ± 4	17.3 ± 1.0	137 ± 9	87 ± 5	-	-	-
DP-11	0	8.8 ± 0.1	-222 ± 1	30 ± 1	40.0 ± 0.4	-13 ± 1	149 ± 1	13.3 ± 0.2	260 ± 1	52 ± 1
DP-12	0	69.5 ± 0.4	35 ± 1	238 ± 1	18.7 ± 0.2	295 ± 1	50 ± 1	-	-	-
DP-13[b]	0	13.6 ± 0.3	-135 ± 1	36 ± 1	23.2 ± 0.3	-20 ± 1	80 ± 1	21.6 ± 0.5	112 ± 3	36 ± 1
DP-14	0	32.1 ± 0.1	-11 ± 1	123 ± 1	6.6 ± 0.3	112 ± 1	30 ± 1	-	-	-
DP-15	1	11.8 ± 0.7	-145 ± 11	99 ± 5	14.6 ± 0.7	93 ± 12	121 ± 6	-	-	-
DP-16	1	27.9 ± 1.2	-125 ± 6	91 ± 3	31.0 ± 1.2	92 ± 5	83 ± 3	-	-	-
DP-18	0	7.9 ± 0.2	-283 ± 1	33 ± 1	31.6 ± 0.4	45 ± 2	230 ± 1	5.6 ± 0.1	274 ± 1	30 ± 1
DP-20	0	7.8 ± 0.3	-38 ± 4	126 ± 3	5.2 ± 0.2	157 ± 1	40 ± 3	-	-	-
DP-21	0	12.6 ± 0.2	-215 ± 1	32 ± 1	37.5 ± 0.4	-89 ± 1	89 ± 1	24.7 ± 0.3	121 ± 1	53 ± 1
DP-22	0	3.9 ± 0.1	-272 ± 1	30 ± 1	21.7 ± 0.4	-59 ± 2	157 ± 1	5.7 ± 0.2	154 ± 1	46 ± 1
DP-23	0	6.0 ± 0.1	-186 ± 1	30 ± 1	14.6 ± 0.4	-1 ± 3	139 ± 1	-	-	-
DP-26	0	52.9 ± 0.3	8 ± 1	129 ± 1	-	-	-	-	-	-
DP-28	0	14.4 ± 0.3	-117 ± 1	62 ± 1	22.2 ± 0.4	112 ± 1	101 ± 1	5.3 ± 0.1	209 ± 1	30 ± 1
DP-29	0	16.5 ± 0.3	-246 ± 1	56 ± 1	20.7 ± 0.7	-45 ± 1	90 ± 1	17.3 ± 0.3	148 ± 1	51 ± 1
DP-30	0	15.0 ± 0.3	13 ± 1	137 ± 1	-	-	-	-	-	-
DP-32	0	12.6 ± 0.2	-63 ± 1	96 ± 1	4.0 ± 0.1	117 ± 1	30 ± 1	6.3 ± 0.2	229 ± 1	32 ± 1
DP-33	1	10.4 ± 1.0	-106 ± 23	120 ± 11	6.8 ± 0.6	121 ± 16	92 ± 8	-	-	-
DP-34	0	6.8 ± 0.2	-93 ± 1	39 ± 1	20.7 ± 0.5	172 ± 2	174 ± 1	-	-	-
DP-35	0	10.8 ± 0.2	-116 ± 1	47 ± 1	26.4 ± 0.3	112 ± 1	106 ± 1	-	-	-
DP-36	0	9.0 ± 0.2	-109 ± 2	69 ± 1	15.1 ± 0.3	144 ± 1	93 ± 1	-	-	-
DP-37	0	26.5 ± 0.2	21 ± 1	121 ± 1	-	-	-	-	-	-
DP-38	0	21.3 ± 0.6	-113 ± 5	175 ± 4	18.8 ± 0.6	291 ± 3	120 ± 4	-	-	-

Notes. Same as Table B.1, but for CO(2-1) measurements.

Table B.3. Results of molecular-gas-mass estimation.

ID	$L'_{CO(1-0)}$	$L'_{CO(2-1)}$	α_{CO}	M_{H_2}	$f_{a\,CO(1-0)}$	$M_{corr\,H_2}$	$\log(\mu_{gas})$	t_{depl}
	10^8 L_l^d	10^8 L_l^d	$M_\odot$ / (K km s^{-1} pc^2)	10^9 $M_\odot$		10^9 $M_\odot$		Gyr
DP-1[a]	7.7 ± 0.1	-	3.9	3.0	1.0	3.0	-1.4	0.6
DP-2	17.5 ± 0.2	8.7 ± 0.1	3.9	6.9	1.6	11.0	-0.9	1.4
DP-3	5.2 ± 0.2	3.1 ± 0.1	3.8	1.9	1.9	3.7	-1.0	1.0
DP-4	4.7 ± 0.1	4.4 ± 0.1	3.8	1.8	1.6	2.9	-1.0	0.8
DP-5	36.2 ± 1.4	21.6 ± 0.8	4.0	14.5	1.9	28.0	-0.7	2.1
DP-6	23.6 ± 0.3	7.9 ± 0.0	4.0	9.4	1.6	15.5	-0.9	2.1
DP-7	5.1 ± 0.2	3.3 ± 0.0	3.8	1.9	1.4	2.6	-1.1	0.4
DP-8	31.7 ± 1.5	15.1 ± 0.7	3.9	12.2	1.2	14.6	-0.7	1.4
DP-9	11.1 ± 0.2	4.8 ± 0.0	3.8	4.2	1.3	5.5	-0.9	0.6
DP-10	9.5 ± 0.2	8.6 ± 0.3	3.9	3.7	1.3	4.8	-1.3	0.1
DP-11	13.7 ± 0.2	10.9 ± 0.1	3.9	5.4	1.3	7.1	-1.2	1.0
DP-12	20.4 ± 0.3	16.5 ± 0.1	4.1	8.3	1.6	13.3	-1.1	1.8
DP-13[b]	24.0 ± 0.2	12.2 ± 0.2	3.9	9.3	1.4	12.7	-0.8	1.0
DP-14	16.9 ± 0.4	9.3 ± 0.1	3.8	6.5	1.3	8.7	-0.9	0.8
DP-15	15.0 ± 0.6	6.5 ± 0.2	3.9	5.9	1.7	9.7	-1.0	1.4
DP-16	18.9 ± 0.2	15.5 ± 0.4	3.8	7.2	1.1	8.3	-0.9	0.3
DP-17[b]	44.9 ± 0.4	-	3.8	16.9	2.1	34.7	0.1	3.8
DP-18	23.3 ± 0.6	15.1 ± 0.1	4.0	9.3	1.4	12.7	-1.0	1.7
DP-19[c]	31.6 ± 1.3	-	3.9	12.4	1.0	12.4	-0.9	0.6
DP-20	15.5 ± 0.5	6.9 ± 0.2	3.8	5.8	1.1	6.4	-0.9	0.4
DP-21	51.1 ± 1.0	41.4 ± 0.3	4.0	20.3	1.2	23.7	-0.7	0.6
DP-22	26.3 ± 1.0	18.0 ± 0.3	3.9	10.2	1.3	12.8	-0.9	1.2
DP-23	25.7 ± 1.1	12.2 ± 0.3	3.9	9.9	1.2	11.8	-0.9	0.5
DP-24[d]	162.2 ± 2.2	-	3.8	60.9	1.0	61.0	0.2	3.5
DP-25[d]	95.9 ± 1.0	-	3.9	37.8	1.0	38.7	-0.5	2.0
DP-26	63.5 ± 0.8	41.1 ± 0.2	3.8	24.4	1.3	31.4	-0.4	1.4
DP-27[c]	80.4 ± 1.2	-	3.9	31.5	1.0	31.5	-0.6	2.7
DP-28	55.8 ± 1.4	34.9 ± 0.4	3.9	21.7	1.1	24.5	-0.6	0.9
DP-29	72.5 ± 2.0	52.0 ± 0.7	3.9	28.4	1.1	31.3	-0.6	1.7
DP-30	17.1 ± 1.0	20.1 ± 0.3	3.8	6.5	1.1	7.3	-0.9	0.2
DP-31[d]	128.9 ± 14.1	-	4.0	51.3	1.0	52.6	-0.5	0.9
DP-32	28.3 ± 1.5	34.3 ± 0.4	3.8	10.7	1.1	11.3	-0.7	0.7
DP-33	36.7 ± 3.1	29.1 ± 2.1	3.8	13.9	1.1	15.1	-0.7	1.2
DP-34	40.3 ± 1.7	47.9 ± 0.8	3.8	15.2	1.1	16.1	-0.6	0.7
DP-35	100.1 ± 2.5	66.9 ± 0.7	4.0	39.8	1.1	41.8	-0.6	0.5
DP-36	94.0 ± 2.6	44.3 ± 0.7	3.8	36.0	1.1	38.3	-0.4	1.1
DP-37	82.7 ± 4.4	62.1 ± 0.6	3.9	31.8	1.0	33.4	-0.5	0.5
DP-38	63.5 ± 3.2	99.3 ± 2.0	3.9	24.6	1.1	27.5	-0.7	0.8
DP-39	75.9 ± 4.1	-	3.8	28.6	1.0	30.0	-0.4	0.6
DP-40	158.9 ± 3.8	-	3.9	61.4	1.1	64.6	-0.3	1.0
DP-41[c]	74.4 ± 4.2	-	3.8	28.0	1.0	28.0	-0.3	0.6
DP-42[c]	85.6 ± 10.2	-	3.8	32.7	1.0	32.7	-0.5	0.7
DP-43[c]	106.8 ± 10.4	-	4.1	43.9	1.0	43.9	-0.8	0.7
DP-44[c]	39.2 ± 5.4	-	3.8	15.0	1.0	15.0	-0.9	0.1
DP-45[c]	70.4 ± 10.1	-	4.0	28.2	1.0	28.2	-0.9	0.4
DP-46	69.7 ± 5.9	-	4.1	28.4	1.1	31.5	-0.9	1.6
DP-47[c]	223.9 ± 12.0	-	4.1	91.1	1.0	91.1	-0.5	1.0
DP-48	87.5 ± 9.3	-	3.8	33.3	1.0	34.1	-0.5	1.6
DP-49[c]	164.6 ± 9.1	-	4.0	65.0	1.0	65.0	-0.5	1.2
DP-50	64.3 ± 8.2	-	3.8	24.1	1.0	24.9	-0.3	2.2
DP-51[c]	104.1 ± 24.8	-	3.8	40.0	1.0	40.0	-0.6	1.6
DP-52[c]	292.6 ± 20.8	-	3.9	115.4	1.0	115.4	-0.4	1.8

Notes. Denotations *a*, *b*, *c*, and *d* are the same as in Table 1. We present the total intrinsic CO(1-0) (resp. CO(2-1)) luminosity $L'_{CO(1-0)}$ (resp. $L'_{CO(2-1)}$) with L_l = K km s^{-1} pc^2, the luminosity-to-molecular-gas-mass conversion factor α_{CO}, the measured molecular-gas mass M_{H_2}, the aperture correction factor $f_{a\,CO10}$, the aperture corrected molecular-gas mass $M_{corr\,H_2}$, the mass fraction $\mu_{gas,}$ and the depletion time t_{depl}.

CHAPTER 5

Conclusion

1 The current state of double-peak emission line galaxies

Double-peak (DP) emission lines, which can be observed with spectroscopic measurements at the centre of some galaxies, are a peculiar phenomenon, as insights on the internal kinematic conditions of the observed galaxies. Therefore, DP emission lines have been used extensively to find dual active galactic nuclei and gas outflows driven by super massive black holes in the centre of galaxies. In this thesis, I have looked at the phenomenon of DP emission-line galaxies from a general perspective. Therefore, I have developed an automatic detection algorithm and selected 5 663 such galaxies in the spectroscopic galaxy survey SDSS. I compared these galaxies with single-peak (SP) emission-line galaxies, which follow the same redshift and stellar-mass distribution as the DP galaxies. This analysis revealed that DP galaxies are predominantly S0 and bulge dominated disc galaxies, whereas SP galaxies are more likely to be late-type spirals. In addition, I found no direct correlations between galaxy inclination and the measured kinematic signatures of DPs. The position on the Tully-Fischer relation, which compares the kinematic footprint with the galaxy mass, showed that DP galaxies deviate strongly from literature values, with which SP galaxies are in line. Galaxies that are classified as star-forming also have an increased central star-formation rate when they have a DP at the centre. Considering these characteristics, the most obvious scenario is a recent minor merger that transported gas into the centre of the galaxy, fuelling star formation and causing a DP signature.

Since the SDSS survey only provides a spectroscopic observation of the central 3″ and an optical image, it is challenging to determine the exact cause of the observed DP signature in individual galaxies. To gain a better understanding of how a DP signature connects to the internal gas kinematics of galaxies, I have investigated this phenomenon using axisymmetric models and simulations. I created SDSS-like synthetic spectroscopic observations and investigated different kinematic processes, showing a DP. The result was that rotational curves of disc galaxies can produce a DP signature and their strength depend on the stellar bulge mass and concentration. In addition, bar structures can produce a DP signature, when observed parallel to its major axis. Major mergers tend to accumulate a central gas disk in late post-merger stages (1 Gyr after the final coalescence), which can be observed as a DP. Minor mergers, on the other hand, show a

DP only during 350 Myr after the final coalescence, which is independent from the direction of observation. Both scenarios are hardly recognisable as mergers in the snapshots. Taking into account that increased star-formation rates are common for DP emission-line galaxies, the major-merger scenario is unlikely since their enhanced star formation might have already faded. Hence, the observations are best explained by bar galaxies and minor mergers.

There is a deep connection between star formation and galaxy mergers as the molecular gas reservoir can be replenished through merging. To better understand the role of DP emission-line galaxies in this context, I performed CO observations with the IRAM 30m telescope and studied the molecular gas content of DP galaxies located above the star-forming main sequence. Using further CO observations from the literature, I created a sample of 52 star-forming DP galaxies and studied their characteristics. It turns out that these galaxies have a much higher molecular gas content than predicted by scaling relations from the literature. In addition, we find the exact same kinematic signatures in optical and CO lines for 20 % of the galaxies. This indicates that the molecular gas is concentrated in the centre of the galaxies. This picture is further supported by the fact that we find strong central star formation enhancement in almost all galaxies. These observations clearly favour the idea that recent minor mergers have effectively funnelled gas into the centre of these galaxies, triggering star formation.

2 High resolution observations

Proposing further observations with special telescopes can shed light on the fundamental processes of carefully selected DP galaxies. However, the time allocation process for some telescopes is very challenging and often only allows for questions of particular importance in the field. In fact, '*archival data products are, in the long term, as important as the PI science programs*' (White et al. 2009). By cross matching the DP galaxy catalog with the Hubble Legacy archive[1], I find 53 galaxies which have been observed with the Hubble Space Telescope (HST) providing the highest resolution in the optical wavelength. Only 17 of these galaxies are already published with a context in DP emission line galaxies, all of them on dual AGN (Liu et al. 2018; Comerford et al. 2015, 2018; Shangguan et al. 2016). Thirty-six of the identified galaxies are not published with any connection to their DP emission lines. This is predominantly because most of the studies were on other topics or the galaxies were located in the exposed field by chance. Regarding the high resolution of the HST, these observations allow detailed studies on the connection between central kinematics and the galaxy morphology. A first inspection of this sample reveals several different galaxy types. However, for 6 of the identified targets it is challenging to draw a conclusion either because the images were observed with a too short exposure time and are therefore not deep enough or the target galaxies are only partly covered by the field of view. Of the remaining 30 galaxies, 17 (57 %) are ongoing mergers, have prominent tidal features or exhibit multiple bright spots in their centres. Five galaxies (17 %) have a large bar, 3 (10 %) are elliptical galaxies and 5 (17 %) are disc galaxies with a large bulge. The latter type is mostly identified as a S0 galaxy from the SDSS image. This relatively small sample already shows a clear increase in galaxy mergers, most of which remain undetected with the SDSS due to the lack of sensitivity. This is an excellent basis for a future detailed study on the origin of DP signatures in individual galaxies. Furthermore, this archival data mining shows the importance of archives on the one hand and the usage of high resolution observations on the other hand.

[1] https://hla.stsci.edu/hlaview.html

3 Resolving kinematics with integrated field spectroscopy

Single-fibre spectroscopy such as SDSS only provides a kinematic estimation of the central 3″. Integrated field spectroscopy (IFS), on the other hand, allows many kinematic measurements over a spatial distribution. One survey of this kind is the Mapping Nearby Galaxies at Apache Point Observatory (MaNGA) survey (Abdurro'uf et al. 2022, DR 17), providing observations for about 10 000 galaxies. Considering the different mechanisms, discussed in Chapter 3, which can create a DP signature in the inner 3″, IFS observations can provide the needed spatial resolution to distinguish between the different scenarios. In Mazzilli Ciraulo et al. (2021), two individual gaseous counter rotating discs were identified in a DP galaxy with MaNGA, reveling two galaxies in the act of merging. The system is considered as a pre-coalescence merger with a mass ratio of 1:9. A key aspect of this analysis was the assumption of a double-Gaussian parametrisation of the ionised-gas emission lines.

Based on high resolution observations of the molecular gas with ALMA, Treister et al. (2020) was able to identify multiple kinematic components in the of the violent merger system NGC 6240. They found rotation patterns around two nuclei and distinguish these components from a giant molecular gas clump and gas outflows. This study shows in great detail how kinematic observations with a high spatial resolution can help to distinguish between different phenomena. Considering the large number of IFS observations from surveys, such as Manga, it is clear that there are numerous opportunities to investigate in individual well-selected DP galaxies. A simple cross-match between the DP sample from Maschmann et al. (2020) and the Manga-DR17 yields to 69 DP galaxies observed by MaNGA (see Mazzilli Ciraulo et al. 2022, in revision). This is a promising sample size to investigate various phenomena such as rotating discs or post-coalescence merger and can help to discuss different scenarios. The number of DP galaxies in the MaNGA survey can even be increased by searching for multiple components over the entire observed area.

4 Double-peak emission line galaxies in cosmological simulations

Given the long time scales of galaxy evolution, the only way to study the change of galaxies over time is through galaxy simulations. How galaxies can generate a DP signature at different evolution stages is discussed in a qualitative way in Chapter 3 (Maschmann et al. 2022a). The simulations considered were only isolated galaxies and idealized galaxy-galaxy mergers. The build up of galaxies, however, does not occur in such idealised scenarios and is rather described as repetitive gas accretion and merger events with large variety of mass ratios (Tonini et al. 2016). A more realistic view on galaxy evolution can be provided by modern cosmological simulations such as the Illustris TNG project (Nelson et al. 2019). This brings the particular possibility to measure DP signatures at different events of galaxy evolution. One can investigate e.g. whether there is a direct link between a recent minor merger or gas accretion and an observed DP signature or in how far galaxy bars and rotating discs are dominating the population of DP galaxies. Finally cosmological simulations can provide an estimation on which process occurs most frequently at what redshift leading to DP signatures as a possible probe for galaxy evolution in surveys at higher redshift.

5 Exploring the high-redshift Universe

The cosmological context is particularly important when trying to understand the evolution of galaxies. We know from observations that the star formation density decreases exponentially since $z \sim 2$ (Madau & Dickinson 2014). We also know that the major merger rate decreased since $z \sim 1$ (Lotz et al. 2011) and that stellar bulges were smaller at higher z (Sachdeva et al. 2017). As described in Chapter 1, close super-massive black holes are the final stage of a galaxy merger. To better understand such stages, Chen et al. (2022) identified dual quasars till $z \sim 3.5$ and find an increasing frequency of dual AGNs towards higher redshift ($z < 1.5$). This is in line with the increase in major mergers towards higher redshifts. What this example shows is that single phenomenons such as dual AGNs can be used to test theories of how galaxies are evolving over cosmic time.

Also DP galaxies can help to identify and understand different scenarios at redshifts beyond the SDSS. Especially in the light of upcoming spectroscopic surveys at higher redshift, this kinematic signature can be used to study gaseous discs and galaxy mergers. For this purpose the future VLT 4MOST survey is of special interest as it observes emission-line galaxies up to a redshift of $z = 1.1$ (Richard et al. 2019). With this survey one can test whether DP galaxies evolve over cosmic time. DP signatures might probe more mergers at higher redshift since stellar bulges are less frequent and the gravitational potential is not sufficient to create a DP signature. Such statistical analysis would also help to understand the connection of galaxy evolution and the declining star-formation rate in this time span.

6 Final remark

In the course of this thesis I got a wide overview of DP emissions-line galaxies. I have gained a good understanding of how the underlying processes can cause this phenomenon. With in-depth studies of smaller sub-samples, I have learned how DP galaxies play a role in the field of galaxy evolution. Especially for future spectroscopic surveys at higher redshift this phenomenon can provide a useful tool. Well adjusted detection algorithms for galaxy mergers can allow us to understand how the merger rate has evolved over cosmic time. In fact, this can open a door to a better understanding of the role galaxy merger play in the context of star formation and star-formation quenching since $z = 1 - 2$. To get there, however, the phenomenon of DP emission lines must be further investigated by means of spatially resolving spectroscopic observations. Furthermore, modern cosmological simulations offer more realistic simulations to characterise further the underlying mechanisms.

Bibliography

Abazajian, K. N., Adelman-McCarthy, J. K., Agüeros, M. A., et al. 2009, ApJS, 182, 543 7

Abdo, A. A., Ackermann, M., Ajello, M., et al. 2010, ApJ, 710, 133 16

Abdurro'uf, Accetta, K., Aerts, C., et al. 2022, ApJS, 259, 35 7, 131

Abel, T., Bryan, G. L., & Norman, M. L. 2002, Science, 295, 93 9

Aird, J., Nandra, K., Laird, E. S., et al. 2010, MNRAS, 401, 2531 23

Akiyama, K., Alberdi, A., Alef, W., et al. 2022, ApJ, 930, L12 32

Allamandola, L. J., Hudgins, D. M., & Sandford, S. A. 1999, ApJ, 511, L115 13

Assef, R. J., Stern, D., Kochanek, C. S., et al. 2013, ApJ, 772, 26 22, 23, 25

Baade, W. & Minkowski, R. 1954, ApJ, 119, 215 22

Baldry, I. K. 2008, Astronomy and Geophysics, 49, 5.25 4

Baldwin, J. A., Phillips, M. M., & Terlevich, R. 1981, PASP, 93, 5 24

Begelman, M. C., Blandford, R. D., & Rees, M. J. 1980, Nature, 287, 307 32

Belfiore, F., Maiolino, R., Maraston, C., et al. 2016, MNRAS, 461, 3111 25

Bell, E. F., Wolf, C., Meisenheimer, K., et al. 2004, ApJ, 608, 752 20

Bergvall, N., Laurikainen, E., & Aalto, S. 2003, A&A, 405, 31 10

Bigiel, F., Leroy, A., Walter, F., et al. 2008, AJ, 136, 2846 15

Blanton, M. R., Hogg, D. W., Bahcall, N. A., et al. 2003, ApJ, 592, 819 28

Bolatto, A. D., Wolfire, M., & Leroy, A. K. 2013, ARA&A, 51, 207 16

Boquien, M., Burgarella, D., Roehlly, Y., et al. 2019, A&A, 622, A103 12, 22, 23, 25, 26

Bothun, G. D. & Dressler, A. 1986, ApJ, 301, 57 10

Bottrell, C., Hani, M. H., Teimoorinia, H., Patton, D. R., & Ellison, S. L. 2022, MNRAS, 511, 100 11

Boulanger, F. 1999, in Astronomical Society of the Pacific Conference Series, Vol. 168, New Perspectives on the Interstellar Medium, ed. A. R. Taylor, T. L. Landecker, & G. Joncas, 173 13

Bournaud, F. & Combes, F. 2004, in SF2A-2004: Semaine de l'Astrophysique Francaise, ed. F. Combes, D. Barret, T. Contini, F. Meynadier, & L. Pagani, 645 8

Bournaud, F., Jog, C. J., & Combes, F. 2007, A&A, 476, 1179 30, 38

Boyle, W. S. & Smith, G. E. 1970, The Bell System Technical Journal, 49, 587 6

Bradt, H., Naranan, S., Rappaport, S., & Spada, G. 1968, ApJ, 152, 1005 22

Bridle, A. H. & Perley, R. A. 1984, ARA&A, 22, 319 23

Brinchmann, J., Charlot, S., White, S. D. M., et al. 2004, MNRAS, 351, 1151 27, 28, 29

Calzetti, D. 2001, PASP, 113, 1449 27

Calzetti, D., Armus, L., Bohlin, R. C., et al. 2000, ApJ, 533, 682 27

Cardelli, J. A., Clayton, G. C., & Mathis, J. S. 1989, ApJ, 345, 245 27

Cattaneo, A., Faber, S. M., Binney, J., et al. 2009, Nature, 460, 213 23

Chambers, G. 1904, The Story of the Stars, University of California Libraries (New York : McClure, Phillips) 1

Charlot, S. & Longhetti, M. 2001, MNRAS, 323, 887 27

Chen, Y.-C., Hwang, H.-C., Shen, Y., et al. 2022, ApJ, 925, 162 132

Chester, C. & Roberts, M. S. 1964, AJ, 69, 635 20

Chilingarian, I., Cayatte, V., Chemin, L., et al. 2007, A&A, 466, L21 5

Chilingarian, I. V., Melchior, A.-L., & Zolotukhin, I. Y. 2010, MNRAS, 405, 1409 19

Chilingarian, I. V., Zolotukhin, I. Y., Katkov, I. Y., et al. 2017, ApJS, 228, 14 19, 21, 24, 25

Ciotti, L. & Bertin, G. 1999, A&A, 352, 447 5

Combes, F., García-Burillo, S., Audibert, A., et al. 2019, A&A, 623, A79 23

Combes, F., Prugniel, P., Rampazzo, R., & Sulentic, J. W. 1994, A&A, 281, 725 10

Comerford, J. M., Gerke, B. F., Newman, J. A., et al. 2009a, ApJ, 698, 956 32

Comerford, J. M. & Greene, J. E. 2014, ApJ, 789, 112 33

Comerford, J. M., Griffith, R. L., Gerke, B. F., et al. 2009b, ApJ, 702, L82 32

Comerford, J. M., Nevin, R., Stemo, A., et al. 2018, ApJ, 867, 66 35, 130

Comerford, J. M., Pooley, D., Barrows, R. S., et al. 2015, ApJ, 806, 219 33, 130

Comerford, J. M., Pooley, D., Gerke, B. F., & Madejski, G. M. 2011, ApJ, 737, L19 9, 33, 34

Condon, J. J. 1984, ApJ, 287, 461 14, 23

Condon, J. J. 1992, ARA&A, 30, 575 14

Condon, J. J., Cotton, W. D., & Broderick, J. J. 2002, AJ, 124, 675 26

Conselice, C. J. 2014, ARA&A, 52, 291 30

Conselice, C. J., Blackburne, J. A., & Papovich, C. 2005, ApJ, 620, 564 11

Conselice, C. J., Wilkinson, A., Duncan, K., & Mortlock, A. 2016, ApJ, 830, 83 2

Cox, T. J. & Loeb, A. 2008, MNRAS, 386, 461 9

Croton, D. J., Springel, V., White, S. D. M., et al. 2006, MNRAS, 365, 11 23

Curtis, H. D. 1918, Publications of Lick Observatory, 13, 9 21

Daddi, E., Bournaud, F., Walter, F., et al. 2010, ApJ, 713, 686 30

Dame, T. M., Ungerechts, H., Cohen, R. S., et al. 1987, ApJ, 322, 706 16

Davé, R., Oppenheimer, B. D., & Finlator, K. 2011, MNRAS, 415, 11 30

Davis, T. A., Rowlands, K., Allison, J. R., et al. 2015, MNRAS, 449, 3503 11

De Propris, R., Liske, J., Driver, S. P., Allen, P. D., & Cross, N. J. G. 2005, AJ, 130, 1516 10

de Sá-Freitas, C., Gonçalves, T. S., de Carvalho, R. R., et al. 2022, MNRAS, 509, 3889 19

de Vaucouleurs, G. 1948, Annales d'Astrophysique, 11, 247 4

de Vaucouleurs, G. 1959, Handbuch der Physik, 53, 275 4

de Vaucouleurs, G. 1961, ApJS, 5, 233 19, 20

Dekel, A. & Birnboim, Y. 2006, MNRAS, 368, 2 9

Dekel, A., Birnboim, Y., Engel, G., et al. 2009, Nature, 457, 451 30

Dekel, A. & Burkert, A. 2014, MNRAS, 438, 1870 30

Dekel, A., Zolotov, A., Tweed, D., et al. 2013, MNRAS, 435, 999 30

Dey, A., Schlegel, D. J., Lang, D., et al. 2019, AJ, 157, 168 4, 10, 15, 19

Di Matteo, P., Combes, F., Melchior, A. L., & Semelin, B. 2007, A&A, 468, 61 10

Di Matteo, T., Springel, V., & Hernquist, L. 2005, Nature, 433, 604 23

Domínguez, A., Siana, B., Henry, A. L., et al. 2013, ApJ, 763, 145 27

Domínguez Sánchez, H., Huertas-Company, M., Bernardi, M., Tuccillo, D., & Fischer, J. L. 2018, MNRAS, 476, 3661 20, 21

Dopita, M. A. & Sutherland, R. S. 2003, Astrophysics of the diffuse universe 17

Draine, B. T. 2003, ARA&A, 41, 241 13

Draine, B. T. & Lee, H. M. 1984, ApJ, 285, 89 13

Draine, B. T. & Li, A. 2007, ApJ, 657, 810 13

Eckart, A. & Genzel, R. 1996, Nature, 383, 415 32

Eggen, O. J., Lynden-Bell, D., & Sandage, A. R. 1962, ApJ, 136, 748 8

Ellison, S. L., Mendel, J. T., Patton, D. R., & Scudder, J. M. 2013, MNRAS, 435, 3627 11

Ellison, S. L., Patton, D. R., Mendel, J. T., & Scudder, J. M. 2011, MNRAS, 418, 2043 10

Ellison, S. L., Patton, D. R., Simard, L., & McConnachie, A. W. 2008, AJ, 135, 1877 10

Ellison, S. L., Patton, D. R., Simard, L., et al. 2010, MNRAS, 407, 1514 10

Evans, Neal J., I., Dunham, M. M., Jørgensen, J. K., et al. 2009, ApJS, 181, 321 14

Event Horizon Telescope Collaboration, Akiyama, K., Alberdi, A., et al. 2019, ApJ, 875, L1 32

Faber, S. M., Willmer, C. N. A., Wolf, C., et al. 2007, ApJ, 665, 265 20

Fabian, A. C. 2012, ARA&A, 50, 455 23

Fabian, A. C., Celotti, A., & Erlund, M. C. 2006, MNRAS, 373, L16 23

Ferrière, K. M. 2001, Reviews of Modern Physics, 73, 1031 15

Fioc, M. & Rocca-Volmerange, B. 2019, A&A, 623, A143 13, 20, 21

Freundlich, J., Bouché, N. F., Contini, T., et al. 2021, MNRAS, 501, 1900 16

Friedmann, A. 1922, Zeitschrift fur Physik, 10, 377 2

Fukugita, M., Ichikawa, T., Gunn, J. E., et al. 1996, AJ, 111, 1748 6, 7

Gaibler, V., Khochfar, S., Krause, M., & Silk, J. 2012, MNRAS, 425, 438 24

Ge, J.-Q., Hu, C., Wang, J.-M., Bai, J.-M., & Zhang, S. 2012, ApJS, 201, 31 33, 35

Geller, M. J. & Huchra, J. P. 1989, Science, 246, 897 6

Genzel, R., Burkert, A., Bouché, N., et al. 2008, ApJ, 687, 59 30

Genzel, R., Tacconi, L. J., Eisenhauer, F., et al. 2006, Nature, 442, 786 30

Genzel, R., Tacconi, L. J., Lutz, D., et al. 2015, ApJ, 800, 20 16

Genzel, R., Thatte, N., Krabbe, A., Kroker, H., & Tacconi-Garman, L. E. 1996, ApJ, 472, 153 32

Gerke, B. F., Newman, J. A., Lotz, J., et al. 2007, ApJ, 660, L23 9, 32, 33

Ghez, A. M., Klein, B. L., Morris, M., & Becklin, E. E. 1998, ApJ, 509, 678 32

Ghez, A. M., Salim, S., Weinberg, N. N., et al. 2008, ApJ, 689, 1044 32

Giovanelli, R., Haynes, M. P., Kent, B. R., et al. 2005, AJ, 130, 2598 15

Goad, M. R., Korista, K. T., & Ruff, A. J. 2012, MNRAS, 426, 3086 18

Gonçalves, T. S., Martin, D. C., Menéndez-Delmestre, K., Wyder, T. K., & Koekemoer, A. 2012, ApJ, 759, 67 19

Gott, J. R., I. 1977, ARA&A, 15, 235 8

Greenstein, J. L. 1963, Nature, 197, 1041 22

Harikane, Y., Inoue, A. K., Mawatari, K., et al. 2022, ApJ, 929, 1 3

Heckman, T. M. 1980, A&A, 87, 152 25

Heckman, T. M. & Best, P. N. 2014, ARA&A, 52, 589 32

Hoyle, F. & Fowler, W. A. 1963a, Nature, 197, 533 22

Hoyle, F. & Fowler, W. A. 1963b, MNRAS, 125, 169 22

Hubble, E. 1929, Proceedings of the National Academy of Science, 15, 168 2

Hubble, E. P. 1925, The Observatory, 48, 139 2

Hubble, E. P. 1926, ApJ, 64, 321 3, 4

Hubble, E. P. 1927, The Observatory, 50, 276 4

Hubble, E. P. 1936, Realm of the Nebulae 4

Huchra, J., Davis, M., Latham, D., & Tonry, J. 1983, ApJS, 52, 89 6

Hunter, D. A., Gillett, F. C., Gallagher, J. S., I., Rice, W. L., & Low, F. J. 1986, ApJ, 303, 171 26

Israelian, G. 1997, BAAS, 29, 1466 22

Johnstone, D., Boonman, A. M. S., & van Dishoeck, E. F. 2003, A&A, 412, 157 16

Kauffmann, G., Heckman, T. M., White, S. D. M., et al. 2003, MNRAS, 341, 33 28, 29

Kauffmann, G., White, S. D. M., Heckman, T. M., et al. 2004, MNRAS, 353, 713 9

Kauffmann, J., Goldsmith, P. F., Melnick, G., et al. 2017, A&A, 605, L5 16

Kennicutt, Robert C., J. 1998a, ARA&A, 36, 189 26, 27

Kennicutt, Robert C., J. 1998b, ApJ, 498, 541 26

Kennicutt, Robert C., J., Tamblyn, P., & Congdon, C. E. 1994, ApJ, 435, 22 27

Kennicutt, R. C. & Evans, N. J. 2012, ARA&A, 50, 531 28

Kewley, L. J., Dopita, M. A., Sutherland, R. S., Heisler, C. A., & Trevena, J. 2001, ApJ, 556, 121 24

Kewley, L. J., Geller, M. J., Jansen, R. A., & Dopita, M. A. 2002, AJ, 124, 3135 27

Kewley, L. J., Groves, B., Kauffmann, G., & Heckman, T. 2006, MNRAS, 372, 961 24, 25

King, A. 2003, ApJ, 596, L27 23

Komossa, S., Burwitz, V., Hasinger, G., et al. 2003, ApJ, 582, L15 32

Kormendy, J. & Richstone, D. 1995, ARA&A, 33, 581 32

Krause, M., Alexander, P., Riley, J., & Hopton, D. 2012, MNRAS, 427, 3196 23

Lacy, M., Baum, S. A., Chandler, C. J., et al. 2020, PASP, 132, 035001 14

Lawrence, A., Warren, S. J., Almaini, O., et al. 2007, MNRAS, 379, 1599 13

Leavitt, H. S. 1908, Annals of Harvard College Observatory, 60, 87 1

Leavitt, H. S. & Pickering, E. C. 1912, Harvard College Observatory Circular, 173, 1 1

Lee, J. C., Whitmore, B. C., Thilker, D. A., et al. 2022, ApJS, 258, 10 14

Lehnert, M. D. & Heckman, T. M. 1996, ApJ, 472, 546 26

Lemaître, G. 1927, Annales de la Société Scientifique de Bruxelles, 47, 49 2

Lemaître, G. 1931, Nature, 127, 706 2

Leroy, A. K., Walter, F., Brinks, E., et al. 2008, AJ, 136, 2782 15

Linfield, R. 1982, ApJ, 254, 465 23

Liu, X., Guo, H., Shen, Y., Greene, J. E., & Strauss, M. A. 2018, ApJ, 862, 29 130

Liu, X., Shen, Y., Strauss, M. A., & Greene, J. E. 2010, ApJ, 708, 427 33

Lotz, J. M., Davis, M., Faber, S. M., et al. 2008, ApJ, 672, 177 11

Lotz, J. M., Jonsson, P., Cox, T. J., et al. 2011, ApJ, 742, 103 11, 132

Lotz, J. M., Primack, J., & Madau, P. 2004, AJ, 128, 163 10, 11

Madau, P. & Dickinson, M. 2014, ARA&A, 52, 415 9, 30, 132

Madau, P., Pozzetti, L., & Dickinson, M. 1998, ApJ, 498, 106 27

Maiolino, R. & Rieke, G. H. 1995, ApJ, 454, 95 22, 23

Malmquist, K. G. 1925, Meddelanden fran Lunds Astronomiska Observatorium Serie I, 106, 1 7

Maness, H. L., Taylor, G. B., Zavala, R. T., Peck, A. B., & Pollack, L. K. 2004, ApJ, 602, 123 32

Martin, D. C., Fanson, J., Schiminovich, D., et al. 2005, ApJ, 619, L1 13

Maschmann, D., Halle, A., Melchior, A.-L., Combes, F., & Chilingarian, I. V. 2022a, arXiv e-prints, arXiv:2212.02529 35, 69, 131

Maschmann, D. & Melchior, A.-L. 2019, A&A, 627, L3 35

Maschmann, D., Melchior, A.-L., Combes, F., et al. 2022b, A&A, 664, A125 3, 35, 93

Maschmann, D., Melchior, A.-L., Mamon, G. A., Chilingarian, I. V., & Katkov, I. Y. 2020, A&A, 641, A171 3, 20, 35, 37, 93, 94, 131

Mazzilli Ciraulo, B., Melchior, A.-L., Maschmann, D., et al. 2021, A&A, 653, A47 35, 131

Meert, A., Vikram, V., & Bernardi, M. 2015, MNRAS, 446, 3943 5

Meisenheimer, K., Roser, H. J., Hiltner, P. R., et al. 1989, A&A, 219, 63 23

Messier, C. 1781, Catalogue des Nébuleuses et des Amas d'Étoiles (Catalog of Nebulae and Star Clusters), Connoissance des Temps ou des Mouvements Célestes, for 1784, p. 227-267 1

Meurer, G. R., Heckman, T. M., Leitherer, C., et al. 1995, AJ, 110, 2665 26

Meyer, M., Robotham, A., Obreschkow, D., et al. 2017, PASA, 34, 52 15

Mhaskey, M., Paul, S., & Krishna, G. 2021, Astronomische Nachrichten, 342, 1126 23

Michelson, A. A. & Pease, F. G. 1921, ApJ, 53, 249 14

Mihos, J. C. & Hernquist, L. 1994a, ApJ, 437, L47 10

Mihos, J. C. & Hernquist, L. 1994b, ApJ, 425, L13 10

Mihos, J. C. & Hernquist, L. 1996, ApJ, 464, 641 10

Milosavljević, M. & Merritt, D. 2001, ApJ, 563, 34 32

Mo, H., van den Bosch, F. C., & White, S. 2010, Galaxy Formation and Evolution 18

Momcheva, I. G., Lee, J. C., Ly, C., et al. 2013, AJ, 145, 47 27

Müller-Sánchez, F., Comerford, J. M., Nevin, R., et al. 2015, ApJ, 813, 103 9, 34

Murray, N., Quataert, E., & Thompson, T. A. 2005, ApJ, 618, 569 23

Naab, T. & Ostriker, J. P. 2017, ARA&A, 55, 59 8, 25

Nelson, D., Springel, V., Pillepich, A., et al. 2019, Computational Astrophysics and Cosmology, 6, 2 131

Neugebauer, G., Habing, H. J., van Duinen, R., et al. 1984, ApJ, 278, L1 13

Nevin, R., Blecha, L., Comerford, J., & Greene, J. 2019, ApJ, 872, 76 11

Nevin, R., Blecha, L., Comerford, J., et al. 2021, ApJ, 912, 45 11

Nevin, R., Comerford, J., Müller-Sánchez, F., Barrows, R., & Cooper, M. 2016, ApJ, 832, 67 34

Noeske, K. G., Faber, S. M., Weiner, B. J., et al. 2007a, ApJ, 660, L47 30

Noeske, K. G., Weiner, B. J., Faber, S. M., et al. 2007b, ApJ, 660, L43 29, 30

Ossenkopf, V. & Henning, T. 1994, A&A, 291, 943 13

Osterbrock, D. E. & Ferland, G. J. 2006, Astrophysics of gaseous nebulae and active galactic nuclei 27

Patton, D. R., Ellison, S. L., Simard, L., McConnachie, A. W., & Mendel, J. T. 2011, MNRAS, 412, 591 10

Peebles, P. J. E. 1993, Principles of Physical Cosmology 2

Peebles, P. J. E., Phelps, S. D., Shaya, E. J., & Tully, R. B. 2001, ApJ, 554, 104 9

Perley, R. A. 1982, AJ, 87, 859 23

Petrosian, V. 1976, ApJ, 210, L53 7

Pilbratt, G. L., Riedinger, J. R., Passvogel, T., et al. 2010, A&A, 518, L1 14

Pimbblet, K. A., Smail, I., Kodama, T., et al. 2002, MNRAS, 331, 333 10

Planck Collaboration, Aghanim, N., Akrami, Y., et al. 2020, A&A, 641, A6 2

Richard, J., Kneib, J. P., Blake, C., et al. 2019, The Messenger, 175, 50 132

Rodighiero, G., Daddi, E., Baronchelli, I., et al. 2011, ApJ, 739, L40 29

Rodriguez, C., Taylor, G. B., Zavala, R. T., et al. 2006, ApJ, 646, 49 32

Rodriguez-Gomez, V., Snyder, G. F., Lotz, J. M., et al. 2019, MNRAS, 483, 4140 11

Rosa-González, D., Terlevich, E., & Terlevich, R. 2002, MNRAS, 332, 283 26

Sachdeva, S., Saha, K., & Singh, H. P. 2017, ApJ, 840, 79 132

Salim, S. 2014, Serbian Astronomical Journal, 189, 1 20

Salim, S., Lee, J. C., Janowiecki, S., et al. 2016, ApJS, 227, 2 28

Salim, S., Rich, R. M., Charlot, S., et al. 2007, ApJS, 173, 267 20

Salpeter, E. E. 1964, ApJ, 140, 796 22

Sanders, D. B. & Mirabel, I. F. 1996, ARA&A, 34, 749 27

Schawinski, K., Thomas, D., Sarzi, M., et al. 2007, MNRAS, 382, 1415 25

Schawinski, K., Urry, C. M., Simmons, B. D., et al. 2014, MNRAS, 440, 889 20

Schmidt, M. 1963, Nature, 197, 1040 22

Schreiber, C., Pannella, M., Elbaz, D., et al. 2015, A&A, 575, A74 29

Searle, L. & Zinn, R. 1978, ApJ, 225, 357 8

Sérsic, J. L. 1963, Boletin de la Asociacion Argentina de Astronomia La Plata Argentina, 6, 41 5

Seyfert, C. K. 1943, ApJ, 97, 28 22

Shabala, S. S., Ting, Y.-S., Kaviraj, S., et al. 2012, MNRAS, 423, 59 11

Shangguan, J., Liu, X., Ho, L. C., et al. 2016, ApJ, 823, 50 130

Shapley, H. 1918, ApJ, 48, 154 1

Shapley, H. & Curtis, H. D. 1921, Bulletin of the National Research Council, 2, 171 1, 2

Shaver, P. A., McGee, R. X., Newton, L. M., Danks, A. C., & Pottasch, S. R. 1983, MNRAS, 204, 53 17

Shields, J. C. 1992, ApJ, 399, L27 25

Shimwell, T. W., Tasse, C., Hardcastle, M. J., et al. 2019, A&A, 622, A1 14

Silk, J. 2005, MNRAS, 364, 1337 24

Silk, J. 2013, ApJ, 772, 112 24

Silk, J. & Rees, M. J. 1998, A&A, 331, L1 23

Smethurst, R. J., Masters, K. L., Simmons, B. D., et al. 2022, MNRAS, 510, 4126 19, 20

Smith, K. L., Shields, G. A., Bonning, E. W., et al. 2010, ApJ, 716, 866 33

Sodré, L., Ribeiro da Silva, A., & Santos, W. A. 2013, MNRAS, 434, 2503 19

Solomon, P. M., Downes, D., Radford, S. J. E., & Barrett, J. W. 1997, ApJ, 478, 144 16

Somerville, R. S. & Davé, R. 2015, ARA&A, 53, 51 8, 37

Sparre, M., Hayward, C. C., Springel, V., et al. 2015, MNRAS, 447, 3548 30

Speagle, J. S., Steinhardt, C. L., Capak, P. L., & Silverman, J. D. 2014, ApJS, 214, 15 29

Stanley, G. J. & Slee, O. B. 1950, Australian Journal of Scientific Research A Physical Sciences, 3, 234 22

Stark, D. P., Swinbank, A. M., Ellis, R. S., et al. 2008, Nature, 455, 775 30

Steinmetz, M. & Navarro, J. F. 2002, New Astronomy, 7, 155 8

Strateva, I., Ivezić, Ž., Knapp, G. R., et al. 2001, AJ, 122, 1861 20

Strong, A. W. & Mattox, J. R. 1996, A&A, 308, L21 16

Tacchella, S., Dekel, A., Carollo, C. M., et al. 2016, MNRAS, 457, 2790 30, 31

Tacchella, S., Trenti, M., & Carollo, C. M. 2013, ApJ, 768, L37 30

Tacconi, L. J., Genzel, R., Saintonge, A., et al. 2018, ApJ, 853, 179 16, 29

Tauris, T. M. & van den Heuvel, E. P. J. 2006, in Compact stellar X-ray sources, Vol. 39, 623–665 23

Tonini, C., Mutch, S. J., Croton, D. J., & Wyithe, J. S. B. 2016, MNRAS, 459, 4109 131

Toomre, A. & Toomre, J. 1972, ApJ, 178, 623 10, 11

Torrey, P., Vogelsberger, M., Genel, S., et al. 2014, MNRAS, 438, 1985 30

Townsley, L. K., Broos, P. S., Chu, Y.-H., et al. 2011, ApJS, 194, 15 17

Treister, E., Messias, H., Privon, G. C., et al. 2020, ApJ, 890, 149 131

Trujillo, I., Graham, A. W., & Caon, N. 2001, MNRAS, 326, 869 5

Turland, B. D. 1975, MNRAS, 170, 281 22

Turner, M. J. L., Abbey, A., Arnaud, M., et al. 2001, A&A, 365, L27 23

Urry, C. M. & Padovani, P. 1995, PASP, 107, 803 23

van der Marel, R. P., Fardal, M., Besla, G., et al. 2012, ApJ, 753, 8 9

VandenBerg, D. A., Brogaard, K., Leaman, R., & Casagrande, L. 2013, ApJ, 775, 134 20

Wang, J.-M., Chen, Y.-M., Hu, C., et al. 2009, ApJ, 705, L76 33

Weinberg, S. 1972, Gravitation and Cosmology: Principles and Applications of the General Theory of Relativity 2

Whitaker, K. E., van Dokkum, P. G., Brammer, G., & Franx, M. 2012, ApJ, 754, L29 29

White, R. L., Accomazzi, A., Berriman, G. B., et al. 2009, in astro2010: The Astronomy and Astrophysics Decadal Survey, Vol. 2010, P64 130

White, R. L., Becker, R. H., Helfand, D. J., & Gregg, M. D. 1997, ApJ, 475, 479 14

White, S. D. M. & Rees, M. J. 1978, MNRAS, 183, 341 8

Williams, J. P., Blitz, L., & McKee, C. F. 2000, in Protostars and Planets IV, ed. V. Mannings, A. P. Boss, & S. S. Russell, 97 16

Wilson, A. S. & Colbert, E. J. M. 1995, ApJ, 438, 62 23

Wilson, T., Rohlfs, K., & Huettemeister, S. 2008, Tools of Radio Astronomy, Astronomy and Astrophysics Library (Springer Berlin Heidelberg) 14

Wolfire, M. G., Hollenbach, D., & McKee, C. F. 2010, ApJ, 716, 1191 16

Wright, E. L., Eisenhardt, P. R. M., Mainzer, A. K., et al. 2010, AJ, 140, 1868 13

Yang, G., Boquien, M., Brandt, W. N., et al. 2022, ApJ, 927, 192 23

Yang, G., Boquien, M., Buat, V., et al. 2020, MNRAS, 491, 740 23

Zeldovich, Y. B. 1964, Dokl. Akad. Nauk SSSR, 155 22

RÉSUMÉ

La caractérisation de la croissance de la masse des galaxies est centrale pour la compréhension de leur évolution au cours du temps cosmique. Les fusions de galaxies jouent un rôle particulièrement important car elles peuvent transformer la morphologie des galaxies et alimenter leur formation d'étoiles. Comme les galaxies issues d'une fusion peuvent atteindre un état dynamique stabilisé rapidement après une fusion ou qu'il se peut qu'elles ne soient pas identifiées comme issues d'une fusion en raison d'un manque de résolution, les méthodes de détection sont cruciales pour les étudier. Les galaxies à raies d'émission doubles ont été beaucoup utilisées afin d'identifier les noyaux actifs de galaxies doubles qui correspondent à des étapes tardives des fusions de galaxies. Dans cette thèse, une discussion plus générale sur le phénomène des galaxies à raies d'émission à doubles-pics est présentée. À cette fin, un échantillon de galaxies à doubles-pics composé de 5663 galaxies est sélectionné dans le Sloan Digital Sky Survey et ses propriétés sont étudiées en détail. Afin de mieux comprendre les mécanismes sous-jacents, les signatures de doubles-pics apparaissant dans les modèles de disques et les simulations de galaxies isolées et de fusions de galaxies sont analysées. Pour mieux comprendre le lien entre la formation d'étoiles et les galaxies à raies d'émission à doubles-pics, des observations de gaz moléculaire, réalisées avec le télescope de 30m de l'IRAM, sont présentées et analysées. En conclusion, les barres et les fusions mineures sont nettement privilégiées comme explications des signatures à doubles-pics car cohérentes avec les caractéristiques trouvées. Cette thèse montre que les galaxies à raies d'émission à doubles-pics sont un aspect important pour les observations à haut redshift et représentent une méthode potentielle d'identification des fusions de galaxies dans les grands relevés à venir.

MOTS CLÉS

galaxies: cinématique et dynamique, galaxies: interactions, galaxies: évolution, galaxies: formation d'étoiles, Méthodes: numériques, techniques: spectroscopiques

ABSTRACT

A central aspect in understanding how galaxies evolved over cosmic time is to characterise their mass growth. Galaxy mergers, in particular, play an important role, since they can transform the galaxy's morphology and fuel star formation. Since galaxy mergers can rapidly relax after colliding or cannot be identified as such due to a lack of resolution, detection methods are crucial to study them. Double-peak emission-line galaxies have been used extensively in order to identify dual active galactic nuclei which are late stages of galaxy mergers. In this thesis, a more general discussion on the phenomenon of double-peak emission-line galaxies is presented. To this end, a double-peak galaxy sample consisting of 5 663 galaxies is selected from the Sloan Digital Sky Survey and the properties are studied in detail. To get a deeper understanding in the underlying mechanisms, double-peak signatures arising in disc models and simulations of isolated galaxies and galaxy mergers are analysed. To further understand the connection between star formation and double-peak emission-line galaxies molecular gas observations, conducted with the IRAM 30m telescope, are presented and analysed. In conclusion, there is a clear favouring of bar structures and minor mergers, which can explain the observed double-peak signatures and are also consistent with the characteristics found. This thesis shows that double-peak emission-line galaxies are an important aspect for high redshift observations and present a potential method of identifying galaxy mergers in larger upcoming surveys.

KEYWORDS

galaxies: kinematics and dynamics, galaxies: interactions, galaxies: evolution, galaxies: star formation, Methods: numerical, techniques: spectroscopic